Results of the B$_4$C Control Rod Test QUENCH-07

M. Steinbrück, C. Homann, A. Miassoedov,
G. Schanz, L. Sepold, U. Stegmaier,
H. Steiner, J. Stuckert
Institut für Materialforschung
Institut für Reaktorsicherheit
Programm Nukleare Sicherheitsforschung

Forschungszentrum Karlsruhe

in der Helmholtz-Gemeinschaft

Wissenschaftliche Berichte

FZKA 6746

Results of the B$_4$C Control Rod Test QUENCH-07

M. Steinbrück, C. Homann, A. Miassoedov, G. Schanz, L. Sepold,

U. Stegmaier, H. Steiner, J. Stuckert

Forschungszentrum Karlsruhe GmbH, Karlsruhe

2004

Zusammenfassung

Ergebnisse des B_4C-Steuerstab-Versuchs QUENCH-07

In den QUENCH-Versuchen soll der Wasserstoffquellterm bei der Einspeisung von Notkühl-wasser in einen trockenen, überhitzten Reaktorkern eines Leichtwasserreaktors (LWR) er-mittelt werden. Mit dem Experiment QUENCH-07, das am 25. Juli 2001 in der QUENCH-Versuchsanlage des Forschungszentrums Karlsruhe durchgeführt wurde, sollte der Einfluss des B_4C-Absorberstab-Versagens auf die Brennelementzerstörung sowie die Einwirkung der B_4C-Oxidation auf die Bildung gasförmiger Reaktionsprodukte, die das Verhalten der Spaltprodukte beeinflussen können, untersucht werden. Als Unterstützung des geplanten PHEBUS-FPT3-Experiments sollte QUENCH-07 insbesondere Informationen über die Bildung der gasförmigen Reaktionsprodukte H_2, CO, CO_2 und CH_4 (wichtig für die Bildung von flüchtigem CH_3J) während der Absorberstab-Zerstörung und der B_4C-Oxidation sowie über die Auswirkungen der Regelstabzerstörung auf die umgebenden Brennstäbe liefern.

Das QUENCH-Testbündel ist mit 20 Brennstabsimulatoren bestückt und hat eine Gesamt-länge von ca. 2,50 m. Die Brennstabsimulatoren sind auf einer Länge von 1024 mm beheizt, der Zentralstab ist unbeheizt. In diesem Versuch ist der Zentralstab ein Regelstabsimulator, der aus einem B_4C-Absorberstab mit der Hülle aus rostfreiem Stahl und einem Führungsrohr aus Zircaloy-4 besteht. Das Massenverhältnis von Stahl zu B_4C beträgt 3,5 und ist damit identisch zu dem im geplanten PHEBUS-FPT3-Experiment. Als Heizer werden Wolfram-Stäbe von 6 mm Durchmesser verwendet, die im Zentrum der Brennstabsimulatoren angeordnet und von ZrO_2-Ringtabletten, die die UO_2-Tabletten simulieren, umgeben sind. Die Stabhüllen sind identisch mit denen kommerzieller LWR-Hüllrohre: Zircaloy-4, 10,75 mm Außendurchmesser und 0,725 mm Wanddicke. Die Teststrecke ist mit Thermoelementen (TE) instrumentiert, die auf Messebenen zwischen -250 und 1350 mm an den Stabhüllen, dem Shroud und dem Kühlmantel befestigt sind. Zusätzlich wurden drei TE in einer Nut der Absorberstabhülle des Zentralstabes sowie je ein Zentral-TE in drei von vier Eckstäben montiert. Der Wasserstoff wurde in erster Linie mit Hilfe eines Massenspektrometers analysiert.

Bis zum Beginn der Kühlphase wurden 3 g/s überhitzter Dampf zusammen mit 3 g/s Argon als Trägergas für die Wasserstoffanalyse am unteren Ende in die Teststrecke eingespeist. Diese verlassen die Teststrecke zusammen mit dem Wasserstoff und anderen gasförmigen Reaktionsprodukten, die sich durch die Reaktion von Zirkonium und B_4C mit Wasserdampf gebildet haben, am oberen Ende. Zum Abschrecken wurden 15 g/s Sattdampf von unten in das Bündel eingespeist und die Argoneinspeisung zum Bündelkopf umgeschaltet.

Der Absorberstab versagte bei ~1585 K ungefähr drei Minuten vor Beginn der Voroxidationsphase (15 Minuten bei ~1723 K). Kurz nach Versagen des Absorberstabs wurden CO, CO_2, H_2, Meta- und Orthoborsäure zusammen mit sehr geringen Mengen an Methan mittels Massenspektrometer detektiert. In der darauf folgenden transienten Phase mit Aufheizraten von 0.35 – 0.45 K/s kam es am oberen Ende der beheizten Zone und darüber zu ersten (moderaten) Temperatureskalationen. In dieser Zeit versagten die meisten Thermoelemente in der heißen Zone, so dass die maximale Bündeltemperatur nicht ein-

deutig bestimmt werden kann. Am Ende der transienten Phase versagten Brennstabhüllen und Shroud (Bündelumgebungsrohr) bei einer Temperatur von ~2000 K.

Bis zur Ebene 650 mm erfolgte die Abkühlung sofort, oberhalb 650 mm wurde die Kühlung verzögert. In den Ebenen oberhalb der beheizten Zone löste die Dampfeinspeisung eine Temperatureskalation aus, die Aufheizraten von über 40 K/s zur Folge hatte. Die gemessene Maximaltemperatur beträgt 2320 K (Ebene 950 mm). Diese Temperatur wie auch die höchsten Temperaturen der darüber liegenden Ebenen wurden zu Beginn der Abkühlphase gemessen. In den unteren Ebenen hingegen dominierte der Kühleffekt durch den erhöhten Dampfdurchsatz. Im Zusammenhang mit den hohen Temperaturen in den oberen Bündelebenen in der Zeit kurz nach dem Beginn der Kühlphase wurde eine erhöhte Freisetzung aller gasförmigen Reaktionsprodukte aus der Absorber-Wechselwirkung beobachtet.

Die Auswertung der Daten des Massenspektrometers unter Einbeziehung des Bündelzustands nach dem Versuch ergab eine Gesamtmenge von ~180 g freigesetztem Wasserstoff. Der Hauptanteil davon, nämlich 120 g, wurde während der Kühlphase gebildet. Ebenfalls in der Kühlphase stieg die Erzeugung von CO und CO_2 an. Weiterhin wurde ein kleiner aber deutlicher Anstieg von Methan zusammen mit einem Anstieg von Borsäure festgestellt. Es ist nicht klar, inwieweit die Temperatureskalation und die erhöhte Gasfreisetzung in der Abkühlphase hauptsächlich durch den Einfluss des B_4C verursacht wurden, da neben dem erstmaligen Einsatz des B_4C-Stahl-Zirkaloy-Regelstabs auch die Dampf-Einspeiserate der Kühlphase gegenüber den früheren Versuchen von 50 auf 15 g/s reduziert worden war.

Die metallografische Nachuntersuchung zeigte die Bildung von Schmelze durch eutektische Wechselwirkung zwischen den Komponenten des Regelstabs, die Ansammlung von Schmelze in seinem Inneren und die Absorberschmelze-Verlagerung außerhalb, in Form nicht-oxidierter Tropfen. Die Absorber-Tablettensäule blieb bis ~800 mm Bündelhöhe erhalten, während darüber keine freiliegenden Reststücke der Absorbertabletten gefunden wurden. In dieser (heißen) Zone fand eine starke Zerstörung des gesamten Bündels statt. Sie ist gekennzeichnet durch die Verteilung von Absorberschmelze, das teilweise Schmelzen des Brennstabhüllrohr-Materials vor seiner vollständigen Oxidation und durch die nahezu abgeschlossene Oxidation von Schmelze-Ansammlungen. Der Endzustand des Stabbündels lässt einen wesentlichen Beitrag der Kühlphase zur Oxidation und Versprödung erkennen.

Mit dem Rechenprogramm SCDAP/RELAP5 wurden Vorausrechnungen durchgeführt, um die Integrität der Versuchsanlage während der Durchführung des Versuchs sicher zu stellen und den Testablauf zu optimieren. Der große Rechenaufwand ist ein Zeichen für die Probleme bei der Festlegung eines brauchbaren Testablaufs. Nachrechnungen mit SCDAP/RELAP5 zeigen die Güte der Modellierung und helfen, die Versuchsergebnisse zu verstehen.

Abstract

The QUENCH experiments are to investigate the hydrogen source term resulting from the water or steam injection into an uncovered core of a Light-Water Reactor (LWR). The QUENCH-07 experiment was to investigate the effect of B_4C absorber rod failure on fuel bundle degradation as well as the B_4C oxidation. Complementary to the planned PHEBUS FPT3 experiment, QUENCH-07 was expected to particularly provide information on the formation of gaseous reaction products during the absorber rod degradation and B_4C oxidation, in particular of H_2, CO, CO_2 and CH_4, and on the impact of control rod degradation on surrounding fuel rods.

The test bundle is made up of 20 fuel rod simulators with a length of approximately 2.5 m. The fuel rod simulators are heated over a length of 1024 mm, the central rod is unheated and in this experiment was made of an absorber rod with B_4C pellets and stainless steel cladding, and of a Zircaloy-4 guide tube. The steel to B_4C mass ratio of 3.5 is identical to that in the future PHEBUS FPT3 experiment. Heating is carried out electrically using 6-mm-diameter tungsten heating elements, which are installed in the center of the rods and which are surrounded by annular ZrO_2 pellets simulating the UO_2 fuel pellets. The Zircaloy-4 rod cladding is identical to that used in LWRs: 10.75 (OD) x 0.725 mm. The test section is instrumented with thermocouples (TC) that are attached to the cladding, the shroud, and the cooling jackets at elevations between −250 mm and 1350 mm. Besides, three TCs are embedded in a groove of the absorber rod cladding inside the central rod, and centerline TCs were mounted inside three of the four corner rods. The hydrogen is analyzed by three different instruments: two mass spectrometers and a hydrogen analyzer "Caldos 7 G" with the principle of measurement based on heat conduction of the sampling gases.

QUENCH-07 performed at the Forschungszentrum Karlsruhe on 25 July, 2001 was the first experiment with an absorber rod in the bundle. Until the onset of cooldown 3 g/s of superheated steam and 3 g/s of argon as carrier gas enter the test bundle at the bottom and exit at the top together with the gases that are produced in the reactions of zirconium, boron carbide, and stainless steel with steam. Cooling was initiated by injecting 15 g/s of saturated steam at the bottom and switching the argon flow to the bundle head.

The control rod failed at ~1585 K (2036 s) shortly before the QUENCH-07 test bundle was conditioned (oxidized) at ~1723 K for 15 minutes. During the conditioning phase CO, CO_2, H_2, metaboric and orthoboric acids were detected by the mass spectrometer together with very small quantities of methane. In the subsequent transient with heatup rates of 0.35-0.45 K/s temperature escalations started at the top of the heated zone and above. It was during this phase that most of the cladding thermocouples failed. The rod cladding as well as the shroud failed at the end of the transient phase at temperatures of around ~2000 K.

Up to the 650 mm level cooling was immediate. Above 650 mm delayed cooling occurred. The maximum measured rod temperature was ~2320 K at the 950 mm level. This temperature as well as the maximum temperatures at the elevations above were measured in the cooldown phase. At the elevations above the heated zone the steam injection of 15 g/s triggered a temperature excursion with subsequent heatup rates of more than 40 K/s. At the

lower elevations, however, the cooling effect dominated due to the increase in the coolant flow.

Associated with the high temperatures at the upper elevations during the period shortly after beginning of the cooldown phase an increased release of all gaseous reaction products was observed.

The evaluation of the mass spectrometer data as well as of the post-test bundle status results in ~180 g of hydrogen release in total, most of which was during the cooldown, i.e. 120 g. In addition, there were large increases in the generation of CO and CO_2 as well as a small but detectable amount of methane, accompanied by an increase in boric acid formation. As not only the B_4C-SS absorber rod material was a novel feature but also the steam flow rate during cooldown was reduced in comparison with previous tests, it is not yet clear to which extent the escalation and the severe test bundle degradation can mainly be attributed to the effect of B_4C.

The metallographic examination showed melt formation by eutectic interaction between the control rod components, control rod-internal melt accumulation and external long-range relocation as non-oxidized melt droplets. The absorber pellets remained as a stack up to ~800 mm elevation. No bare residues of absorber pellets were observed above this level. In this hot zone a strong degradation of the whole bundle took place characterized by melt dispersion of control rod material, partial melting of the fuel rod cladding before complete oxidative consumption, and almost total oxidation of the local melt pools. The final bundle state indicated essential contributions of the cool-down phase to oxidation and fragmentation mechanisms.

Pretest calculations with the SCDAP/RELAP5 computer code were done to provide sufficient confidence that the integrity of the QUENCH facility would be maintained during the test and to optimize the test conduct. The large computational effort is an indication for the problems to define a feasible test conduct. SCDAP/RELAP5 posttest calculations show the quality of modelling and help to understand the test results.

Contents

List of Tables

List of Figures

List of Figures

List of Figures

Introduction

The most important accident management measure to terminate a severe accident transient in a Light Water Reactor (LWR) is the injection of water to cool the uncovered degraded core. Analysis of the TMI-2 [1] accident and the results of integral out-of-pile (CORA [2, 3]) and in-pile experiments (LOFT [4], PHEBUS, PBF) have shown that before the water succeeds in cooling the fuel pins there can be an enhanced oxidation of the Zircaloy cladding that in turn causes a sharp increase in temperature, hydrogen production and fission product release.

Besides, quenching is considered a worst-case accident scenario regarding hydrogen release to the containment. For in- and ex-vessel safety analyses one has to prove that the hydrogen release rate and total amount do not exceed limits for the considered power plant. The hydrogen generation rate must be known to design appropriately accident mitigation measures as passive autocatalytic recombiners and igniters.

The physical and chemical phenomena of the hydrogen release are, however, not sufficiently well understood. The increased hydrogen production during quenching cannot be determined on the basis of the available Zircaloy/steam oxidation correlations. Presently it is assumed that the following phenomena lead to an enhanced oxidation and hydrogen generation:

- Melt oxidation,

- Steam starvation conditions,

- Crack surfaces oxidation.

In most of the code systems describing severe fuel damage, these phenomena are either not considered or only modeled in a simplified empirical manner.

In addition, no models are yet available to predict correctly the thermal-hydraulic or the clad behavior of the quenching processes in the CORA and LOFT LP-FP-2 tests. An extensive experimental database is therefore needed as a basis for model development and code improvement.

The Forschungszentrum Karlsruhe has therefore started the QUENCH program on the investigation of coolability and determination of the hydrogen source term. The main objectives of this program are:

- The provision of an extensive experimental database for the development of detailed mechanistic fragmentation models,

- The examination of the physico-chemical behavior of overheated fuel elements under different flooding conditions,

- The provision of an improved understanding of the effects of water injection at different stages of a degraded core,

- The determination of cladding failure criteria, cracking of oxide layers, exposure of new metallic surfaces to steam

- The investigation of the oxide layer degradation under steam starvation conditions and influence of this phenomenon on subsequent flooding,

- The investigation of the melt oxidation process,

- The determination of the hydrogen source term.

The experimental part of the QUENCH program began with small-scale experiments with short Zircaloy fuel rod segments [5, 6]. On the basis of these results well-instrumented large-scale bundle experiments with fuel rod simulators under nearly adiabatic conditions are performed in the QUENCH facility at the Forschungszentrum Karlsruhe. The large-scale bundle experiments are more representative of prototypic reactor accident conditions than are the single-rod experiments. Important parameters of the bundle test program (see Table 1) are: quench medium, i.e. water or steam, fluid injection rate, cladding oxide layer thickness, and the temperature at onset of flooding [8].

The seventh bundle experiment, QUENCH-07, was performed at the Forschungszentrum Karlsruhe on 25 July, 2001. This test was the first in QUENCH series with B_4C absorber rod. The main objectives of the test were the investigation of the impact of B_4C and stainless steel on bundle degradation and composition of the gaseous reaction products formed during oxidation of the B_4C and B, C containing melts. This report describes the test facility and the test bundle, and the main results of the QUENCH-07 experiment including the posttest examination. In addition, two sections are dedicated to the calculational support performed with the SCDAP/RELAP5 computer code and the CALUMO bundle code.

The bundle test QUENCH-07 was conducted as one part of the program on the investigation of severe fuel damage at FZK consisting of integral tests, separate-effects tests, modeling, and code application. Most of the results were obtained within the frame of the "fifth framework programme of the European Community for research, technological development and demonstration activities (1998 to 2002)", particularly within the COLOSS program in the years 2000-2002. Extensive single-effects experiments have been conducted on the oxidation of boron carbide and absorber melts as well as on the degradation of $B_4C/SS/Zry$ control rods, which has been reported elsewhere [18, 19].

1 Description of the Test Facility

The QUENCH test facility consists of the following component systems:

- the test section with 21 fuel rod simulators (QUENCH-07: 20 fuel rod simulators and one control rod)
- the electric power supply for the test bundle heating
- the water and steam supply system
- the argon gas supply system
- the hydrogen measurement devices
- the process control system
- the data acquisition system.

A simplified flow diagram of the QUENCH test facility is given in Fig. 1, a three-dimensional schematic of the components in Fig. 2. The main component of the facility is the test section with the test bundle (Figs. 3 and 4). The superheated steam from the steam generator and superheater together with argon as the carrier gas for the hydrogen detection systems enter the test bundle at the bottom end. The steam that is not consumed, the argon, the hydrogen, and the carbon and boron containing gases produced in the zirconium-steam and B_4C-steam reactions flow from the bundle outlet through a water-cooled off-gas pipe to the condenser (Figs. 1 and 2). Here the steam is separated from the non-condensable gases. The cooldown phase with steam is initiated by turning off the superheated steam of 3 g/s and injecting the saturated steam with 15 g/s whereas the argon mass flow rate remains unchanged.

The design characteristics of the test bundle are given in Table 2. The test bundle is made up of 20 fuel rod simulators, each with a length of approximately 2.5 m, of one central control rod, and of four corner rods (see cross section in Fig. 5). Twenty fuel rod simulators are heated electrically over a length of 1024 mm, the one unheated fuel rod simulator is located in the center of the test bundle. The fuel rod simulators are held in their positions by five grid spacers, four of zircaloy, and one of inconel in the lower bundle zone (Figs. 6, 7, and 9). The cladding of the fuel rod simulators is identical to that used in PWRs with respect to material and dimensions, i.e. Zircaloy-4, 10.75 mm outside diameter, 0.725 mm wall thickness (see also Table 2). The rods are filled with a mixture of 95 % argon and 5 % krypton to approx. 0.22 MPa, i.e. a pressure slightly above the system pressure. The gas filling of all the heated rods is realized by a channel-like connection system inside the lower sealing plate. The krypton additive allows detecting rod failure of the heated rods during the experiment with help of the mass spectrometer. In this experiment the central rod contains boron carbide (B_4C) pellets with a stack length of ~1 m (to represent the neutron absorber), stainless steel cladding, and is surrounded by a Zircaloy-4 guide tube. The steel to B4C mass ratio of 3.5 is identical to that in the planned PHEBUS FPT-3 experiment. The filling gas for the central rod is helium with a pressure of 0.12 MPa to detect absorber rod failure. To avoid stagnant steam conditions around the absorber rod the guide tube holds four holes of 4 mm diameter each at the bottom (-34 mm) and the top (1179 mm).

Heating of the 20 fuel rod simulators is electrical. The total heating power available is 70 kW, distributed among the two groups of heated rods with 35 kW each. The first group consists of the inner eight rods (rod numbers 2-9), the second group consists of the outer twelve rods (rod numbers 10-21). The rod designation can be taken from Fig. 8. Tungsten heating elements of 6 mm diameter are installed in the center of the rods and are surrounded by annular ZrO_2 pellets (Fig. 6). The tungsten heaters are connected to electrodes made of molybdenum and copper at each end of the heater. The molybdenum and copper electrodes are joined by high-frequency/high-temperature brazing performed under vacuum. For electrical insulation the surfaces of the brazed electrodes are plasma-coated with 0.2 mm ZrO_2. To protect the copper electrodes and the O-ring-sealed wall penetrations against excessive heat they are water-cooled (lower and upper cooling chamber). The copper electrodes are connected to the DC electric power supply by means of special sliding contacts at the top and bottom.

The four corner positions of the bundle are occupied either by solid zircaloy rods with a diameter of 6 mm or by solid rods (upper part) and zircaloy tubes (lower part) of $\varnothing$ 6 x 0.5 mm for thermocouple instrumentation at the inside (Fig. 8). The positioning of the four corner rods avoids an atypically large flow cross section at the outer positions and hence helps to obtain a rather uniform radial temperature profile. A solid zircaloy rod (rod B) can be pulled out to determine the axial oxide layer thickness at that time.

The lower boundary for the lower cooling chamber is a sealing plate made of stainless steel with plastic inlays for electrical insulation, sealed to the system by O-shaped rings. The upper boundary of the lower cooling chamber is a sealing plate of stainless steel. An insulation plate made of plastic (PEEK) forms the top of the upper cooling chamber, and a sealing plate of Al_2O_3 (heat-protection shield) is the lower boundary of the upper cooling chamber (see Fig. 6).

In the region below the upper Al_2O_3 plate the copper electrode is connected firmly to the cladding. This is done by hammering the cladding onto the electrode with a sleeve of boron nitride put between electrode and cladding for electrical insulation. The axial position of the fuel rod simulator in the test bundle is fixed by a groove and a locking ring in the upmost region of the Cu electrodes. Referred to the test bundle the fixation of the fuel rod simulators is located directly above the upper edge of the upper insulation plate. So, during operation the fuel rod simulators are allowed to expand downwards. Clearance for expansion of the test rods is provided in the region of the lower sealing plate. Also in this region relative movement between cladding and internal heater/electrode can take place.

The test bundle is surrounded by a 2.38 mm thick shroud (80 mm ID) made of zircaloy with a 37 mm thick ZrO_2 fiber insulation and an annular cooling jacket made of stainless steel (Figs. 4 and 5). The 6.7 mm annulus of the cooling jacket is cooled by an argon flow. Above the heated zone, i.e. above the 1024 mm elevation there is no ZrO_2 fiber insulation to allow for higher radial heat losses. This region of the cooling jacket is cooled by a water flow (Figs. 3 and 4). Both, the lack of ZrO_2 insulation above the heated region and the water cooling force the axial temperature maximum downward.

2   Test Bundle Assembly

The test section consists of three subassemblies pre-assembled separately. One subassembly comprises the cooling jacket with the bundle head casing; the second subassembly includes the instrumented shroud with the bundle foot; and the third subassembly is composed of the instrumented test bundle with the bundle head. The test bundle and the shroud, including the respective thermocouples, must be replaced for each experiment. The instrumentation of the bundle head and the foot as well as the cooling jacket, however, remains unchanged in the standard-type tests.

3   Test Bundle Instrumentation

The test bundle was instrumented with sheathed thermocouples attached to the rod claddings at 17 different elevations between –250 mm and 1350 mm and at different orientations (Figs. 8 and 9). The elevations of the surface-mounted shroud thermocouples are from –250 mm to 1250 mm. In the lower bundle region, i.e. up to the 550 mm elevation, NiCr/Ni thermocouples (1 mm diameter) are used for temperature measurement of rod cladding and shroud as is illustrated in Fig. 9. The thermocouples of the hot zone are high-temperature thermocouples with W-5Re/W-26Re wires, HfO_2 insulation, and a duplex sheath of tantalum (internal)/zirconium with an outside diameter of 2.1 mm (Fig. 10). The leads of the thermocouples from –250 mm to 650 mm leave the test section at the bottom whereas the TCs above 650 mm are routed to the top. Problems resulting from those thermocouples when TC cables pass through the hot zone are discussed in the appendix of the QUENCH-09 report [20] as well as at the QUENCH web site [21].

The thermocouple attachment technique for the surface-mounted high-temperature TCs is illustrated in Fig. 11. The TC tip is held in place by two clamps of zirconium. As these clamps are prone to oxidation and embrittlement in a steam environment, an Ir-Rh wire of 0.25 mm diameter is additionally used in the experiments with pre-oxidation as it was the case in test bundle QUENCH-07.

The thermocouples attached to the outer surface of the rod cladding at elevations between -50 and 1350 mm are designated "TFS" for the heated rods, and "TCRI" is the designation for the NiCr/Ni-type thermocouples embedded in grooves of the absorber rod cladding outer surface at 750, 850, and 950 mm elevation. The shroud thermocouples with the designation "TSH" are mounted at the outer surface between –250 mm and 1250 mm.

The wall of the inner tube of the cooling jacket is instrumented between –250 mm and 1150 mm with 22 NiCr/Ni thermocouples (designation "TCI"). Five NiCr/Ni thermocouples are fixed at the outer surface of the outer tube of the cooling jacket ("TCO"). The designation of the thermocouples inside the zircaloy instrumentation rods (corner positions) is "TIT" (Fig. 12). Three of the four corner rods of the QUENCH-07 test bundle were instrumented as follows:

- Rod A: W/Re, 2.1 mm diameter, Zr/Ta duplex sheath, 950 mm elevation (TIT A/13)
- Rod C: NiCr/Ni, 1 mm diameter, stainless steel sheath, 550 mm elevation (TIT C/9)

- Rod D: W/Re, 2.1 mm diameter, Zr/Ta duplex sheath, 850 mm elevation (TIT D/12).

A list of the instruments for experiment QUENCH-07 installed in the test section and at the test loop is given in Table 3. The thermocouples that failed prior or during the test are listed in Table 4.

4   Hydrogen Measurement Devices

The hydrogen is analyzed by three different measurement systems: (1) a Balzers mass spectrometer (MS) "GAM 300" (Fig. 13) located at the off-gas pipe between the test section and the condenser, (2) a hydrogen detection system "Caldos 7 G" (Fig. 15) located downstream the condenser, (3) a second, simpler mass spectrometer "Prisma" made by Balzers installed close to the Caldos device (see Fig. 2). So, the non-condensable off-gas passed at first the "GAM 300" MS, then the condenser, the "Prisma" MS, and eventually the Caldos analyzer before it exited to the outside. Due to their different locations in the facility the mass spectrometer "GAM 300" responds almost immediately (less than 5 s) to a change in the gas composition in the bundle whereas the mass spectrometer "Prisma" and the Caldos device have a delay time of about 20 – 30 s.

The mass spectrometer "BALZERS GAM 300" is a completely computer-controlled quadrupole MS with an 8 mm rod system which allows quantitative measurement of gas concentrations down to about 10 ppm. For the MS measurement a sampling tube is inserted in the off-gas pipe (Fig. 14). It has several holes at different elevations to guarantee that the sampling of the gas to be analyzed is representative. The temperature and pressure of the analyzed gas are measured near the inlet valve of the MS. To avoid steam condensation in the gas pipes between the sampling position and the MS the temperature of the gas at the MS inlet is controlled by a heat exchanger to be between 110 °C and 150 °C (the upper operating temperature of the MS inlet valves). This allows the MS to analyze the steam production rate assuming that no significant condensation takes place in the off-gas pipe upstream the sampling position. Besides, the concentrations of the following species were continuously measured by the mass spectrometer during all test phases: argon, hydrogen, CO, CO_2, CH_4, oxygen, as well as krypton and helium.

The absorber rod was filled with helium allowing the detection of the first failure of the control rod cladding. The MS is calibrated for H_2, CO, CO_2, and CH_4 with well-defined argon/gas mixtures and for steam with mixtures of argon and steam supplied by the steam generator of a Bronkhorst controlled evaporator mixing (CEM) system. He, Kr as well as boric acids are only qualitatively measured. As the fuel rod simulators are filled with a mixture of argon and 5% krypton, the measurement of krypton can be used as an indicator for a cladding failure. The MS off-gas is released into the atmosphere because the amount of the gases taken out of the system is negligible.

The principle of measurement of the Caldos system is based on the different heat conductivities of different gases. To avoid any moisture the analyzed gas passes a gas cooler, which is controlled at 296 K (Fig. 15). The response time of the gas analyzer is documented in the manufacturer's manual to be 2 s, i.e. a time in which 90 % of the final value should be reached. As the Caldos analyzer is calibrated for an argon/hydrogen

mixture, the accuracy of the hydrogen measurement is affected by the presence of additional gases, e.g. reaction products from the B_4C oxidation during the QUENCH-07 experiment.

5   Data Acquisition and Process Control

A computer-based control and data acquisition system is used in the QUENCH facility. Data acquisition, data storage, online visualization as well as process control, control engineering and system protection are accomplished by four computer systems that are linked in a network.

The data acquisition system allows recording of about 200 measurement channels at a maximum frequency of 25 Hz per channel. The experimental data and the date and time of the data acquisition are stored as raw data in binary format. After the experiment the raw data are converted into SI units and stored as ASCII data.

For process control, a system flow chart with the most important actual measurement values is displayed on the computer screen. Furthermore, the operating mode of the active components (pumps, steam generator, superheater, DC power system, valves) is indicated. Blocking systems and limit switches ensure safe plant operation. Operating test phases, e.g. heatup or quenching phases, are pre-programmed and can be started on demand during the experiment. The parameter settings of the control circuits and devices can be modified online.

Online visualization allows to observe and to document the current values of selected measurement positions in the form of tables or plots. Eight diagrams with six curves each can be displayed as graphs. This means that altogether 48 measurement channels can be selected and displayed online during the course of the experiment.

The data of the main data acquisition system and of the mass spectrometers were stored on different computers. Both computers were synchronized by radio-controlled clocks.

The data of the main acquisition system were stored at the following frequencies:

0 – 328 s	0.25 Hz
328 – 3123 s	1 Hz
3123 – 4126.6 s	5 Hz
4126.6 – 5530.6 s	0.25 Hz

The mass spectrometer data were recorded at a frequency of around 0.25 Hz during the entire test.

6 Test Conduct and Pertinent Results

In general, a QUENCH experiment consists of the following test phases: Heatup, pre-oxidation (optional), transient, and cooldown. During all phases except the cooldown superheated steam and argon as carrier gas enter the test bundle at the bottom and leave it at the top together with the gaseous reaction products resulting from the oxidation of bundle components. Cooldown is accomplished by injecting water or saturated steam at the bottom of the test section. For both cases the superheated steam is turned off upon injection.

The conduct of the QUENCH-07 experiment is illustrated in Fig. 16. The sequence of events is summarized in Table 5. The test phases are illustrated in Fig. 17, top with help of the temperature measured by thermocouple TIT A/13. QUENCH-07 test phases and objectives were as follows.

  I. Heatup to ~873 K.
 II. Heatup with 0.3-0.5 K/s to ~1723 K. Failure of B_4C control rod leading to B_4C-SS-Zry melt formation and relocation.
III. Conditioning the test bundle at a temperature plateau of ~1723 K for ~15 min, i.e. oxidation of cladding, shroud, and of the residual B_4C and relocated products under stationary conditions.
 IV. Transient phase with a heatup rate of 0.35-0.45 K/s to a maximum temperature of ~2300 K. Delayed oxidation of B, C - containing compounds at high temperature.
  V. Cooldown of the partially degraded bundle. Exposure of non-oxidized B, C-containing materials.

Up to the end of test phase IV the atmosphere consisted of flowing argon (3 g/s) and overheated steam (3 g/s). Then the steam flow of 3 g/s was turned off and the cooldown steam (saturated) of 15 g/s turned on.

At phase I the electrical power was 3.8 kW, then raised smoothly and held constant at 13.1 kW in phase II until the target temperature of ~1723 K was reached at 2200 s. In phase III the power was decreased from 13.1 kW to 8 kW and then controlled to maintain the temperature at that level for a period of ~15 minutes (Fig. 17 bottom). Fig. 18 bottom presents the coolant temperatures at the bundle inlet (T 511), -250 mm elevation (TFS 2/1), and at the bundle outlet (T 512). The rod cladding temperatures at the lower bundle elevations are given in Fig. 19 and the shroud temperatures in Fig. 20. In addition, the axial temperature profiles of the cladding thermocouples located in the inner coolant channel (TFS at rod type 2), of those located in the outer coolant channel (TFS at rod type 5), and of the shroud thermocouples (TSH) are given in Figs. 22 and 23. The temperature profiles are representative for the B_4C oxidation phase, i.e. 2700 s in the test, and for the start of the transient, i.e. 3150 s, respectively.

Even before phase III began, i.e. at 2036 s, helium was first detected in the off-gas, in conjunction with a local perturbation of the control rod temperature, thus indicating control rod failure at ~1585 K (Figs. 21 and 25 bottom). The formation of CO and CO_2 was observed shortly afterwards (see first increase of the data in Fig. 30 top). During the 15 minutes temperature plateau the production rates of CO, CO_2 and H_2 were approximately constant as

can also be seen in this figure. Some methane was also observed but in a much smaller quantity. Metaboric and orthoboric acids were also detected by the mass spectrometer (Fig. 31). Fig. 32 provides information on the boron concentration in the off-gas measured off-line in the steam condensate of the mass spectrometer.

At the end of the temperature plateau (phase III) corner rod B was removed from the bundle in order to check the extent of oxidation (see section on "Metallographic Examination"), before going into transient phase IV. This phase started at 3140 s by increasing the power in a linear mode, at 6 W/s. This was continued until the pre-determined maximum temperature of ~2300 K was reached. The temperature increase in the bundle led to failures of most of the outer cladding thermocouples (type TFS) in the hot zone (see Table 4) due to their exposure to the steam atmosphere at high temperature in the previous test phase. The increase in temperature was accompanied by a significant increase of all the gaseous reaction products except methane. Towards the end of this phase there were indications of failure of some heater rods and the shroud. The heatup rate of the rod bundle during the transient evaluated on the bases of TIT A/13 (see Fig. 18 top) and TSH 13/90, both at level 950 mm, was 0.44 K/s (1770-1850 K) and 0.35 K/s (1700-1770 K), respectively. To compare with previous experiments the shroud data, i.e. TSH 13/90, should be taken as they reflect similar rise rates as the TCRC 13 data which are available from tests without absorber rod.

A first temperature excursion in the rod bundle was observed at the 950 mm elevation when the temperature there reached ~1850 K (TIT A/13, see Table 6). Shortly after this time the shroud thermocouples TSH 15/0 and 15/180 indicated a temperature excursion at the 1150 mm level at around 1680 K. The rod cladding as well as the shroud failed at the end of the transient phase, i.e. at 3481 s and 3486 s, respectively, at temperatures of around ~2000 K. The times were evaluated with help of the rod internal pressure P 411 and the krypton signal for the rod failure and by means of the pressure in the insulation annulus P 406 for the shroud failure (Fig. 25 top and 26).

The cooldown (phase V) was initiated at 3557 s when the two shroud thermocouples at 950 mm, i.e. TSH 13/90 and TSH 13/270, had exceeded 2073 K. Cold steam was then injected at a rate of 15 g/s. The power ramp was continued for ~20 s and then the electric power was reduced from 18.5 to 4 kW in 15 s and kept constant for ~150 s. The electrical power was then shut off but the steam injection continued until cooldown to ~473 K had been achieved.

The maximum rod temperature of 2316 K was measured with thermocouple TIT A/13 at 3591 s, i.e. in the cooldown phase. The maximum temperatures at this elevation (950 mm) and above were all measured in the cooldown phase (Tables 7 and 8). Up to the 650 mm level cooling was immediate (see "onset of cooling" in Table 9). Above 650 mm a delayed cooling occurred. At the elevations above the heated zone the steam injection of 15 g/s triggered a temperature excursion starting as low as 1200 K with subsequent heatup rates of more than 40 K/s. For instance, TFS 5/17 thereafter reached a maximum of 2146 K at 3609 s. At the upper (hot) elevations the temperature escalated because the oxidation was enhanced by the increase of the steam supply (from 3 to 15 g/s). At the lower elevations, however, the cooling effect dominated due to the increase in the coolant flow.

Associated with the high temperatures at the upper elevations during the period shortly after beginning of the cooldown phase an increased release of all gaseous species was observed.

The concentrations of the main gas components, i.e. argon, steam, and hydrogen, at the end of the transient and during the cooldown phase measured by the mass spectrometer are given in Fig. 27. 40-50 vol-% hydrogen were measured in the off-gas pipe during these phases of the experiment. The steam concentration is reduced from 64 vol-% to about 35 vol-% due to its increasing consumption by the oxidation reactions. This corresponds to a total consumption of 30 % of the injected steam at the end of the transient phase.

The MS steam measurement is compared to the first derivative of the condensed steam mass (LM 701) and to the injected steam mass (F 205 and F 204) in Fig. 24. Based on this evaluation the integral values of steam input and output, respectively, are as follows:

- Total mass of steam injected based on the F 204 data: ~23.6 kg,
- Total mass of water accumulated in the condensate collection tank (from the onset of cooldown to the end of the data acquisition) (L 701): ~20.1 kg,
- Total mass of steam measured by the mass spectrometer: ~20.4 kg,
- Total mass of steam loss which can be explained by a leakage in the shroud (shroud failure prior to the cooldown phase): ~23.6 - ~20.1 kg $\approx$ 3.5 kg.

The total values show a good agreement between the condensed steam data L 701 (the condensed water was present as steam during the experiment) and the mass spectrometer measurement. (The L 701 data were converted to the unit mass based on a calibration that 1 mm H_2O corresponds to 13.84 g.) The course of the two curves is in fairly good agreement. The growing difference between injected and measured steam in the off-gas tube after initiation of the cooldown phase confirms the shroud failure at that time.

The evaluation of the hydrogen data from the mass spectrometer data give 198 g of hydrogen release in total, most of which (136 g) was during the cooldown (Figs. 28 and 29). The values have been corrected to 182 g for the total release and 120 g of hydrogen released during the cooldown, based on the analysis of the MS data referred to the steam flow rates and a detailed post-test analysis with respect to the degree of oxidation of all bundle components [31].

In addition, there were large increases in the generation of CO and CO_2 as well as a small but detectable amount of methane, accompanied by an increase in boric acid formation (Figs. 30 and 31). During the test condensate was collected at the sampling point for the mass spectrometer. Analysis of the chemical composition performed after the test shows a good correlation between the boron content in the condensate and release rate of boric acids detected by the mass spectrometer (Fig. 31).

The total oxidation of B_4C was evaluated to be ~20 % based on the post-test evaluation of the bundle, and the hydrogen resulting from the B_4C oxidation was analyzed to be ~4.3 g, i.e. 2.4 % of the total H_2 produced. These values replace the ones given in earlier reports (e.g. COLOSS Data Report) which were based on the release of CO and CO_2. Due to overlapping MS signals for these gases with nitrogen and boric acid the data had to be re-evaluated.

The CALDOS system could not be used for quantitative H_2 measurement during the test QUENCH-07 because it can be only applied to measure (binary) $Ar-H_2$ mixtures and no multi-component mixtures of B_4C oxidation products.

The results obtained in the bundle test correspond well with the results obtained in separate-effects tests on boron carbide oxidation regarding gas production [18]. The main reaction products of the B_4C oxidation are H_2, CO, CO_2, and boric acids HBO_2 and H_3BO_3. Only very limited amounts of methane CH_4 were produced at the high temperatures in the bundle. This is in agreement with thermo-chemical equilibrium calculations which predict significant methane production only below 600-700 °C.

7   Posttest Examination

7.1   Posttest Appearance Prior to Bundle Sectioning

Test bundle and shroud appear severely damaged in the region from ~750 mm elevation upward (Figs. 33-35). In this region the shroud and the bundle were partially molten. The major part of the shroud above the heated zone relocated to the region below 1000 mm so that the shroud has become the shape of a large "bubble" between ~750 and 1000 mm. Furthermore the shroud has reacted with its ZrO_2 fiber insulation, and shroud and bundle are severely oxidized. There are two large longitudinal cracks in the shroud at 90° and 270° orientation. These cracks were used to remove two large pieces of the shroud from the bubble zone prior to bundle encapsulation (see shroud fragment in Fig. 36). Another damage zone is apparent at the level of the topmost grid spacer, i.e. at 1410 – 1450 mm. There the Zircaloy spacer and the rod claddings encountered an enhanced oxidation. The claddings are broken and the spacer disappeared almost completely. Below the 750 mm elevation the shroud is intact and so are the lower thermocouples which are still attached to the shroud surface.

Corner rod B which was withdrawn from the test bundle after the conditioning phase, prior to the transient, reveals light gray ZrO_2 in the region between the 800 and 1050 mm level where the oxide layer thickness is around ~100 μm. The oxidation was strongest in the region between the 900 and 1000 mm where splitting of the oxide scale (two concentric layers) occurred. The analysis performed after the experiment by metallographic examination resulted in a maximum oxide layer thickness of ~230 μm at the 950 mm elevation.

7.2   Sectioning of the Test Bundle

The encapsulation of the test bundle was performed in three steps. First, a cap was placed over the bottom of the copper electrodes and a low-melting metal alloy (containing Pb, Bi, Sn, and In; density of ~10 kg/dm^3; melting point of 331 K) was used to seal the bottom of the bundle. Secondly, a small amount of the same resin as used for the encapsulation of the bundle was placed on top of the metal to generate an interface of around 0.2 m that prevents the metal from being liquefied after starting to epoxy the bundle together with its shroud. The mould for filling the bundle with epoxy resin surrounds the shroud over the entire bundle length and is set up vertically. It is evacuated before charging with the resin to allow filling of pores and cracks. So, the bundle is filled from the bottom with approx. 20 kg of resin and

hardener. The epoxy system Rütapox 0273 with the hardener designated LC (manufactured by Bakelite GmbH, Iserlohn) was chosen based on the experience with the CORA and the previous QUENCH test bundles. The shrinkage effect is small. After epoxying the bundle the resin is allowed to harden for one week. To obtain the cross sections a saw with a 2.0 mm-thick diamond blade (mean diamond size 138 μm) of 350 mm OD is used to cut the slabs at 1300 rpm. As an overview the sectioning map is given for test bundle QUENCH-07 in Fig. 37. The exact elevations are listed in Table 10. The top surface cross sections that were polished for metallographic examination can also be taken from Table 10.

7.3   Metallographic Examination

7.3.1   Introductory Remarks

The metallographic preparation of cross section slabs of 13 mm thickness consisted of grinding and polishing of their top surfaces. Macrographs of those cross sections are shown in Figs. 38-41. As corner rod B had been pulled out during the transient test phase before onset of escalation its previous south-west position is empty. For the special purpose of illustrating the axial transition from remaining to destroyed absorber rod the respective part was divided in longitudinal direction by one eccentric and one concentric cut (see Figs. 42 and 43).

Obtaining all necessary information required careful microscopic inspection of several cross sections, a systematic measurement of the oxide scale thicknesses of all rods at four azimuthal positions, a thorough photo documentation into highly magnified details and an energy-dispersive element analysis in supporting scanning electron microscope (SEM) studies. This is the basis for the description of the final bundle state as given below. As far as possible, the findings are interpreted in terms of the mechanisms of the oxidation of the components, their physico-chemical materials behavior and their interaction. For this purpose it was helpful to proceed from the lower bundle elevations upward, in the direction of increasing temperatures, and thus intensified interaction extent. In this sense the bundle state at the lower elevations can be understood to resemble interim states for the higher elevations. The cooldown related phenomena deserved special concern as well.

7.3.2   Bundle Elevation 73 mm

The polished cross section for this elevation can be taken as a reference for the unchanged condition of the bundle arrangement relative to the lowest zircaloy spacer grid (see Fig. 38). Several thermocouples are seen to cross the elevation; the thinner ones of the NiCr-Ni type can be distinguished from the thicker ones, i.e. the W-Re type. The absorber rod is intact. Several droplets of melt are seen to have relocated to this low elevation from positions above, at which the absorber rod got destroyed.

7.3.3   Bundle Elevation 550 mm

Close to the mid elevation of the heated axial bundle length, at the position of the next zircaloy spacer grid the overview of the cross section shows a still intact components arrangement (Fig. 44). The loss of some fuel simulator pellets and heater rod stubs is a

preparation artifact. Those components simply fell out during cutting of the thin cross section slab because they were not fixed by the resin. So they indicate that there was no interaction with the rod cladding.

An increased number and size of relocated melt droplets is found, compared to the previous cross section. For both elevations the spacer grid has contributed to catch and accumulate a part of the droplets, which had mostly fallen down freely. The "imported" heat of the droplets was generally not sufficient to allow interaction with the solid structures of comparatively low temperature, so that fast solidification must have taken place. It is therefore not necessary to present micrographs on details.

7.3.4 Bundle Elevation 650 mm

Apart from some missing pellets and heater stubs, the bundle and shroud are still intact (Fig. 45). This allows to concentrate on the control rod arrangement which is shown in the lower part of the figure. Most obviously the annular gap between Zry guide tube and stainless steel absorber rod cladding has got filled by internally relocated melt. This is illustrated and explained in more detail in Figs. 46 and 47. Melt, formed by interaction of absorber components at higher level must have relocated to the given elevation. At place, interaction at the inner side of the solid guide tube structure is identified by an interaction zone, which itself is composed of an "epitactic" and a "topotactic" part, which correspond to diffusive exchange into guide tube and melt, respectively (Fig. 46). Further, Fig. 47 shows the boundary between the absorber melt and the embedded external absorber cladding surface (micrograph in the middle). In addition the lower micrograph shows the formation of an interaction zone between the stainless steel (SS) control rod cladding (inner side) and the B_4C pellet. Of course this is the result of a solid state interaction at place, by which a low-melting eutectic product mixture was formed. Although this interaction is in principle independent from the before-described melt relocation it is reasonable to assume that it has been favored by the "imported" heat carried with the relocating absorber melt. A part of the CR cladding still remained solid despite being melt-covered from both sides. A variable and still rather limited extent of consumption around the B_4C pellet took place, artifacts exaggerate the real pellet porosity, and some melt infiltration can be identified.

7.3.5 Bundle Elevation 750 mm

Obvious degradation of the bundle is seen in the cross section overview only in central regions (Fig. 48): Some melt within the flow channels is found adherent to rods and TCs, which are partly covered and locally attacked. The state of the CR is documented in Fig. 49. The B_4C pellet is reduced in diameter by dissolution. Both, CR cladding and guide tube are essentially transformed into the surrounding absorber melt, which is the common, but not yet homogeneous, interaction product. A more detailed description requires supporting information from SEM-EDX analyses at different positions of the inhomogeneous melt. Thus, the given highly magnified microstructure in the lower micrograph is understood only for illustration of the multi-component character and the multi-phase condition of the absorber melt after re-solidification. Further items to be mentioned are the large voids from downward melt relocation, some small-scale melt porosity, and the fracturing of pellet, melt and guide tube scale during late experimental phases. The lumps of metallic melt outside the control

rod show the same special oxidation items as absorber melt within the CR, which are addressed next.

Some melt within the CR must have been exposed to steam according to scale formation. This is shown in Fig. 50 at two positions. For one of them the ZrO_2 scale, originating from guide tube oxidation, might have served as protective layer for some period. Later on, scale fragmentation should have opened more direct steam access. Stainless steel oxidation in steam is known to result in multi-layered scales and some internal alloy attack below. Obviously, absorber melts and re-solidified Zr-containing products oxidize similarly. Below an external ZrO_2 sub-layer a porous scale is growing and the serrated growth front indicates selective components oxidation. Three-dimensional growth stress from volume effects are assumed to contribute to scales of imperfect protection and non-parabolic growth kinetics. Occasional and local loss of scale protection would lead to a time dependence between parabolic and linear. Parametric separate-effect studies would be necessary to verify the given tentative but plausible interpretation.

Fig. 51 illustrates distribution and state of melt on top of two fuel rods. Whereas rod No. 7 (2nd ring, slightly lower temperature) carries a thin partial cover of melt, rod No. 3 (1st ring, facing central rod, slightly higher temperature) is mostly surrounded by melt. Common for both positions is the complete conversion of the melt to ceramic due to steam exposure, its porosity in varying scale and the fair wetting. The reason for porosity along the interface is a still open question, whereas metallic inclusions, scarcely seen as in the bottom micrograph, can be interpreted to consist of the most oxidation resistant bundle components as nickel and tin. This and the composition ought to be verified by EDX analysis.

Fig. 52 documents the oxidation state of the fuel rods in general, the absence of surface oxidation of cracks through the a-Zr(O) layer and the cladding/pellet interaction. Voids, formed by melt-down of cladding matrix, indicate peak temperatures above ~2030 K, and void surface oxidation, seen here and at many other positions of the bundle, reveals the steam exposure along axially oriented secondary flow channels within some rods. The latter is an oxidation phenomenon described for the first time on the basis of direct observation. However, its contribution to total bundle oxidation kinetics remains rather limited.

7.3.6 Longitudinal Sections Between Elevations 759 and 835 mm

In order to obtain information on the exact axial elevation for onset of control rod degradation longitudinal sections of slab QUE-07-i were prepared by two cuts and preparation of both side surfaces of both cuts. Fig. 43 shows both sides facing the eccentric cut, arranged in mirror-like position. The translucence of the epoxy resin facilitates the orientation. It is important to notice that the shroud thickening by melt accumulation ends in the upper half of the images. Here, absorber melt is distributed in porous form, and directly below as massive agglomeration. Fig. 42 combines the correspondingly arranged pieces of the central cut, for which the CR and a row of surrounding fuel rod simulators were cut almost centrally. The control rod region is shown and interpreted in more detail in Fig. 53.In the lower part the B_4C pellet stack is essentially intact, the pellets being glued together and surrounded by melt. The absorber pellet stack is essentially intact up to ~800 mm elevation. Above this level an obliquely fixed pellet residue, also melt-infiltrated, shows items of ongoing dissolution under

formation of an interaction zone. Thin ceramic structures are identified as guide tube scale. At the elevation of the separate B_4C pellet CR interaction with the adjacent fuel rod is seen to begin by dissolution of the guide tube scale, after getting embedded into melt from both sides. This additional interaction can be studied in the cross sections above, whereas the onset of the phenomena, described up to now are overrun by more severe damage.

7.3.7 Bundle Elevation 850 mm

Even in the overview this elevation shows most serious degradation of bundle and shroud (Fig. 54). Residues at central bundle position, consisting of deformed guide tube scale mark the previous position of the completely consumed or relocated control rod. Every fuel rod indicates at least some damage, most of them are in contact with melt lumps or fragments. Some of them are in mutual contact, one of them in contact with the shroud, in the sense of the so-called necking mechanism, previously described for the bundle QUENCH-03 [7]: This phenomenon of enclosure of residual metallic material into a common scale develops by scale dissolution in contact with metallic melt of sufficient oxygen solution capacity and in competition to oxidation in contact to steam flow channels. Extended, common melt pools can be formed according to this mechanism.

The embrittled shroud structure on the east side has been lost during removing of the insulation. On most other sides the shroud is found transformed to a rigid body of massive material, thickened by shroud melt relocation from above. This melt was channeled and confined by the internal shroud scale and the external scale, which has grown after shroud penetration and steam leakage. The ZrO_2 fiber insulation could not withstand shroud expansion and might well have acted as oxygen source, driving interaction. Finally the shroud melt pool has acted as crucible to collect rubble fragments (see north-west position).

The typical oxidation state of the shroud in Fig. 55 is quite different for the outer and inner part. Thick internal scale in contact to an oxygen-saturated metallic matrix with ZrO_2 precipitates can be interpreted by the usually observed solid state oxygen gradients and diffusion mechanisms. Precipitation of ZrO_2 phase from the matrix is assumed to have occurred during the cool-down phase of the experiment, however, it cannot be excluded that melting has taken place for limited time. In contrast, the morphology of the thinner external shroud scale and of the matrix clearly indicate their different history: Here, metallic melt oxidation resulted in scale growth as well as in oxygen enrichment of the matrix melt, which proceeded by fast oxygen transfer together with the assumed melt movement. Obviously, this transfer was not terminated by matrix saturation, but strong and very homogeneous ZrO_2 phase precipitation took place further on.

For this observation it is convincing to refer to the mechanistic model for melt oxidation, recently developed by M. Veshchunov within the COLOSS project [9]. This model explains a precipitation phase as part of the melt oxidation process by the continued action of a driving force for oxygen transfer in the case of a temperature gradient in a transition layer between scale and melt pool. The model thus describes and explains enhanced inward oxygen transfer at the expense of a correspondingly reduced scale growth rate, so that the global kinetics is enhanced and its time dependence shifted from parabolic towards linear.

Despite the fact that the relatively thick-walled shroud of the test bundle is not reactor typical, the above described behavior and interpretation are considered as most important and as applicable for severe accident scenarios in which melt pools are formed and continuously oxidized until conversion to ceramic state. Especially for extended time periods of oxidation the materials behavior may deviate strongly from the parabolic treatment, still assumed in codes.

Coming back to the above mentioned necking mechanism Fig. 56 shows the result of neck formation between rod No. 19, corner rod C and shroud. A large melt pool formed during the transient, which remained confined by the common scale. This pool is seen to be extended into the interior of rod 19. The illustrated details are the precipitation of ZrO_2 phase particles from the melt and the ability of the melt to dissolve the previously grown interaction zone between pellet and cladding. The pool of considerable volume has remained essentially metallic. There is no indication of any interference with control rod degradation for this melt of simple zirconium type.

At most other positions of this elevation the metallic fuel rod components are found almost or totally oxidized. Fig. 57 shows a fuel rod in contact with external melt, both mostly converted to ceramic. Some embedded metallic residues are dispersed in the previous melt, some a-Zr(O) phase particles dispersed in the ZrO_2 of the converted cladding wall. The form of the cavity, released by cladding matrix melt-out, indicates a peak temperature above 2030 K. Fig. 58, showing a lump of metallic melt between two fuel rods, refers to the otherwise complete oxidative conversion of rod No. 2 and the resulting brittle fragmentation. In Fig. 59 the final status of two rods is compared with respect to the region of pellet/cladding contact. Whereas both rods have a comparable temperature history (the same as rod No. 13 of Fig. 57, according to the melt-out cavities), the distribution of residual metallic phase and the pellet degradation are quite variable.

Fig. 60 is concentrating on the fragment of a melt lump found in contact to a fuel rod. According to its microstructure it can be identified as zirconium type melt, however, the considerable oxygen content and the missing of thick scale seem to be in contradiction. It has to be assumed that either scale loss occurred by fragmentation or artefact, or that melt relocation occurred in an event, late enough to exclude further scale growth.

Another melt lump, having solidified on a fuel rod, is found split off (Fig. 61). The melt shows long-range deviations from homogeneity, some irregular porosity and finally multi-phase microstructure. Thus, formation by multi-component interaction is clearly indicated. Unfortunately, even the time-consuming task of EDX analysis of local compositions would only give information on one individual lump of melt. Trying to obtain global results would require many of such studies and a statistically meaningful analysis.

Two melt droplets in fuel rod contact are recognized to have resulted from multi-component interaction (Fig. 62). Without proof by EDX analysis, the form, porosity, and especially the morphology of oxidation are sufficiently informative. Instead of a sound scale, which would be typical for a zirconium type melt, the observed scale is irregular, locally porous, and tends to spall and crack. The underlying alloy is attacked by oxide incursions and resists against

oxidation at spots of residual alloy, which can be assumed to be enriched in the most oxidation resistant components.

7.3.8 Bundle Elevation 950 mm

The overview, Fig. 63, is described by the missing control rod, the oxidized fuel rods with some fractured cladding, attached melt aggregates in oxidized condition, and the inward-bent parts of the fractured shroud. One of the scarce still metallic melt lumps had been protected against steam oxidation by confinement into an isolated volume by the necking mechanism (Fig. 64). The melt seems to be of zirconium type. By oxidation a ZrO_2 scale has formed, distinguished from cladding scale by a porosity marked, otherwise hardly visible interface. The pores are speculated to result from incomplete wetting of the cladding scale by the originally oxygen-poor melt.

The thin cover of melt on a fuel rod, as shown in Fig. 65, is interpreted to result from a "candling" process: As candle wax may drop down from a candle stick or flow down in contact to it, metallic melt is understood to relocate by dropping or candling. The latter process is determined mainly by melt viscosity and surface wetting. Since wetting of ceramic substrates is known to improve due to oxygen transfer, which on the other hand increases melt viscosity, it is plausible to assume candling conditions varying in position and time, depending on the capacity of the melt as oxygen sink. In the illustrated example the melt cover thickness is rather low, so that rather fast relocation should have occurred. It is tentatively assumed that the porous foam-like melt structure did not result from a real foaming process, but from repeated relocation events together with surface oxidation in steam contact. Thus the "foam cell walls" would have to be interpreted as the scales, formed after individual candling flow events. Those could have dried out by continued downward relocation of the metallic cores of the flow paths.

The last example for the elevation, Fig. 66 describes a melt aggregate, suspicious to contain additional components from control rod degradation. This is indicated by the irregular form and porosity, as well as the inclusion of more oxidation resistant droplets.

7.3.9 Bundle Elevation 1150 mm

The severe degradation above the heated length resulted in the still regularly arranged molybdenum rod electrodes, the heavily bent, "flowered" or fragmented cladding, distributed melt and rubble aggregates, and the partly remaining inward-bent shroud pieces (Fig. 67).

The considerable dissolution of one of the electrode stubs should be taken as clear indication of a facility-typical result of superheating. The rod cladding and the plasma-sprayed ZrO_2 cover layer of the respective electrode have not survived sufficiently long to prevent steam oxidation of molybdenum and formation of lower-melting metallic and ceramic products. The reaction heat should have triggered this degradation, contributions to off-gas aerosol, hydrogen signal and melt relocation should be kept in mind. This is why a more detailed analysis for the elevation is not considered simple enough to be justified.

7.3.10 Bundle Elevation 1410 mm

At the elevation of the top spacer grid (Fig. 68) the molybdenum electrodes are in far better condition than in the previous elevation. This is mainly due to the less severe temperature history. The control rod cladding made of stainless steel has vanished without any identified residues. The bent and fragmented cladding and spacer relicts can be only partly distinguished. Some melt is observed and a downward relocation of some melt from this elevation is assumed to have taken place.

7.3.11 Lateral and Axial Oxidation Profiles

Quantitative information on the extent of the steam oxidation of the bundle components was obtained by systematic and comprehensive oxide scale thickness measurement. The results may serve as basis for comparison with the final bundle status, the measured integral hydrogen release, the "chemical" heat evolution, as well as for comparison with respective results of code calculations.

In this sense the measurements for corner rod B, withdrawn from the bundle during the transient before escalation, give valuable information as a "calibration" point for evaluation of time dependence. In Fig. 69 the axial oxide layer thickness profile along rod B is drawn in comparison to that of the respective rod of test QUENCH-07, both according to the destructive metallographic determination on prepared cross sections.

The series of scale thickness measurements at different bundle elevations, comprising some measurements on both sides of the shroud and, mainly, the systematic determination of the scale thickness at both cladding surfaces and two to four azimuthal positions of each rod, wherever feasible, are illustrated in Figs. 70 through 76. Up to mid-elevation (Fig. 70) the oxidation remained relatively unimportant and the lateral variation rather small. The control rod guide tube grew the thickest scale for this elevation (36 µm and less). For the elevation 650 mm (Fig. 71) the relatively weaker oxidation of shroud and corner rods (up to 50 µm) compared to the fuel rod simulators and the control rod (up to 68 µm) can be seen in relation to small temperature gradients. At the elevation 750 mm (Fig. 72) the variations of the extent of oxidation are found much increased, but limited in relative terms. At 850 mm (Fig. 73), 950 mm (Fig. 74) and 1150 mm (Fig. 75) complete external cladding oxidation is determined for essentially all measured positions. Thus, some relatively low values given for the latter elevation have to be understood as due to cladding melt relocation, so that no further scale growth could take place. At the top elevation 1410 mm (Fig. 76) a sub-layer of metallic cladding has remained.

The essence of the described information for the individual elevations is collected and summarized in Fig. 77, the axial profiles of the oxide scale thickness distribution. Those are given for the different rod types and the interior shroud surface, as well as for the common average and range of values for all the components.

7.3.12 Summary of the Metallographic Examinations

A comprehensive metallographic investigation of the prepared bundle cross sections, a detailed photo documentation including high magnifications, and a supporting SEM-EDX analysis of melts formed as products of bundle components interaction (see next section) were performed. The composition of selected photos into thematic illustrations and the microstructural analysis of the observed phenomena were the basis of the given description of the final state of the bundle. A discussion of its behavior in time dependence and as result of simultaneous and competing mechanisms was deduced as far as possible. The oxidation state of the bundle was quantified by systematic scale thickness measurement at all polished cross sections and along the removed bundle components, and was also documented in axial profiles.

The axial oxidation profile reflects the pronounced temperature dependence of Zircaloy-4 / steam oxidation. This reaction proceeded with the well-known kinetics, controlled by growth of protective scale. Steam oxidation of the cladding was accompanied by chemical interaction with the ZrO_2 pellets at positions of solid-state contact. In total, however, the corresponding oxygen transfer to the cladding remained relatively unimportant. No indications for early mechanical cladding failure at temperature were found. In the peak temperature region below and within the upper electrode zone complete oxidative conversion of the fuel rod simulator cladding took place.

Melting of local cladding matrix volumes, rod-internal melt relocation, resulting melt agglomeration and gap-filling at the expense of void formation were observed in local variations at many positions. Melt pool formation and confinement according to the "necking mechanism" and by the "crucible effect" of the oxygen-enriched surrounding scale structures took place at a few positions. Occasional cladding failure, understood in terms of the "chemical thinning process" could be observed at these locations. Cladding through-wall cracking, breach formation, steam ingress and internal steam oxidation under supply limitation conditions have to be correlated mainly to the cool-down phase of the experiment. The fact that most of the crack surface network remained non-oxidized, indicates its formation at a late stage of low temperature.

Whereas a limited amount of external melt, found in form of oxidized lumps on some rod surfaces, is interpreted to result from metallic cladding residues only, other lumps consist of mixtures involving the components of the degraded control rod. This is deduced from the observed melt porosity and the less regular and protective scale. The latter is often composed of an external ZrO_2 sub-layer, which tends to spall, a porous internal sub-layer and serrated scale incursions into the metallic substrate.

The results obtained in the bundle test confirm the observations of the separate-effects tests [19]. The formation and relocation of eutectic $B_4C/SS/Zry$ melts starts at approx. 1250 °C. First relocation occurs inside the guide tube oxide scale (crucible effect). After failure of the oxide scale by chemical thinning or mechanical break also radial relocation of the melt is possible. Absorber melt oxidizes very fast and attacks ZrO_2 scales of adjacent fuel rod simulators.

7.4   SEM Inspection of Melts and EDX Analysis

7.4.1   Intentions, Scope and Procedures

In addition to the comprehensive metallographic inspection and light-optical documentation, a scanning electron microscopy (SEM) study was performed, as this offers improved material contrast for multi-phase microstructures of melts. Further, the element analysis of such melts was intended, mainly to get indications on kind, origin, as well as mechanisms and timing of melt formation. Such information was obtained for melts, resulting from the control rod degradation due to interaction of its components. In comparison, the well-known fuel rod cladding degradation did not require this complementary effort. It turned out that the severe degradation conditions, which came close to test device limitations, allowed to study the degradation of the upper molybdenum electrodes. Those items were considered, although being non-representative for power plant accident conditions.

Melt lumps from four different cross section elevations of the bundle between 550 and 1150 mm were investigated. They were inspected by use of an SEM (Jeol, type JSM6100), equipped with an energy dispersive X-ray (EDX) analyzer (Kevex, SiLi detector with BN window), which allowed identification and determination of the components, including light elements. Micrographs in back-scattered and secondary-electron contrast and element spectra of small area or spot measurement type were taken. The analysis system allowed automatic ZAF correction without use of standards, to obtain fairly well defined (± 10 % relative) element concentrations.

7.4.2   Results

<u>Relocated melts of control rod origin, studied at 550 mm bundle elevation</u>

Premature (low temperature) melt formation within the control rod arrangement due to the eutectic interactions at contact between stainless steel CR cladding and zircaloy (Zry) guide tube as well as between cladding and boron carbide absorber is a well-known fact. However, the behavior is influenced by mass relations, to some extent by the pre-oxidation of the structural components, by CR penetration and relocation features. Melt relocation was observed in form of relatively small individual lumps, either sticking between the bundle structures or having fallen to its bottom. For the 550 mm elevation the distribution of melt is schematically illustrated together with the lateral oxidation profile in Fig. 70. For some of the melt lumps identification numbers are given in this figure which are used for orientation here. <u>Figs. 78 and 79</u> describe two examples: Isotropic or striped distribution of two main phases can be recognized in Fig. 78 and 79, respectively; and in both spectra the steel components (Fe, Cr, Ni) dominate. Zirconium as further component is identified by one peak in Fig. 78, and in a larger amount in the lump of Fig. 79. Further characterized three lumps, not illustrated, vary in microstructure (distribution of phases with rounded, edged or elongated form) and spectrum. In summary, all of them result from cladding / guide tube interaction and may contain minor boron and carbon concentrations according to additionally precipitated phases, which were not analyzed.

Detailed melt analysis at 750 mm bundle elevation, and control rod microstructures

The detailed analysis of melt No. 2, located close to the CR, as seen in Fig. 72, is presented in Fig. 80. Its microstructure consists of at least two types of an elongated phase, distributed in the matrix together with at least one interdendritic phase. Despite this, the overview spectrum reveals only stainless steel and Zry as main sources, the latter in a higher concentration compared to Figs. 78 and 79. As this lump was expected to contain considerable amounts of boron and carbon from B_4C dissolution, an analysis with reduced electron beam voltage was especially dedicated to the determination of light elements. In this spectrum a peak for B and C was identified, and the semi-quantitative evaluation resulted in B and C mass fractions of together <1 %, and an Fe/Zr ratio of ~ 2/1. Those results should be taken as an example, only.

Fig. 81 presents two different overviews of a control rod / guide tube area at elevation 750 mm together with four micrographs in total. Shown are (from left to right) pellet / cladding interaction melt (Pos. 1, detail b), intermediate range (Pos. 1, detail c), cladding/guide tube interaction melt (Pos. 1 and 2, details a), and guide tube scale. Common for all are the complex form and distribution of several phases in a continuous matrix. No composition analysis was performed.

Molybdenum rich melt, analyzed at 750, 850 and 1150 mm elevation

As low as 750 mm elevation a melt lump was identified to consist mainly of molybdenum. It appeared as a grey primary phase, surrounded by a darker phase, formed by decomposition of the residual melt. A very similar melt lump from the 850 mm elevation (Pos. 1 in Fig. 73) is illustrated in Fig. 82. As Ta and Fe were identified as minor constituents, one has to assume three different sources for the formed mixture, i.e. Mo from the upper electrode zone, Ta from thermocouple sheath and Fe from the control rod cladding.

Fig. 75 gives the positions of Mo identification at 1150 mm elevation. At Pos. 1 of this figure a detailed melt analysis is documented in Figs. 83 and 84. The 20 kV spectrum of this melt (Fig. 83) reveals only Mo, and the typical melt microstructure is quite similar to that of Fig. 82. The additional analysis aiming at light element components (Fig. 84) included the melt at primary crystal position (center of figure), and residual melt area (bottom), both in comparison to a molybdenum electrode (top). The spectra and the obtained compositions give a clear increase in oxygen for the top to bottom sequence, i.e. from the electrode to the grain boundary phase of the melt. It shall not be claimed that even the massive electrode bulk has picked up oxygen and carbon during its exposure to the atmosphere after failure of the flame-sprayed ZrO_2 protection layer. However, in any case the molybdenum melting and relocation is related to this oxidative exposure.

7.4.3 Discussion in Relation to Literature Results

With respect to the exposure of molybdenum electrode to steam, phase diagram information on the Mo-O system supports the above given interpretation: Eutectic melt formation takes place between Mo and MoO_2. A melting point of 2300 +/-150 °C is given for the latter phase, and the data for the eutectic composition are reported to be 2150 +/-100 °C and

~4.5 mass-% O [10]. Thus, the composition analysis for the dark phase (Fig. 85, bottom), interpreted to result from this eutectic, fits very well. A strong tendency to form carbides is also known for molybdenum. In total, it has to be kept in mind that Mo as structural material is not stable at high temperatures under oxidizing and carburizing conditions, since interaction with gaseous species and melts may occur.

The eutectic interaction between Zry and stainless steel reflects the binary eutectics between Zr and the steel components Fe, Cr and Ni. The eutectic temperatures on the Zr-rich side are 947 °C, 1332 °C, and 960 °C, respectively. A ternary eutectic at 930 °C with the composition of 73 at.% Zr – 22 at.% Fe – 5 at.% Ni was stated for the Zr-Fe-Ni system [11].

A brief review is given on pertinent binary and ternary phase diagrams of Zr, Fe, Cr, and Ni with C and B, reflecting basic metal affinities and product stabilities. Zr is known to form the ZrC carbide phase and the ZrB_2 boride phase. The knowledge on carbide formation of stainless steel (including an intermetallic phase formation in dependence on carbon content) is tremendous and complex. Carbide phases of the types M_3C, $M_{23}C_6$ and M_7C_3 may form (M=Cr, Fe, ..), some of them have enough boron solubility to be understood as boro-carbides. Ni is known to form Ni_3B in the binary system, but should be the less reactive component of SS compared to Cr and Fe, which tend so strongly to form a mixed boride of $(Cr, Fe)_2B$ type that the boron solubility of the residual melt is limited to a few ppm. The carbon solubility in borides is considered as low.

The most stable compounds, thus expected to precipitate from an "absorber melt" mixture, are ZrC, ZrB_2, $(Cr, Fe)_2B$ and (Cr, Fe) carbides. Their presence as solid particles, distributed in residual melt, can give rise to rather high melt viscosity.

Experiments on the B_4C / stainless steel (DIN 1.4919, AISI 316) interaction were performed at 1000, 1100 and 1200 °C for different duration and were evaluated towards parabolic growth rates of the interaction layers and Arrhenius-type temperature dependence [12]. At 1100 °C a layered interaction zone was observed adjacent to B_4C: a layer of MeB phase, a layer of Me_2B and a two-phase layer of Me_2B precipitates in the Cr-depleted and Ni-enriched steel matrix, where Me stands for (Cr, Fe). For 1000 °C the behavior is similar. At 1200 °C no continuous MeB phase layer was formed and only during short-term experiments some MeB precipitation in the Me_2B layer took place. For longer tests at 1200 °C B_4C is covered firstly by a Me_2B layer and secondly by a liquid phase layer, identified by constant concentrations in the matrix of the decomposed melt microstructure. Thirdly follows a layer with similar Me_2B precipitates but a matrix composition gradient, which indicates that it was formed and remained solid at temperature. Obviously, the diffusion path goes through a liquid field at 1200 °C and above.

In view of an application to temperature transients a detailed physical model was developed, based on first principles and the measured interaction layers growth, the concentrations of the components at the boundaries and concentration profiles across the layers, all in order to treat the interaction as a diffusion problem [13]. The multi-component phase diagram was reduced (referring to literature results on pertinent systems) to a pseudo-ternary (Fe, Ni)-Cr-B diagram and the considered diffusion path therein. As it was experimentally observed that essentially no carbon diffuses into the B_4C/ss interaction layers, this carbon diffusion was not

taken into account. Chromium diffusion was found to exceed literature values considerably; this is discussed as result of the extremely high boron mobility and diffusion cross term relations. Extension of this analysis to higher temperatures would require to perform additional annealing experiments.

Experiments on the interaction of B_4C and Zircaloy-4 were performed at 800 to 1650 °C for different duration and evaluated with respect to parabolic interaction layers growth rates and Arrhenius-type temperature dependence [12]. Between 800 and 1100 °C one reaction layer was observed, consisting of a mixture of zirconium diboride (ZrB_2) and zirconium carbide (ZrC). In the temperature range of 1200 to 1500 °C a similar phase mixture, which forms a first layer adjacent to B_4C, is followed by a second one, mainly consisting of zirconium diboride (ZrB_2), adjacent to the Zry. At 1600 °C such a double layer was also observed, and in addition the onset of a localized liquid phase formation, apparently responsible for abrupt increase in the reaction rate. At 1650 °C the reaction couple liquefied completely during heat-up to test temperature.

The development of an analytical model [14], which was started by treating the problem in its general form for the range 800 to 1100 °C and using literature results on the pertinent phase diagrams, followed a similar strategy as for the B_4C/SS system. The strategy allowed finally to solve the simplified differential equations for the diffusive transport of the components. For the temperature range of 1200 to 1500 °C the experimentally observed additional reaction layer, verified as single phase ZrB_2, did not require a more detailed description. For the whole temperature range of 800 to 1500 °C it was concluded that the reaction kinetics of the couple B_4C/Zr is completely defined by boron diffusion in the ZrB_2 phase. The realistic diffusion coefficient, obtained, indicates, that application to relatively fast temperature transients should be possible. A development of the theory for 1600 °C and above was, however, not possible without further thermodynamic information and kinetic results.

The separate effect experiments on B_4C / Zry interaction and the model development on its kinetics are - in a strict sense - not directly applicable to the three components interaction problem, as B_4C pellet and Zry guide tube get contact only by interaction with the SS cladding. Respective "ternary" experiments were not performed, and the considered interaction behavior would require more supporting experimental information at higher temperatures.

7.4.4 Summary and Conclusion

The SEM / EDX study has contributed to the understanding of some features of the complex interaction behavior of the control rod components in a typical bundle geometry and of molybdenum, as an additional structural component. Both must be considered in relation to the time of steam exposure and the release of gaseous reaction products. The scope of this analysis, which had to be restricted due to other priorities, is reasonable, but of course not adequate to resolve all information deficits:

Quantitative analyses of integral experiments are quite generally problematic, at least highly time consuming. This holds especially for the composition analysis of reaction products. Determination of composition ranges can be arbitrary, since they depend on the definition of

product types. A statistically sufficient and representative choice of samples is also required. Many more cross sections would be needed for the analysis of melt lumps, inclusion of melt which dropped to the base plate and investigation of not yet relocated melt. Determination of mean compositions would, in addition, require a volume-averaged evaluation. As the multi-component systems are not completely known in their phase formation, a further helpful step towards more detail would be the phase analysis of multi-phase material, complicated by analysis limits to detection, resolution and correction.

It is also mentioned, that semi-liquid products of the types studied above have a complex oxidation behavior. This is characterized by preferential formation of a ZrO_2 scale, below which formation of mixed oxides and embedding of more oxidation-resistant phase particles take place. Simple oxidation kinetics cannot be expected. Thus, the additional task arises, to study the oxidation behavior in separate-effects investigations, including model development and verification. Respective results could give trends for the oxidative release of carbon compounds from "absorber melt" in QUENCH-07, and might contribute to an interpretation of the obtained mass spectrometry results.

7.5 Hydrogen Absorption by Zircaloy

The hydrogen absorbed in the remaining Zircaloy-4 metal was analyzed by hot extraction in the so-called LAVA facility, which is an inductively heated furnace coupled to a mass spectrometer. Specimens were taken from bundle slabs especially prepared for destructive analytical purposes (see Table 10). They were heated for 20 min to some 1800 K under a well defined argon flow. The hydrogen extracted was measured by the mass spectrometer. Results are shown in Fig. 85. The maximum value of absorbed hydrogen in the metal phase was measured to be 20 at-%, which is considerably higher than in the former tests with steam cooling. The integral value of the absorbed hydrogen was estimated to be approx. 3 g.

8 Calculational Support

8.1 Investigation of Oxidation and Hydrogen Behavior with the FZK Bundle Code CALUMO

As an absorber rod with B_4C pellets was installed at the center position of the bundle in the QUENCH-07 test the CALUMO code had to be improved considerably in order to be able to deal with this new bundle design in a proper way. As described in [15] the evolution of the temperatures in the test section is calculated with the help of balance equations obtained from the integral form of the energy conservation law. In the old version of the code there was one balance equation for all the 21 fuel rods of the bundle together with balance equations for the shroud and the coolant. In the new version of the CALUMO code we have a balance equation for the outer ring of 12 heated fuel rods and of four corner rods, a balance equation for the inner cluster of 8 heated fuel rods, and a balance equation for the central rod. In case of QUENCH-07 this is an absorber rod with a zircaloy guide tube. But there is also the possibility to deal with an unheated fuel rod of normal bundle design.

A model for B_4C oxidation and boric acid formation, BORCA, has also been implemented in the CALUMO code. This para-linear oxidation model is described in more detail in ref. [16]

and shall not be repeated here. As the equilibrium B_2O_3 oxide film thickness is very small, i.e. 1-3 μm, under the steam flow conditions of QUENCH-07, a simplified version of the BORCA model is implemented in the code directly starting with the phase of constant oxide film thickness. Thus, the early short phase of growing oxide films is neglected. The same is true for the so-called pore effect, as no model was available when the post test calculations for QUENCH-07 have been done.

An empirical model for heat transfer by natural convection in the argon volume in the upper part of the test section between the shroud and the cooling jacket was also implemented in the CALUMO code. It was also assumed that the upper part of the ZrO_2 fiber insulation (z$\geq$ 750 mm) is affected by this upward transportation of heat in the space outside the shroud. Without this new convection model no temperature plateau of sufficient duration could be achieved in the axial region between about 700 and 1000 mm.

The main interest of the calculations with CALUMO is the oxidation and gas production phenomena (H_2, CO, and CO_2). A good simulation of the temperature evolutions in the fuel rod simulators and the shroud must, of course, be achieved by the code; otherwise one has no chance to obtain reasonable results. It should also be noted that the oxidation correlations of Leistikow et al. [17] were used as for all the other post test calculations of QUENCH tests done so far. It appears that these correlations allow a good simulation of the experimental findings of the oxidation behavior.

Results of code calculations in comparison to the respective data of the test instrumentation are to be found in Figs. 86-89. These are the temperature evolutions between 150 and 1350 mm, the axial profiles of oxide scale thickness for the fuel rod simulators and the shroud, and the results on gas production (rates and overall production). It should be noted that the calculation starts at about 230 s into the test with the increase of the electrical power and ends at about 3700 s. Thus, the calculation was stopped a bit too early in the cooldown phase.

In Figs. 86 and 87 are plotted the average temperature in the outer ring of fuel rod simulators "tsurz", that of the inner cluster of 8 fuel rod simulators "tcenz" , that of the absorber rod with its guide tube "tcrz", and the average shroud temperature "tshrz". They are compared to the available thermocouple readings.

In the overall, the temperature evolution in the bundle and the shroud is simulated in a satisfactory way by the code, especially in the lower part of the heated zone (z $\leq$ 450 mm). Most of the features of the temperature evolution are relatively well reproduced in this axial zone. The temperature rise to steady-state conditions, the pre-oxidation phase, the temperature transient, and the cooldown phase are to a good extent well matched. As the temperature evolution in this part of the test section is mainly determined by the electrical heating, we can be rather confident that this effect is correctly simulated by the code. There are some problems with the calculated temperature evolutions between about 550 and 650 mm, as the calculated temperature rise in the pre-oxidation phase is somewhat higher than measured. But as the oxidation rates in this axial zone are not very high, this does not result in bigger problems for the hydrogen production.

There is some difference between measured and calculated temperature values between 750 and 950 mm during the pre-oxidation phase, but the flat temperature evolution could in the overall be reproduced by the code, although not in all details. It should be noted that the information on the temperature evolution is only based on shroud thermo-couple readings.

Due to the recently implemented natural convection model the situation in the upper part of the test section (1000 – 1400 mm) looks now relatively good, especially in the pre-oxidation phase. This axial zone seems to be rather important for the outcome of QUENCH-07. A considerable part of the produced hydrogen originates from oxidation in the upper part of the test section. In the second part of the transient phase about 200 s before cooldown a temperature escalation happened in the axial region around 950 mm, as indicated by the thermocouple TIT A/13 and the shroud thermo-couples. As all the inner thermo-couples had failed, we can only discern the consequences leading to an abrupt rise of the outer thermo-couple signals due to radiation heat transfer from the fuel rods. This temperature rise is distinctly higher, than would be expected from the increase of the electrical heating alone.

With the help of some modification in the radial heat transfer and in the coolant flow model the temperature escalation could to some extent be simulated by the code. Bending of some fuel rods was at first viewed to lead to disturbances in the coolant flow and radiation heat transfer within the bundle. As is known from post-test examinations (PTE) of QUENCH-03 [7], the bending of the fuel rods may even lead to mutual contact. We hold that this effect leads to a formation of hot spots, which then might act as origins of the temperature escalation affecting a certain axial region of the test section. The axial region between 750 and 850 mm is most favored for such an effect to occur, as it is far from the spacers at 550 and 1050 mm and as the fuel rod temperatures seem to be high enough for the loss of clad strength. There are some indications from PTE of QUENCH-07 on bending of fuels especially at 850 mm. But the evidence is not so strong as in the case of QUENCH-03 and, of course, PTE cannot give us a clue on the time, when this effect occurred.

Another mechanism for the initiation of a temperature escalation could be provided by the relocation of molten material. We know from the detection of He by the GAM 300 mass spectrometer that the absorber rod failed at about 2040 s. Also, the temperature of the absorber rod was then high enough for melting of the steel cladding and for eutectic melt formation between steel and B_4C. Thus, there was ample time for the relocation of molten material. The spacer at 1050 mm most probably played an important role in a partial blockage formation, as it constitutes an obstacle for material relocation. The temperature escalation around 950 mm finally led to shroud failure and is therefore the main cause for the severe damage in the upper part of the test section.

It is known from PTE that the shroud is largely destroyed above 850 mm; it partially or even totally disappeared in this axial region. But this is not indicated by the shroud thermo-couple readings, which show a rather regular behavior. The destruction and relocation of the shroud, of course occurred after shroud failure (3486 s), and later on part of the coolant flow could have passed through the space between the shroud and the stainless steel cooling jacket, the so-called Ar volume. Thus, it seems that the shroud thermo-couples located in this axial zone have been cooled by this diverted flow and have therefore remained intact. In this way

they did not indicate the temperatures of the inner part of the test section, which must have been considerably higher, but rather the temperature of the diverted coolant flow.

The calculated axial profiles of the oxide scale thickness at the time, when the calculation stopped are plotted in Fig. 88 together with experimental values from post test examinations, with "dox" denoting the oxide scales of the inner cluster of nine heated fuel rods, "doxc" that of the guide tube of the absorber rod, "doxa" that of the outer ring of 12 heated fuel rods and "doxsh" the oxide scale of the shroud. It should be noted that in the CALUMO code the zircaloy guide tube of the absorber rod experiences inside and outside oxidation of an equal amount. Thus, for comparison with the experimental data doxc has to be multiplied by a factor 2. Therefore with complete oxidation of the guide tube we have a maximum value of a bit less than 600 μm. Thus the guide tube is calculated to be fully oxidized above about 800 mm.

The oxidation features up to an axial position of about 750 mm are rather well met by the code. PTE has provided the maximum, the mean and the minimum values of the oxide scale thickness of all rods but it is not distinguished between inner and outer rods. If one could identify the maximum values with that of the inner rods the feature of almost complete oxidation of the claddings above about 850 mm is also well met by the code, with the maximum possible oxide scale thickness determined by the Pilling-Bedworth ratio and the as-fabricated wall thickness. There is a big difference between minimum and maximum oxide scale values determined by the metallography, the reason for this effect is not yet clear. It may be that some of the sub-channels are better cooled than the remaining part of the bundle, or that there has been partial spalling of the oxide scales.

For the outer part of the bundle and for the shroud the calculated values of oxide scale thickness are much too low between about 800 and 1100 mm. The strong growth of the oxide scales in the upper part of the test section occurred most probably after shroud failure with the consecutive loss of the coolant channel geometry. Also there are indications from PTE that in the upper part of the bundle clad ballooning did occur, leading to a further disturbance of the coolant flow. Clad ballooning must have occurred, when the oxide scales were still relatively thin, as the oxide scales increase the clad strength. For this reason it occurred only in the upper part of the test section, where also the temperature was high enough. We hold that clad ballooning ended in clad failures from about 3480 s onwards. It should also be noted that these effects allowed inside clad oxidation, contributing to the overheating of the bundle.

Thus, it seems that in the upper part of the test section the bundle and the shroud were insufficiently cooled even with a steam flow of 15 g/s. This seems to be the main reason for the strong temperature escalation in the upper part of the test section leading to a high oxidation and hydrogen production during the cooldown phase in this axial zone. At the time end of the calculation oxidation and hydrogen production were certainly not finished, but as the CALUMO code did not simulate the main effects (loss of coolant channel geometry and relocation of material) a comparison of calculated and measured values in the late phase of the test would in any case make not so much sense.

A comparison of measured and calculated hydrogen values (production rate and time integrated values) is to be seen in <u>Fig. 89</u>. The agreement is satisfactory up to the onset of cooldown. The measured hydrogen production rate shows a very high peak with a maximum value of about 2.3 g/s a bit after the onset of cooldown, which corresponds to a temporal steam consumption of about 21 g/s. At the time instant of this hydrogen peak (3607 s) the destruction of the shroud in the upper part of the test section was presumably under way. Therefore part of the steam flow passed through the Ar volume and was therefore not available for the oxidation and could, of course, not be consumed. This is in accord with the fact that the GAM300 mass spectrometer observed still a considerable steam flow around 3600 s. The measured high peak value of hydrogen production is therefore a bit doubtful, it could also not be reproduced by the code with a maximum value of a bit less than 0.6 g/s in the hydrogen production rate. But the increase of the signal before onset of cooldown is rather well met as well as the time of the peak, and the accumulated hydrogen up to the onset of cooldown. The overall produced hydrogen up to the end of the calculation (which was stopped a bit too early) was about 125 g, considerably less than the measured value of about 182 g. It is clear that the amount of hydrogen production which stems from the oxidation of the shroud and the outer heated fuel rods in the upper part of the test section is distinctly higher than calculated by the code. This would explain some of the difference between measured and calculated hydrogen production.

The accumulated hydrogen production measured after onset of cooldown comprises about 120 g. This corresponds to an oxidation of about 3.0 kg zircaloy, a considerable amount. The evaluation of the measurements of gas data is based on the Ar flow of 3 g/s. With the loss of the coolant channel geometry this assumption is temporarily no longer correct. It could well be that this effect occurred around 3600 s and that the Ar flow was for a certain time lower than assumed.

The oxidation of B_4C leads among other gases to a production of CO and CO_2 measured by the GAM300 mass spectrometer. These results can be compared to that of the BORCA model implemented in CALUMO (see <u>Fig. 90</u>). The oxidation rate depends on the steam flow rate [18] and it has been estimated that the test condition of the FZK BOX tests are somewhat representative for QUENCH-07. But this does not mean that they are perfectly identical. Therefore we can for the time being only expect a qualitative agreement between measured and calculated data. Further on, there is the competing phenomenon of eutectic reaction between molten steel and B_4C, which is not yet simulated in the CALUMO code. In view of these shortcomings we can note that the calculated production rates are in the correct order of magnitude up to about the onset of cooldown. The measured CO and CO_2 production rates show two high peaks with the first peak arising a few seconds later than the sole peak in the calculated production rates. The second peak might be due to an interaction of steam with the eutectic melt of steel and boron carbide.

The main oxidation phenomena in QUENCH-07 occurred in the upper part of the test section above about 800 mm after onset of cooldown mainly due to the loss of the coolant channel geometry by the destruction of the shroud. It is not clear in what way relocation of molten material participated in this effect. It certainly led to some local, partial obstruction of sub-channels and this effect may have induced the first temperature escalation around 950 mm. In any case, all these effects are not yet simulated in the bundle code CALUMO explaining to

a good deal the difference between code results and experimental findings in the cooldown phase. But up to the onset of cooldown the code provides a rather satisfying simulation of the experiment. This is especially true for the part of the test section below about 800 mm where even the end state is well met. In this axial zone the geometry of the coolant channel remained intact and it seems that material relocation did not have severe consequences.

8.2 Analytical Support for the B$_4$C Control Rod Test QUENCH-07 Using the SCDAP/RELAP5 Computer Code

8.2.1 Introduction

Test QUENCH-07 was to fulfil two aims. Firstly it should provide experimental data on degradation of B$_4$C control rods, its impact on surrounding fuel rods, and the production of gas (in particular H$_2$ and CH$_4$) before and during reflood in conditions as representative as possible of commercial 1300 MW PWR and BWR. Secondly, it should provide a useful database for the preparation of the future PHEBUS FPT3 in-pile experiment [22]. For the last reason, test QUENCH-07 was intended to be run as similar as possible to the planned PHEBUS test FPT3. For a comparison of the two test facilities it should be kept in mind that in the PHEBUS facility, the main heat sink is the heat loss in radial direction through the shroud whereas in the QUENCH facility the convective heat loss to the fluid determines the thermal behavior of the fuel rod bundle.

As the experiment itself, analytical support of QUENCH-07 was done within the COLOSS project of the Euratom 5th Framework Programme on Nuclear Fission Safety. Since the projected test differed in more than one aspect from previous QUENCH tests, it was thought prudent to rely on more than one institution and on more than one code system to prepare the test and to determine the test conduct. The engaged institutions are in alphabetic order Forschungszentrum Karlsruhe (FZK), Germany, with SCDAP/RELAP5 (S/R5) [23], Institut für Kernenergetik und Energiesysteme (IKE) at Stuttgart University, Germany, with ATHLET-CD, Paul Scherrer Institut (PSI), Villigen, Switzerland, with S/R5, and Universidad Politécnica de Madrid (UPM), Madrid, Spain, with ICARE2.

The aims of the pre-test calculations were twofold. They should give a sufficient confidence that the integrity of the QUENCH facility would be maintained in the test, and they should help to optimize the test conduct, so that as much benefit as possible could be drawn from the experiment. Post-test calculations show the quality of the modelling and help understanding the test.

In this report, only FZK pre- and post-test calculations are presented. They document the large computational effort, which was necessary to perform test QUENCH-07. They also give a first insight of the quality of this work by comparing results, calculated according to the real experimental conditions, with the measured data and identifying open points and needs for further interpretation of the test. A detailed presentation of analytical support by FZK and others is given in [26], but also in [27] and [28] for PSI, showing similar results as FZK.

8.2.2 FZK Calculations

All results were obtained with the in-house version of S/R5 mod 3.2. The new code version of S/R5, mod 3.3, is still inoperable; severe code errors have been reported to the code developers, but user support by the code developer is not any longer available. Among others, the current in-house version contains an adaptation of the CORA heater rod model to the conditions of the QUENCH facility, the material property data for ZrO_2 instead of those for UO_2 to model the pellets [24], and an improved model for heat transfer in the transition boiling region [25]. The calculations rely on the experience gained from calculations, done up to then.

Modelling of the QUENCH Facility

The modelling of the QUENCH facility with S/R5 is the same for all tests that are investigated. In the radial direction, the whole facility including the containment is modelled (Fig. 91), because the radial heat losses out of the bundle depend ultimately on the ambient room temperature. This modelling is mandatory for all work performed before experimental data are available, and it is desirable for all post-test analyses, because the calculated data are more detailed than the experimental ones.

The central rod, the two rings of rods to be heated independently, the four Zircaloy corner rods, the inner and outer cooling jacket, and the containment are modelled as SCDAP components. In this way two-dimensional heat conduction within the structures and radiation between adjacent structures are taken into account. As a central rod, an unheated fuel rod is modelled for nearly all calculations, the original code model of B_4C absorber rods being rather poor or even inappropriate. Meanwhile, however, the SCDAP model for the PWR control rod was extended for the correct B_4C material property data. B_4C oxidation is not yet taken into account, because the development of a respective code model requires further interpretation of separate effect tests at FZK and elsewhere. Use of this model is mentioned explicitly in the text. The corner rods are modelled as fuel rods. The ZrO_2 fibre insulation is modelled to end at the upper end of the heated zone. With this exception, all structures must be modelled to have the same length because of limitations in the code. Therefore, the upper and lower head cannot be modelled in all details.

The bundle flow and the gas atmospheres outside the outer cooling jacket, i.e. in the containment and the laboratory, are represented by a single channel each. The gas atmospheres outside the outer cooling jacket are assumed stagnant, thus neglecting natural convection in these regions. Because of restrictions in the code, where only a limited number of materials can be specified, these atmospheres are modelled to consist of argon.

The off-gas pipe is taken into account with its whole length of 3 m, including the orifice at the position where the gas sample for the mass spectrometer is taken and the orifice at the outlet of the off-gas pipe to simulate correctly the pressure boundary conditions during reflood phase. The mass flows in the off-gas pipe and the adjacent cooling jacket are modelled to be one-dimensional, the structures are modelled as RELAP heat structures, thus taking into account radial heat transfer within the structures.

For most calculations, the region of the heated part is axially modelled with ten 0.1 m long mesh cells. In the lower and upper electrode zones 0.45 and 0.6 m, respectively, of the test section are considered, each by three mesh cells. For the lowermost node in the lower electrode zone copper as electrode material is assumed and molybdenum elsewhere. In addition to this 16 nodes facility (16f) model a 32 nodes facility (32f) model is now available, where the whole facility is modelled as in the 16f model, but all axial mesh lengths in the heated zone as well as in the electrode zones are halved.

Original Test Protocol

Since test QUENCH-07 was also intended to support preparation of the planned PHEBUS in-pile test FPT3, a first proposal for the test conduct, the original test protocol, was derived as outlined in the following. As usual in QUENCH tests, the experiment begins with a stabilisation phase with a constant maximum bundle temperature of about 800 K. To be as close to FPT3 as possible, a power transient similar to previous QUENCH experiments is applied afterwards. When a maximum bundle temperature of 1500 K is reached, the nominal steam mass flow of 3 g/s, used up to then, is reduced to such a low value that steam starvation occurs in the bundle. As a first guess, "steam starvation" means a steam mass flow of not more than 10 mg/s at the end of the heated zone. The test is continued at a constant maximum bundle temperature of about 2000 K for 15 to 20 minutes (plateau phase) before initiating the cool-down phase. During the steam-starved phase, electrical power is assumed still to increase linearly for a certain time as in the projected FPT3 test. Some more details of the test conduct were to be derived from the results of pre-test calculations.

First Pre-Test Calculations

Pre-test calculations show that the original test protocol is not adequate for the QUENCH test. Firstly the electrical power transient should be continued for some time after steam flow reduction only to reach elevated temperatures as soon as possible, but then be reduced to a much lower value and be kept constant. Besides, the argon flow must be increased for a sufficient heat removal. Otherwise, too high temperatures occur, and even clad melting must be faced before the end of the envisaged duration of the high temperature test phase.

In subsequent calculations, electrical power input, steam, and mass flow rates were therefore varied. The results show that for a modified test protocol the bundle reacts sensitively to changes of physical parameters during the plateau phase because of the low convective heat transfer: the two cases shown in Fig. 92 differ only by the argon mass flow rate as a test parameter. For a value of 8 g /s, the bundle temperatures in the upper half of the heated zone have a maximum somewhat above 1600 K, whereas temperatures increase steadily for an argon mass flow of 6 g/s. This leads to clad melting, when the low steam flow phase is longer, and anyway constant temperatures as desired do not occur. To give an impression of this sensitivity, results for all calculations, done up to this time, are given in Fig. 93.

Fig. 92 also shows that just after power reduction chemical power due to oxidation has about the same value as electrical power. In contrast to electrical power, which is released into the whole bundle, chemical power release is mainly constrained to a small region in the upper half of the heated zone, and hence local chemical power input exceeds local electrical power

input by far. Since maximum temperature depends strongly on local power input, these results demonstrate the limits to influence the behaviour of the bundle by varying global electrical power input.

Final Test Protocol

Consequently a new test conduct, the final test protocol (FTP) as indicated in Fig. 94, was proposed during the COLOSS topical meeting on QUENCH-07 [22]. It is closer to previous QUENCH tests. The main difference to the previous test protocols is the phase after reaching elevated temperatures, which shall now be performed with nominal steam mass flow. In addition, some specifications of the test conduct are fixed in more detail than before. Clad temperature increase is limited to 0.3 – 0.5 K/s during test phase II to guarantee a benign temperature increase and so to minimize the risk of temperature escalations and premature rod damage. Furthermore, details of the cool-down phase are specified.

It was agreed to perform three sets of pre-test calculations. The first one should be performed exactly according to Fig. 94; test phase IV should be achieved by increase of electrical power input at constant steam mass flow rate of 3 g/s. The second one should be done with test phase III to be extended to 15 to 20 minutes. The third one should be performed with constant electrical power and reduced steam flow during test phase IV to obtain steam starvation in the bundle at least before cool-down initiation.

For a better organisation of the work, first calculations were done for test phases I to III only, in this way combining the first and second computational set for those test phases. The limitation of temperature increase before reaching the high temperature plateau implies a power history different from that assumed for the previous suggestion for test conduct. Maintaining the high temperature plateau over a sufficiently long time, but keeping maximum temperature below clad melting point, proved to be another laborious work, above all because of the high temperature level and hence the small safety margin for the facility. Fig. 95 shows the effort to be done for this purpose. Like Fig 3, this figure also gives an impression of predicted sensitivity of the facility with respect to changes of electrical power input showing that even minor changes decide about clad melting or an acceptable temperature range during test phase III.

The calculation labelled "final" shows that a temperature plateau of about 1800 K can be maintained for 20 minutes without difficulties except for a careful tuning of electrical power input. In internal discussions at FZK a maximum oxide layer thickness of 400 µm at the end of test phase III was considered reasonable in the sense that effects expected in the following phases, mainly oxidation, should be sufficiently large. Therefore, test phase III is restricted to 15 minutes and ends at 4000 s.

Results on the first alternative for test phase IV (power ramp at constant steam and argon mass flow rates) show that temperature increase is rather small in the beginning of the power transient. A maximum temperature of 2150 K, i.e. shortly below clad melting temperature, is reached at t = 4579 s, i.e. nearly 10 min after the beginning of test phase IV. For the second alternative for test phase IV (steam mass flow reduction at constant electrical power input) this maximum temperature of 2150 K is reached at t = 4160 s, i.e. only 2.5 min after the

beginning of phase IV. Steam consumption is somewhat more pronounced than predicted for the first alternative. The axial temperature profiles in these two cases are rather similar to one another for the same maximum temperature. However, temperature increase is much faster in case of steam mass flow reduction. Therefore, temperature levels are generally higher in this case and hydrogen production rate and hence oxide layer thickness are also higher.

Due to the fast temperature increase in case of steam mass flow reduction, the transient is very short and much faster than in the case of electrical power increase. Hence time for measurements as well as for operator intervention is very limited in the first case. The duration of the transient might be increased, when the electrical power is reduced at the time of steam mass flow reduction. This procedure had been proposed by UPM to avoid an undesired temperature escalation. This variant was not investigated in our calculations because such a test conduct is considered rather difficult to realize. In fact, an inappropriate change of electrical power might either jeopardize the integrity of the bundle or cool it down unintentionally; Fig. 92 demonstrates well the sensitivity of temperature with electrical power under similar conditions. Furthermore, the results of the CODEX B_4C test [29] suggest that not much CH_4 formation can be expected for a steam mass flow of 1 g/s. For these reasons, a test conduct with a power transient instead of a steam mass flow reduction is favoured at FZK. Cool-down is calculated to occur without temperature escalation.

Post-Test Calculations

Post-test calculations are based on the real test conduct with the same modelling as for the pre-test calculations. Results are given in Figs. 96 – 97. Long-dashed lines refer to the 16f model. In the first transient, phase II, calculated temperatures are underestimated (Fig. 96), whereas during oxidation (phase III) a significant temperature increase is calculated which has not been measured (stabilized temperatures in the test). This leads to sensible deviations of calculated hydrogen production from measured values. With the 32f model, results for phase II are not improved, but the agreement with the experiment for higher temperatures as in phase III is. This leads to a later calculated onset of temperature escalation, giving better agreement of oxide layer thickness and a smoother profile of linear electrical rod power at the time when the corner rod is withdrawn.

The difference of the results for the two axial discretizations is very pronounced for the oxide layer thickness and hydrogen production rate (Fig. 97), because for the fine axial discretization an escalation is calculated just to have started, whereas for the coarse discretization it is calculated to begin about 120 s earlier. For this reason, the peak value of hydrogen production rate is calculated to be one order of magnitude larger for the coarse axial discretization. As can also be seen from the axial temperature profiles (Fig. 97), the fine axial discretization generally improves the agreement in the upper electrode zone. During cool-down differences between experiment and calculation mainly seem to rise from different temperatures at the initiation of cool-down.

In a further calculation, the recommendations for Zircaloy oxidation [30], made during the COLOSS project, have been applied instead of the standard correlations in S/R5 (Cathcart and Urbanic-Heidrick for low and high temperatures, respectively). Discussions during

COLOSS meetings showed that a steam supply limitation in the code is mandatory for the new oxidation model. In the standard version of S/R5 [23] a steam supply limitation model is already implemented. It is based on an analogy of heat and mass transfer and, because dimensionless numbers are used, it should essentially be applicable irrespective of the oxidation model. It is therefore applied without any change for all calculations presented in this report. First results with this oxidation model suggest that the calculated hydrogen production agrees somewhat better with experimental data for lower temperatures. In the high temperature regime, however, a large over-estimation is calculated, even though the steam available for oxidation is assumed limited. Though error checks are not yet complete, the results seem credible, because similar experience was made for calculations of accident scenarios in commercial reactors, done by participants of the Plant Analysis Group PAG as part of COLOSS. Their work also suggests that a sound approach for steam limitation is either not possible or too laborious in view of the benefit that can be expected. Consequently, no further work will be devoted to this issue.

Calculations for test QUENCH-09, performed meanwhile, suggest that a decrease of thermal conductivity of the shroud insulation material might improve the agreement in phase II. This item needs some more work to be done, because it is an aim of the analytical support at FZK to perform the calculations for all QUENCH tests with the same modelling. However, no further investigation of that sort is made presently, because SCDAPSIM is being implemented as an alternative to S/R5 with a better user support.

8.2.3 Conclusions

The conduct of test QUENCH-07 was originally planned to be similar to the planned PHEBUS in-pile test FPT3, keeping in mind that in the PHEBUS facility the main heat sink is the heat loss in radial direction through the shroud whereas in the QUENCH facility the convective heat loss to the fluid determines the thermal behaviour of the fuel rod bundle. Since QUENCH-07 differed in more than one aspect from previous tests in the QUENCH facility at FZK, more attention than for other QUENCH tests had to be paid to define the test conduct.

FZK pre-test calculations with in-house version SCDAP/RELAP5 mod 3.2 show that for the original test protocol the various aims of the test cannot be fulfilled in the QUENCH facility at the same time. Even for a modified test protocol, pre-test calculations predicted, that due to the elevated temperatures to be maintained for a long time, the QUENCH facility would be rather sensitive to changes of experimental parameters as electrical power input and that the facility might even be damaged during the test. When the steam mass flow is reduced, this sensitivity is enhanced because of the lower conductive heat removal. Out of the variants for the final test protocol, proposed on the basis of such calculations, a power transient to reach very high temperatures in the bundle before final cool-down is considered advantageous in comparison to a steam mass flow reduction. The other participants, engaged in these analyses, calculated the same trends of results. In sum, a large computational effort was necessary to define an appropriate test conduct, but the comparison of experimental data of this and the subsequent test, QUENCH-09, justified this work and the insight gained during its course.

The post-test results show the necessity of a sufficiently fine spatial resolution of the computational domain. They also show deviations to measured temperatures in the first transient (phase II) already, but further work is not done actually, because S/R5 is being replaced by SCDAPSIM, because S/R5 user support is no longer available. First calculations with the recommendations for Zircaloy oxidation correlations gave some improvement for lower temperatures, but essential deviations for high temperatures. Because of the difficulties to develop a sound model for steam limitation, indispensable in this context and also encountered by other COLOSS partners, no more work is done on this issue. Further programme work probably also depends on further interpretation of experimental results, especially of QUENCH-09 and related separate effect tests, obtained in COLOSS.

References

[1]   J.M. Broughton, P. Kuan, and D.A. Petti, "A Scenario of the Three Mile Island Unit 2 Accident," Nuclear Technology, 87, 34, 1989.

[2]   P. Hofmann, S. Hagen, V. Noack, G. Schanz, L. Sepold, "Chemical-Physical Behavior of Light Water Reactor Core Components Tested under Severe Reactor Accident Conditions in the CORA Facility," Nuclear Technology, vol. 118, 1997, p. 200.

[3]   S. Hagen, P. Hofmann, V. Noack, L. Sepold, G. Schanz, G. Schumacher, "Comparison of the Quench Experiments CORA-12, CORA-13, CORA-17," FZKA 5679, Forschungs-zentrum Karlsruhe, 1996.

[4]   S.M. Modro and M.L. Carboneau, "The LP-FP-2 Severe Fuel Damage Scenario; Discussion of the Relative Influence of the Transient and Reflood Phase in Affecting the Final Condition of the Bundle," OECD/LOFT Final Event, ISBN 92-64-03339-4, 1991, p. 388.

[5]   P. Hofmann, V. Noack,   M.S. Veshchunov, A.V. Berdyshev, A.V. L.V. Matweev, A.V. Palagin, V.E. Shestak, "Physico-Chemical Behavior of Zircaloy Fuel Rod Cladding Tubes During LWR Severe Accident Reflood," FZKA 5846, Forschungszentrum Karlsruhe, 1997.

[6]   P. Hofmann, A. Miassoedov, L. Steinbock, M. Steinbrück, M. Veshchunov et al. "Quench Behavior of Zircaloy Fuel Rod Cladding Tubes. Small-Scale Experiments and Modeling of the Quench Phenomena," FZKA 6208, Forschungszentrum Karlsruhe, 1999.

[7]   P. Hofmann, C. Homann, W. Leiling, A. Miassoedov, D. Piel, G. Schanz, L. Schmidt, L. Sepold, M. Steinbrück, "Experimental and Calculational Results of the Experiments QUENCH-02 and QUENCH-03," FZKA 6295, Forschungszentrum Karlsruhe, 2000.

[8]   L. Sepold, P. Hofmann, W. Leiling, A. Miassoedov, D. Piel, L. Schmidt, M. Steinbrück, "Reflooding Experiments with LWR-Type Fuel Rod Simulators in the QUENCH Facility," Nuclear Engineering and Design 204, 2001, 205 - 220.

[9]   M. S. Veshchunov, J. Stuckert, A. V. Berdyshev, "Modelling of Zr-O and U-Zr-O melts oxidation and new crucible tests," FZKA 6792, Forschungszentrum Karlsruhe, 2002

[10] B. Massalski, "Binary Alloy Phase Diagrams," Vol. 3, 2nd Ed., ASM, 1990

[11] H. Kleykamp, R. Pejsa, "Chemical and X-ray Diffraction Analysis on Selected Samples from the TMI-2 Reactor Core," KfK 4872, 1991

[12] P. Hofmann, M. E. Markiewicz, J. L. Spino, "Reaction Behavior of B_4C Absorber Material with Stainless Steel and Zircaloy in Severe Light Water Reactor Accidents," Nucl. Technol. 90 (1990) 226

[13] M.S. Veshchunov, P. Hofmann, "Modelling of the Interactions between B_4C and Stainless Steel at High Temperatures," J. Nucl. Mater. 226 (1995) 72-91

[14] M.S. Veshchunov, P. Hofmann, "Modelling of B_4C Interactions with Zircaloy at High Temperatures," J. Nucl. Mater. 210 (1994) 11-20

[15] H. Steiner, M. Heck, "The code CALUMO, a tool for the analysis for temperature transients in QUENCH tests," FZKA 6501, 2000.

[16] H. Steiner, M. Steinbrück, "Modelling of boron carbide oxidation and boric acid formation," Contribution to the PSF Annual Report 2001, FZKA 6741, Forschungszentrum Karlsruhe, 2002, pp. 168-174.

[17] S. Leistikow et al., „Kinetik und Morphologie der isothermen Dampfoxidation von Zircaloy-4 bei 700 bis 1300 °C," KFK 2587, 1978.

[18] M. Steinbrück, A. Meier, U. Stegmaier, L. Steinbock, J. Stuckert, "BOX Tests on the Oxidation of B_4C at High Temperatures. Test Data Report," SAM-COLOSS-P026, Forschungszentrum Karlsruhe, 2002.

[19] M. Steinbrück, A. Meier, U. Stegmaier, L. Steinbock, J. Stuckert, "Degradation and Oxidation of B_4C Control Rod Segments at High Temperatures. Test Data Report," SAM-COLOSS-P028, Forschungszentrum Karlsruhe, 2003.

[20] M. Steinbrück, C. Homann, A. Miassoedov, G. Schanz, L. Sepold, U. Stegmaier, H. Steiner, J. Stuckert, "Results of the QUENCH-09 Experiment with a B_4C Control Rod Simulator," FZKA 6829, Forschungszentrum Karlsruhe, 2003.

[21] http://www.fzk.de/quench

[22] A. Miassoedov, Minutes of the COLOSS Topical Meeting on QUENCH-07 Test, Karlsruhe, Feb. 8, 2001, SAM-COLOSS-M006, Forschungszentrum Karlsruhe, 2001.

[23] The SCDAP/RELAP5 Development Team: SCDAP/RELAP5/MOD 3.2 Code Manual, NUREG/CR-6150, INEL-96/0422, Idaho Fall, Idaho, USA, 1997.

[24] W. Hering, Ch. Homann, "Improvement of the Severe Accident Code SCDAP/RELAP5 mod 3.2 with respect to the FZK QUENCH facility," FZKA 6566, to be published.

[25] V. Sanchez, E. Elias, Ch. Homann, W. Hering, D. Struwe, "Development and Validation of a Transition Boiling Model for the RELAP5/MOD3 Reflood Simulation," FZKA 5954, Sep. 1997.

[26] Ch. Homann, W. Hering, J. Birchley, J. A. Fernandez Benitez, M. Ortega Bernardo, "Analytical Support for B_4C Control Rod Test QUENCH-07," FZKA 6822, April 2003.

[27] J. Birchley, "QUENCH-07 Preliminary Post-test Calculations using SCDAP/RELAP5/MOD 3.2," SAM-COLOSS-P015, 2003.

[28] J. Birchley, "Analysis of QUENCH-06, -07, and -09 Experiments using MELCOR 1.8.5," SAM-COLOSS-P059, 2003.

[29] Z. Hozer, I. Nagy, P. Windberg, M. Balasko, L. Matus, O. Prokopiev, A. Czitrovszky, A. Nagy, P. Jani, "CODEX-B4C Experimental Data Report," SAM-COLOSS-P020, D17, Budapest, Oct. 2001.

[30] G. Schanz, "Recommendations and Supporting Information on the Choice of Zirconium Oxidation Models in Severe Accident Codes," FZKA 6827, SAM-COLOSS-P043, March 2003.

[31] M. Steinbrück, "Analysis of hydrogen production in QUENCH bundle tests," FZKA 6968, to be published in 2004.

Acknowledgements

Table 1: QUENCH Test Matrix

Test	Quench medium	Flooding rate[1]	Heat-up rate	Max. ZrO$_2$ layer thickness[2]	Temp. at onset of flooding[3]	Remarks, objectives	Date of test conduct
QUENCH-00	Water	2.8 cm/s from bottom	1.0 K/s	≈ 500 µm	≈ 1800 K	COBE Project; commissioning tests.	Oct. 9 - 16, 97
QUENCH-01	Water	1.6 cm/s; from the bottom	0.5 K/s	≈ 300 µm	≈ 1900 K	COBE Project; partial fragmentation of pre-oxidized cladding.	February 26, 98
QUENCH-02	Water	1.6 cm/s; from the bottom	0.5 K/s	completely oxidized	> 2400 K	COBE Project; no additional pre-oxidation, quenching from high temperatures.	July 7, 98
QUENCH-03	Water	1.4 cm/s from the bottom	0.6 K/s	completely oxidized	> 2400 K	No additional pre-oxidation, quenching from high temperatures.	January 20, 99
QUENCH-04	Steam	≈ 50 g/s; from the bottom	0.5 K/s	≈ 170 µm	≈ 2300 K	Cooldown behaviour of slightly pre-oxidized cladding by cold steam injection.	June 30, 99
QUENCH-05	Steam	≈ 50 g/s from the bottom	0.5 K/s	≈ 400 µm	≈ 2300 K	Cooldown behaviour of pre-oxidized cladding by cold steam injection.	March 29, 2000
QUENCH-06	Water	1.4 cm/s from the bottom	0.5 K/s	≈ 660 µm	≈ 2300 K	OECD-ISP 45; blind test predictions by different computer codes.	December, 13 2000
QUENCH-07	Steam	≈ 15 g/s from the bottom	0.5 K/s	completely oxidized	> 2300 K	COLOSS Project; impact of B$_4$C absorber rod failure on H$_2$, CO, CO$_2$, and CH$_4$ generation.	July 25, 2001

[1] Flooding rate for water: rise of the water level at the -250 mm bundle elevation (single-phase flow).
[2] Measured post-test at the bundle elevation of max. temperature.
[3] Maximum measured or estimated temperature in test section

Revised: March, 2002

Table 2: Design characteristics of the QUENCH-07 test bundle

Bundle type		PWR, 21 rods
Pitch		14.3 mm
Number of rods heated/ unheated		20/ 1
Cladding	heated rod	Zircaloy-4, $\varnothing$ 10.75 / 9.3 mm L = 2278 mm (EL -593 to 1685)
Cladding	control (central) rod	SS, $\varnothing$ 10.24 / 7.72 mm L = 1083 mm (EL -20 to 1063)
Pellet	heated rod (annular) control rod (full)	ZrO_2, $\varnothing$ 9.15/ 6.15 mm, L=11 mm B_4C, $\varnothing$ 7.48 mm, L=14 mm
Internal rod pressure	heated rod control rod	0.22 MPa abs. Ar5%Kr 0.12 MPa abs. He
Central rod guide tube		Zircaloy-4, $\varnothing$ 12.1 / 11.3 mm L = 1187 mm (EL -42 to 1145) Holes: 4 x $\varnothing$ 4 mm at EL –34 and +1179 mm
Overall rod length	heated rod (levels) control rod (levels)	2480 mm (EL -690 to 1790) 2842 mm (EL -827 to 2015, incl. extension piece)
Heater material		Tungsten (W)
Heater diameter		6 mm
Heated length		1024 mm
Pellet stack length	heated rod control rod	EL 0 to 1024 mm EL 0 to 1008 mm
Grid spacer (5)	material length location of lower edge	Zircaloy-4 (Zry), Inconel 718 (Inc) Zry 42 mm, Inc 38 mm Inc: -200 mm; Zry: 50, 550, 1050, 1410 mm
Shroud	material wall thickness outside diameter length (extension)	Zircaloy-4 2.38 mm 84.76 mm 1600 mm (EL -300 to 1300)
Shroud insulation	material insulation thickness extension	ZrO_2 fiber ~ 37 mm EL -300 to 1000 mm

Molybdenum-copper electrodes:
   length of upper electrodes
   length of lower electrodes
   diameter of electrodes: - prior to coating
                 - after coating with ZrO_2
		
		766 mm (576 Mo, 190 mm Cu)
		690 mm (300 Mo, 390 mm Cu)
		8.6 mm
		9.0 mm

Cooling jacket	material inner tube outer tube	1.4541 stainless steel $\varnothing$ 158.3 / 168.3 mm $\varnothing$ 181.7 / 193.7 mm

Table 3: **List of instrumentation for the QUENCH-07 Test**

Chan-nel	Designation	Instrument, location	Output in
0		Reserve	
1	TFS 2/11	TC (W/Re) fuel rod simulator 8 (type 2), 750 mm, 135°	K
2	TFS 2/13	TC (W/Re) fuel rod simulator 2 (type 2), 950 mm, 225°	K
3	TFS 2/15	TC (W/Re) fuel rod simulator 4 (type 2), 1150 mm, 315°	K
4	TFS 2/17	TC (W/Re) fuel rod simulator 6 (type 2), 1350 mm, 45°	K
5	TSH 15/180	TC (W/Re) shroud outer surface, 1150 mm, 206°	K
6	TFS 3/10	TC (W/Re) fuel rod simulator 7 (type 3), 650 mm, 135°	K
7		Reserve	K
8	TFS 3/13	TC (W/Re) fuel rod simulator 3 (type 3), 950 mm, 315°	K
9	TFS 3/14	TC (W/Re) fuel rod simulator 5 (type 3), 1050 mm, 45°	K
10	TFS 4/11	TC (W/Re) fuel rod simulator 14 (type 4), 750 mm, 45°	K
11	TFS 4/13	TC (W/Re) fuel rod simulator 20 (type 4), 950 mm, 135°	K
12		Reserve	K
13	TFS 5/11	TC (W/Re) fuel rod simulator 13 (type 5), 750 mm, 45°	K
14		Reserve	K
15	TFS 5/13	TC (W/Re) fuel rod simulator 16 (type 5), 950 mm, 135°	K
16	TFS 5/14	TC (W/Re) fuel rod simulator 18 (type 5), 1050 mm, 45°	K
17	TSH 16/180	TC (W/Re) shroud outer surface, 1250 mm, 206°	K
18	TSH 13/90	TC (W/Re) shroud outer surface, 950 mm, 116°	K
19	TSH 14/90	TC (W/Re) shroud outer surface, 1050 mm, 116°	K
20	TSH 11/0	TC (W/Re) shroud outer surface, 750 mm, 26°	K
21	TSH 12/0	TC (W/Re) shroud outer surface, 850 mm, 26°	K
22	TFS 2/5	TC (NiCr/Ni) fuel rod simulator 2 (type 2), 150 mm, 225°	K
23	TFS 2/7	TC (NiCr/Ni) fuel rod simulator 6 (type 2), 350 mm, 45°	K
24	F 902	Off-gas flow rate before Caldos (H_2)	Nm³/h
25	FM 401	Argon gas mass flow rate	g/s
:			
32	TIT A/13	TC (W/Re) corner rod A, center, 950 mm	K
33	TFS 5/10	TC (W/Re) fuel rod simulator 12 (type 5), 650 mm, 225°	K
34	TFS 2/12	TC (W/Re) fuel rod simulator 2 (type 2), 850 mm, 315°	K

Chan-nel	Designation	Instrument, location	Output in
35	TSH 9/90	TC (NiCr/Ni) shroud outer surface, 550 mm, 116°	K
36	TSH 9/270	TC (NiCr/Ni) shroud outer surface, 550 mm, 296°	K
37	TFS 3/16	TC (W/Re) fuel rod simulator 7 (type 3), 1250 mm, 135°	K
38	TFS 5/9	TC (NiCr/Ni) fuel rod simulator 10 (type 5), 550 mm, 315°	K
39	TFS 2/9	TC (NiCr/Ni) fuel rod simulator 8 (type 2), 550 mm, 135°	K
40	TIT D/12	TC (W/Re) corner rod D, center, 850 mm	K
41		Reserve	K
42	TFS 5/8	TC (NiCr/Ni) fuel rod simulator 21 (type 5), 450 mm, 135°	K
43	TFS 3/8	TC (NiCr/Ni) fuel rod simulator 5 (type 3), 450 mm, 45°	K
:			
45		Reserve	
46	TIT C/9	TC (NiCr/Ni) corner rod C, center, 550 mm	K
47	TFS 5/15	TC (W/Re) fuel rod simulator 19 (type 5), 1150 mm, 225°	K
48	TFS 5/16	TC (W/Re) fuel rod simulator 21 (type 5), 1250 mm, 135°	K
49	TFS 5/17	TC (W/Re) fuel rod simulator 10 (type 5), 1350 mm, 315°	K
50	TFS 3/12	TC (W/Re) fuel rod simulator 9 (type 3), 850 mm, 225°	K
51	TFS 5/12	TC (W/Re) fuel rod simulator 15 (type 5), 850 mm, 315°	K
52	TSH 13/270	TC (W/Re) shroud outer surface, 950 mm, 296°	K
53	TSH 14/270	TC (W/Re) shroud outer surface, 1050 mm, 296°	K
54	TSH 11/180	TC (W/Re) shroud outer surface, 750 mm, 206°	k
55	TSH 12/180	TC (W/Re) shroud outer surface, 850 mm, 206°	K
:			
58		Reserve	K
:			
66	TSH 15/0	TC (W/Re) shroud outer surface, 1150 mm, 26°	K
67	TSH 16/0	TC (W/Re) shroud outer surface, 1250 mm, 26°	K
68	T 512	Gas temperature bundle outlet	K
:			
71	Ref. T 01	Reference temperature 1	K
72	TFS 2/1	TC (NiCr/Ni) fuel rod simulator 4 (type 2), -250 mm, 315°	K
73	TFS 2/2	TC (NiCr/Ni) fuel rod simulator 6 (type 2), -150 mm, 45°	K

Chan-nel	Designation	Instrument, location	Output in
74	TFS 2/3	TC (NiCr/Ni) fuel rod simulator 8 (type 2), -50 mm, 135°	K
75	TCRI 11	TC (NiCr/Ni) B_4C control rod, SS cladding, 750 mm	K
76	TFS 2/6	TC (NiCr/Ni) fuel rod simulator 4 (type 2), 250 mm, 315°	K
77	TCRI 12	TC (NiCr/Ni) B_4C control rod, SS cladding, 850 mm	K
78	TFS 5/4/0	TC (NiCr/Ni) fuel rod simulator 15 (type 5), 50 mm, 315°	K
79	TFS 5/4/180	TC (NiCr/Ni) fuel rod simulator 21 (type 5), 50 mm, 135°	K
80	TFS 5/5	TC (NiCr/Ni) fuel rod simulator 16 (type 5), 150 mm, 135°	K
81	TFS 5/6	TC (NiCr/Ni) fuel rod simulator 18 (type 5), 250 mm, 45°	K
82	TFS 5/7	TC (NiCr/Ni) fuel rod simulator 19 (type 5), 350 mm, 225°	K
83	TSH 4/270	TC (NiCr/Ni) shroud outer surface, 50 mm, 296°	K
84	TSH 3/180	TC (NiCr/Ni) shroud outer surface, -50 mm, 206°	K
85	TSH 4/180	TC (NiCr/Ni) shroud outer surface, 50 mm. 206°	K
86	TSH 7/180	TC (NiCr/Ni) shroud outer surface, 350 mm, 206°	K
87	TSH 4/90	TC (NiCr/Ni) shroud outer surface, 50 mm, 116°	K
88	TSH 1/0	TC (NiCr/Ni) shroud outer surface, -250 mm, 26°	K
89	TSH 4/0	TC (NiCr/Ni) shroud outer surface, 50 mm, 26°	K
90	TSH 7/0	TC (NiCr/Ni) shroud outer surface, 350 mm, 26°	K
91	TCI 9/270	TC (NiCr/Ni) cooling jacket inner tube wall, 550 mm, 270°	K
92	TCI 10/270	TC (NiCr/Ni) cooling jacket inner tube wall, 650 mm, 270°	K
93	TCI 11/270	TC (NiCr/Ni) cooling jacket inner tube wall, 750 mm, 270°	K
94	TCI 13/270	TC (NiCr/Ni) cooling jacket inner tube wall, 950 mm, 270°	K
95	TCRI 13	TC (NiCr/Ni) B_4C control rod, SS cladding, 950 mm	K
96	TCI 1/180	TC (NiCr/Ni) cooling jacket inner tube wall, -250 mm, 180°	K
97	TCI 4/180	TC (NiCr/Ni) cooling jacket inner tube wall, 50 mm, 180°	K
98	TCI 7/180	TC (NiCr/Ni) cooling jacket inner tube wall, 350 mm, 180°	K
99	TCI 11/180	TC (NiCr/Ni) cooling jacket inner tube wall, 750 mm, 180°	K
100	TCI 12/180	TC (NiCr/Ni) cooling jacket inner tube wall, 850 mm, 180°	K
101	TCI 13/180	TC (NiCr/Ni) cooling jacket inner tube wall, 950 mm, 180°	K
:			
103		Reserve	K
104	TCI 9/90	TC (NiCr/Ni) cooling jacket inner tube wall, 550 mm, 90°	K

Chan-nel	Designation	Instrument, location	Output in
105	TCI 10/90	TC (NiCr/Ni) cooling jacket inner tube wall, 650 mm, 90°	K
106	TCI 11/90	TC (NiCr/Ni) cooling jacket inner tube wall, 750 mm, 90°	K
107	TCI 13/90	TC (NiCr/Ni) cooling jacket inner tube wall, 950 mm, 90°	K
:			
109	TCI 1/0	TC (NiCr/Ni) cooling jacket inner tube wall, -250 mm, 0°	K
110	TCI 4/0	TC (NiCr/Ni) cooling jacket inner tube wall, 50 mm, 0°	K
111	TCI 7/0	TC (NiCr/Ni) cooling jacket inner tube wall, 350 mm, 0°	K
112	TCI 11/0	TC (NiCr/Ni) cooling jacket inner tube wall, 750 mm, 0°	K
113	TCI 12/0	TC (NiCr/Ni) cooling jacket inner tube wall, 850 mm, 0°	K
114	TCI 13/0	TC (NiCr/Ni) cooling jacket inner tube wall, 950 mm, 0°	K
115	TCI 15/0	TC (NiCr/Ni) cooling jacket inner tube wall, 1150 mm, 0°	K
116		Reserve	K
117	TCO 9/270	TC (NiCr/Ni) cooling jacket outer tube surface, 550 mm, 270°	K
118	TCO 4/180	TC (NiCr/Ni) cooling jacket outer tube surface, 50 mm, 180°	K
:			
120	TCO 1/0	TC (NiCr/Ni) cooling jacket outer tube surface, -250 mm, 0°	K
121	TCO 7/0	TC (NiCr/Ni) cooling jacket outer tube surface, 350 mm, 0°	K
:			
123	T 601	Temperature before off-gas flow instrument F 601	K
:			
128	T 104	Temperature quench water	K
129	T 201	Temperature steam generator heating pipe	K
130	T 204	Temperature before steam flow instrument location 50 g/s	K
131	T 205	Temperature before steam flow instrument location 10 g/s	K
132	T 301A	Temperature behind superheater	K
133	T 302	Temperature superheater heating pipe	K
134	T 303	Temperature before total flow instrument location	K
135	T 401	Temperature before gas flow instrument location	K
136	T 403	Temperature at inlet cooling gas	K
137	T 404	Temperature at outlet cooling gas	K
138	T 501	Temperature at containment	K

Chan-nel	Designation	Instrument, location	Output in
139	T 502	Temperature at containment	K
140	T 503	Temperature at containment	K
141	T 504	Temperature at containment	K
142	T 505	Temperature at containment	K
143	T 506	Temperature at containment	K
144	T 507	Temperature at containment	K
145	T 508	Temperature at containment	K
146	T 509	Temperature bundle head outside (wall)	K
147	T 510	Temperature at containment	K
148	T 511	Gas temperature at bundle inlet	K
149	T 901	Temperature before off-gas flow instrument F 901	K
:			
151	Ref. T 02	Reference temperature 2	K
152	P 201	Pressure steam generator	bar
153	P 204	Pressure at steam flow instrument location 50 g/s	bar
154	P 205	Pressure at steam flow instrument location 10 g/s	bar
155	P 303	Pressure before total flow instrument location	bar
156	P 401	Pressure before gas flow instrument location	bar
157	P 511	Pressure at bundle inlet	bar
158	P 512	Pressure at bundle outlet	bar
159	P 601	Pressure before off-gas flow instrument F 601	bar
160	P 901	Pressure before off-gas flow instrument F 901	bar
161	L 201	Liquid level steam generator	mm
162	L 501	Liquid level quench water	mm
163	L 701	Liquid level condensation vessel	mm
164	Q 901	H_2 concentration, off-gas (Caldos)	% H_2
165	P 411	Pressure Ar-Kr supply	bar
166	P 403	Pressure Ar cooling of cooling jacket	bar
167	P 406	Pressure insulation shroud/cooling jacket	bar
168	F 104	Flow rate quench water	l/h
169	F 204	Flow rate steam 50 g/s	g/s

Chan-nel	Designation	Instrument, location	Output in
170	F 205	Flow rate steam 10 g/s	g/s
171	F 303	Flow rate at bundle inlet (steam + argon), orifice	mbar
172	F 401	Argon gas flow rate	Nm³/h
173	F 403	Flow rate cooling gas	Nm³/h
174	F 601	Flow rate off-gas (orifice)	mbar
175	F 901	Off-gas flow rate before Caldos (H_2)	m³/h
176	E 201	Electric current steam generator	A
177	E 301	Electric current superheater	A
178	E 501	Electric current inner ring of fuel rod simulators	A
179	E 502	Electric current outer ring of fuel rod simulators	A
180	E 503	Electric voltage inner ring of fuel rod simulators	V
181	E 504	Electric voltage outer ring of fuel rod simulators	V
182	Hub_V302	Steam supply valve lift	%
183	Ref. T 03	Reference temperature 3	K
:			
250	E 505	Electric power inner ring of fuel rod simulators	W
251	E 506	Electric power outer ring of fuel rod simulators	W

Note: Tip of thermocouple TFS 2/1 bent into flow channel to measure the fluid temperature

Table 4:   QUENCH-07; Failure of thermocouples

Thermocouple	Elevation [mm]	Time at failure [s]	Failure temperature [K]
TFS 3/8	450	3471	1208
TFS 2/11	750	3257	1666
TFS 4/11	750	3215	1704
TFS 5/11	750	3400	1868
TCRI 11[*)]	750	3839	864
TFS 2/12	850	3157	1670
TFS 3/12	850	3185	1625
TFS 5/12	850	3176	1757
TCRI 12[*)]	850	3917	766
TFS 2/13	950	3182/	1708
TFS 3/13	950	2875	1704
TFS 4/13	950	2751	1647
TFS 5/13	950	2982	1681
TCRI 13 [*)]	950	3534	1631
TIT A/13	950	3468	2114
TCO 13/0	950	Pre-test failure	
TFS 3/14	1050	3382	1775
TFS 5/14	1050	3534	2448
TFS 2/15	1150	3572	2111
TFS 5/15	1150	3628	1944
TFS 3/16	1250	3572	2110
TFS 2/17	1350	3578	2051
T 512	1350	3578	1727

[*)] Data must be treated with caution since these NiCr-Ni TCs are located in a groove of the SS control rod cladding and are not robust enough to withstand very high temperatures or local rod degradation.

Table 5:   QUENCH-07; Sequence of events

Time [s]	Event
0	Start of data recording, test bundle at ~873 K, data acquisition frequency at 0.25 Hz; start of heatup from ~873 K to ~1723 K
328	Data acquisition frequency at 1 Hz
2040	Absorber rod failure (helium detection at the mass spectrometer) at ~1585 K (TCRI 13)
2160	First measurement of CO, CO_2
2200	Start of B_4C oxidation phase (TIT A/13: ~1723 K)
3090	Withdrawal of corner rod B
3123	Data acquisition frequency at 5 Hz
3140	Start of the transient phase (TIT A/13: ~1770 K)
3322	Begin of temperature escalation at the 950 mm level (TIT A/13: ~1850 K)
3481	Rod failure (based on P 411)
3486	Shroud failure (based on P 406)
3557	Cooldown initiation
3558	Cooldown steam at the test section inlet (T 511)
3585	Start of electric power reduction from 18.5 kW to 3.9 kW
3602	Electric power at 3.9 kW
3749	Electric power shutoff
4126.6	Data acquisition frequency at 0.25 Hz
5107	Cooldown steam turned off
5530.6	End of data recording

0 s = 09:56:56 h on July 25, 2001

Table 6: **QUENCH-07; Excursion temperatures**

Elevation [mm]	Thermocouple	Time at excursion [s]	Excursion temperature [K]
850	TSH 12/0	3451	1731
850	TSH 12/180	3448	1789
850	TIT D/12	3414	1781
950	TIT A/13	3322	1846
950	TSH 13/90	3349	1783
950	TSH 13/270	3443	1722
1050	TFS 5/14	3418	1767
1050	TSH 14/90	3357	1564
1150	TFS 2/15	3352	1612
1150	TFS 5/15	3333	1435
1150	TSH 15/0	3361	1677
1150	TSH 15/180	3334	1676
1250	TFS 3/16	3479	1479
1250	TFS 5/16	3486	1452
1250	TSH 16/0	3394	1703
1350	TFS 2/17	3563*	1362
1350	TFS 5/17	3564*	1220

*) After cooldown initiation

Table 7: **QUENCH-07; Maximum measured test rod temperature of each elevation**

Elevation [mm]	Thermocouple	Time [s]	Maximum temperature [K]
- 250	TFS 2/1	3571	639
- 150	TFS 2/2	3564	708
- 50	TFS 2/3	3562	768
50	TFS 5/4/0	3485	814
50	TFS 5/4/180	3504	823
150	TFS 2/5	3533	961
250	TFS 2/6	3539	1090
350	TFS 2/7	3502	1174
450	TFS 5/8	3563	1225
550	TFS 2/9	3563	1335
650	TFS 5/10	3564	1566
750	TFS 2/11	3240	1825
850	TFS 5/12	3557	2152
950	TIT A/13	3591*	2316*
1050	-		
1150	TFS 5/15	3616	2225
1250	-		
1350	TFS 5/17	3609	2146

*) Unreliable, TC could have failed earlier (see Table 4)

Table 8: QUENCH-07; Maximum measured shroud temperature of each elevation

Elevation [mm]	Thermocouple	Time [s]	Maximum temperature [K]
- 250	TSH 1/0	3576	583
- 50	TSH 3/180	3565	690
50	TSH 4/0	3496	754
350	TSH 7/180	3565	1108
550	TSH 9/270	3565	1277
750	TSH 11/180	3572	1717
850	TSH 12/0	3568	2102
950	TSH 13/270	3572	2107
1050	TSH 14/270	3611	2151
1150	TSH 15/0	3571	2107
1250	TSH 16/180	3575	2127

Table 9: **QUENCH-07; Onset of cooling based on cladding TCs (TFS), central rod TCs (TCRI), corner rod TCs (TIT), and shroud TCs (TSH)**

Thermocouple	Elevation	Onset of cooling		Mean value per elevation	
	[mm]	Time [s]	Temp. [K]	Time [s]	Temp. [K]
TFS 2/1	- 250	3571	639		
TFS 2/2	- 150	3564	708		
TFS 2/3	- 50	3562	768		
TFS 5/4/0	50	3563	810	3564	814
TFS 5/4/180	50	3565	818		
TFS 2/5	150	3563	959	3563	938
TFS 5/5	150	3563	917		
TFS 2/6	250	3565	1081	3565	1063
TFS 5/6	250	3565	1044		
TFS 2/7	350	3563	1171	3563	1149
TFS 5/7	350	3563	1127		
TFS 5/8	450	3563	1225		
TFS 2/9	550	3563	1335	3563	1318
TFS 5/9	550	3563	1301		
TFS 3/10	650	3562	1527	3563	1547
TFS 5/10	650	3564	1566		
TFS 5/17	1350	3609	2146		
TCRI 11	750	3582	1700		
TCRI 12	850	3575	1682		
TIT C/9	550	3565	1246		
TIT D/12	850	3580	2086		
TSH 1/0	- 250	3576	583		
TSH 3/180	- 50	3565	690		
TSH 4/0	50	3566	751	3566	743

Thermocouple	Elevation [mm]	Onset of cooling		Mean value per elevation	
		Time [s]	Temp. [K]	Time [s]	Temp. [K]
TSH 4/90	50	3566	741		
TSH 4/180	50	3566	741		
TSH 4/270	50	3566	740		
TSH 7/0	350	3565	1108	3565	1108
TSH 7/180	350	3565	1108		
TSH 9/90	550	3565	1242	3565	1260
TSH 9/270	550	3565	1277		
TSH 11/0	750	3567	1624	3570	1671
TSH 11/180	750	3572	1717		
TSH 12/0	850	3568	2102	3567	2102
TSH 12/180	850	3565	2102		
TSH 13/90	950	3565	2106	3569	2107
TSH 13/270	950	3572	2107		
TSH 14/90	1050	3562	2060	3590	2105
TSH 14/270	1050	3617	2150		
TSH 15/0	1150	3571	2107	3576	2096
TSH 15/180	1150	3580	2085		
TSH 16/0	1250	3564	2114	3571	2120
TSH 16/180	1250	3578	2125		

Table 10: QUENCH-07; Cross sections for the metallographic examination 12.11.01

Sample	Sample length(mm)	Axial position Bottom(mm)	Top (mm)	Remarks
QUE-07-a			48	Remnant
Cut	2	48	50	Coarse cut #1 *)
QUE-07-b	8	50	58	
Cut	2	58	60	
QUE-07-1	13	60	73	Reference, 73 mm polished
Cut	2	73	75	
QUE-07-c	349	75	424	
Cut	2	424	426	Coarse cut #2 $\Rightarrow$ slab length = 374 mm
QUE-07-e	109	426	535	
Cut	2	535	537	
QUE-07-3	13	537	550	Elevation 9, 550 mm polished
Cut	2	550	552	
QUE-07-4	5	552	557	Sample for H_2 absorption
Cut	2	557	559	
QUE-07-f	76	559	635	
Cut	2	635	637	
QUE-07-12	13	637	650	
Cut	2	650	652	
QUE-07-g	63	652	715	
Cut	2	715	717	Coarse cut #3 $\Rightarrow$ slab length = 289 mm
QUE-07-h	18	717	735	
Cut	2	735	737	
QUE-07-5	13	737	750	Elevation 11, 750 mm polished
Cut	2	750	752	
QUE-07-6	5	752	757	Sample for H_2 absorption
Cut	2	757	759	
QUE-07-i	76	759	835	
Cut	2	835	837	
QUE-07-13	13	837	850	Elevation 12, 850 mm polished

Sample	Sample length(mm)	Axial position Bottom(mm)	Top (mm)	Remarks
Cut	2	850	852	
QUE-07-14	5	852	857	Sample for H_2 absorption
Cut	2	857	859	
QUE-07-j	76	859	935	
Cut	2	935	937	
QUE-07-7	13	937	950	Elevation 13, 950 mm polished
Cut	2	950	952	
QUE-07-8	5	952	957	Sample for H_2 absorption
Cut	2	957	959	
QUE-07-k	91	959	1050	
Cut	2	1050	1052	Coarse cut #4 $\Rightarrow$ slab length = 283 mm
QUE-07-l	83	1052	1135	
Cut	2	1135	1137	
QUE-07-9	13	1137	1150	Elevation 15, 1150 mm polished
Cut	2	1150	1152	
QUE-07-10	5	1152	1157	Sample for H_2 absorption
Cut	2	1157	1159	
QUE-07-m	191	1159	1350	
Cut	2	1350	1352	Coarse cut #5 $\Rightarrow$ slab length = 298 mm
QUE-07-n	43	1352	1395	
Cut	2	1395	1397	
QUE-07-11	13	1397	1410	Top grid spacer, 1410 mm polished
Cut	2	1410	1412	
QUE-07-o		1412		Remnant

- *) The coarse cuts are made with help of a machine which can handle the entire length of the test bundle. Afterwards the slabs of a length < 600 mm are cut into slices of a higher precision in a different machine.

Fig. 1: Flow diagram of the QUENCH test facility
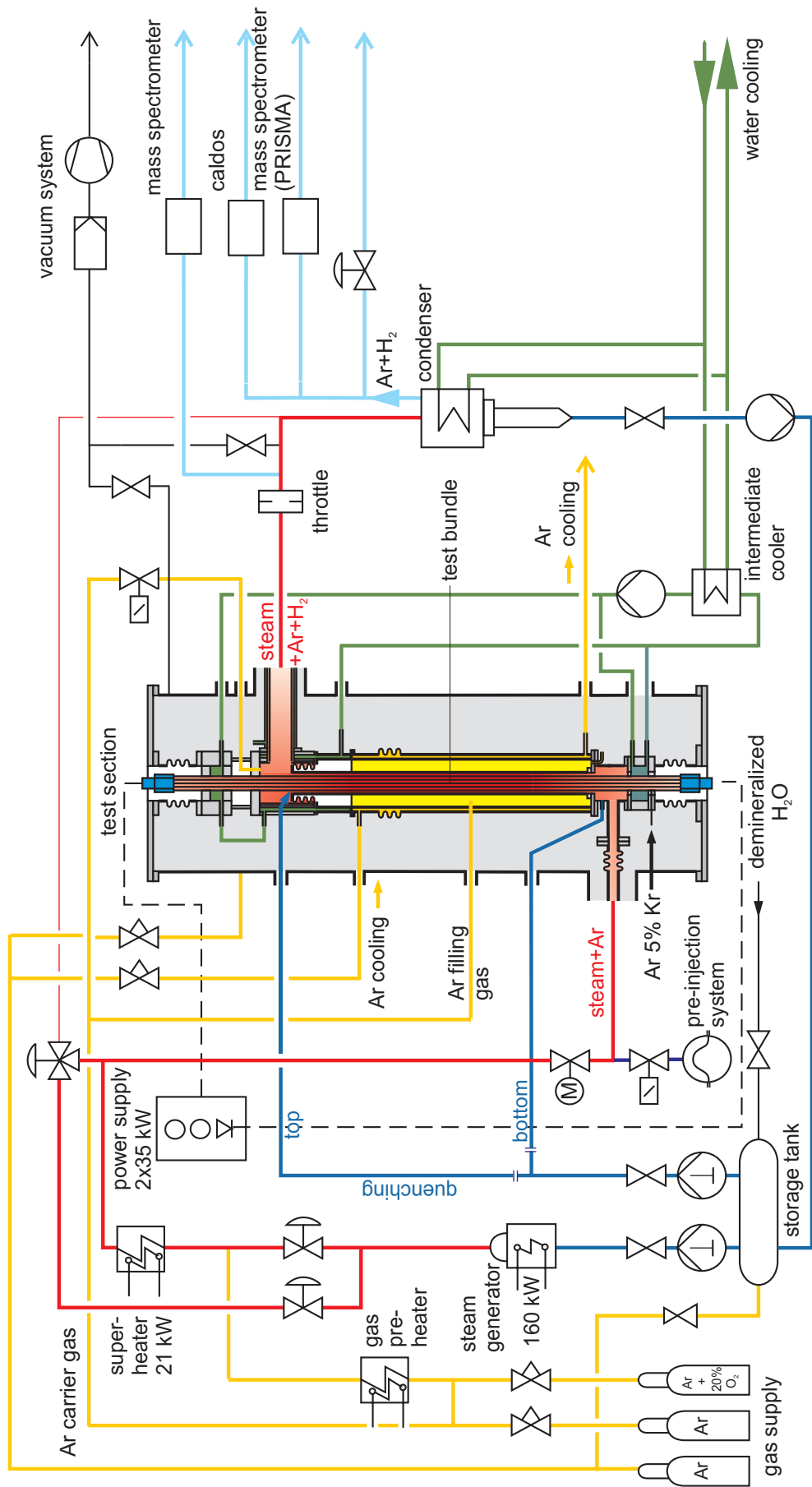
Fig.1-QUE07-Flow diagram.cdr
17.07.02 - IMF

Power supply
of inner rods
DC

Caldos (H₂)

MS-Prisma

$Ar + H_2$

6.7 m

Water cooling

Condenser

Mass spectrometer
GAM 300

4.0 m

Ar
carrier
gas

Test bundle

$Ar + steam + H_2$

Superheater

Water
quench
line

Containment

Cooling
steam
line

Condensate collector

Ar
carrier
gas

Water
storage
tank

2.2 m

Power supply
of outer rods

Pre-injection
system

Steam
generator

Pump

Quench
pump

Feedwater
pump

0.2 m
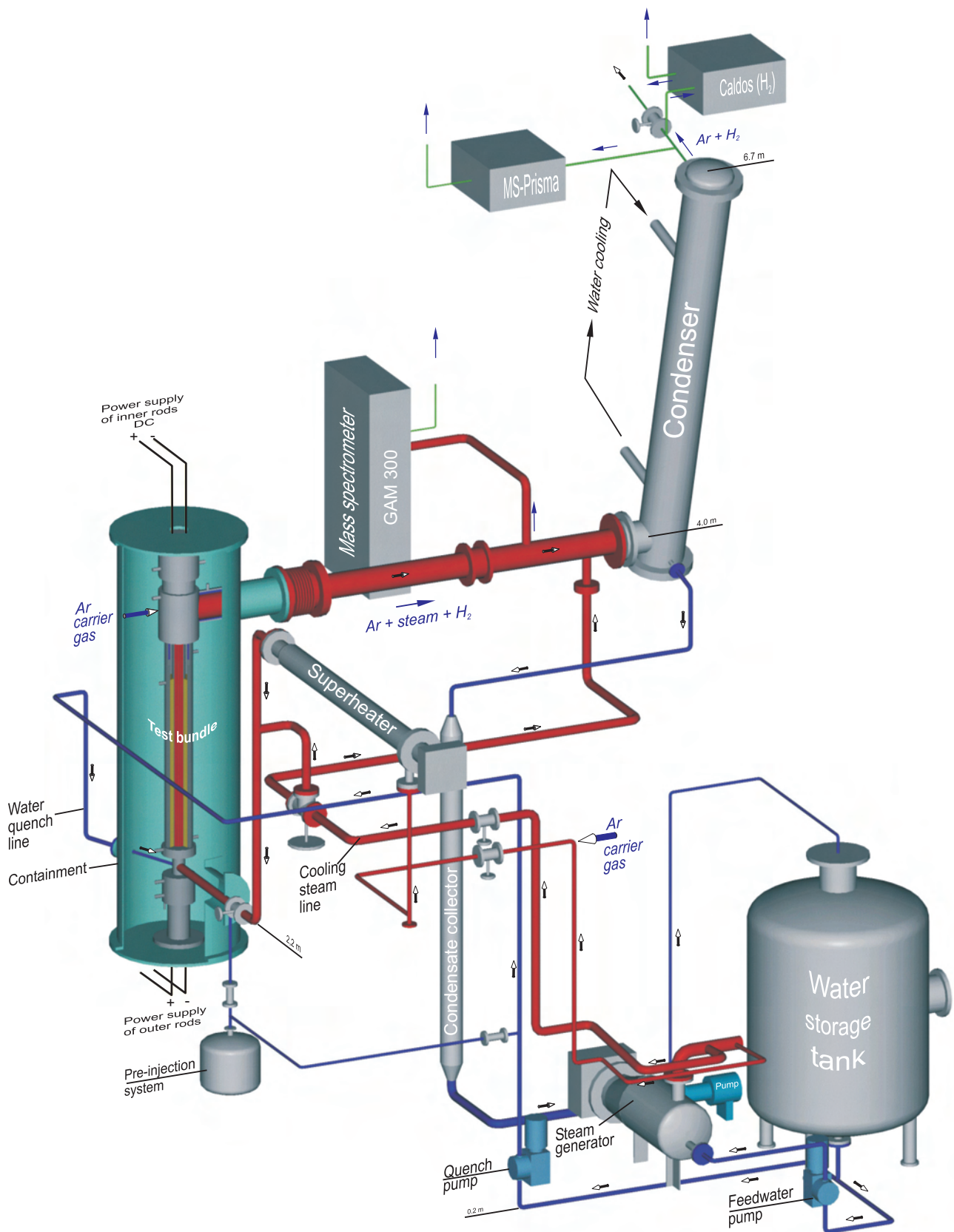
Fig.2-QUE07 Gesamtanlage 3D.cdr
07.04.03 - IMF

Fig. 2:   QUENCH Facility; main components

Cooling bundle head

H₂O cooling off-gas pipe

Steam+Ar+H₂

H₂O cooling

Off-gas pipe

Containment

ZrO₂ insulation

Ar cooling jacket

Shroud

Test bundle

Bottom quenching

Ar filling

Steam+Ar

Cooling bundle foot

Ar-5% Kr test rods
(ca. 2 bar)
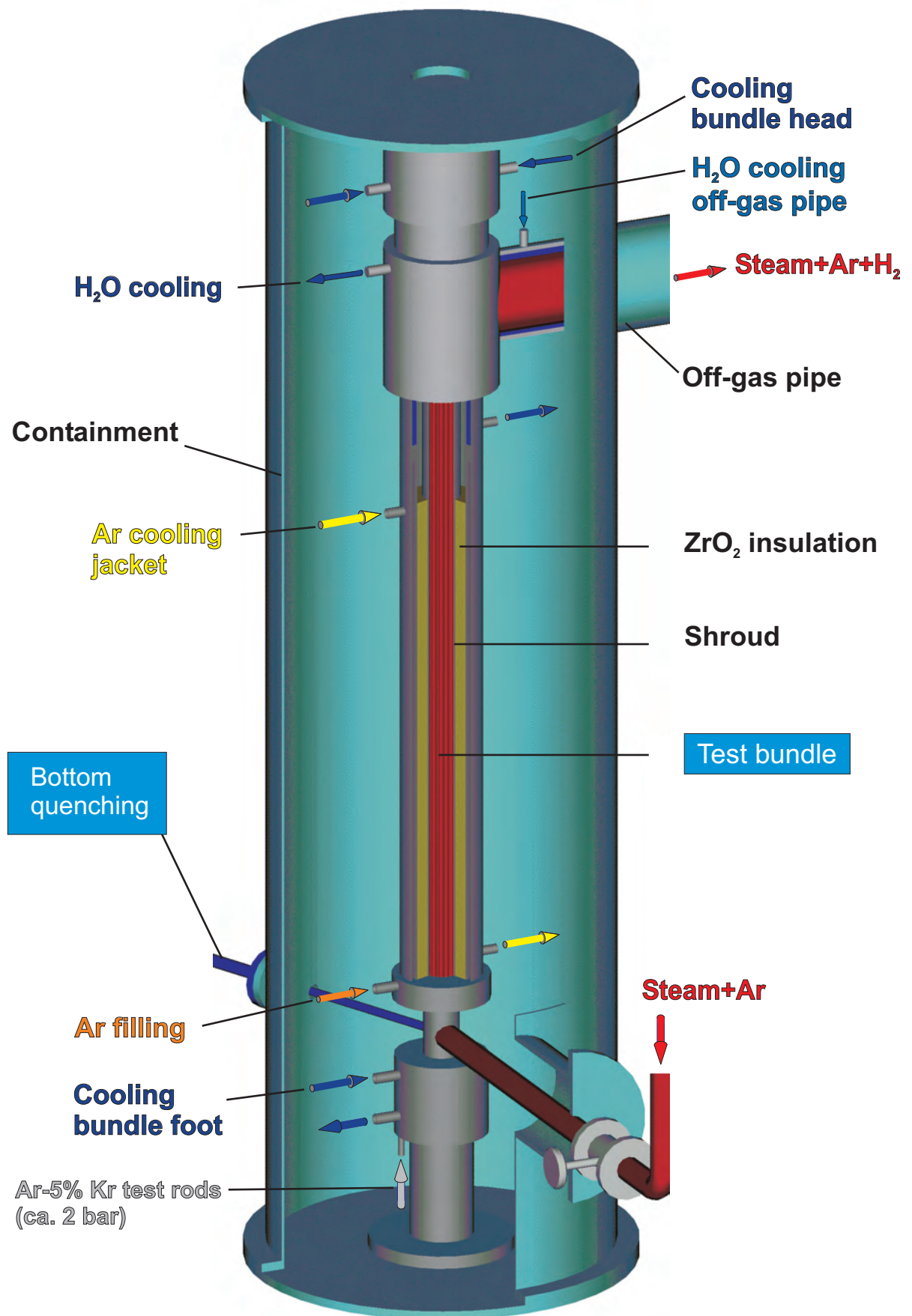
Fig.3-QUE07 Containment 3D.cdr
03.02.04 - IMF

Fig. 3:   QUENCH Facility; containment and test section
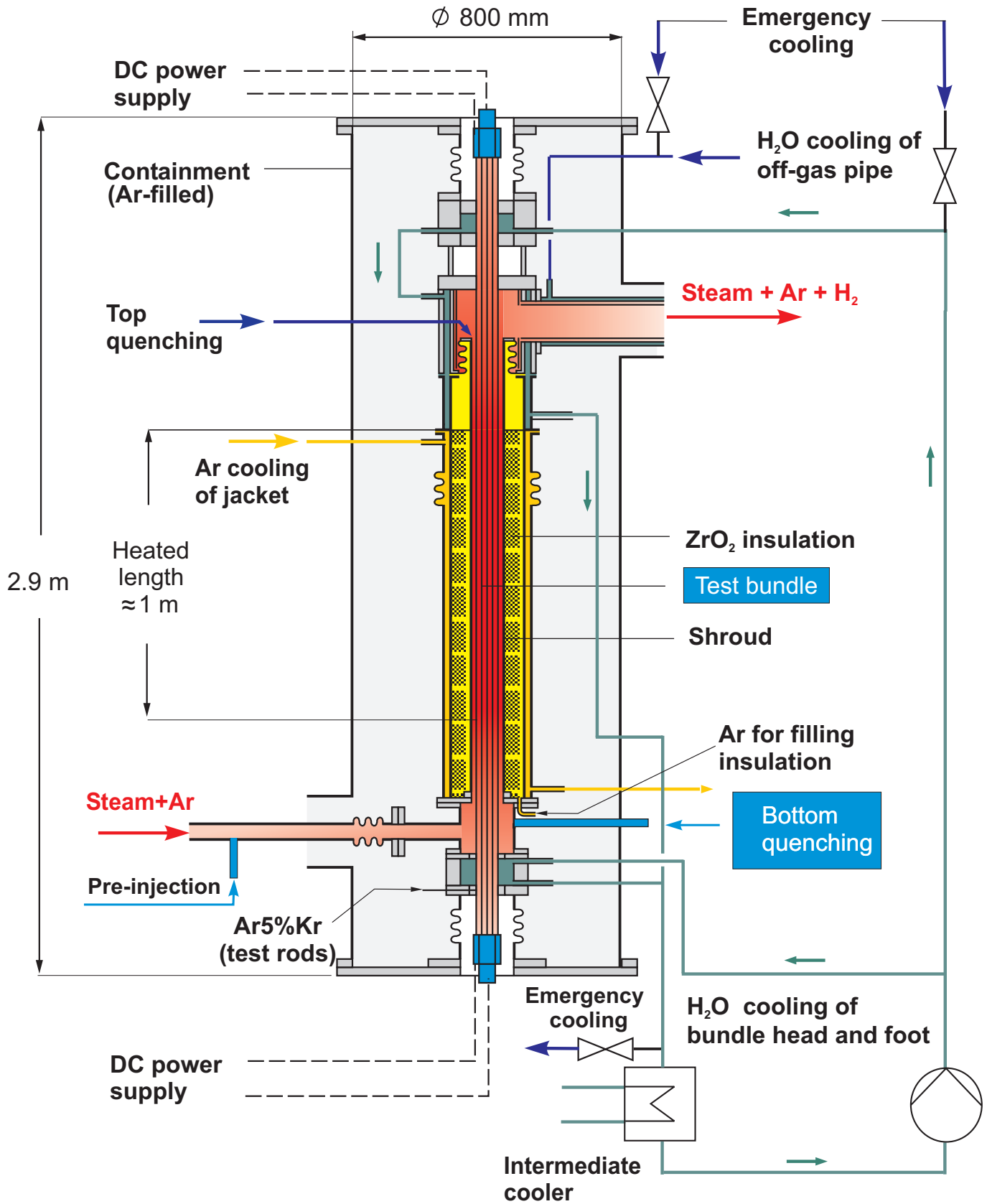
Fig 4 QUE07 Flow lines (ab QUE05).cdr
17.07.02 - IMF

Fig. 4:   QUENCH test section; flow lines

sliding contact

+1720

45

locking ring
insulation plate
Cu electrode
water cooled

+1630   30 Al_2O_3 plate

+1500   30   thermal shield
Al_2O_3 plate

+1410 Zry
spacer   Mo electrode

+1050 Zry
spacer   tungsten heater

ZrO_2 annular pellet

heated length
1024 mm

+550 Zry
spacer   Zircaloy cladding $\varnothing$ 10.75 mm
wall thickness 0.725 mm

0   +50 Zry
spacer

-200 Inconel
spacer   Mo electrode

-475   Cu electrode

30   SS plate

water cooled

sealing plate

45   Ar5%Kr

-625   electric insulation

2480 mm

sliding contact

Fig.5-QUE07 Heated fuel rod sim.cdr
17.07.02 - IMF

Fig. 5:   Heated fuel rod simulator

Labels in figure:

Zircaloy guide tube Ø12.1/ Ø11.3

B₄C pellet Ø 7.48 x 14 mm

SS cladding Ø10.24/Ø 7.72

3 NiCr/Ni thermocouples (750, 850, 950 mm)

Zry shroud Ø 80/84.76 mm

Zry rod Ø6 mm removable

A,C,D: Zry rod (top), Zry tube (bottom) Ø 6 mm

Ar cooling gap 6.7 mm

ZrO₂ fiber insulation 37 mm

Unheated rod
Zry guide tube
SS cladding
B₄C pellet

Stainless steel cooling jacket Ø 181.7/193.7 mm Ø 158.3/168.3 mm

14.3

Heated rod
Tungsten heater
ZrO₂ annular pellet
Zircaloy cladding Ø 10.75 mm x 0.725 mm

S 0°
90° W
180° N
O 270°

Fig.6-QUE07 B4C cross section.cdr
11.10.01 - IMF

Fig. 6:   QUENCH-07; Fuel rod simulator bundle (cross section) with control rod simulator in the center

extension piece

Note:
There are 4 holes of 4 mm diam. in the Zry guide tube at EL -34 (steam inlet) and EL +1179 (steam outlet)

2610 mm

+1500

+1410 Zry spacer

spring

+1050 Zry spacer
+1008

+950 Cladding TC (TCRI 13)
+850 Cladding TC (TCRI 12)
+750 Cladding TC (TCRI 11)

+550 Zry spacer

B$_4$C pellet

Zry-4 guide tube

+50 Zry spacer
0

SS cladding
SS pellet

-200 Inconel spacer

thermocouple penetration
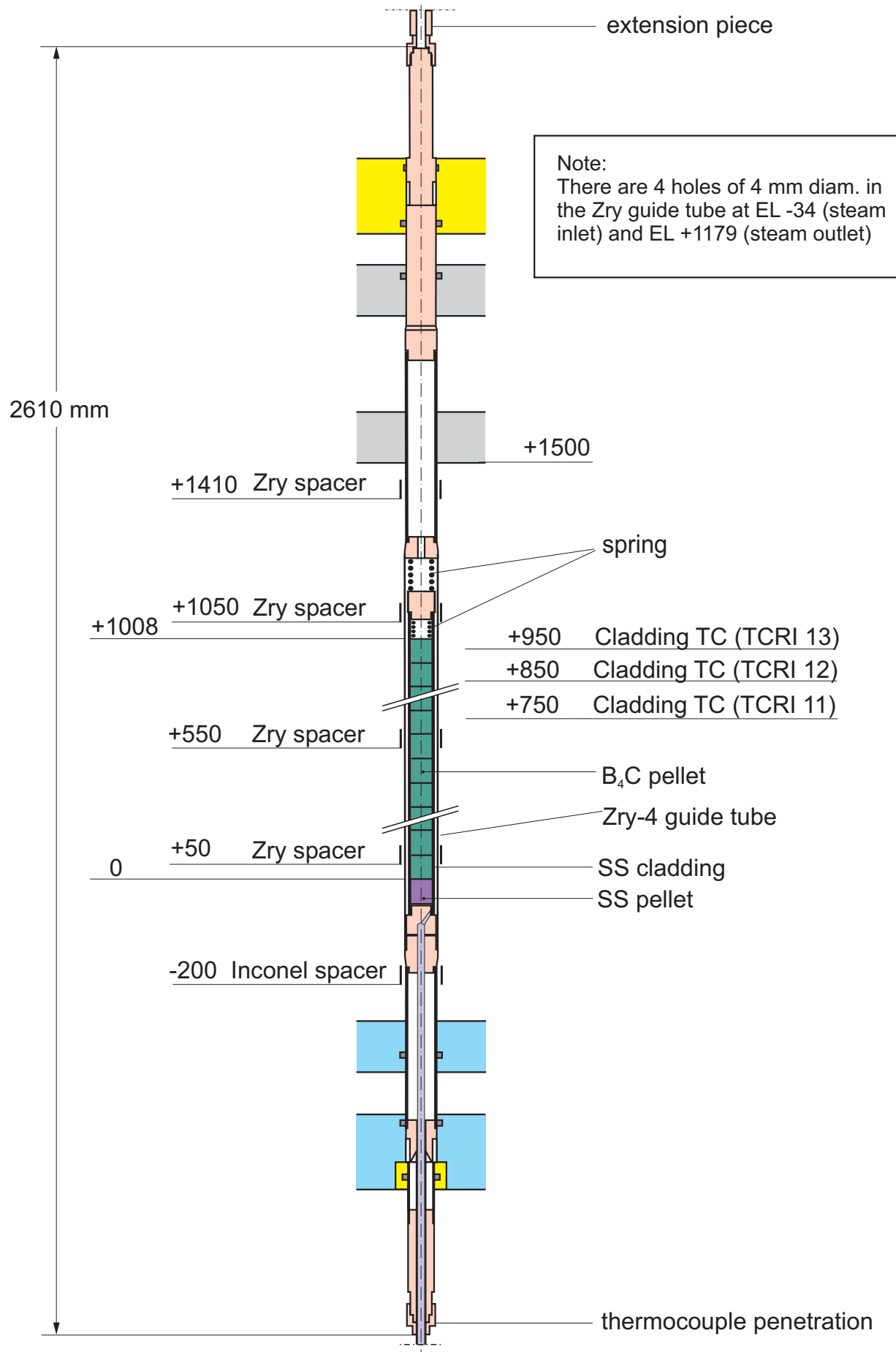
Fig.7-QUE07 Unheated control rod sim.cdr
16.03.04 - IMF

Fig. 7:   Control rod simulator
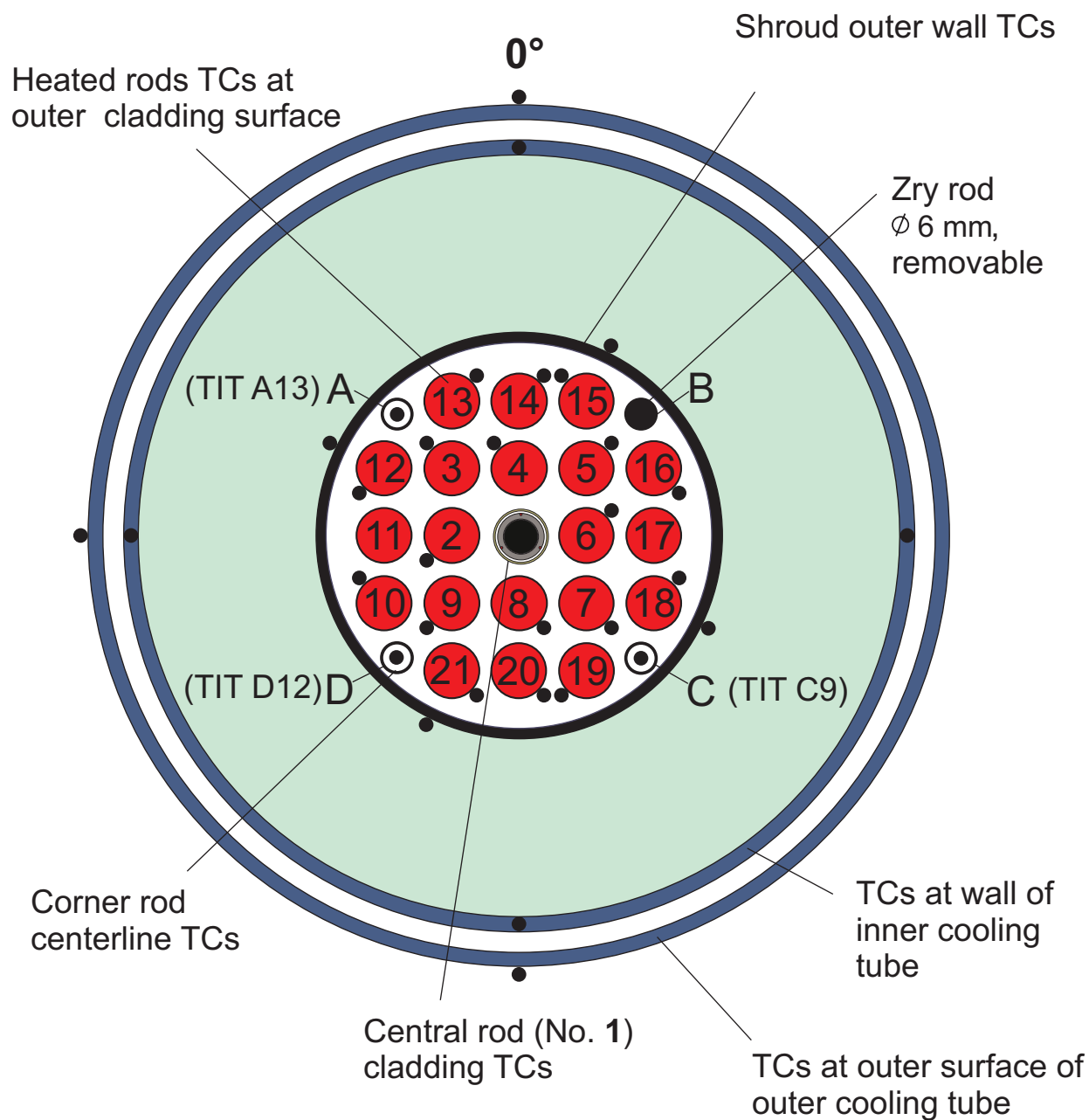
Fig. 8: QUENCH-07; Test bundle instrumentation (azimuthal orientation) and rod designation (top view)

temperature measurement elevations

+1350	⓱	
+1300		
+1250	⑯	
+1150	⑮	
+1050	⑭	+1024
+950	⑬	
+850	⑫	
+750	⑪	
+650	⑩	
+550	⑨	
+450	⑧	
+350	⑦	
+250	⑥	
+150	⑤	
+50	④	
-50	③	0
-150	②	
-250	①	

H_2O →

H_2O cooling jacket

+1050 Zry spacer grid

H_2O ←

Ar →

ZrO_2 fiber insulation, argon-filled

Ar cooling jacket

+550 Zry spacer grid

Zry shroud

fuel rod simulator

+50 Zry spacer grid

-200 Inconel spacer grid

Ar ←

TFS thermocouples routing to:

top
↑
↓
bottom

heated length

◎ W/Re TC

○ Ni/Cr TC

Fig.9-QUE TC elevations.cdr
15.04.03 - IMF

Fig. 9: Axial temperature measurement locations in the QUENCH test section

(TIT A13, TIT D12, TIT C9)

SS sleeve brazed

Swagelok tube fitting

Zry tube ⌀ 6 x 1.0

Thermocouple

10 mm

b

a

Zry rod ⌀ 6
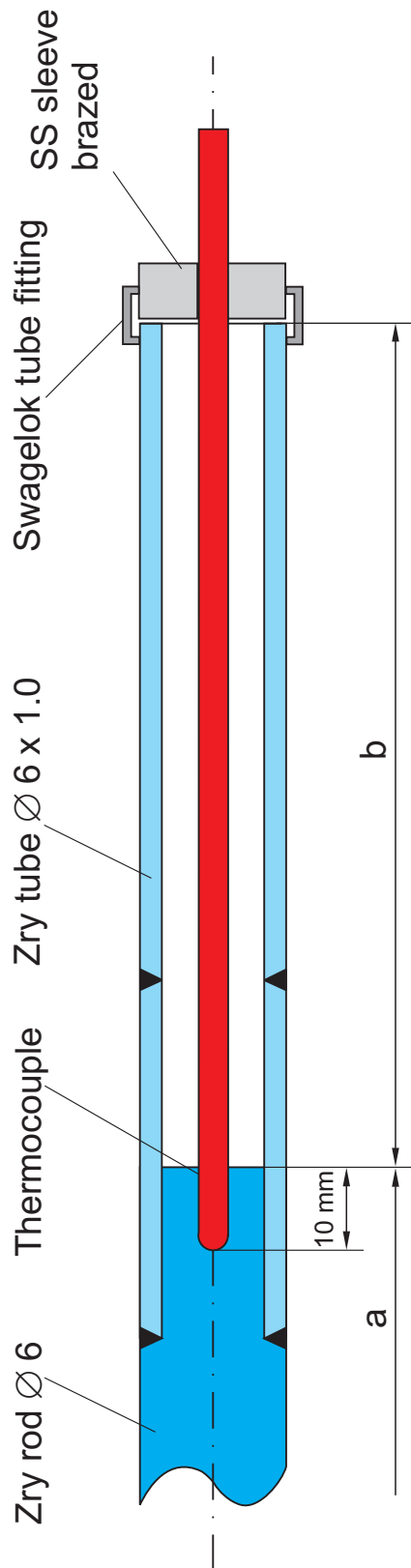
Rod A: TIT A13 (950 mm), W/Re, ⌀ 2.1 mm, a = 360 mm, b = 2080 mm

Rod D: TIT D12 (850 mm), W/Re, ⌀ 2.1 mm, a = 460 mm, b = 1980 mm

Rod C: TIT C 9 (550 mm), NiCr/Ni, ⌀ 1 mm, a = 760 mm, b = 1680 mm

(Rod B: Zry-4 rod, ⌀ 6 mm, removable)

Fig 10 QUE07 TC in Zry-rod.cdr
11.03.04 - IMF

Fig. 10:   QUENCH-07; Arrangement of the thermocouples
            inside the corner rods

connector

compensation cable Ø 1 mm

1000

Ø 3.4 mm

transition piece

30

W/Re thermocouple Ø 2.1 mm

L*)

Zr sheath
Ø 2.1 mm
wall thickness 0.35 mm

W26%Re wire

W5%Re wire

Ta sheath
Ø 1.4 mm
wall thickness 0.23 mm

Laser weld

HfO_2 insulation

disc

Hot junction
laser welded

Zircaloy cap
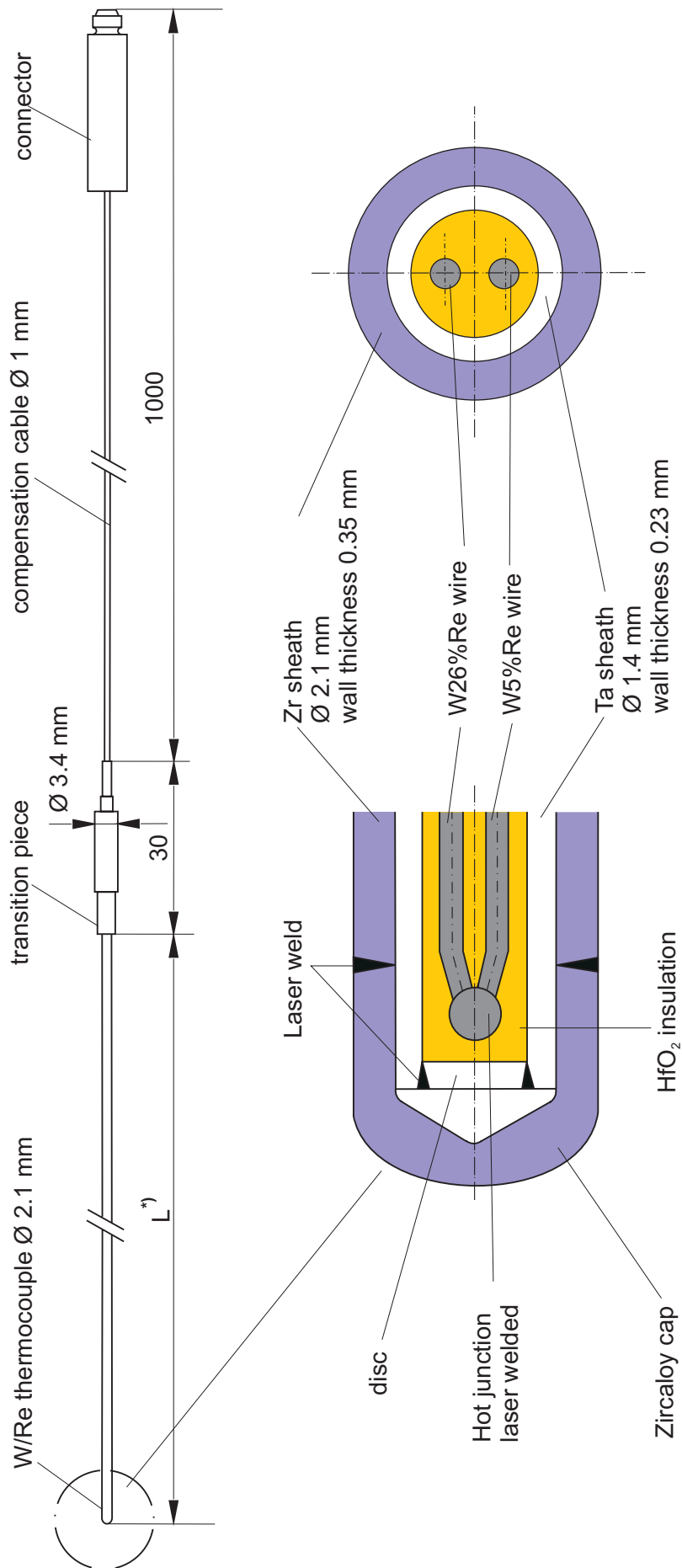
*) L: high-temperature section length dependent on the TC position in the test bundle 500 mm - 1700 mm

Fig.11-QUE07 High-temp thermocouple.cdr
16.03.04 - IMF

Fig. 11:   QUENCH; High-temperature thermocouple

ZrO$_2$ pellets

Tungsten heater

Zircaloy cladding

TC 2.1 mm duplex sheath

Zr clamp (0.2 mm)

Ir 40/Rh 60 wire (0.25 mm)
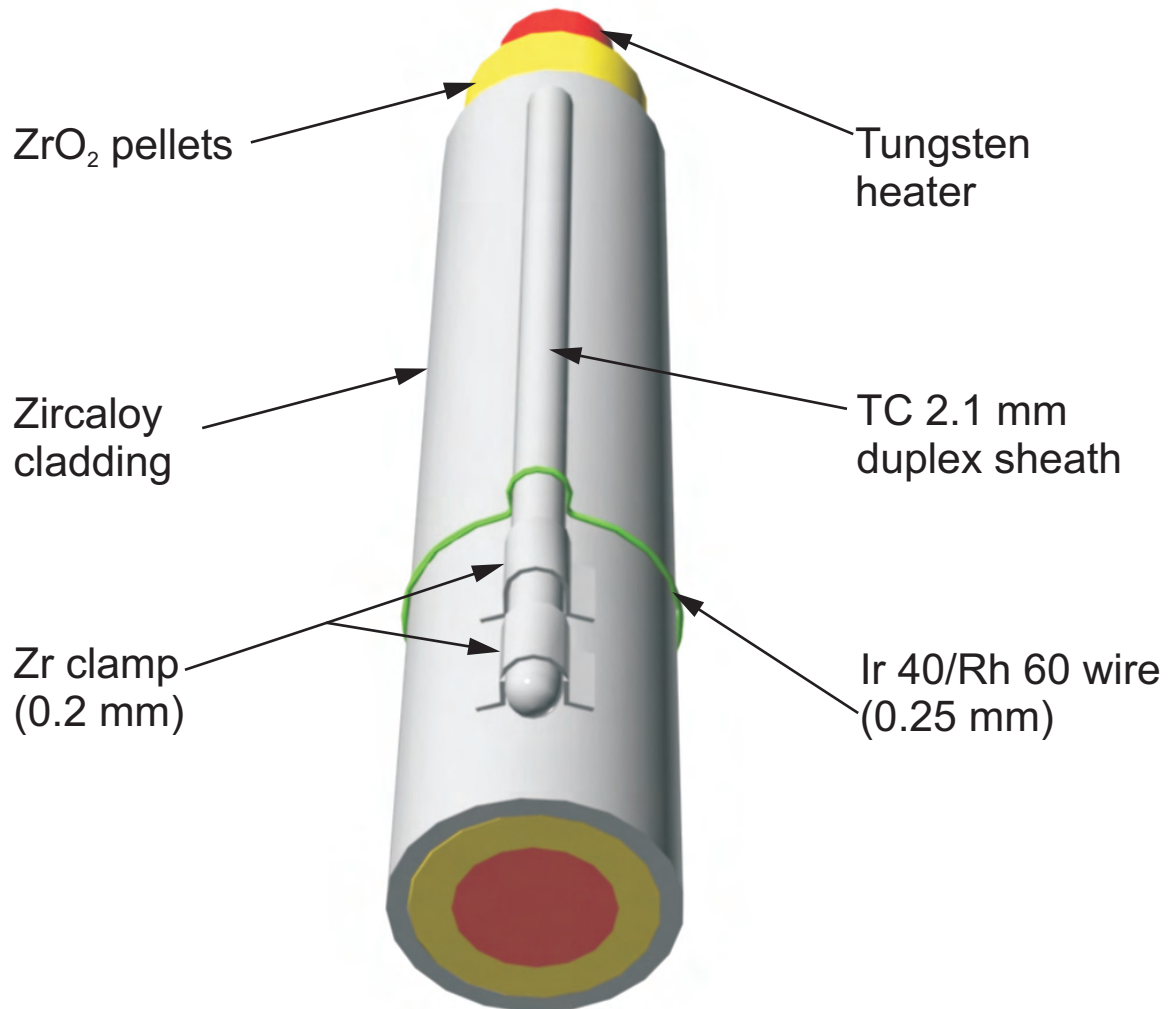
Tests with pre-oxidation: Zr clamp + wire

Tests without pre-oxidation: Zr clamp

Fig 12-QUE07 TC Fastening3.cdr
20.01.04 - IMF

Fig. 12:   TC fastening concept for the QUENCH test rods
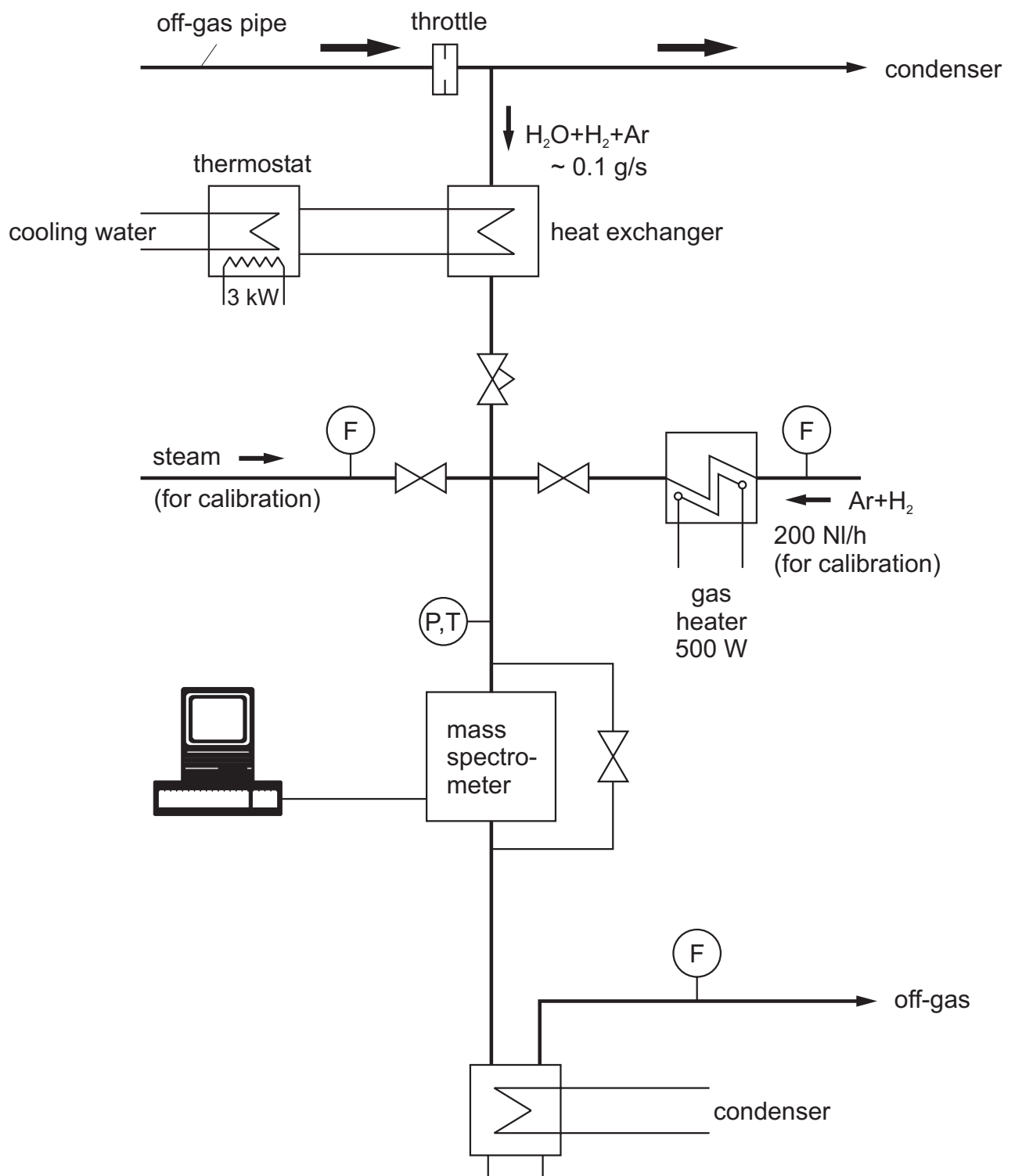
Fig 13 QUE07 MS QUENCH-Facility.cdr
15.10.01 - IMF

Fig. 13: H_2 measurement with the mass spectrometer connected to the off-gas pipe of the QUENCH test facility

heater

mass spectrometer
steam + Ar + H_2

thermal insulating gap

sampling tube penetration

H_2O cooling jacket

off-gas steam
+ Ar + H_2

thermal insulation
gap stagnant gas
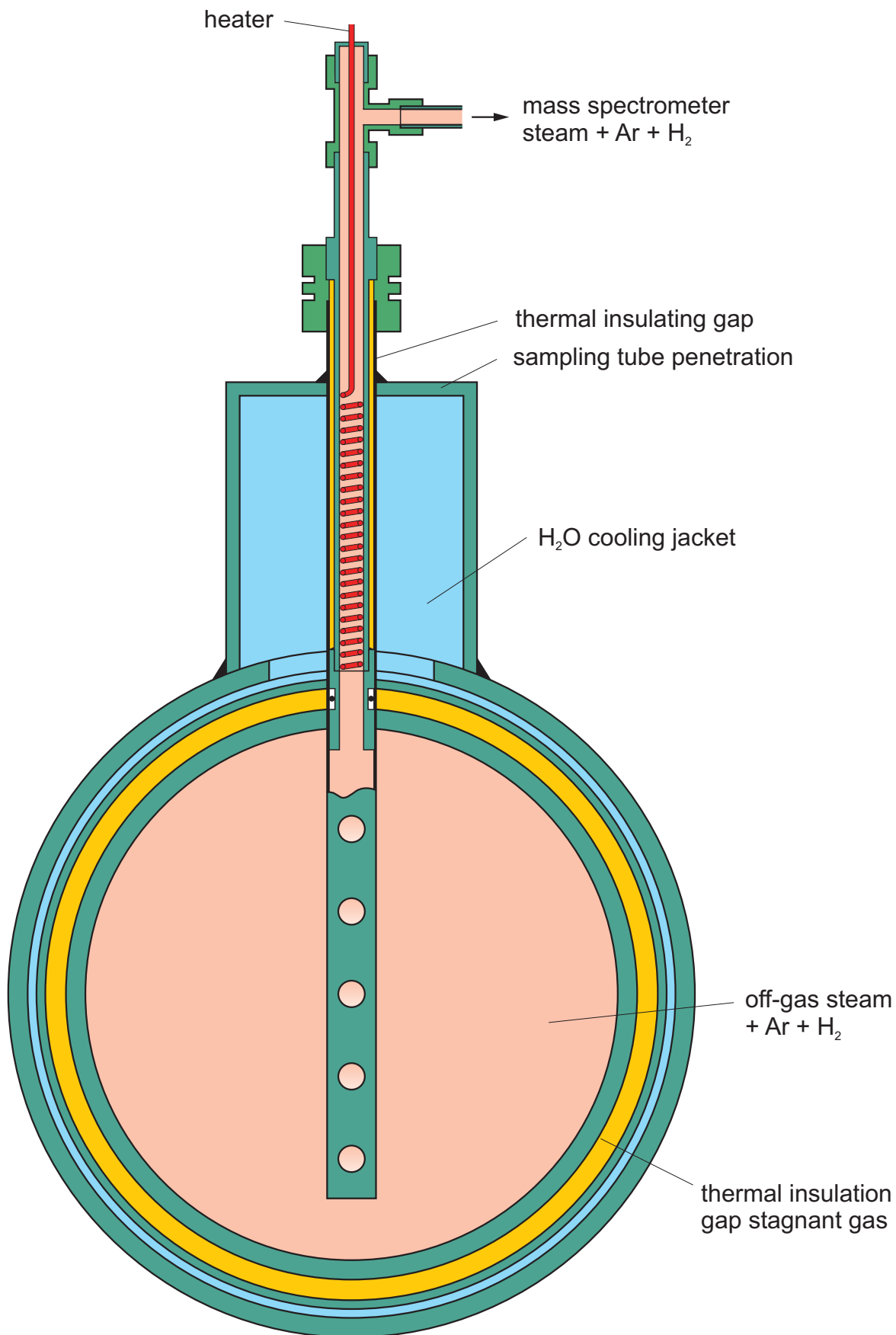
Fig 14 QUE07 MS sampling position new.cdr
15.10.01 - IMF

Fig.14: Mass spectrometer sampling position at the off-gas pipe of the QUENCH test facility

From condenser

To exit

To exit

Off-gas for
analysis

Flow meter
with needle valve

Test gases
(Ar-H₂)

Argon

Vol.%

E

Gas analyzer
CALDOS

Sweep gas
(N₂)

Bypass pump
(max. 280 l/h)

Flow meter
with needle valve

Gas cooler
with condensate
discharger

Membrane pump
(max. 100 l/h)
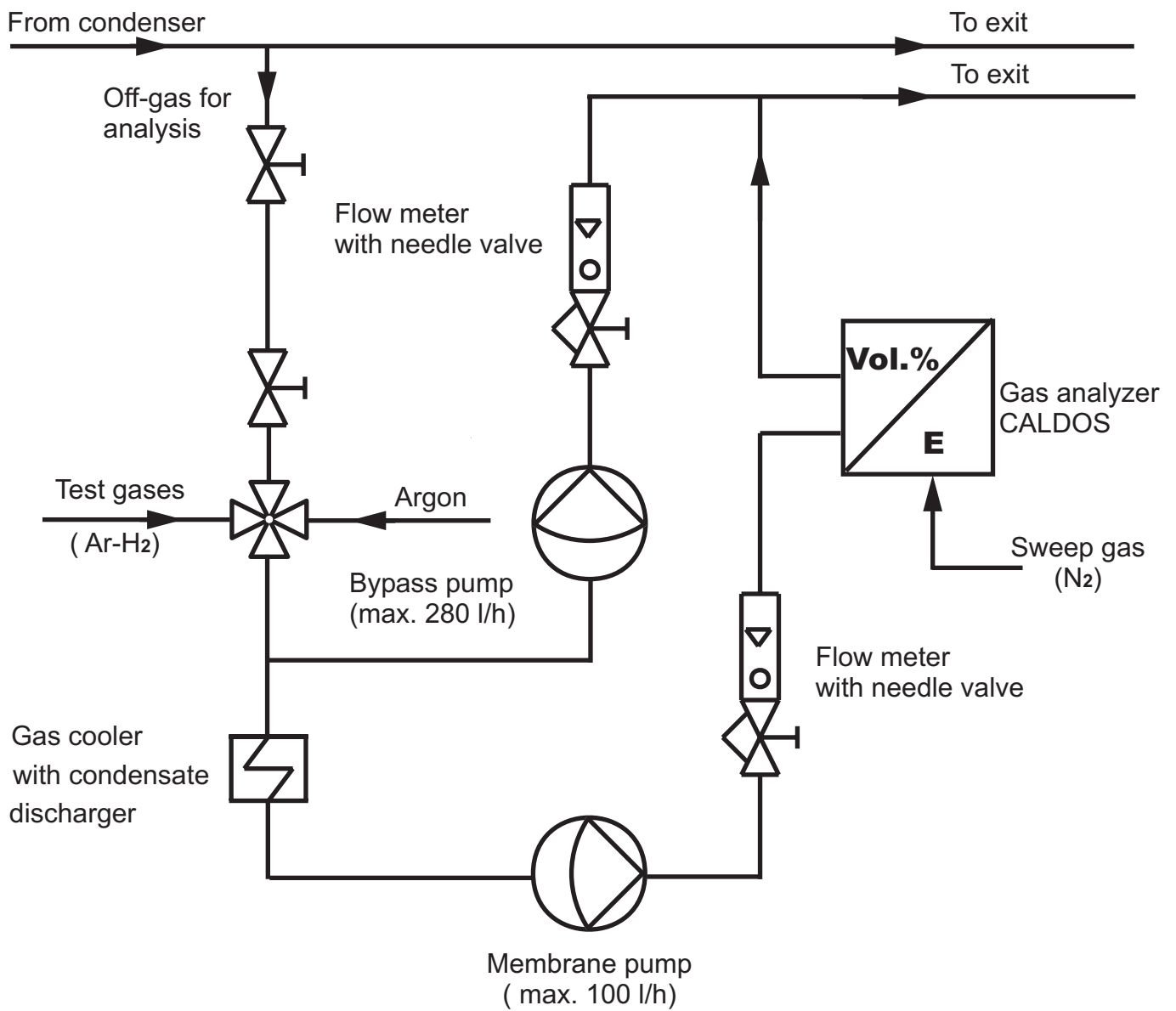
Fig 15 QUE07 Caldos Schema (ab QUE04).cdr
21.10.01 - IMF

Fig.15:   Hydrogen measurement with the CALDOS analyzer connected to
the exhaust gas pipe of the QUENCH facility
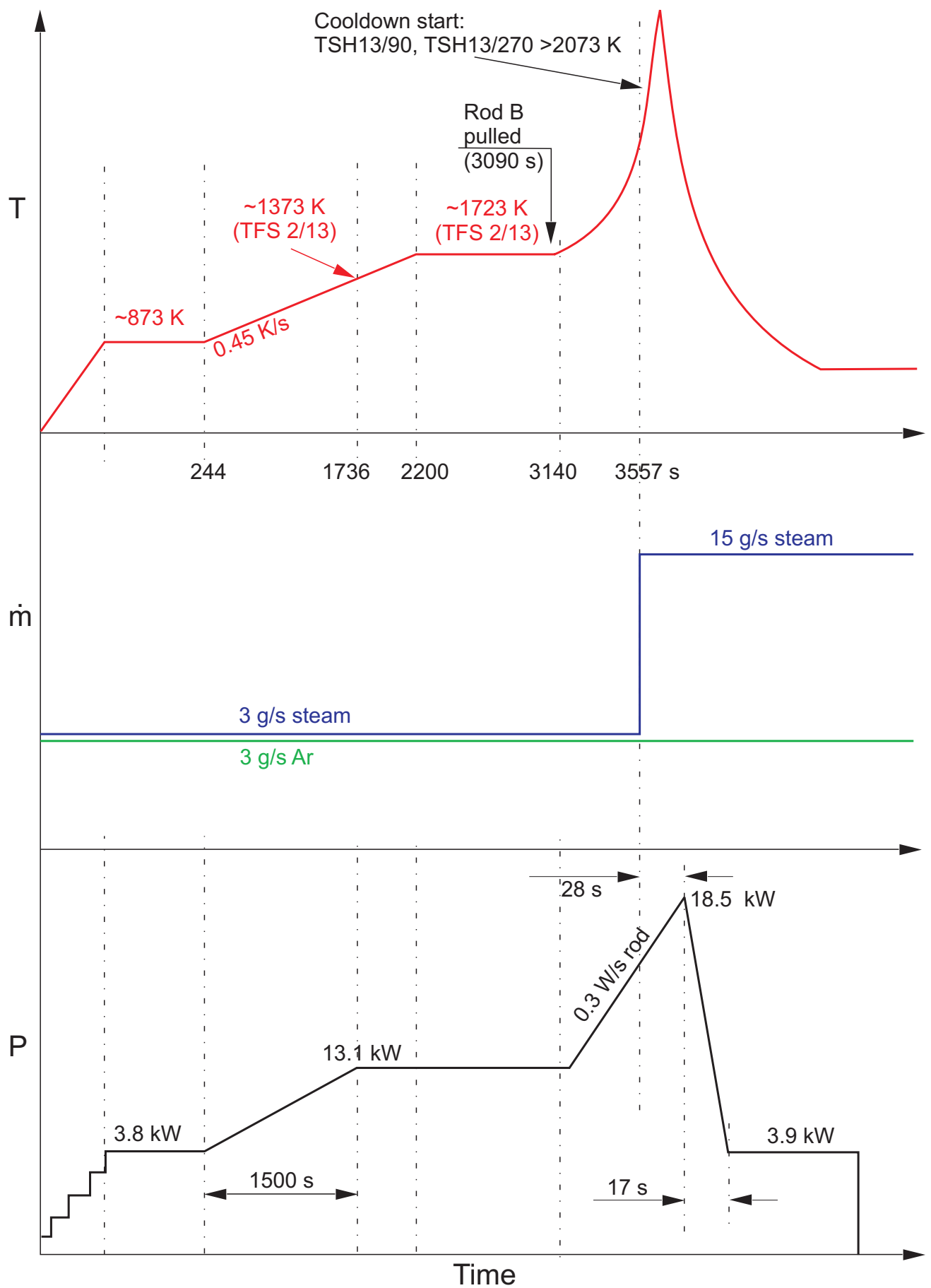
Fig.16 : QUENCH-07 test conduct
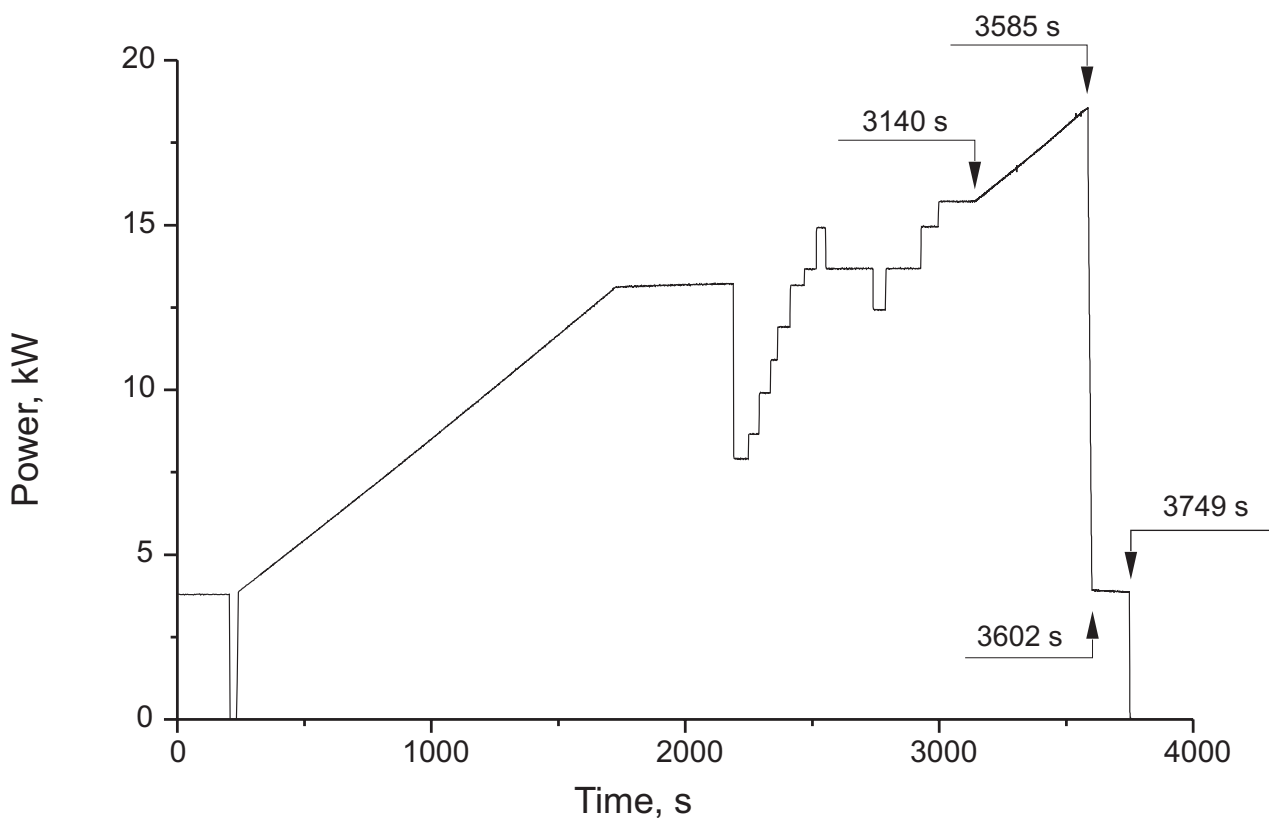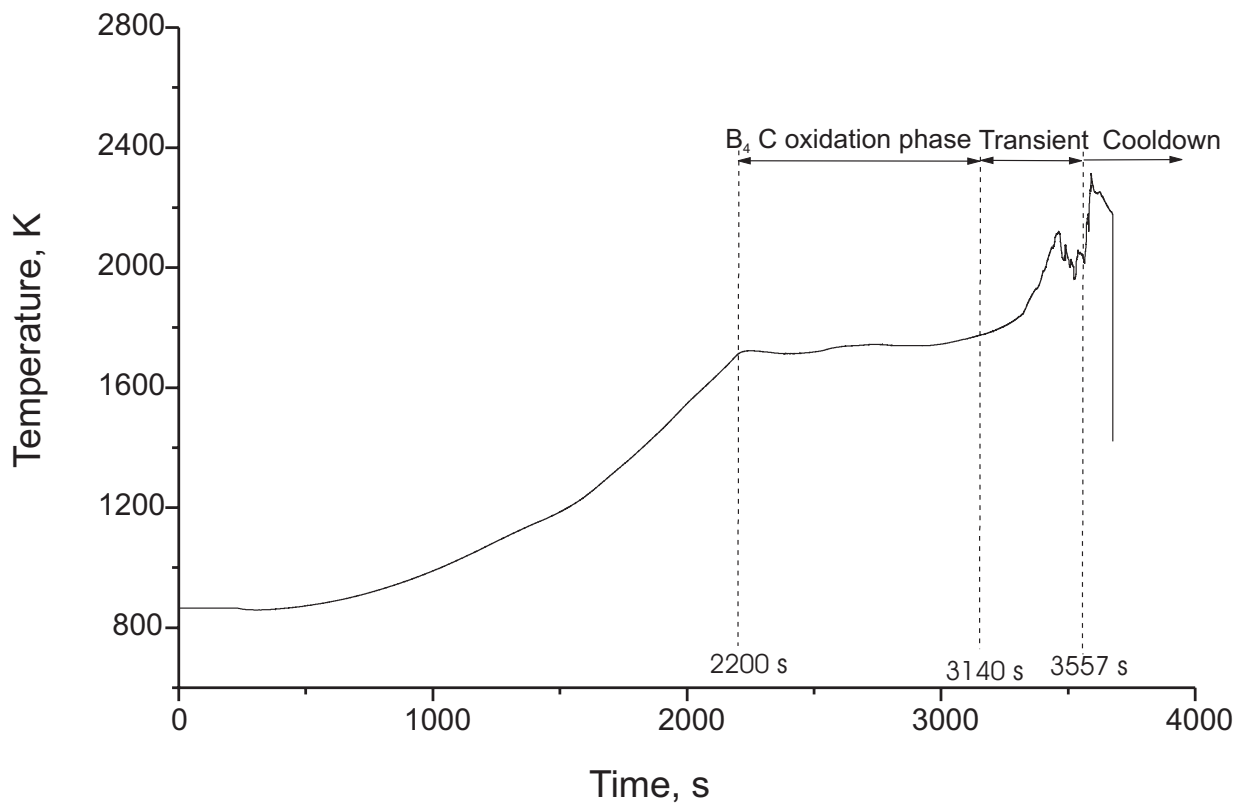
Fig. 17: QUENCH-07; Test phases illustrated with help of the temperature measured by the thermocouple TIT A/13, top, and total electric power vs. time, bottom

Fig.18-QUE07-Heatup+T511.cdr
18.07.02 - IMF
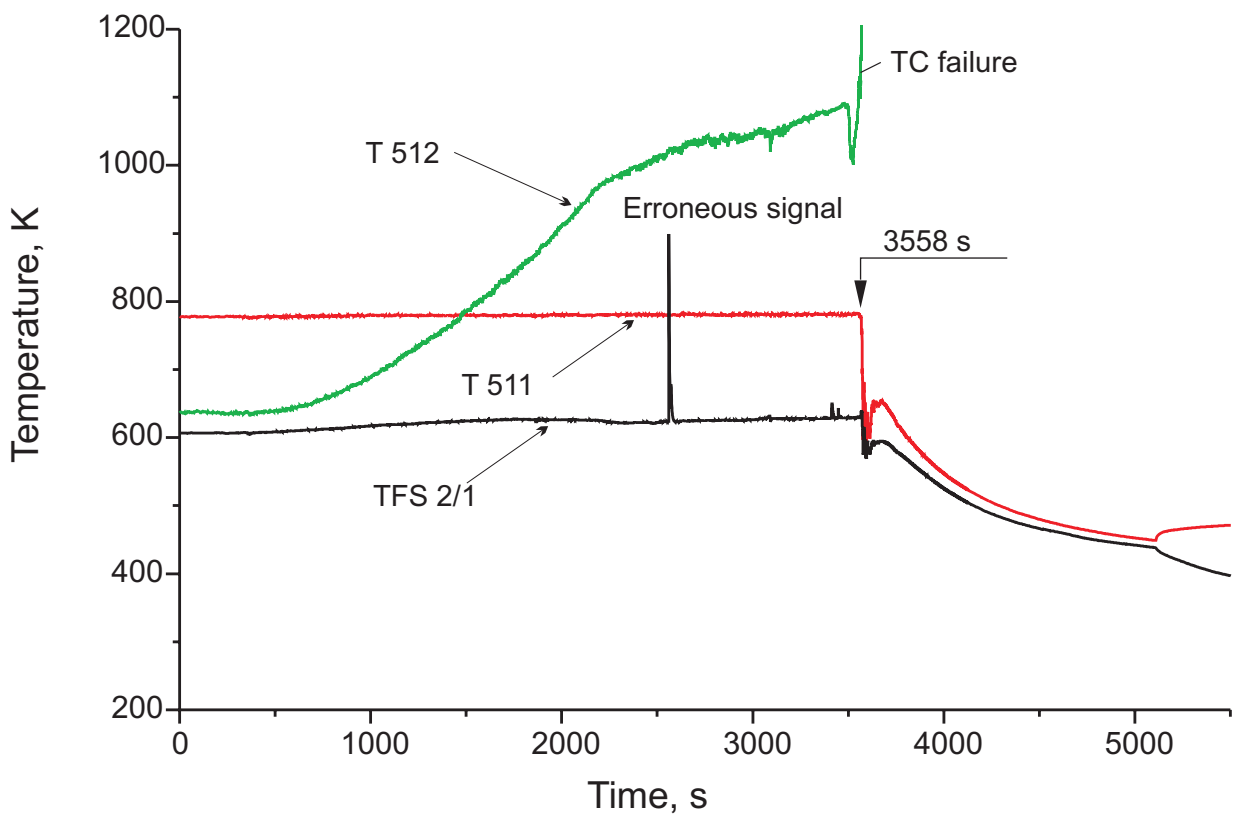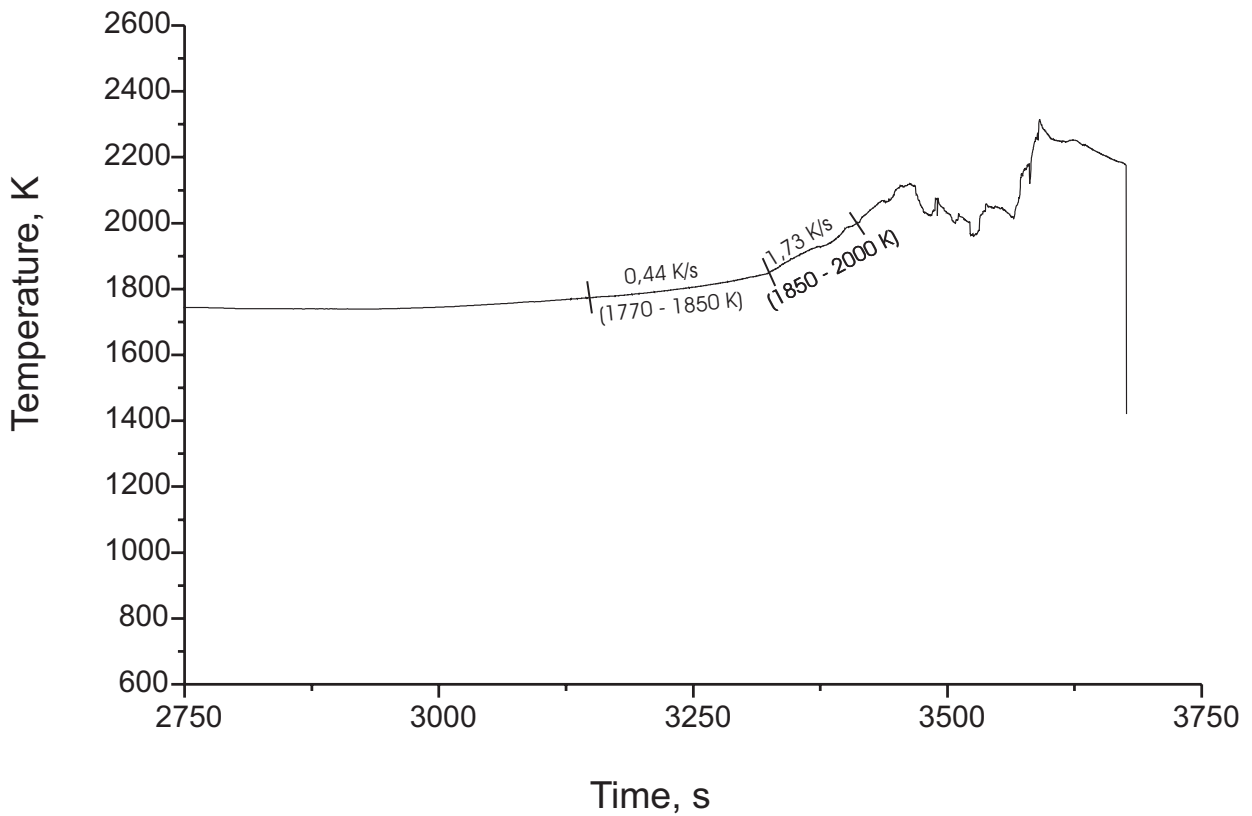
Fig. 18:   QUENCH-07; Heatup rate during the transient phase determined on
the basis of thermocouple TIT A/13, top, and coolant temperatures
T 511 (at bundle inlet), T 512 (at bundle outlet), TFS 2/1 (at -250 mm),
bottom
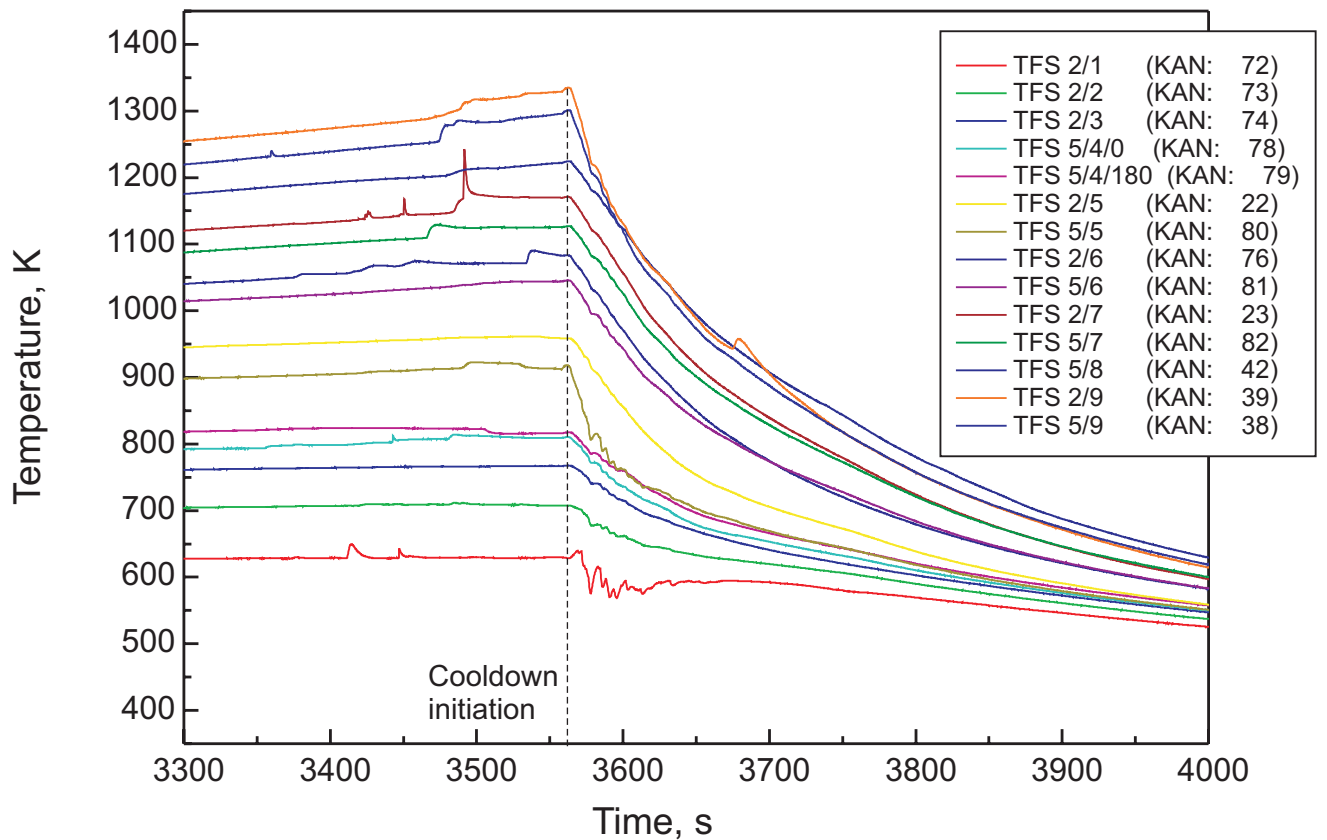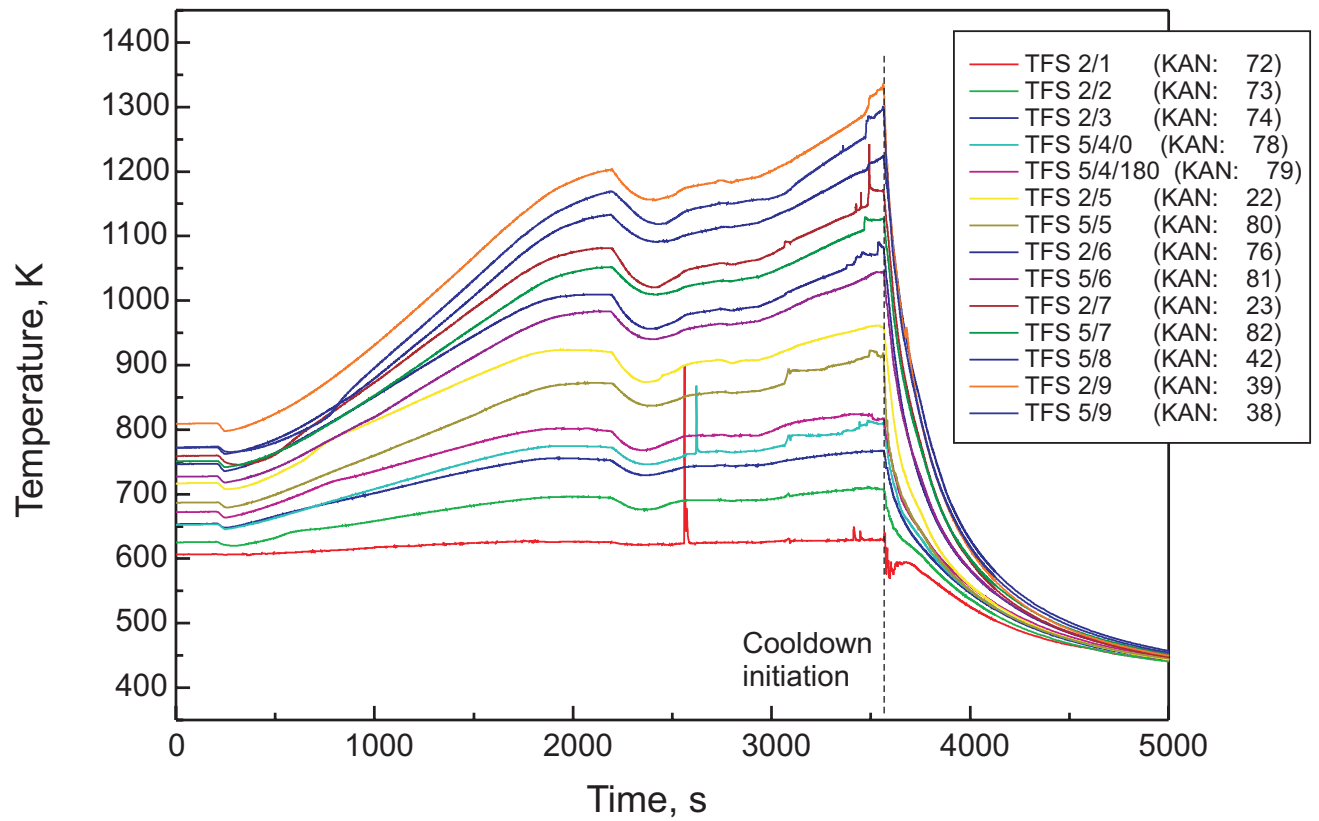
Fig.19-QUE07-Temp-Zeit-ebe all-TFS1-9.cdr
17.07..02 - IMF

Fig. 19:   QUENCH-07; Cladding temperatures at lower bundle elevations, i.e.
-250 to 550 mm
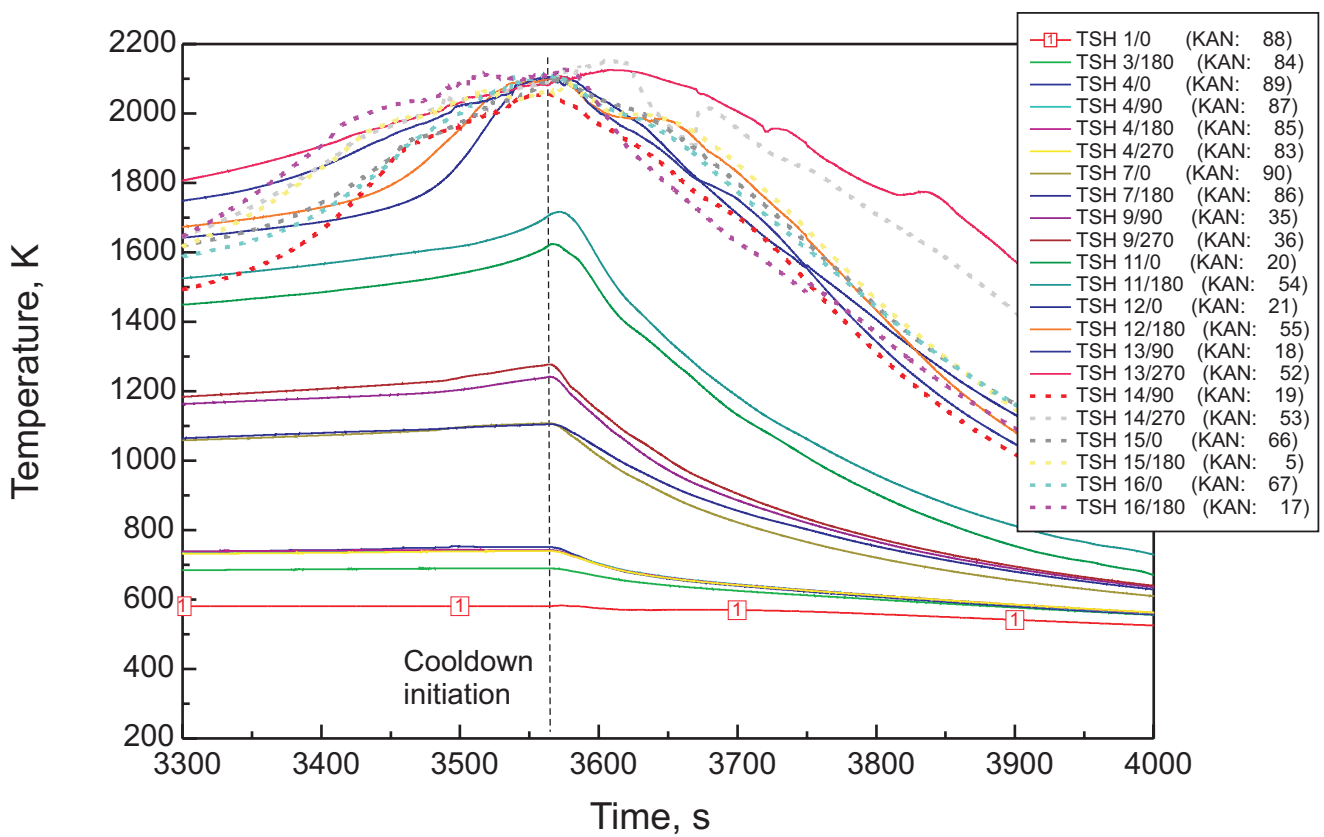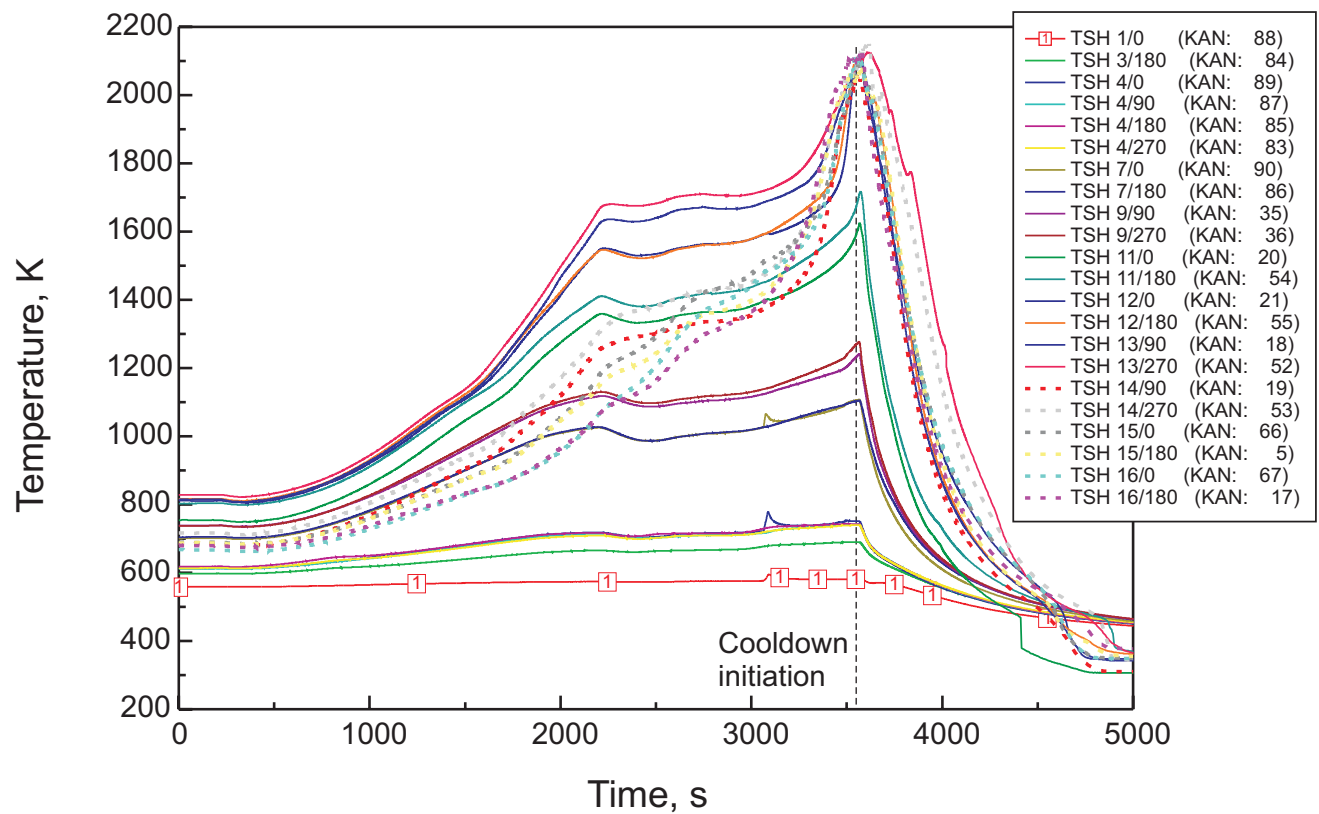
Fig.20-QUE07-Temp-Zeit-ebe all-Shroud.cdr
17.07..02 - IMF

Fig. 20:   QUENCH-07; Shroud temperatures
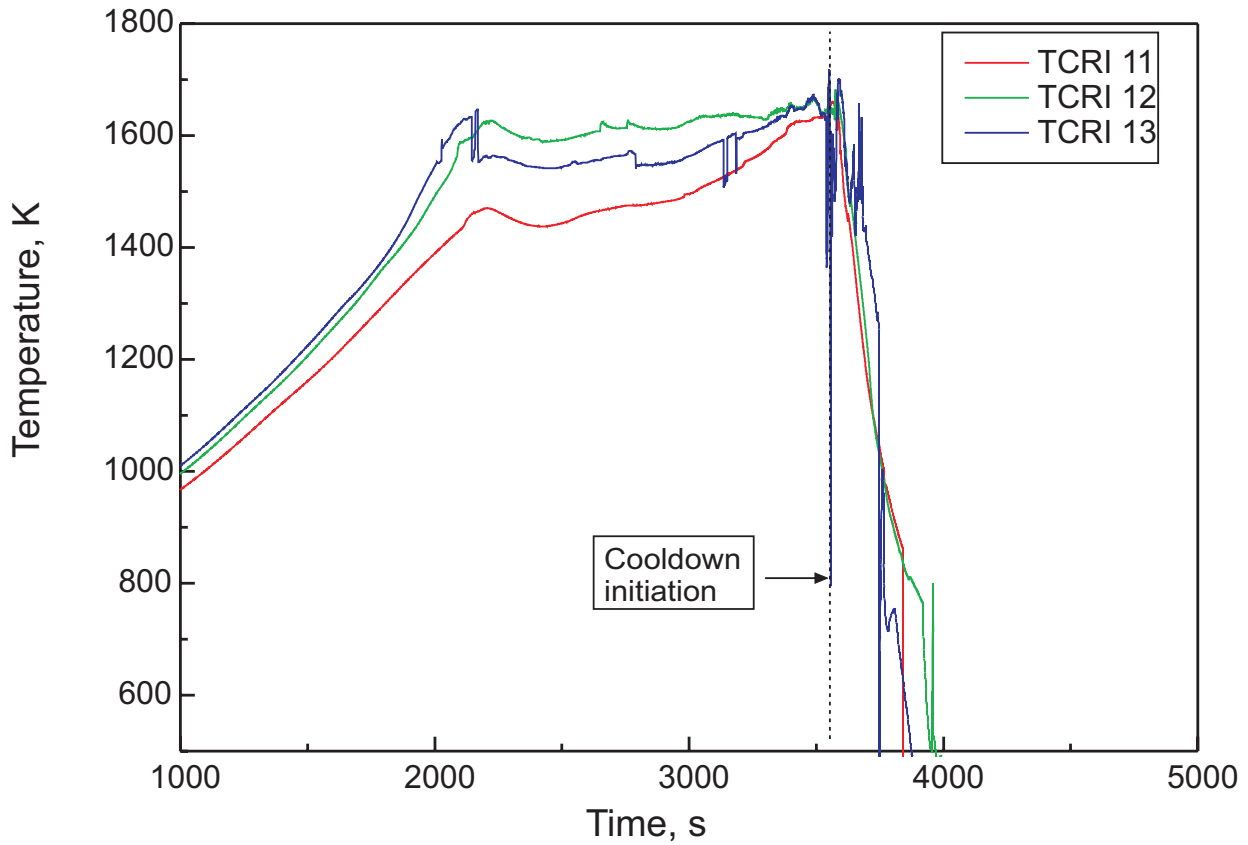
Fig.21-QUE07 absorber temp.cdr
17.07.02 - IMF

Fig. 21:   QUENCH-07; Control rod temperatures at elevations 750, 850, and 950 mm.
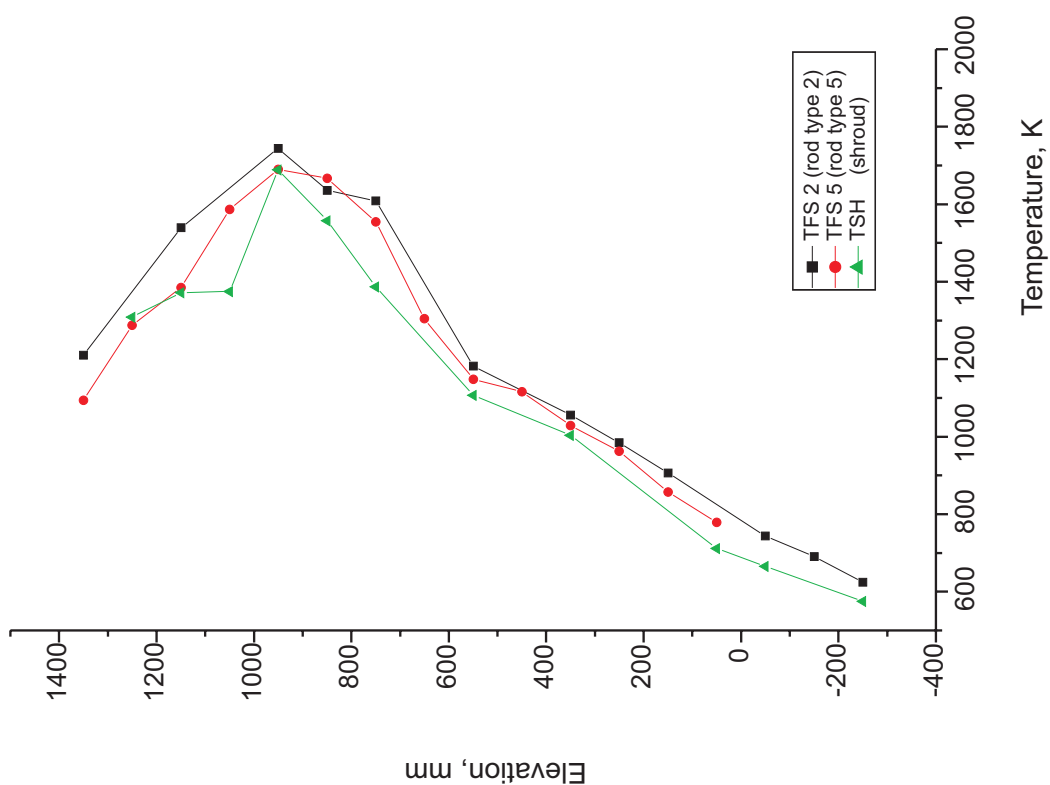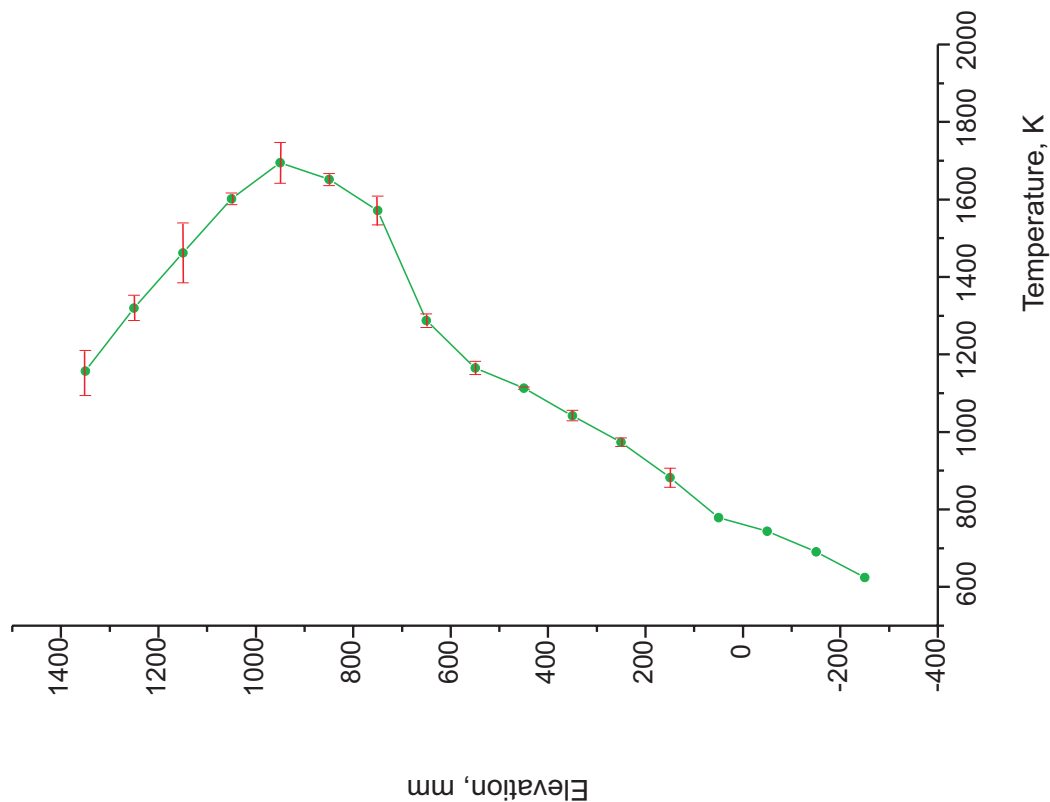
Fig.22-QUE07-axial-2700s.cdr
17.07.02 - IMF

Fig. 22:   QUENCH-07; Axial temperature profile of TFS 2 (inner coolant channel), TFS 5 (outer channel), and TSH (shroud) thermocouples, left, and axial profile of all TFS thermocouples, right, at 2700 s (B_4C oxidation phase)
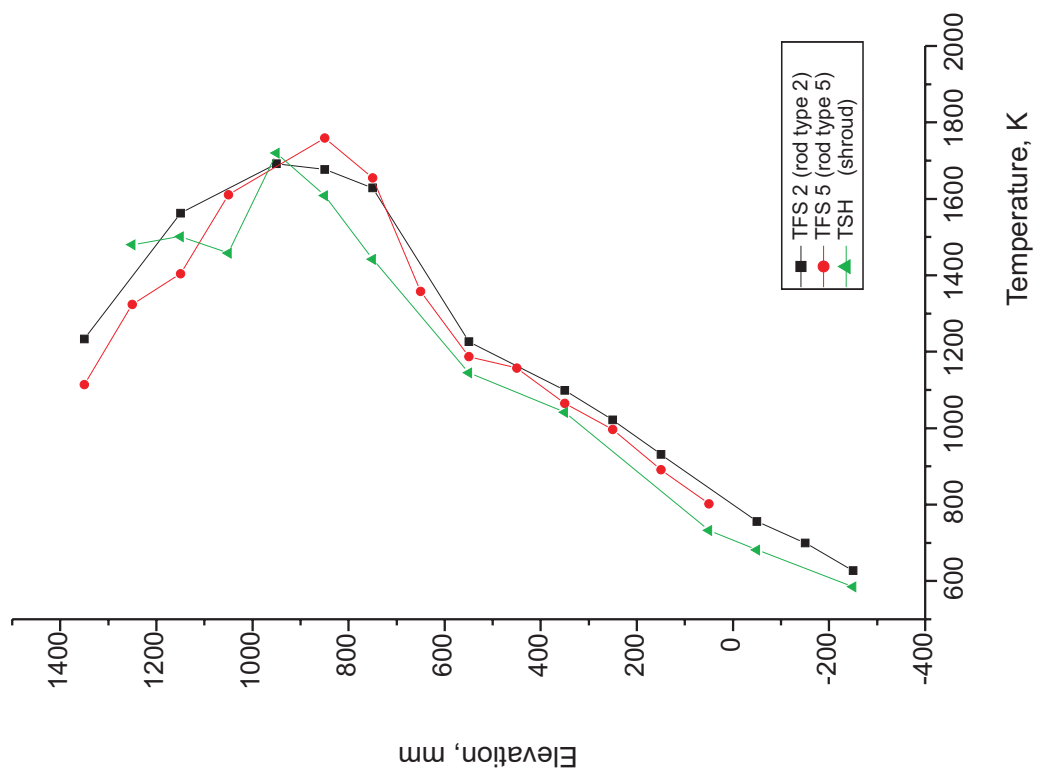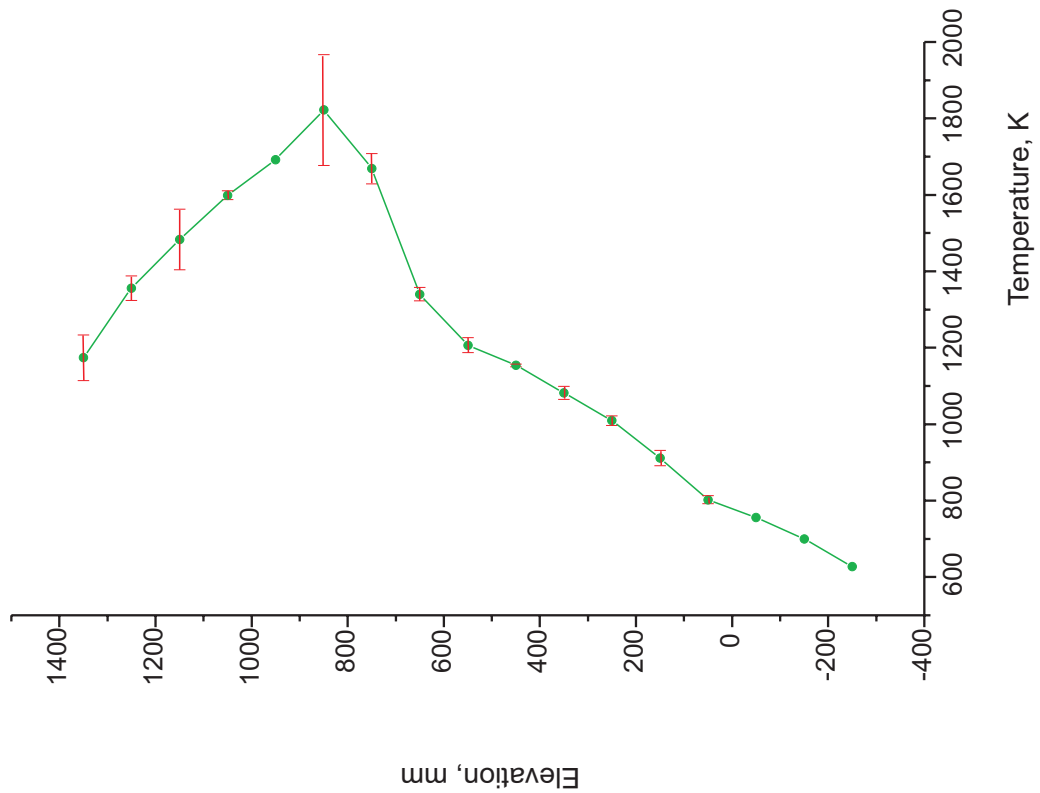
Fig.23-QUE07-axial-3150s.cdr
18.07.02 - IMF

Fig. 23: QUENCH-07; Axial temperature profile of TFS 2 (inner coolant channel), TFS 5 (outer channel), and TSH (shroud) thermocouples, left, and axial profile of all TFS thermocouples, right, at 3150 s (start of transient)
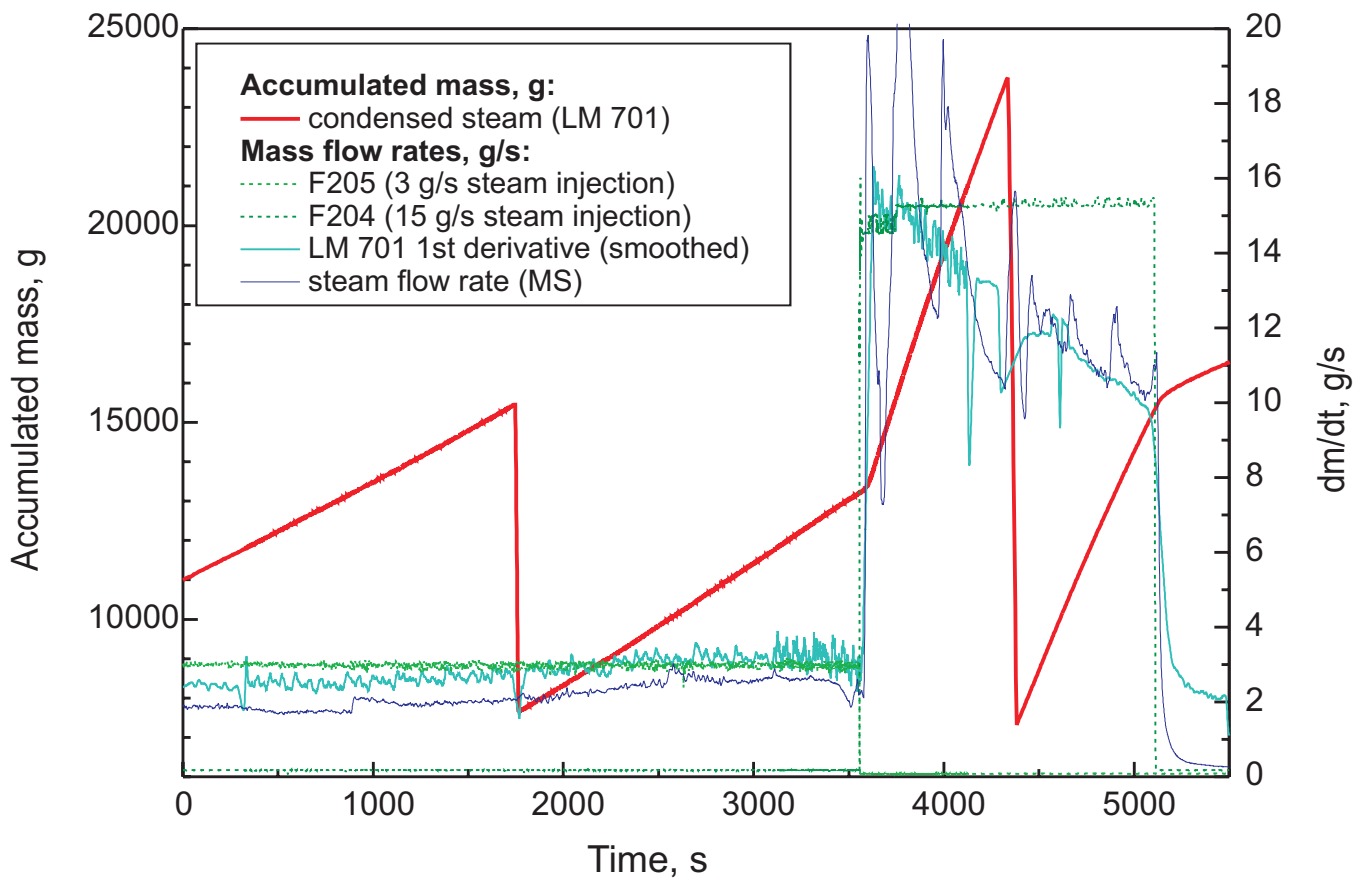
Fig. 24:   QUENCH-07; Steam injection rate, steam flow rate measured by
            MS, and condensed steam (LM 701, as accumulated mass and as
            flow rate).
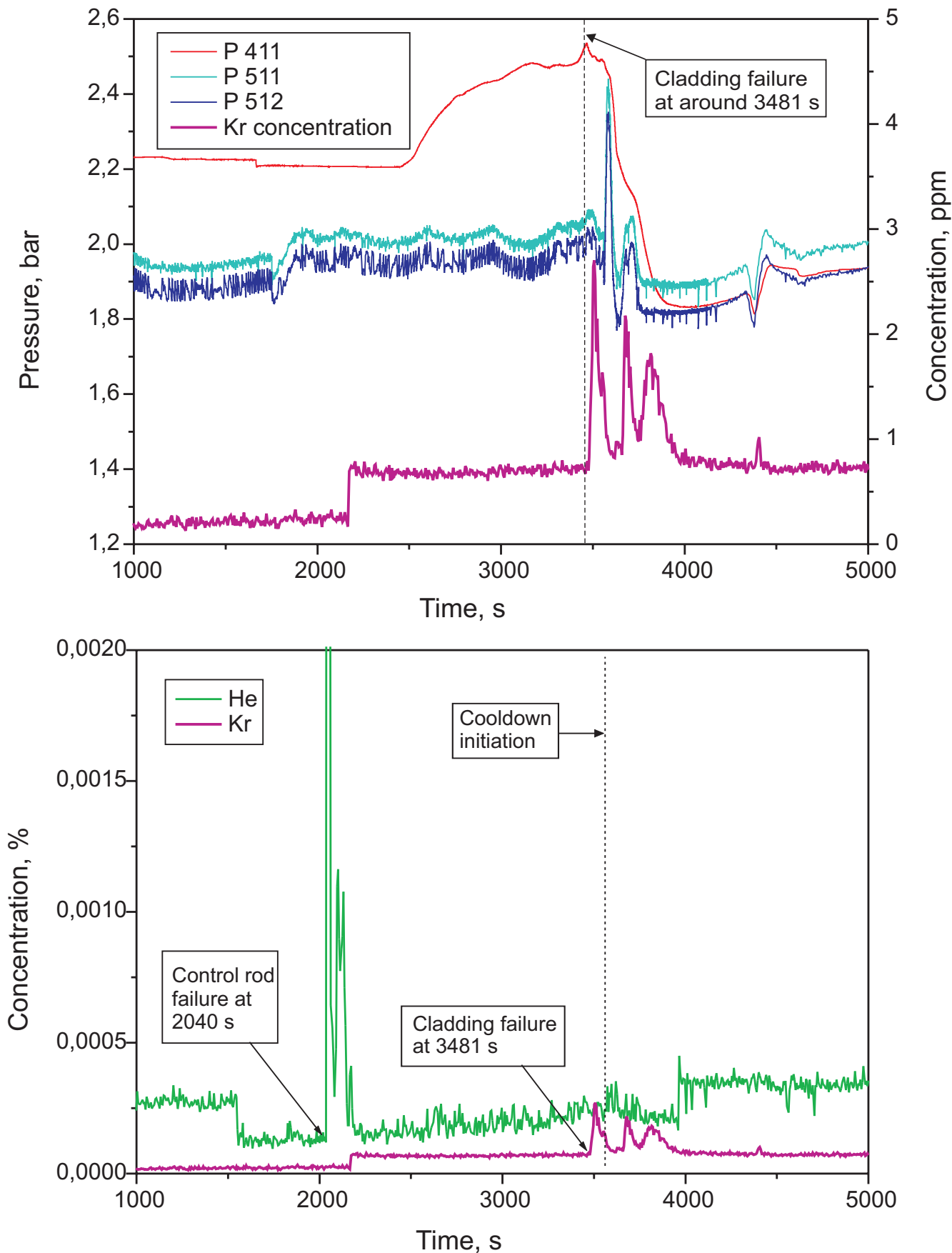
Fig. 25: QUENCH-07; Rod cladding failure indicated by P 411 pressure drop together with krypton release, top, and helium release to indicate control rod failure together with Kr release, bottom.
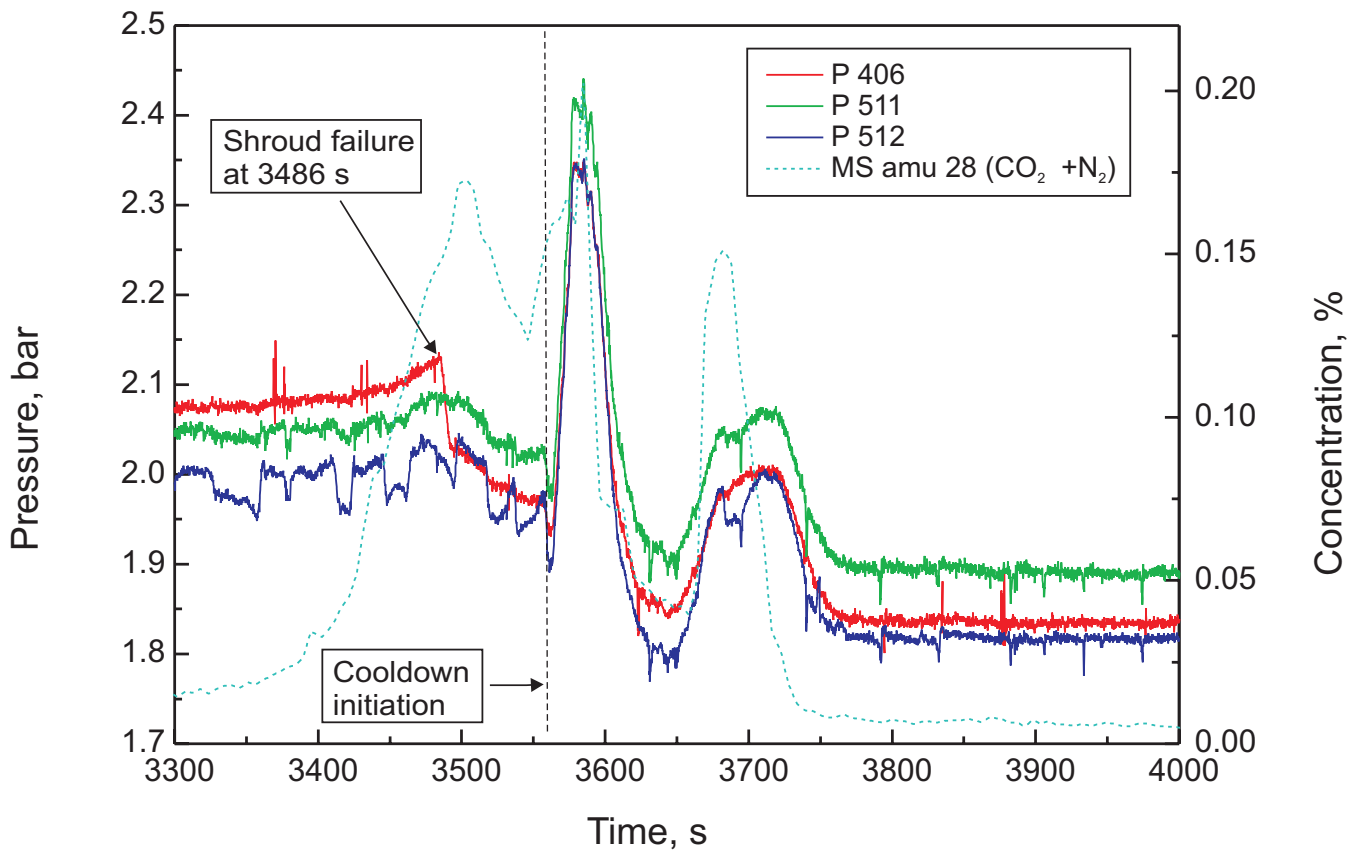
Fig.26-QUE07 shroud failure.cdr
22.07.02 - IMF

Fig. 26: QUENCH-07; Pressure in the annulus between shroud and cooling jacket (P 406) indicating shroud failure together with the system pressure in the test section (P 511, P 512)
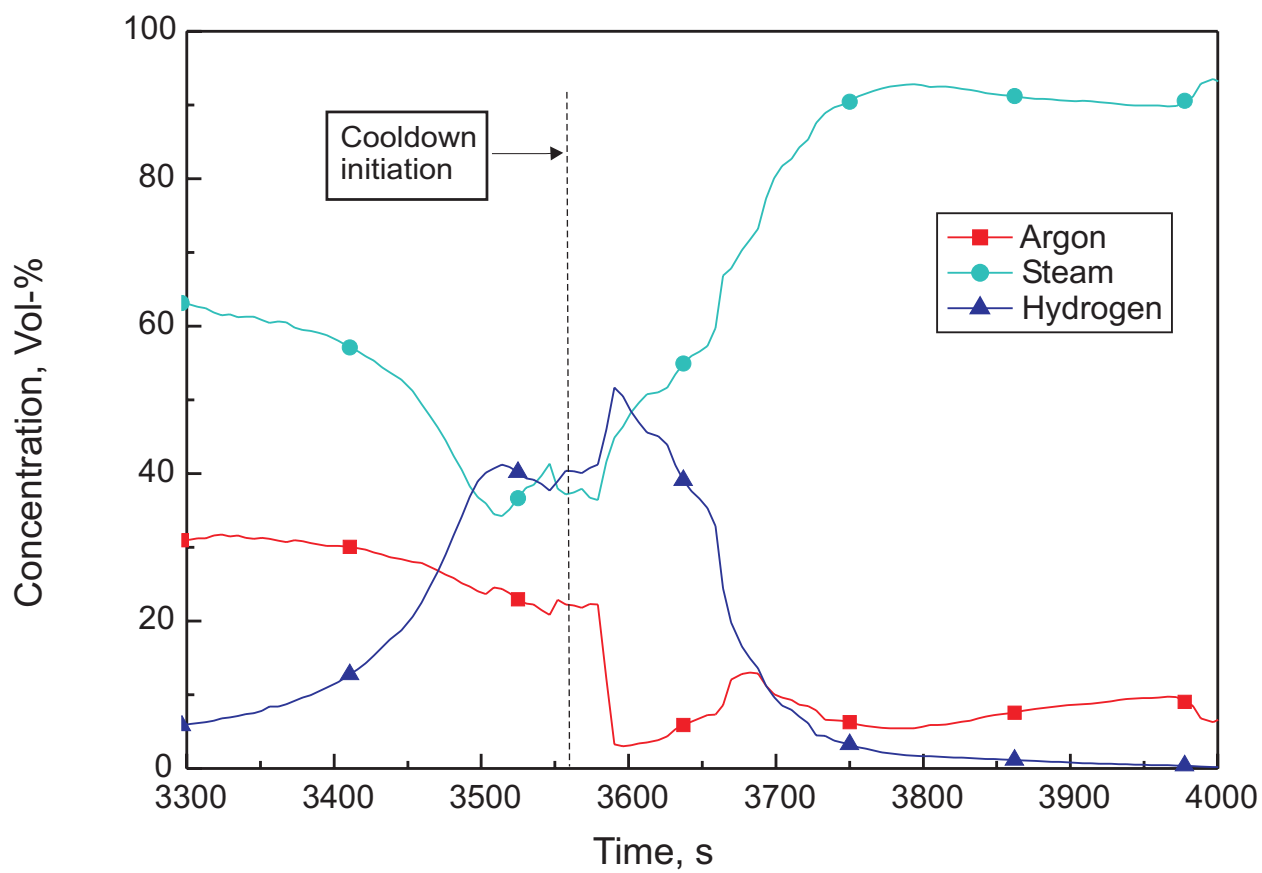
Fig.27-QUE07 MS all Graph9.cdr
22.07.02 - IMF

Fig. 27:   QUENCH-07; Concentrations of the main off-gas components measured
           by the mass spectrometer
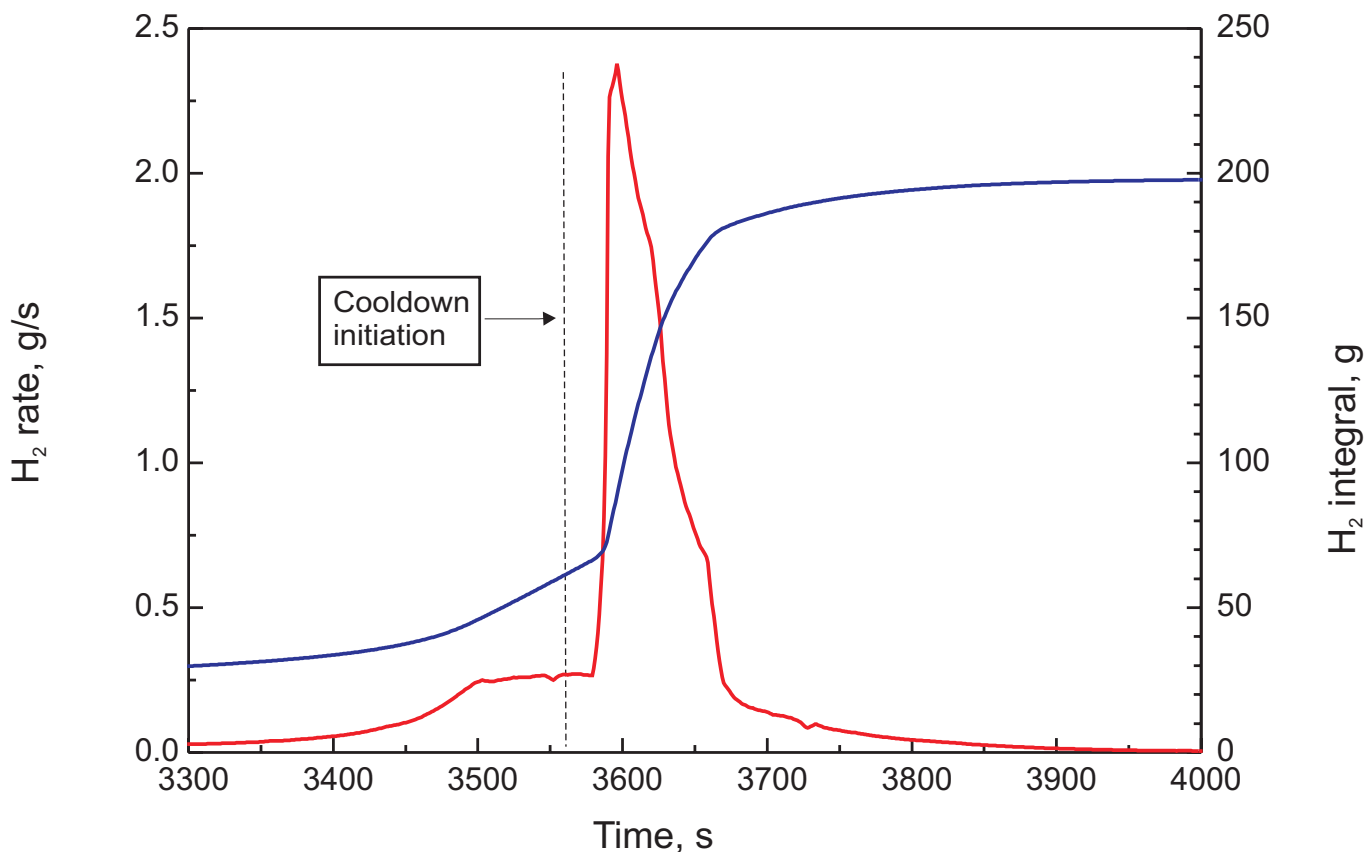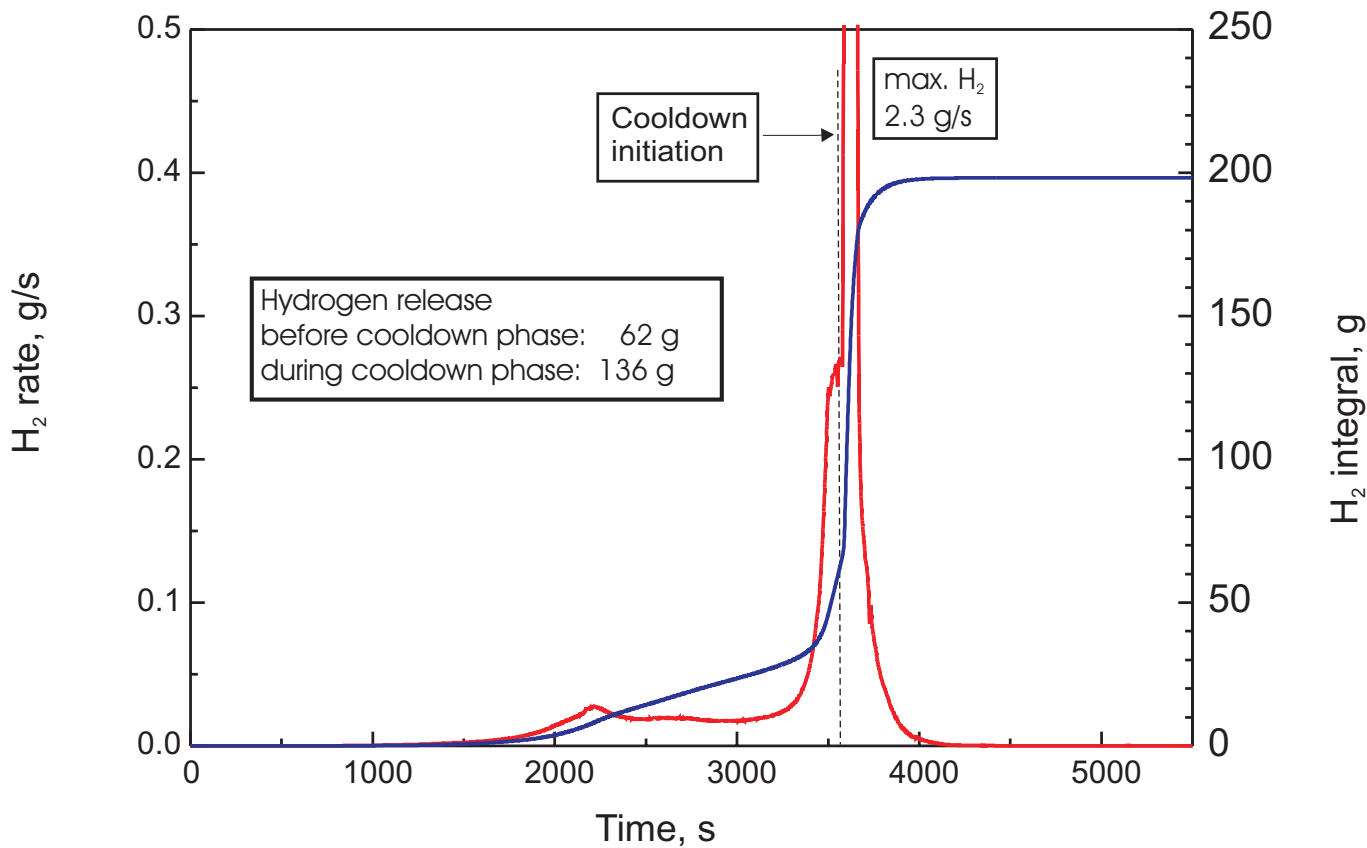
Fig. 28: QUENCH-07; Hydrogen release rate and accumulated total H_2 release measured by the GAM 300 mass spectrometer
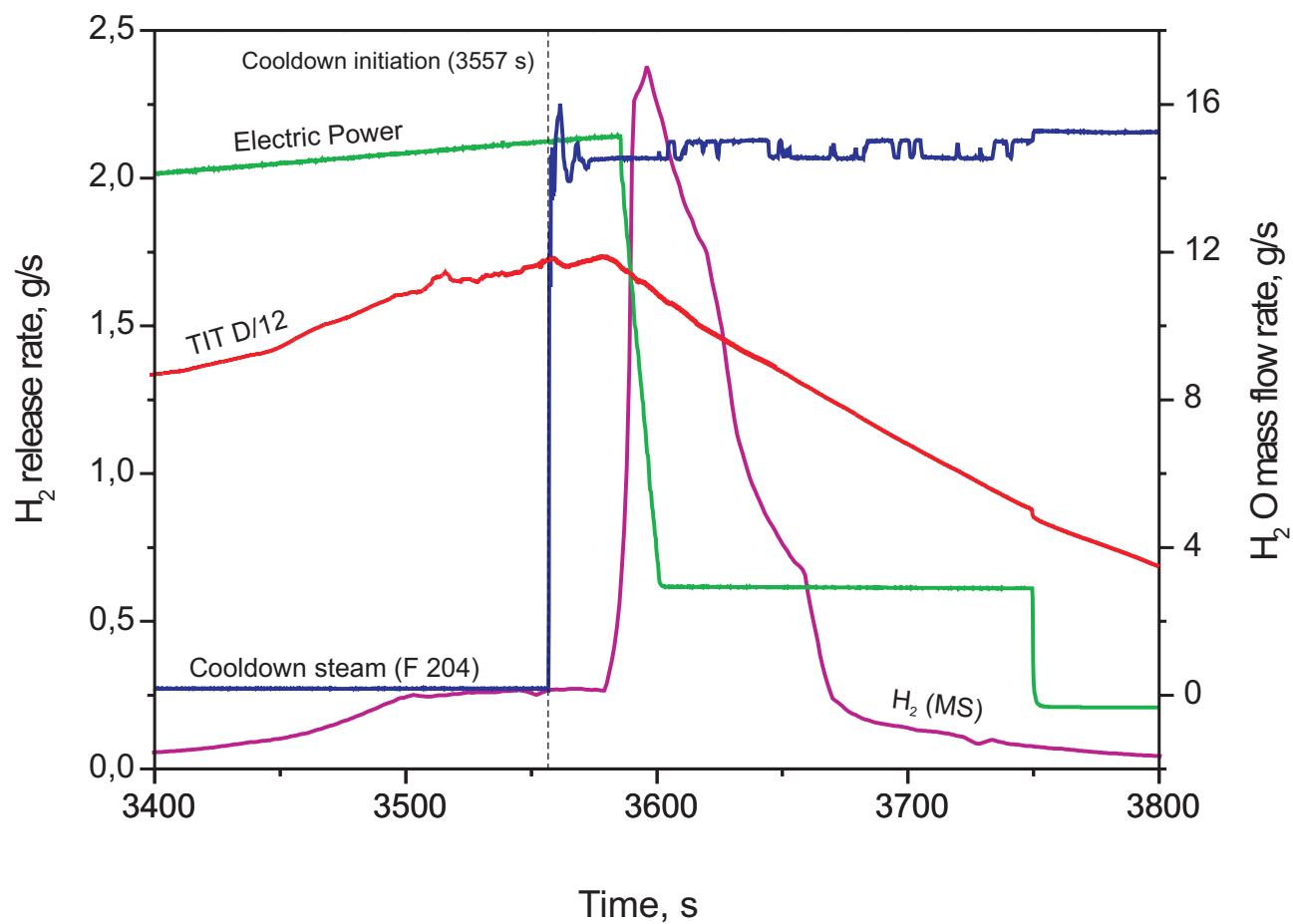
Fig. 29:   QUENCH-07; Synopsis of power input, rod temperature, cooldown
            steam injection, and hydrogen generation
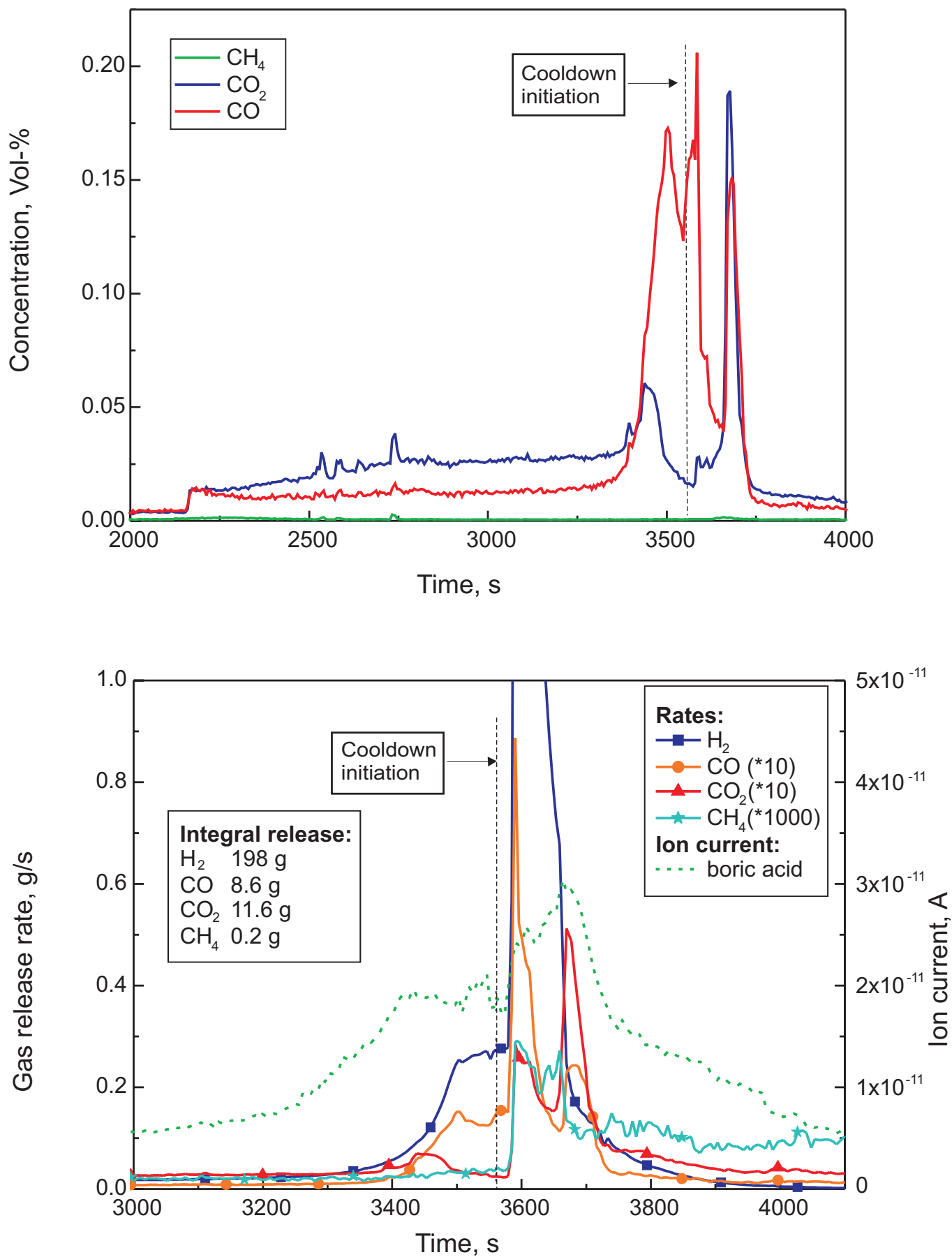
Fig. 30:   QUENCH-07; Gas release rates of carbon- and boron-containing
           species
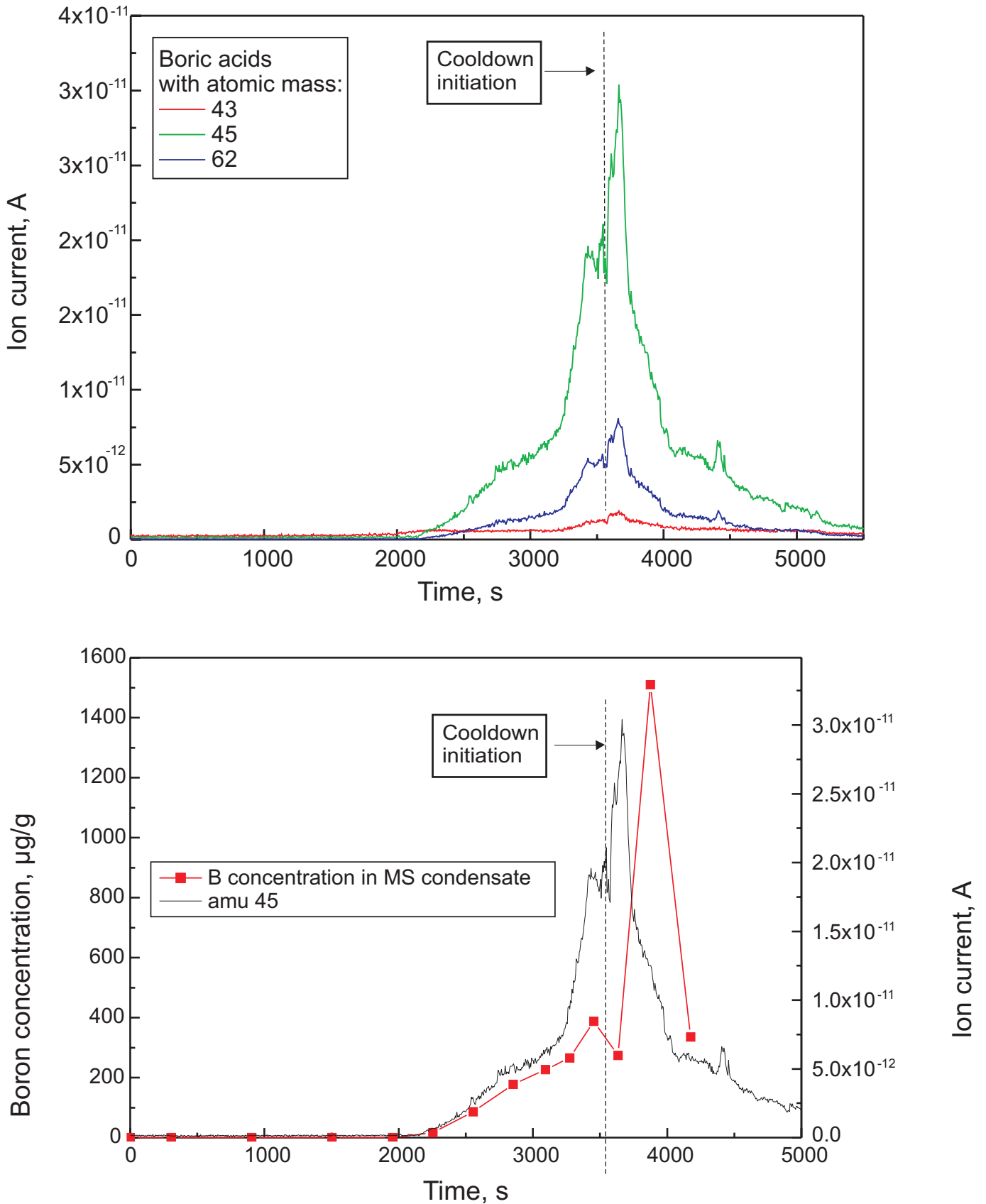
Fig. 31: QUENCH-07; Mass spectrometer signals of boric acid species, top, and boron concentration in the off-gas condensate taken at different times at the MS location, together with the MS signal of the atomic mass 45, bottom
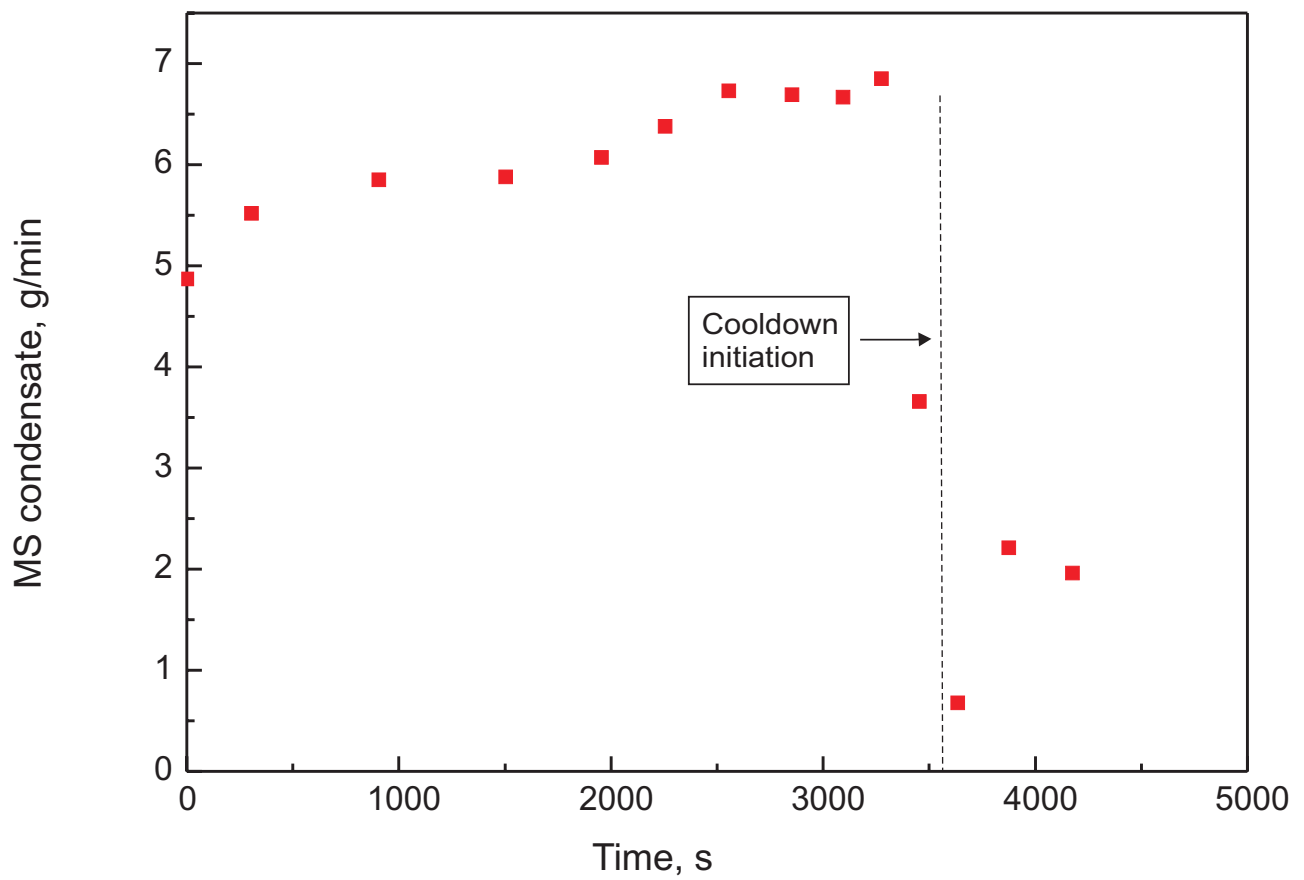
Fig.32-QUE07-MS condensate.cdr
23.07.02 - IMF

Fig. 32:   QUENCH-07; Condensate flow taken at the MS outlet used for boron
            analysis

Fig 33-QUE07 Posttest 90°b.cdr
16.03.04 - IMF

Fig. 33:   QUENCH-07; Posttest appearance of bundle and shroud
at ~ 700 - 1000 mm elevation, 90° orientation

Fig 34-QUE07 Posttest 90°c.cdr
16.03.04 - IMF

Fig. 34:   QUENCH-07; Posttest appearance of bundle and shroud
at ~ 1000 - 1300 mm elevation, 90° orientation

Fig. 35:   QUENCH-07; View of the bundle after removal of shroud fragments
in the region 780 - 1000 mm, 0° orientation

Fig 36-QUE07 Posttest shroud frag.cdr
16.03.04 - IMF

Fig. 36: QUENCH-07; Shroud fragment removed from the region 780 - 860 mm elevation

Fig 37-QUE07 Schnittplan.cdr
30.07.02 - IMF
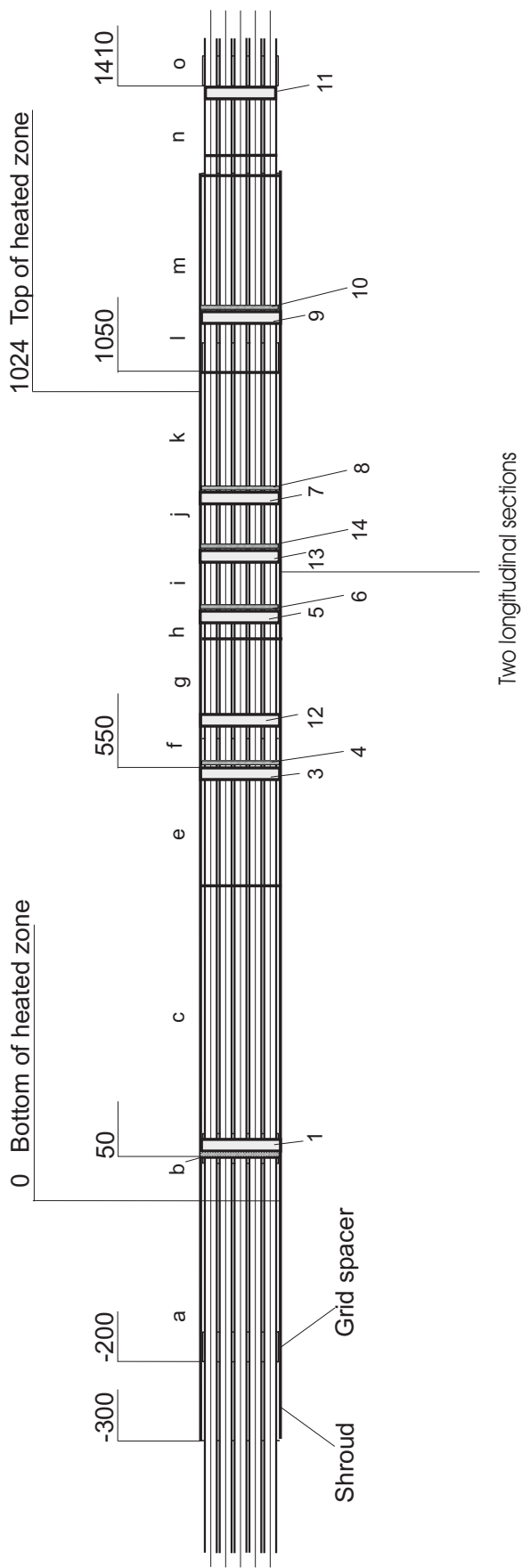
Fig. 37:   QUENCH-07; Sectioning of test bundle

QUE-07-1 bottom 60 mm

QUE-07-1 top 73 mm

QUE-07-3 bottom 537 mm

QUE-07-3 top 550 mm
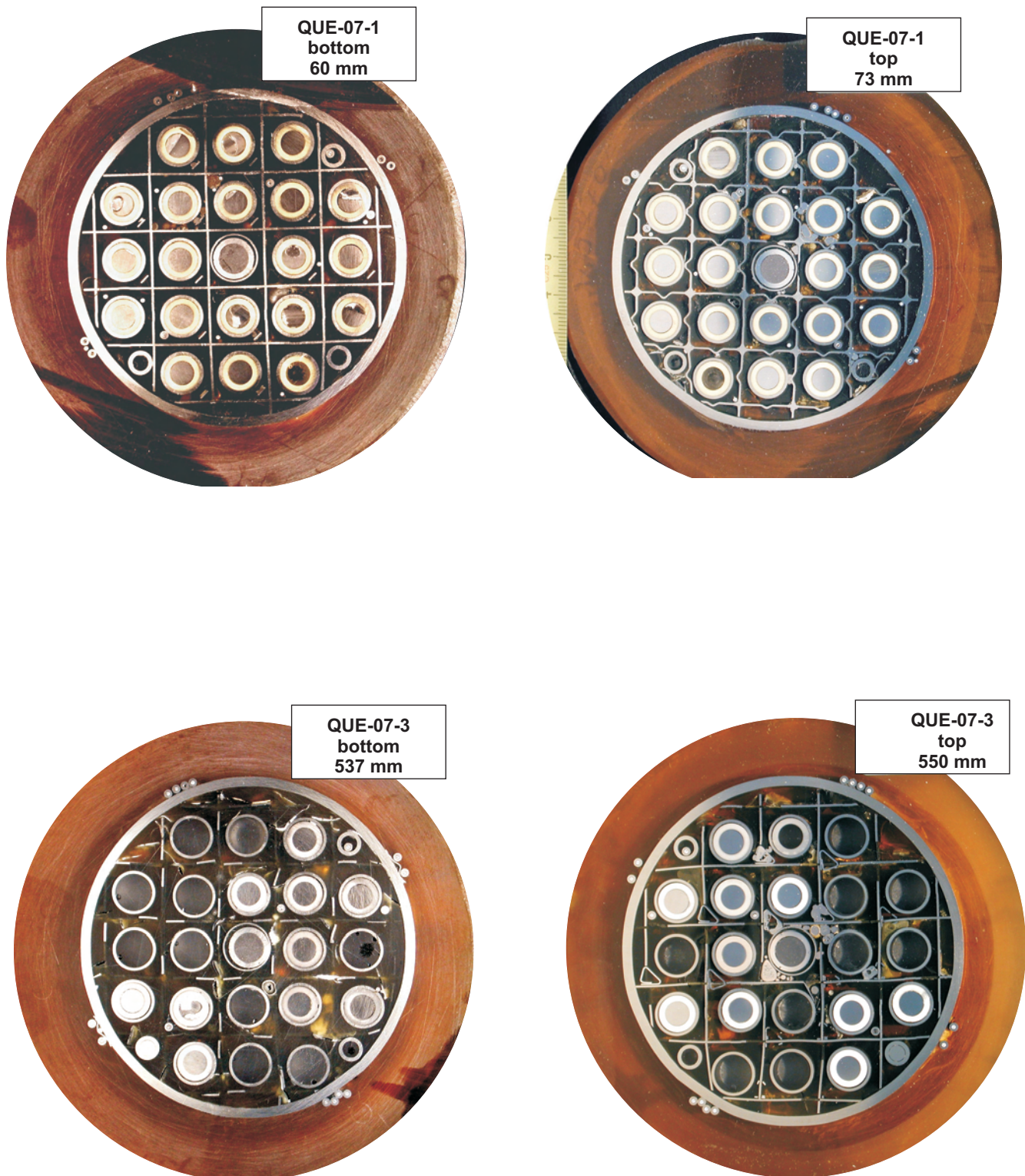
Fig 38-QUE07 Cross section1-3.cdr
23.07.02 - IMF

Fig. 38:   QUENCH-07; Cross sections at 60 mm, 73 mm, 537 mm, and 550 mm

QUE-07-12
bottom
637 mm

QUE-07-12
top
650 mm

QUE-07-13
bottom
837 mm

QUE-07-13
top
850 mm
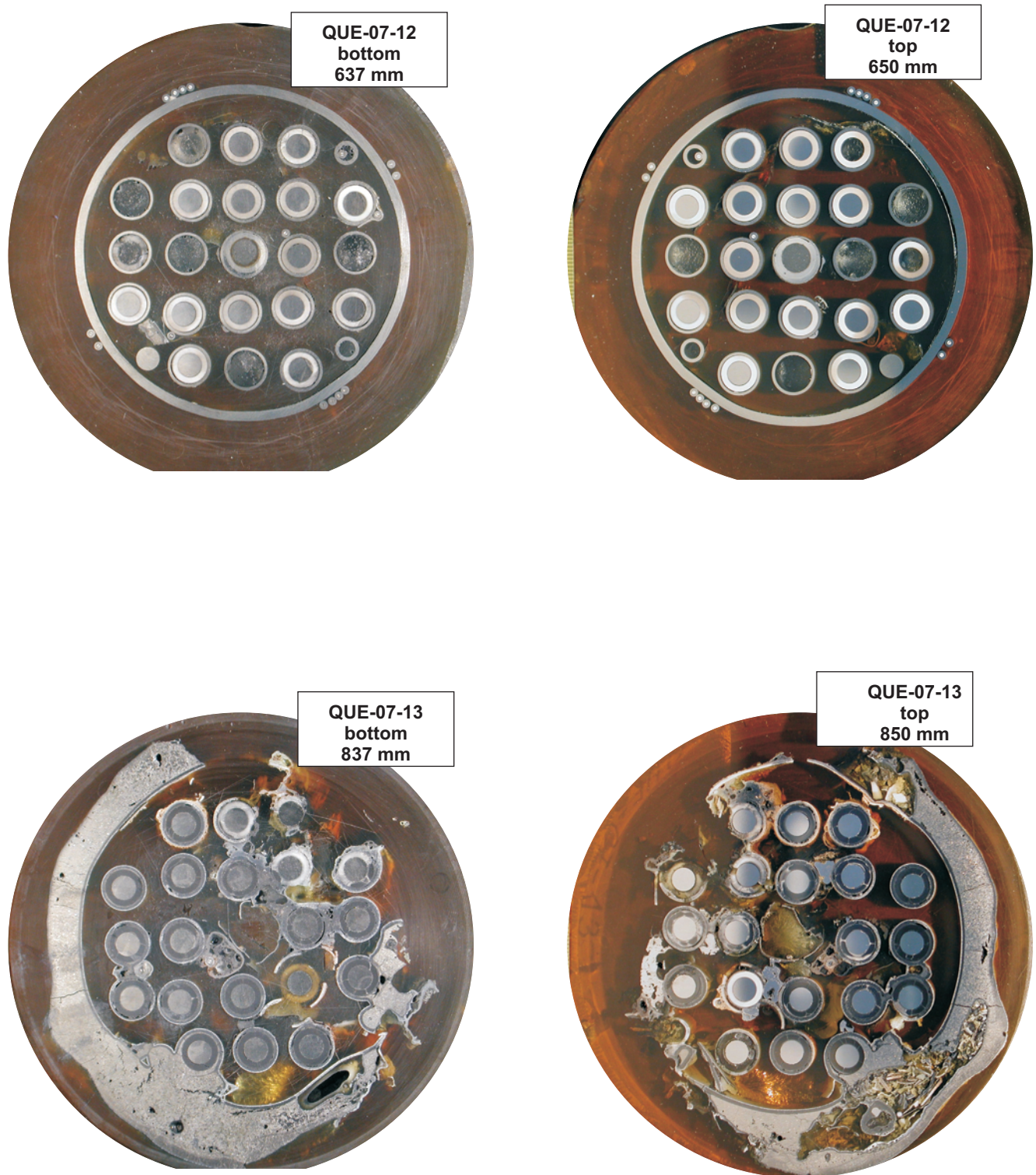
Fig 39-QUE07 Cross section12-13.cdr
23.07.02 - IMF

Fig. 39:   QUENCH-07; Cross sections at 637 mm, 650 mm, 837 mm, and
850 mm

QUE-07-5
bottom
737 mm

QUE-07-5
top
750 mm

QUE-07-7
bottom
937 mm
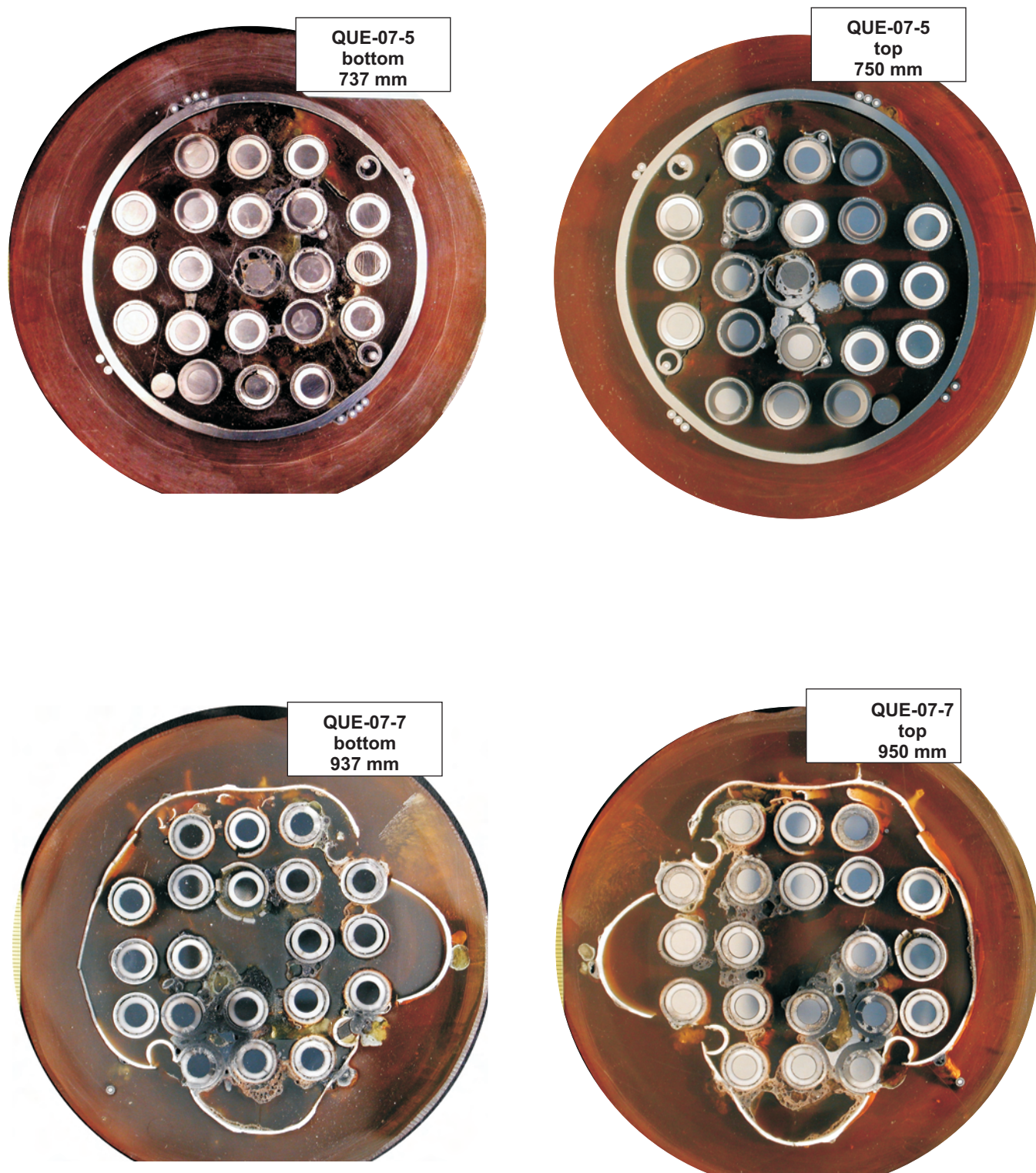
QUE-07-7
top
950 mm

Fig 40-QUE07 Cross section5-7.cdr
23.07.02 - IMF

Fig. 40: QUENCH-07; Cross sections at 737 mm, 750 mm, 937 mm, and 950 mm

QUE-07-9
bottom
1137 mm

QUE-07-9
top
1150 mm

QUE-07-11
bottom
1397 mm

QUE-07-11
top
1410 mm
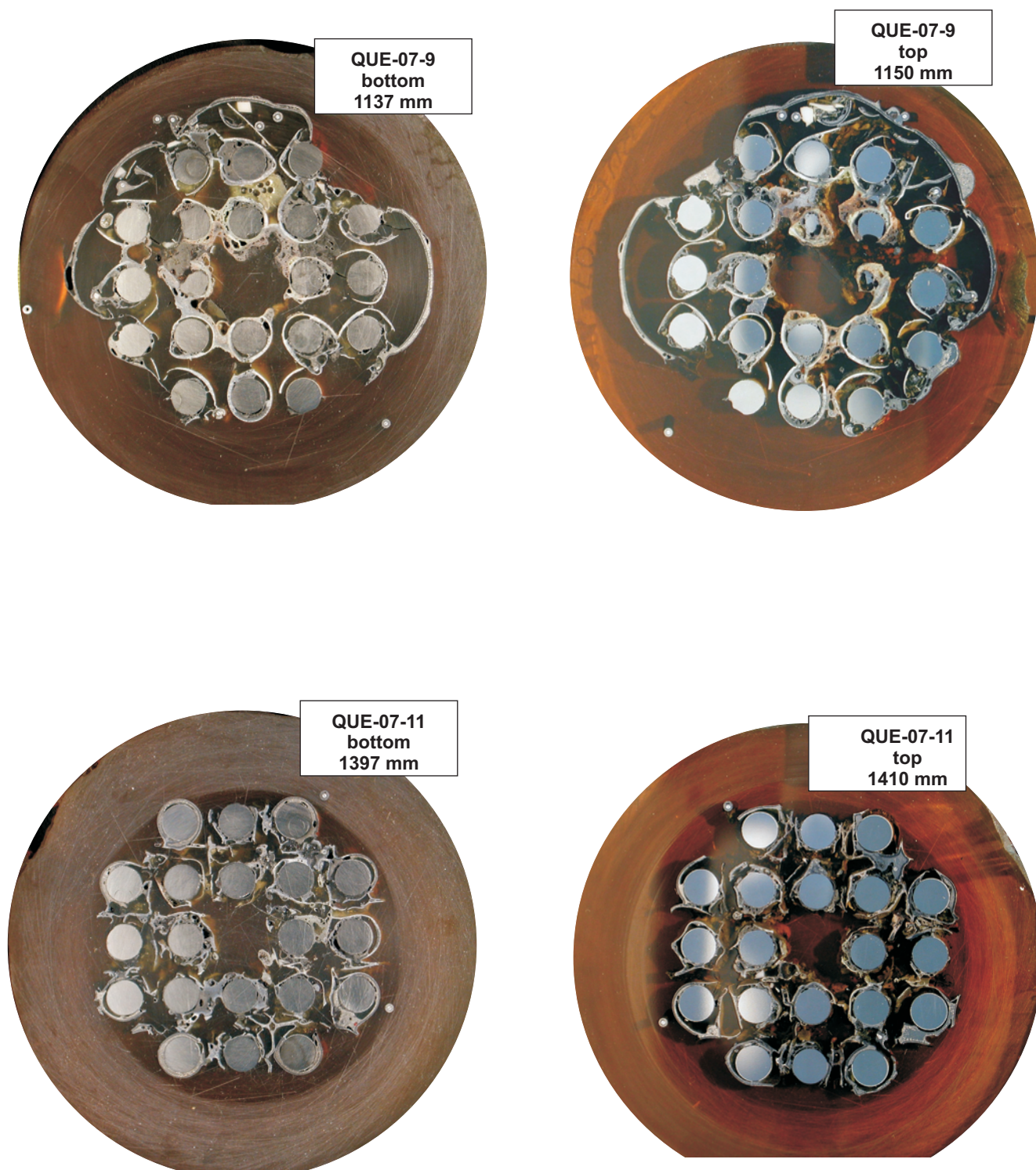
Fig 41-QUE07 Cross section9-11.cdr
24.07.02 - IMF

Fig. 41: QUENCH-07; Cross sections at 1137 mm, 1150 mm, 1397 mm, and 1410 mm

835 mm

759 mm

835 mm

759 mm
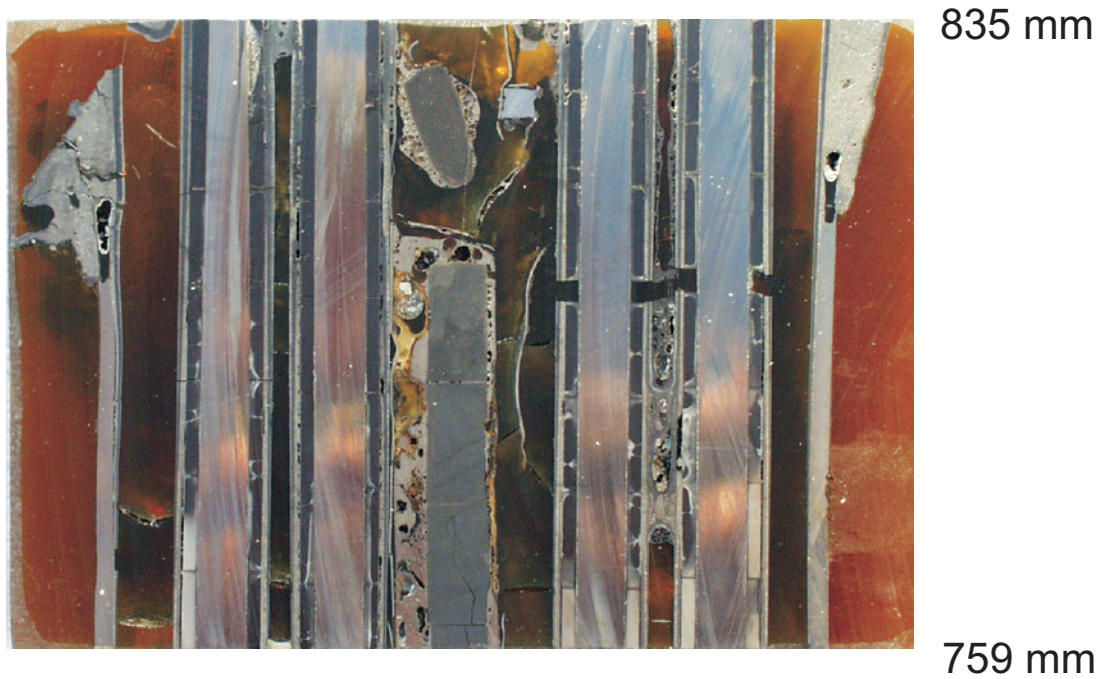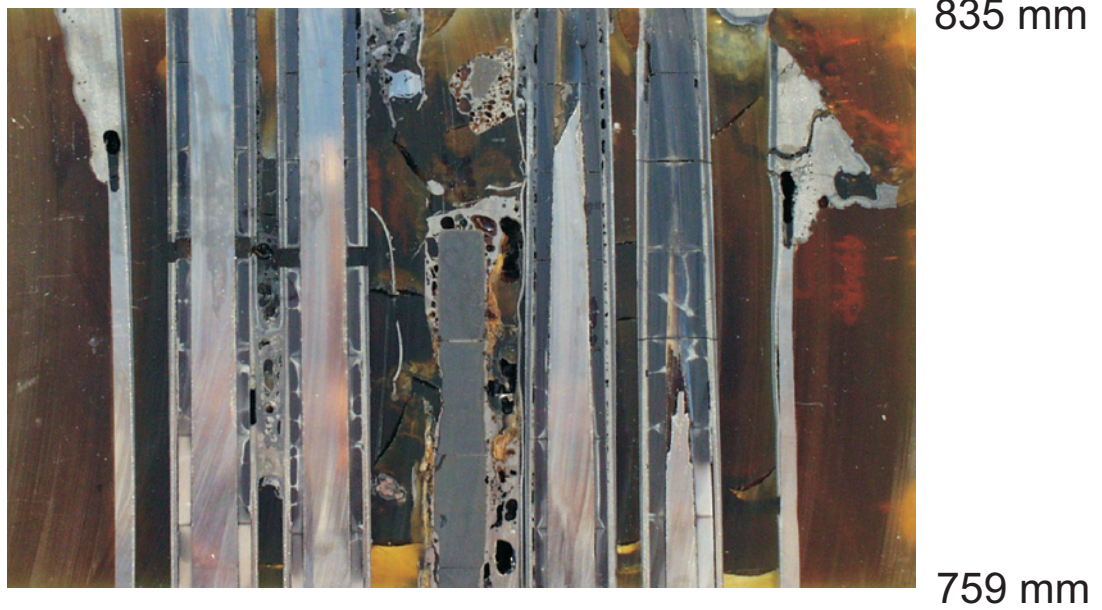
Fig.42-QUE07-longitudinal section1.cdr
16.03.04 - IMF

Fig. 42: QUENCH-07; Failure region of the control rod at around 800 mm
elevation; two longitudinal sections of slab QUE-07-i that was cut
through the bundle center at the
90 - 270° orientation.

835 mm

759 mm

835 mm

759 mm
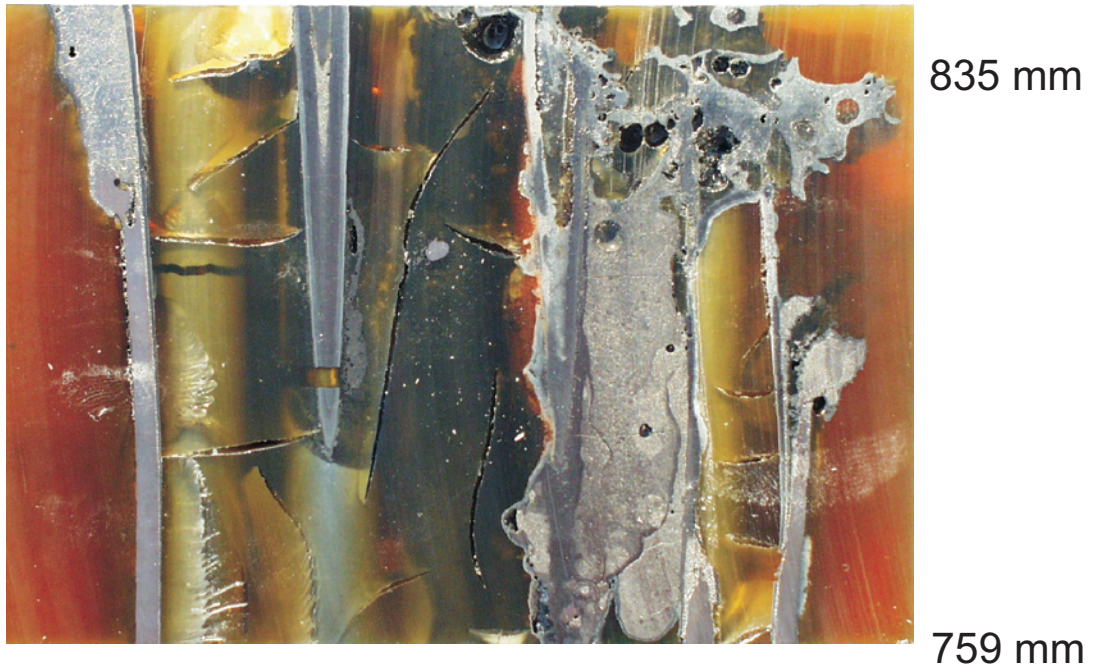
Fig.43-QUE07-longitudinal section2.cdr
16.03.04 - IMF

Fig. 43: QUENCH-07; Failure region of the control rod at around 800 mm
elevation; longitudinal sections of slab QUE-07-i cut excentrically at
the 90 - 270° orientation.
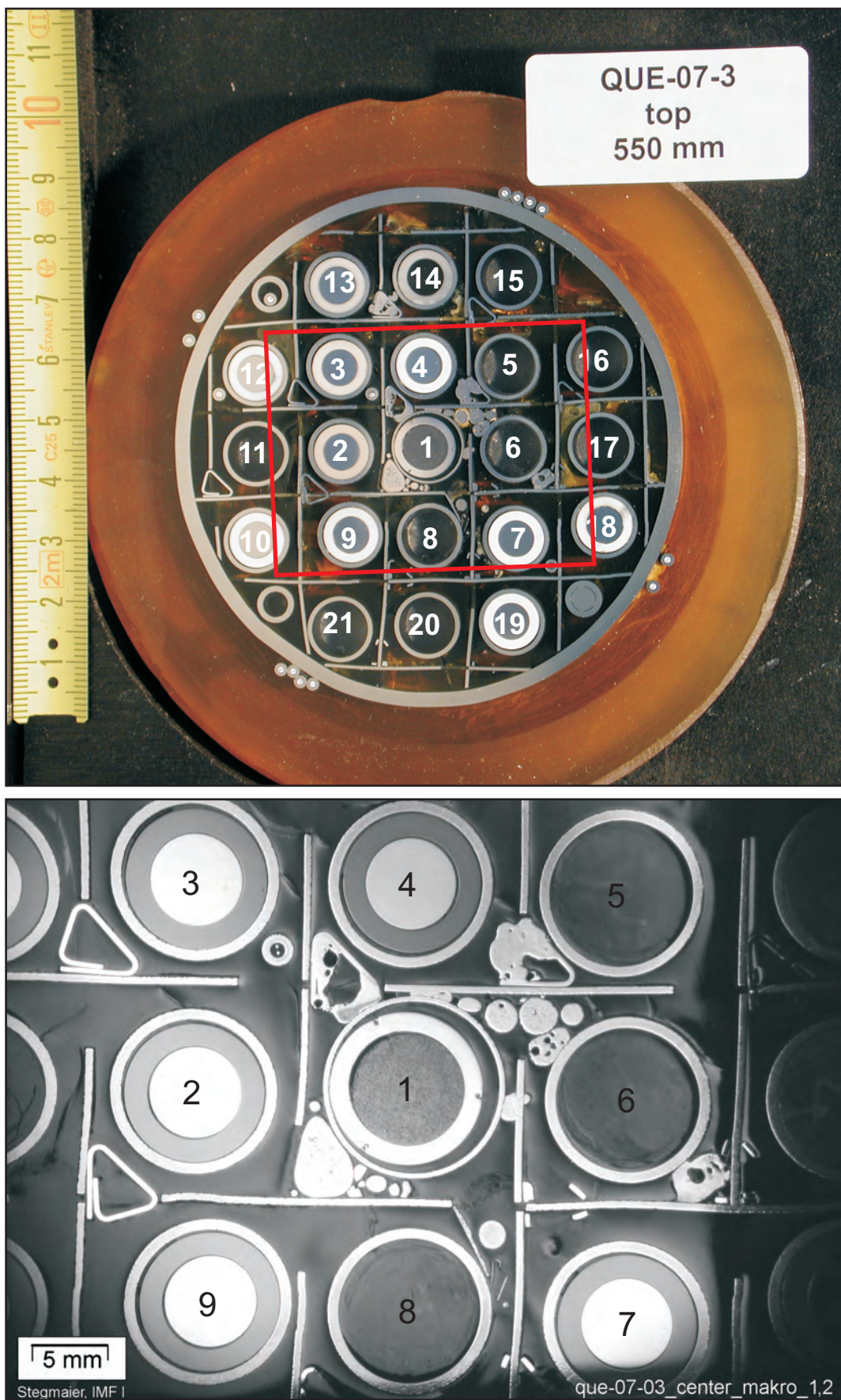
Fig. 44: QUENCH-07; Cross section at bundle elevation 550 mm (QUE-07-3, top); overview.
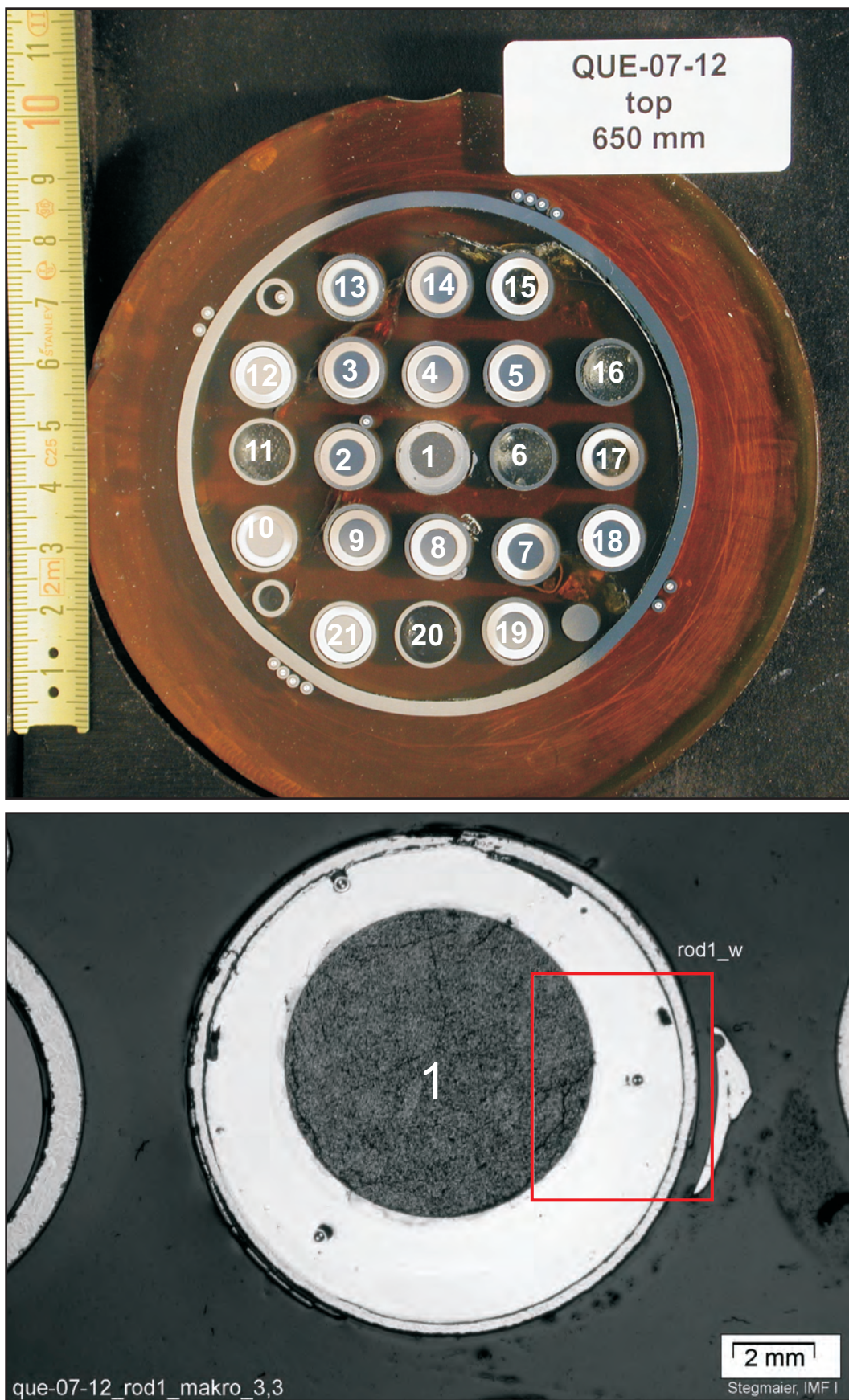
Fig. 45: QUENCH-07; Cross section at bundle elevation 650 mm (QUE-07-12, top); overview and control rod.

Overview, showing filled gap between guide tube and control rod by relocated melt from the interaction of absorber components at higher elevation.
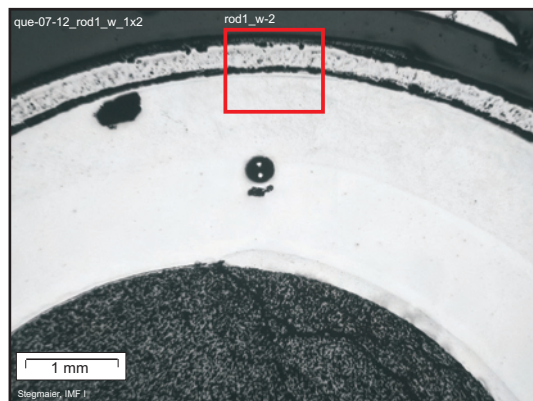
ZrO$_2$ scale of guide tube

Guide tube

Guide tube/melt interaction zones

Melt, formed by absorber components interaction, relocated
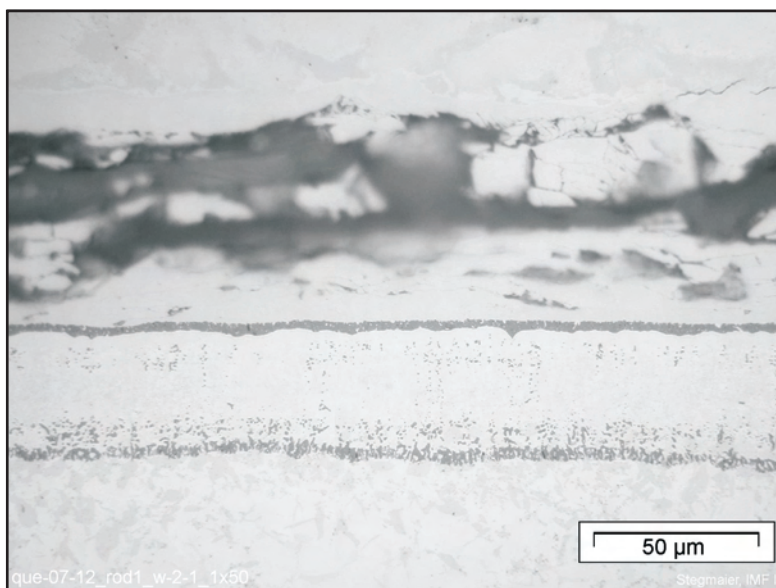
Guide tube

Zone of interaction towards guide tube (artefacts due to embrittlement)

Zone of interaction towards melt

Absorber melt

QUE07-12- F650-2.cdr 08/2002   **FZK - IMF**

Fig. 46:   QUENCH-07; Cross section at bundle elevation 650 mm (QUE-07-12, top); control rod and guide tube state.

Overview, showing interface absorber melt/CR cladding, melt-embedded TC, and CR cladding/B_4C interaction zone
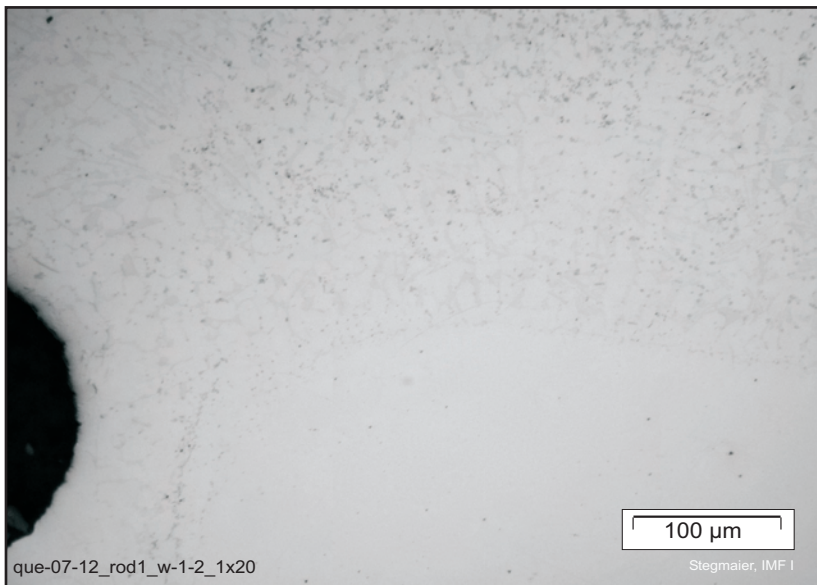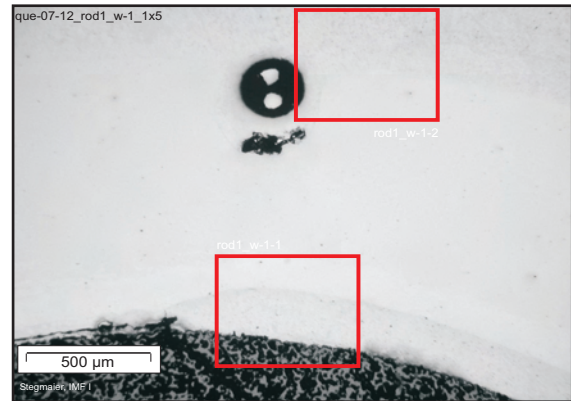
Relocated melt from absorber interaction at higher elevation

Non melted SS CR cladding
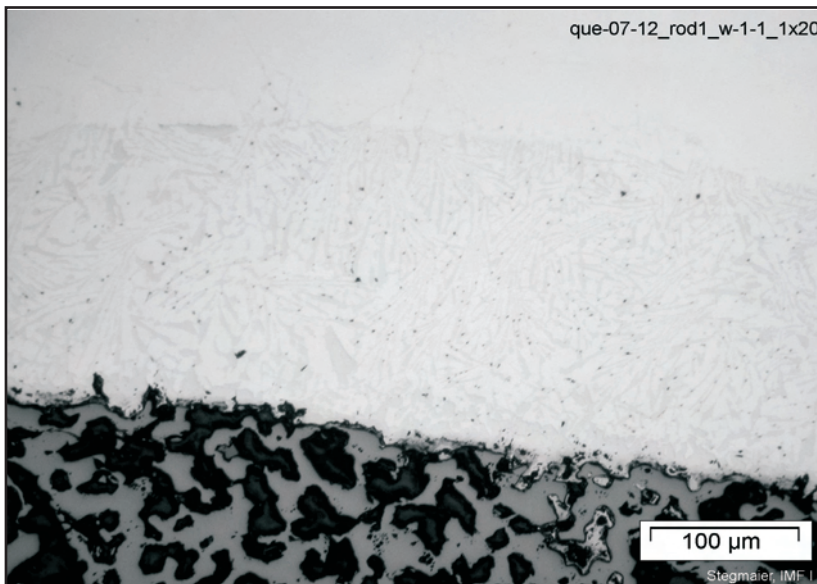
Non melted SS CR cladding

Melt from CR cladding/B_4C interaction as formed at place

B_4C pellet, infiltrated by melt

QUE07-12- F650-3.cdr 08/2002 **FZK - IMF**

Fig. 47:   QUENCH-07; Cross section at bundle elevation 650 mm (QUE-07-12, top); state of control rod.
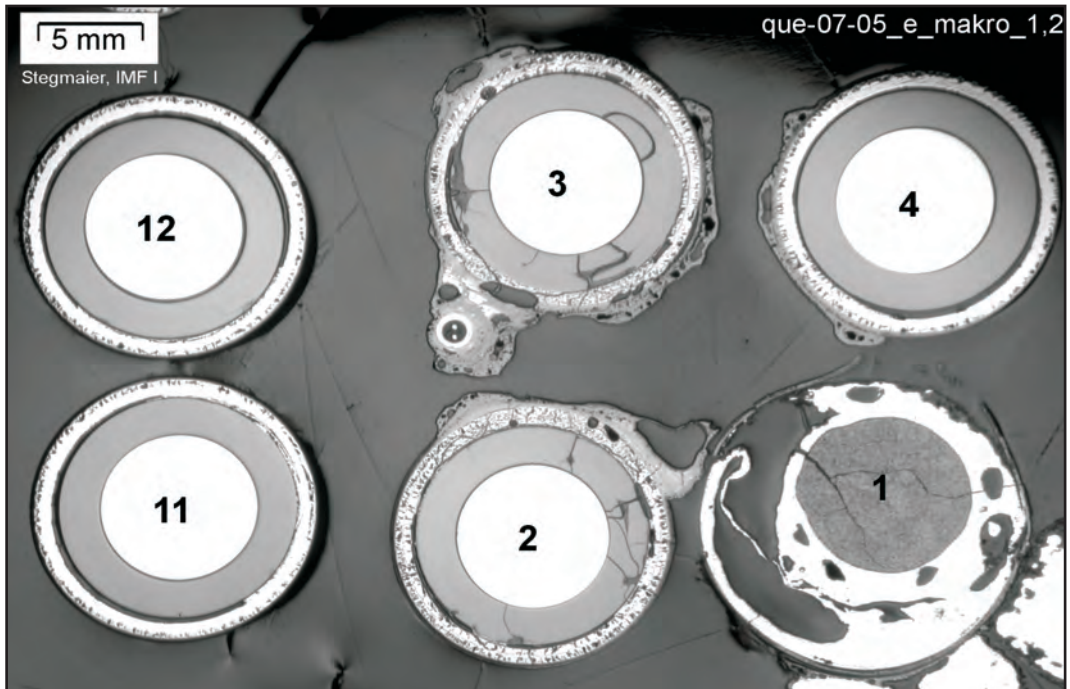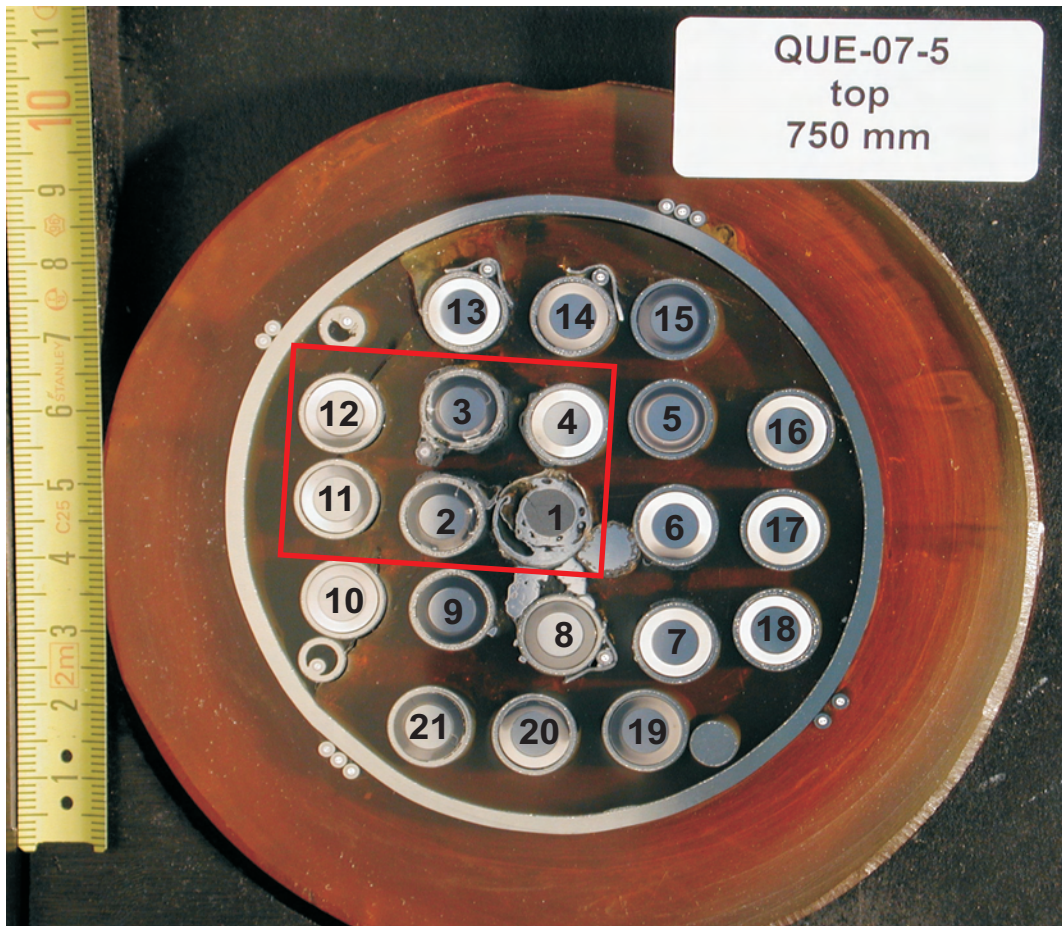
QUE07-05- F750-1.cdr 06/2002 **FZK - IMF** / heck

Fig. 48:   QUENCH-07; Cross section at bundle elevation 750 mm (QUE-07-5, top); overview.

que-07-05_rod1_makro_3,3

2 mm

Stegmaier, IMF I

rod1_nw

Overview on absorber rod

que-07-05_rod1_nw_1x2

External absorber melt, partially oxidized

Absorber melt, confined between guide tube scale and B_4C pellet

1 mm

Stegmaier, IMF I

Example for observed multi-phase absorber melt microstructures

50 µm

que-07-05_rod1_s-1-3_1x50

Stegmaier, IMF I
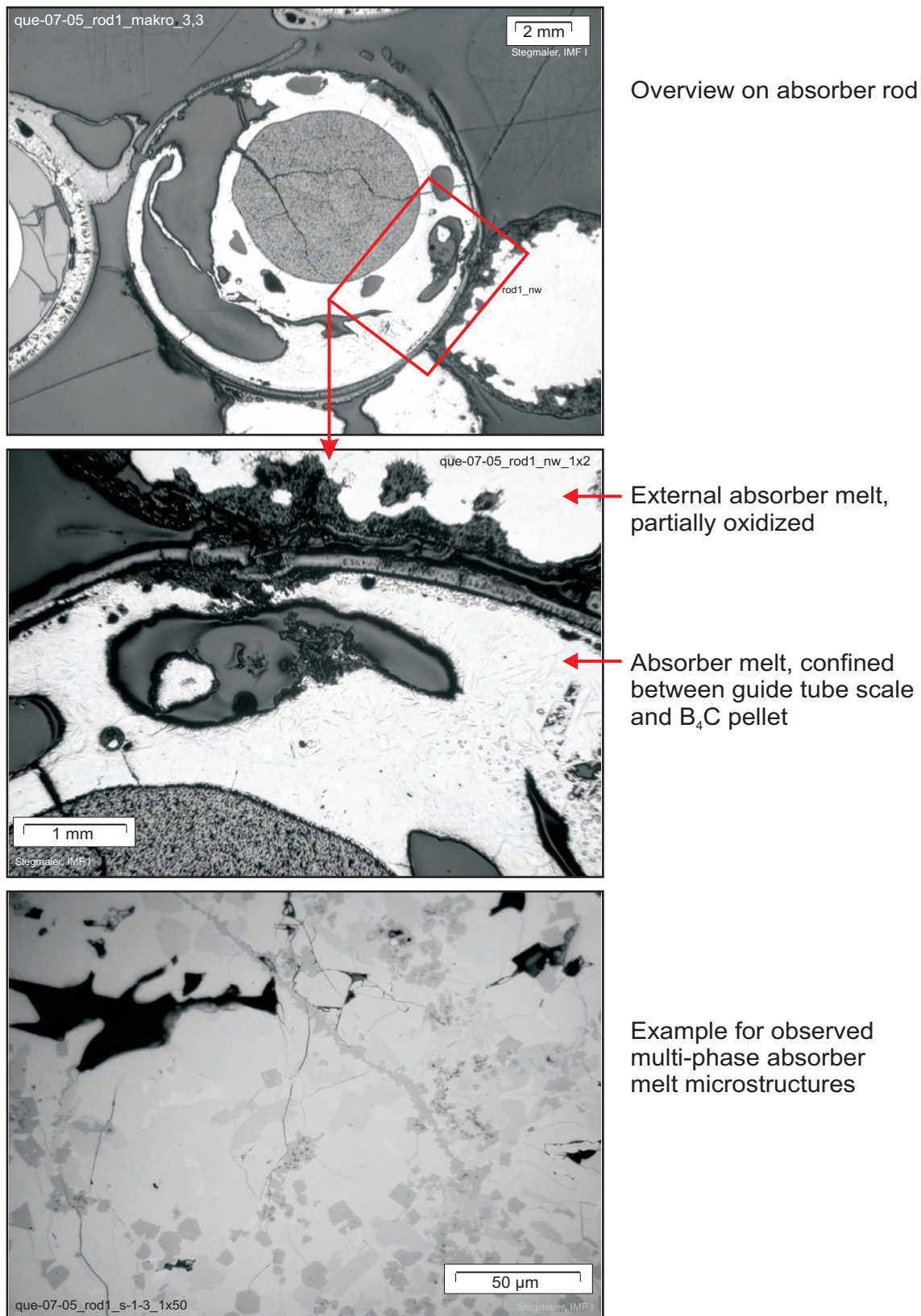
QUE07-05- F750-2a.cdr 06/2002   **FZK - IMF** / heck

Fig. 49:   QUENCH-07; Cross section at bundle elevation 750 mm (QUE-07-5, top); state of absorber rod.
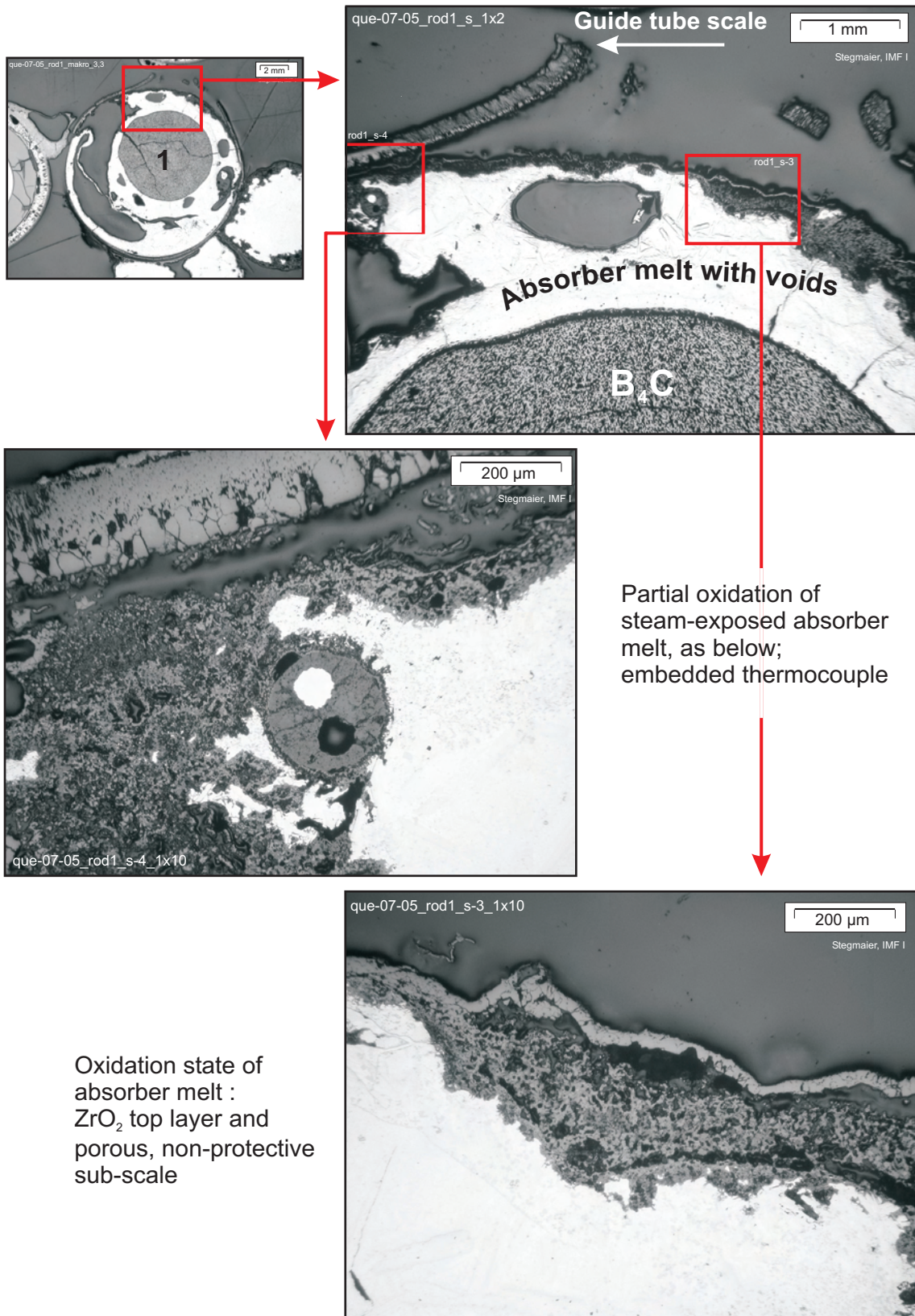
Fig. 50: QUENCH-07; Cross section at bundle elevation 750 mm (QUE-07-5, top); oxidation state of steam-exposed absorber melt.
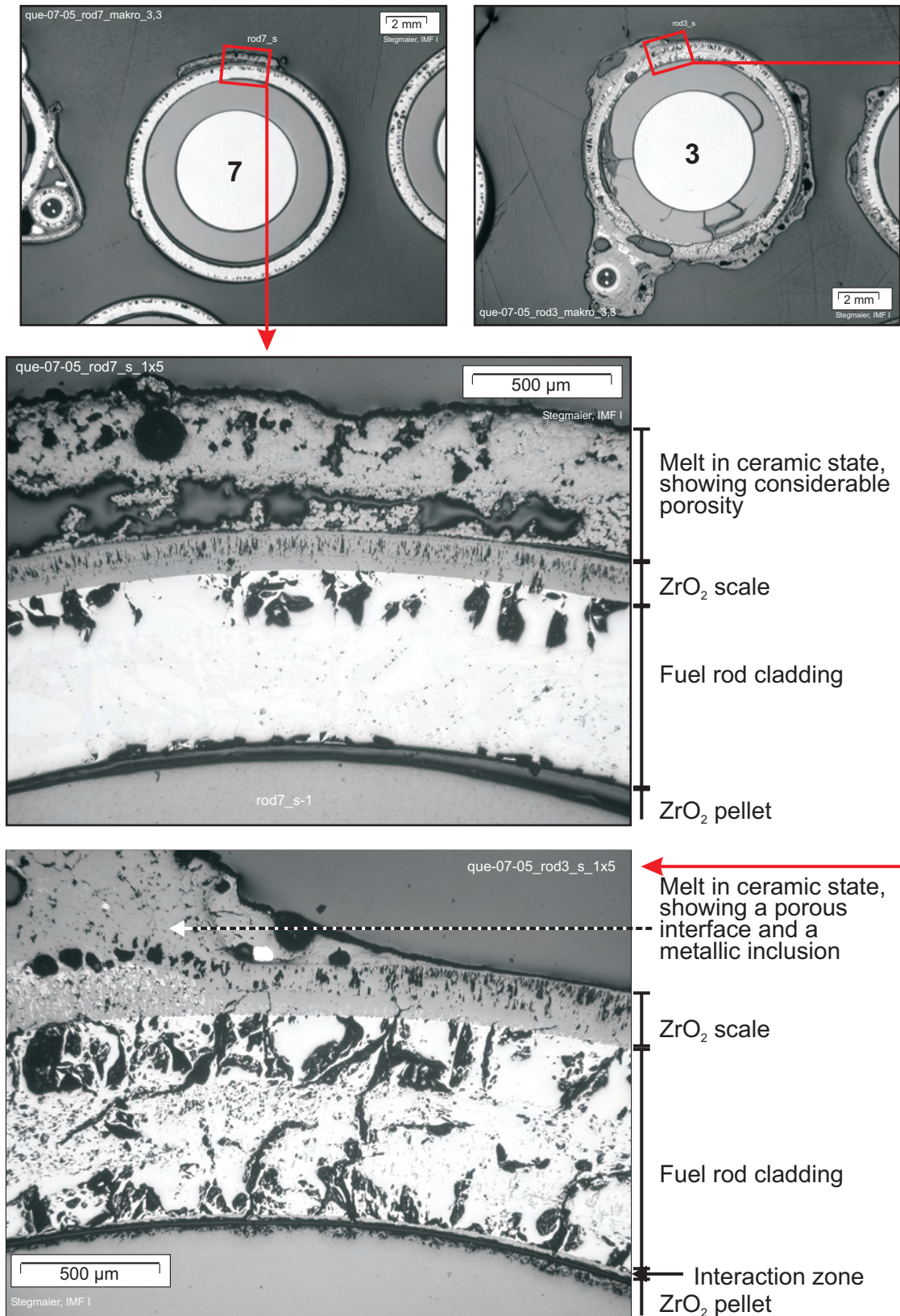
Fig. 51:   QUENCH-07; Cross section at bundle elevation 750 mm (QUE-07-5, top); relocated melt on fuel rods, formed in connection with absorber rod destruction.
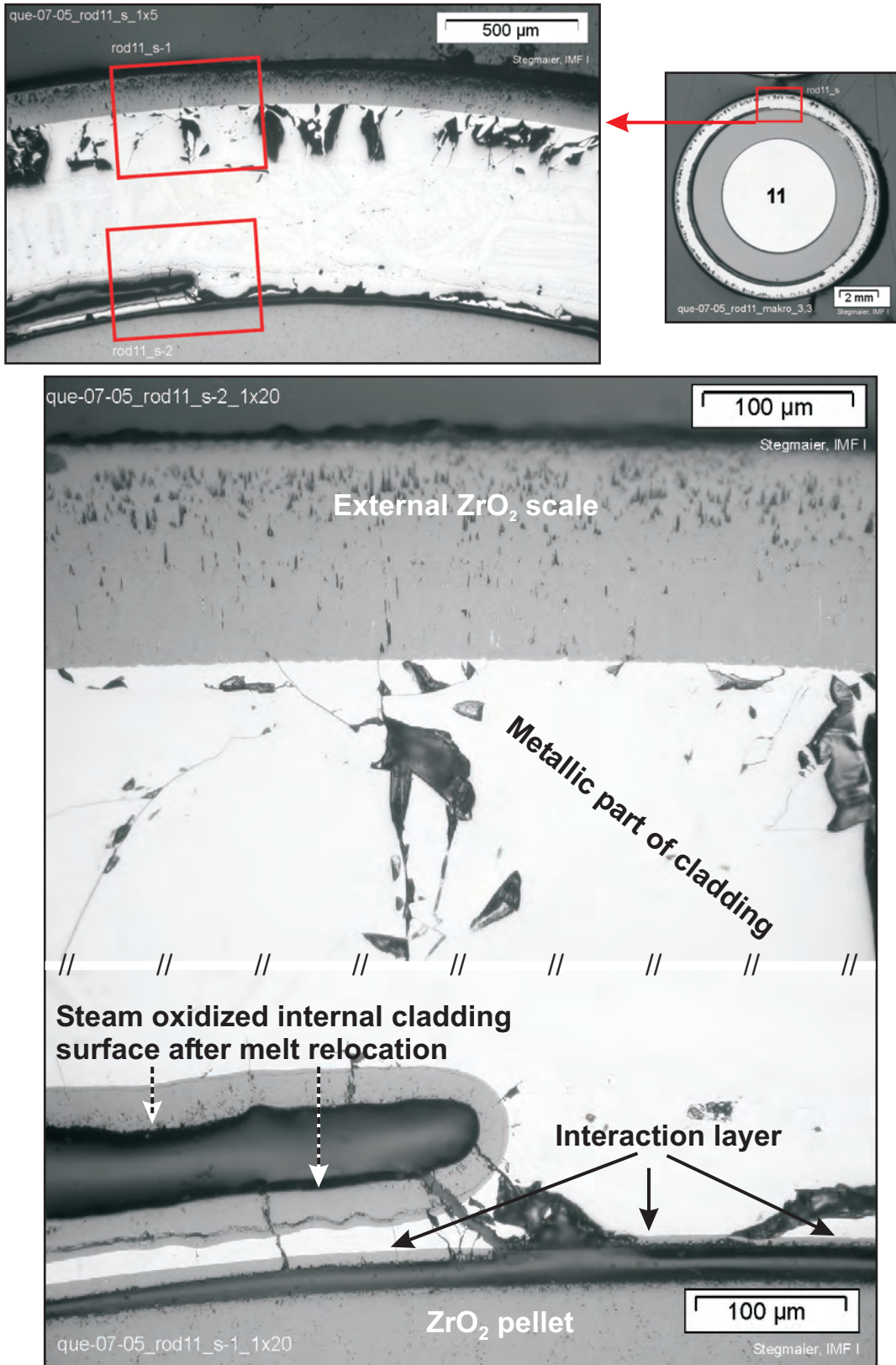
Fig. 52: QUENCH-07; Cross section at bundle elevation 750 mm (QUE-07-5, top); fuel rods oxidation state.

Fuel rod simulator: heater rod , ZrO$_2$ pellet , partially molten cladding , cladding scale

Absorber: B$_4$C pellet , absorber melt , guide tube scale , partially dissolved B$_4$C pellet
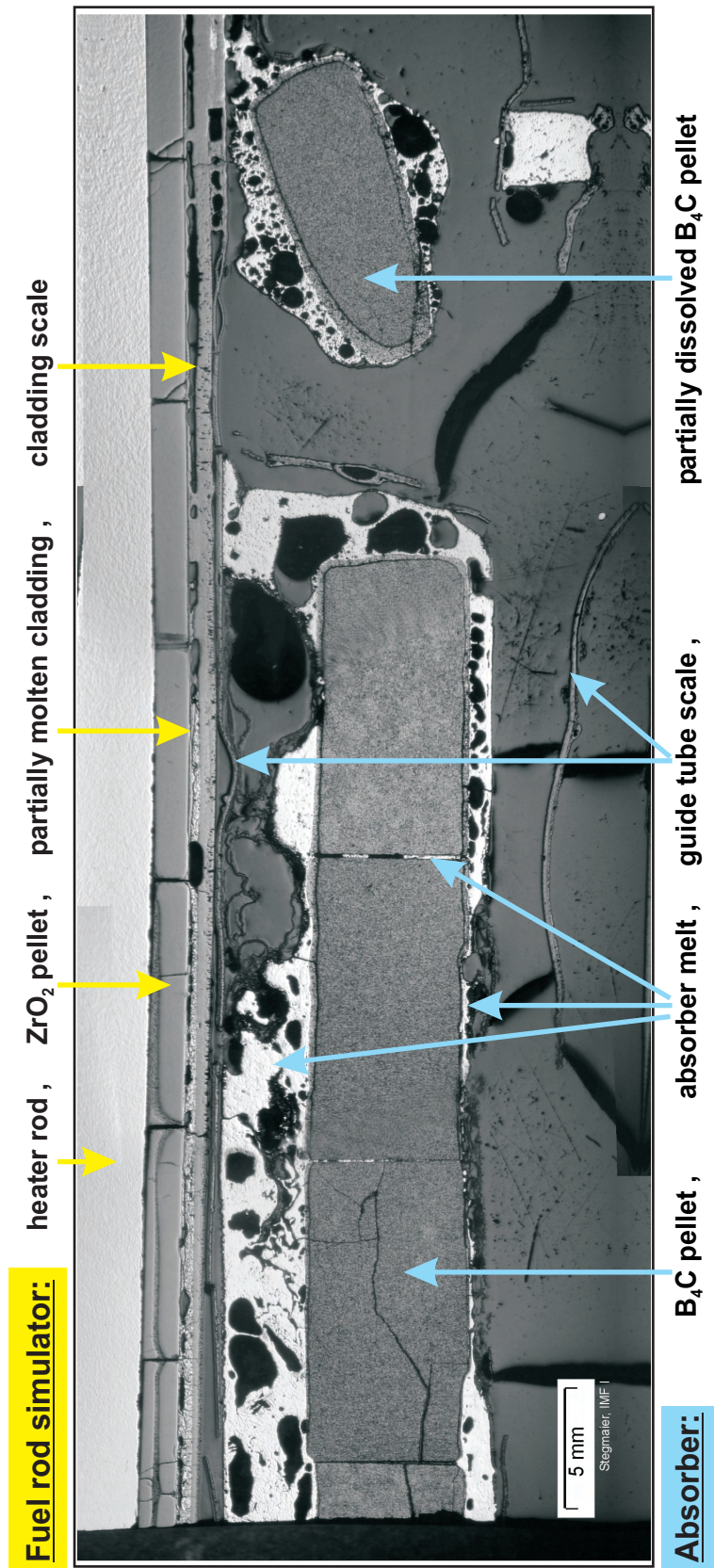
QUE07-05- F750-6.cdr 06/2002   **FZK - IMF** / heck

Fig. 53:   QUENCH-07; Longitudinal section from 760 to ~ 822 mm bundle elevation (left to right); transition zone from intact B$_4$C pellet stack towards absorber rod destruction.
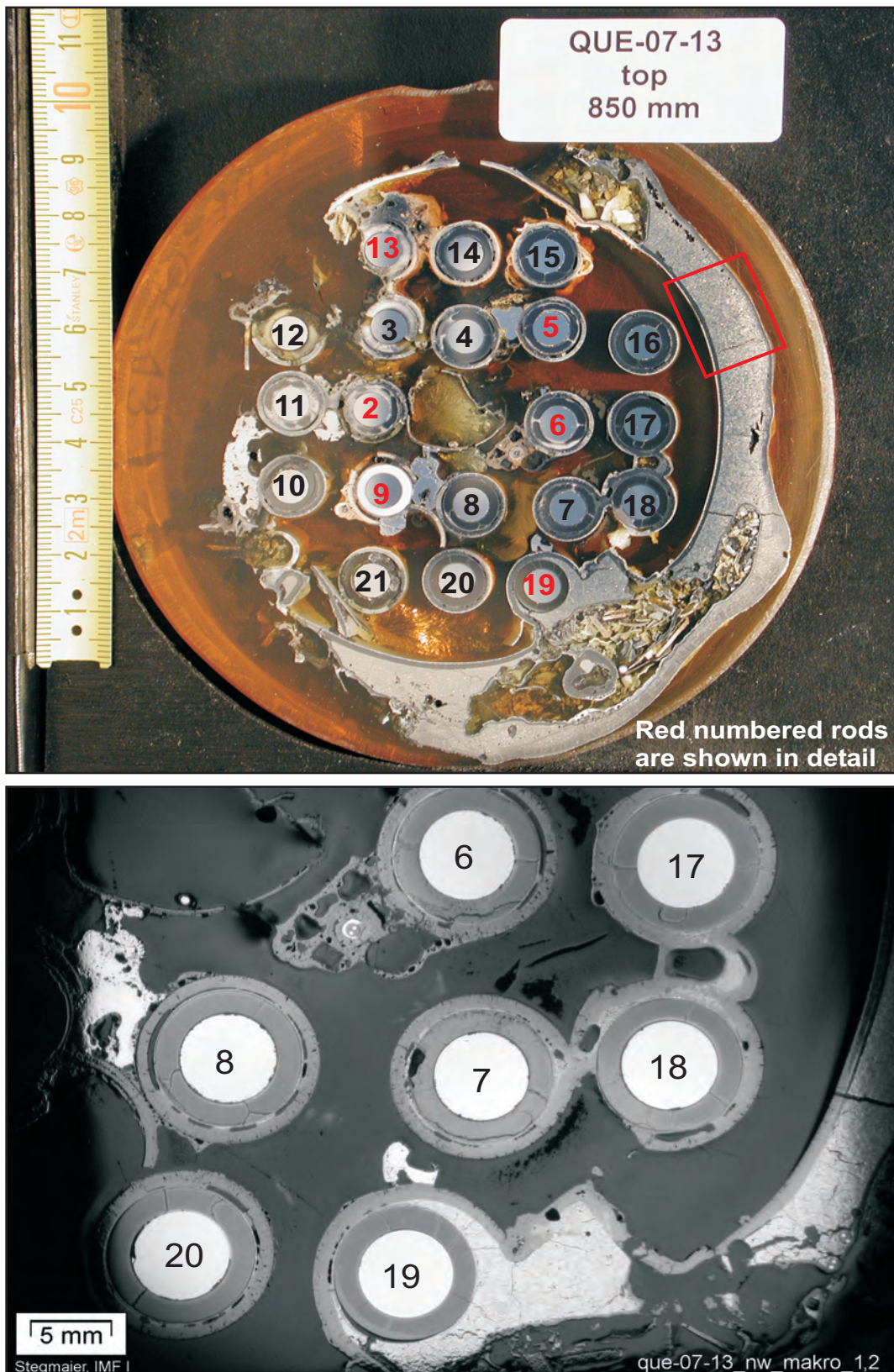
Fig. 54: QUENCH-07; Cross section at bundle elevation 850 mm
(QUE-07-13, top); overview.

Scale at internal surface and adjacent matrix

Scale at external surface and adjacent matrix
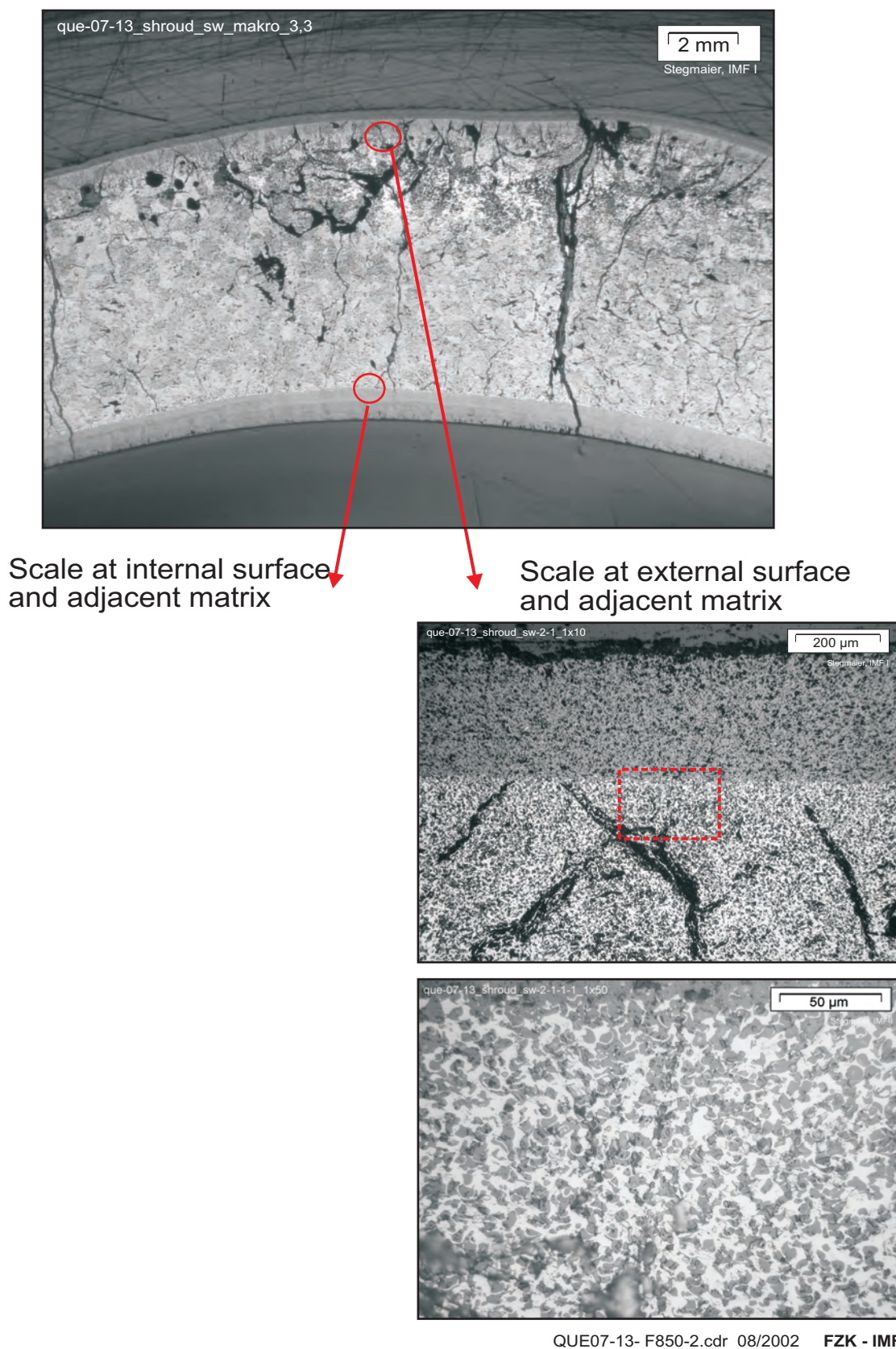
Fig. 55:   QUENCH-07; Cross section at bundle elevation 850 mm
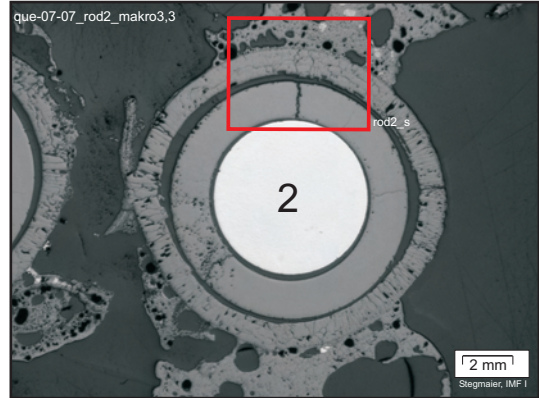(QUE-07-13, top); shroud oxidation state.

Neck formation in contact between rod No.19, corner rod and shroud. The common scale has formed a crucible, which confined the melt pool. Melt microstructure within rod No.19.
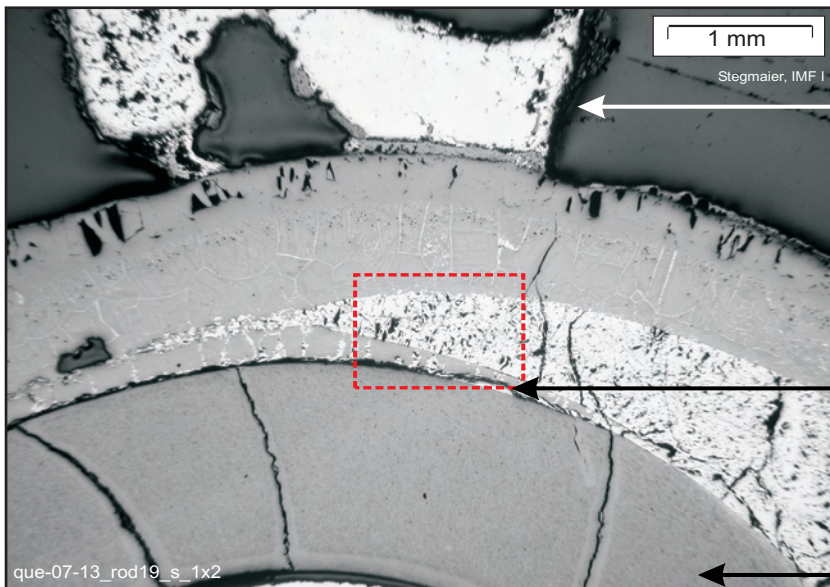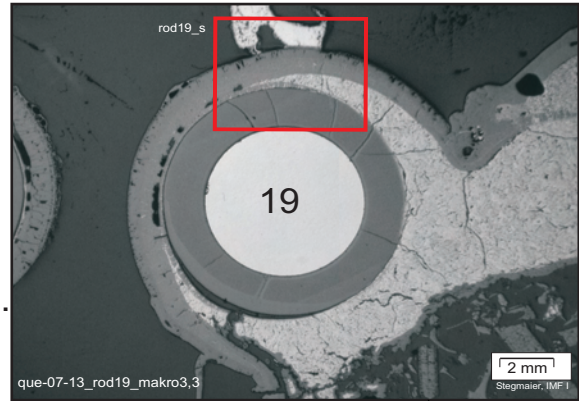
Rubble fragments

External metallic melt, probably with control rod components

Cladding scale

Interaction zone under dissolution by melt

Melt pool of Zr(O) type

Pellet
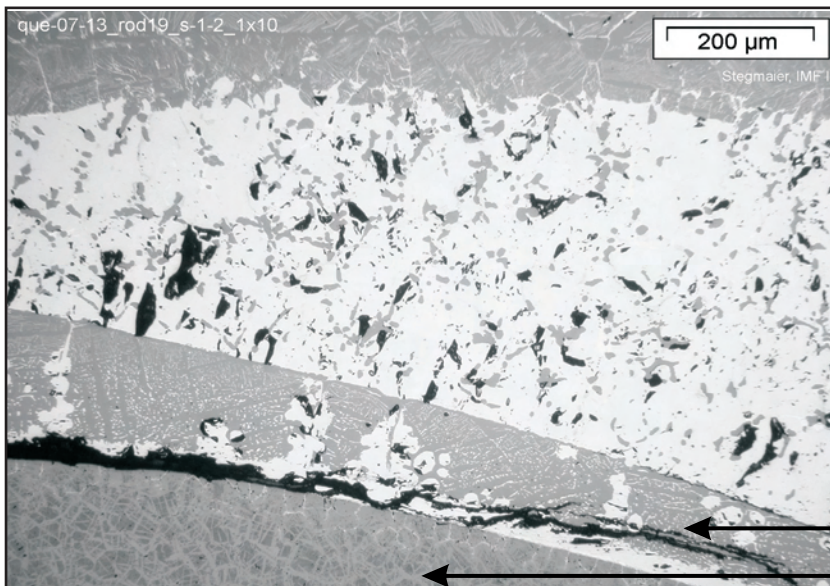
Cladding scale

Melt pool of Zr(O) type, showing precipitates of ZrO_2 phase

Interaction zone

Pellet

QUE07-13- F850-3.cdr 08/2002   **FZK - IMF**

Fig. 56:   QUENCH-07; Cross section at bundle elevation 850 mm (QUE-07-13, top); melt pool, formed by necking mechanism.

Fuel rod simulator in contact with external melt
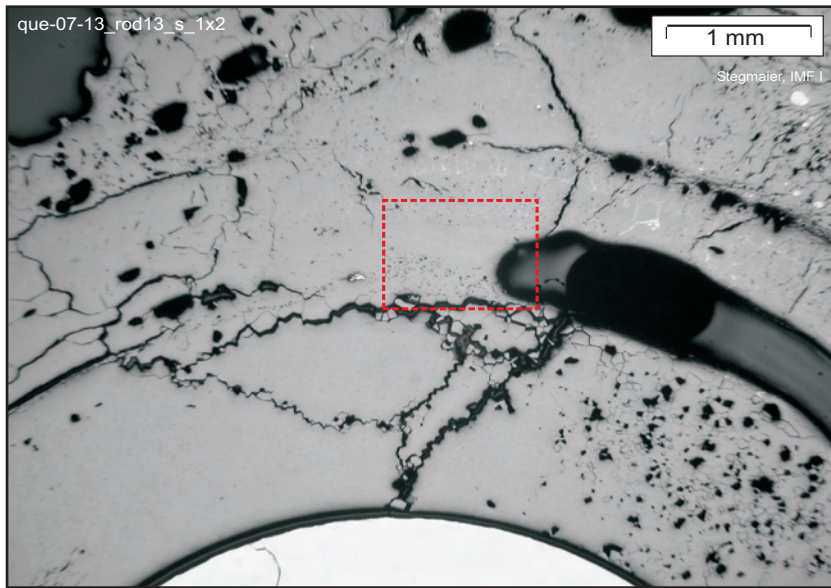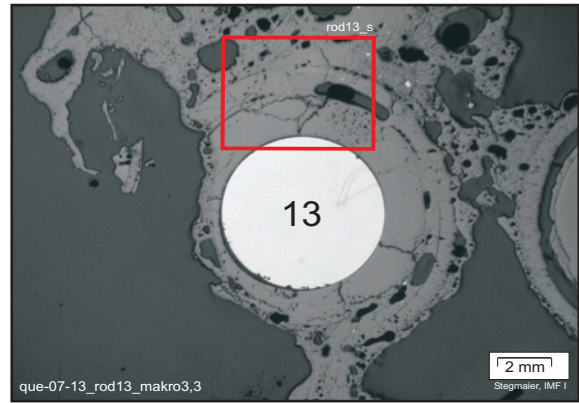
Melt, showing porosity and some residual metallic inclusions

Cladding, fully oxidized

Cavity after cladding melt-out

Pellet
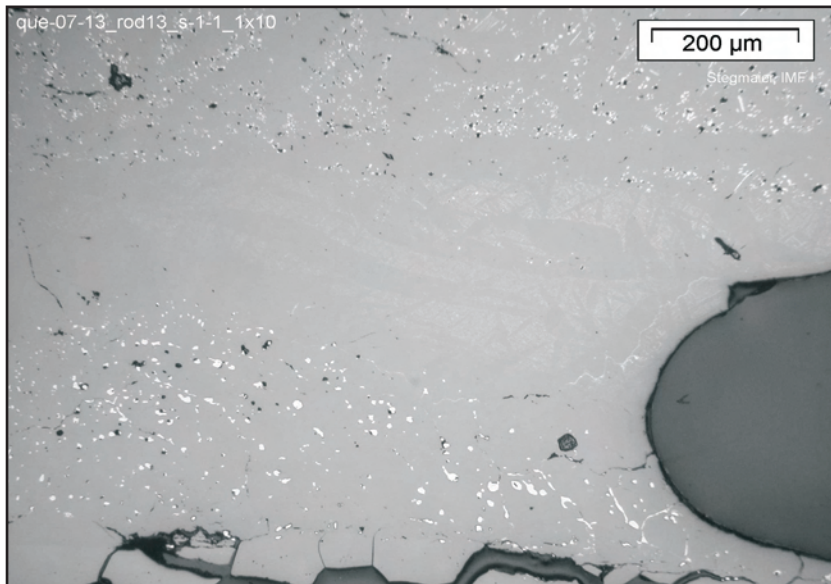
Cladding, showing α-Zr(O) residues in ZrO_2 matrix

Cavity

Pellet

QUE07-13- F850-4.cdr 08/2002   **FZK - IMF**

Fig. 57:   QUENCH-07; Cross section at bundle elevation 850 mm
(QUE-07-13, top); almost fully oxidized bundle components.

Fuel rod simulator in
contact with external melt
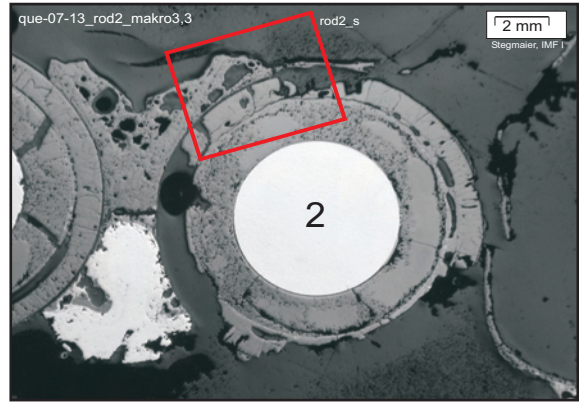
Melt,
showing porosity

Cladding, partially
missing due to
fragmentation

Pellet

Melt

Cladding
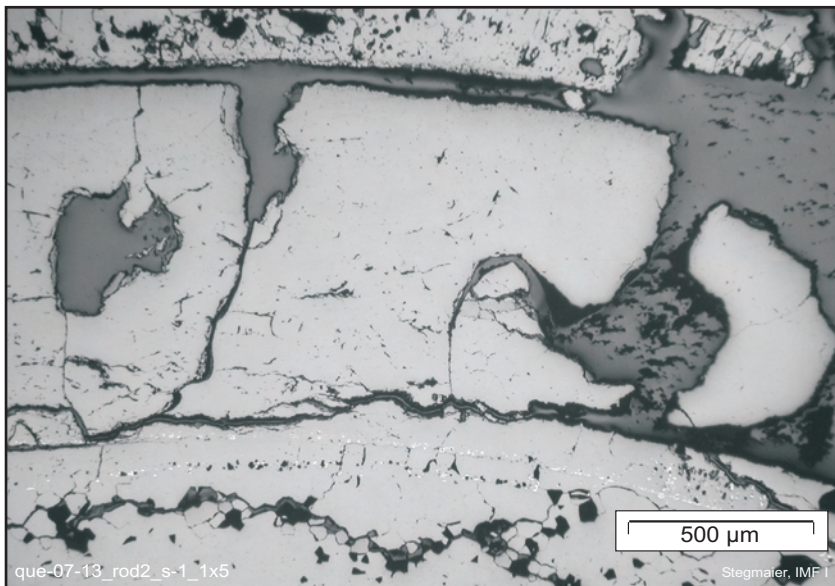
Pellet

QUE07-13- F850-5.cdr 08/2002   **FZK - IMF**

Fig. 58:   QUENCH-07; Cross section at bundle elevation 850 mm
(QUE-07-13, top); fully oxidized bundle components.

Cladding, showing ZrO$_2$ (gray) distribution of α-Zr(O) phase (light), cavity from melt-out (left side, dark) and cracks

Pellet

Cladding, showing ZrO$_2$ (gray), α-Zr(O) phase mainly in interaction zone (light), cavity from melt-out (right side, dark) and cracks

Pellet, showing disintegration into individual grains
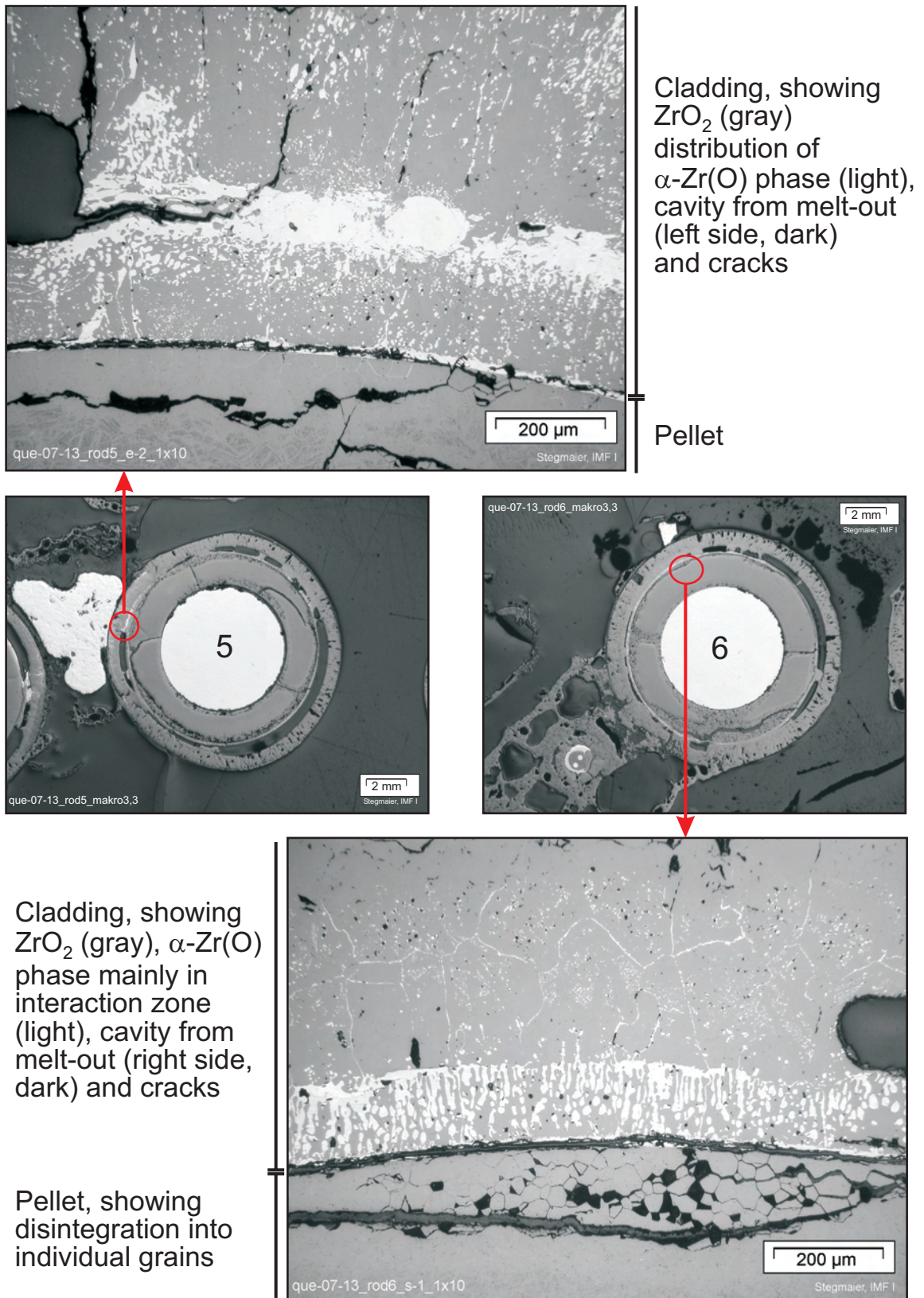
QUE07-13- F850-6.cdr 08/2002   **FZK - IMF**

Fig. 59:   QUENCH-07; Cross section at bundle elevation 850 mm (QUE-07-13, top); internal part of almost oxidized cladding.

Residual fragment of an original melt lump in direct contact with rod No.6

Melt interaction zone, ceramic

Oxidized cladding
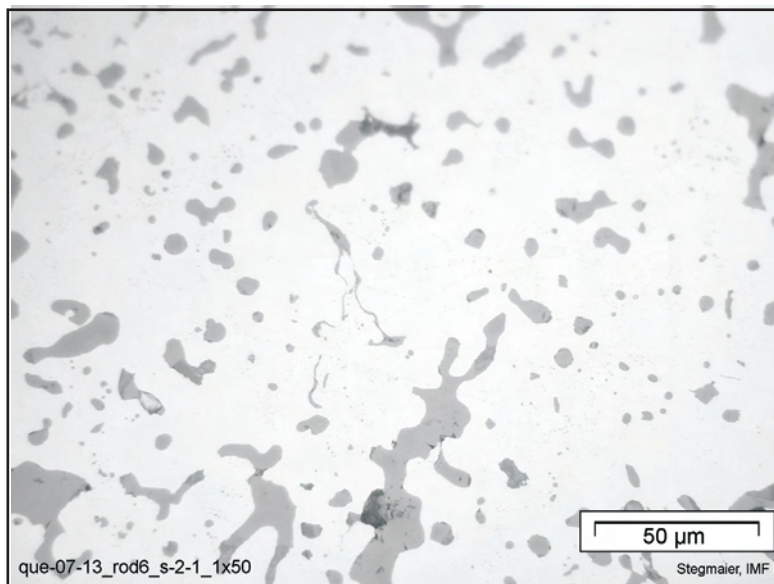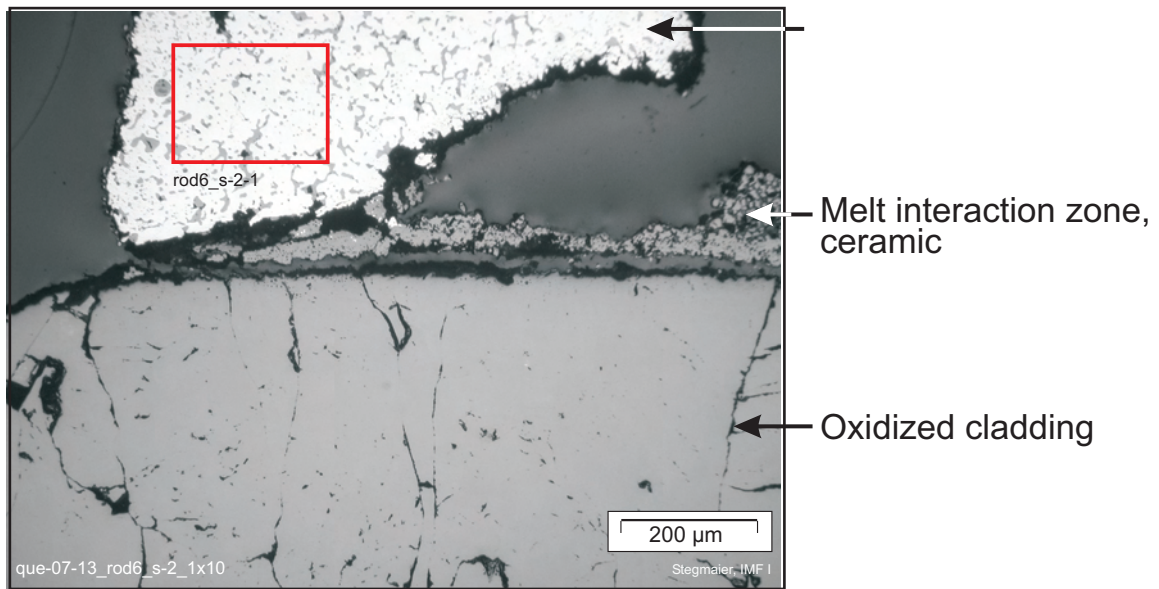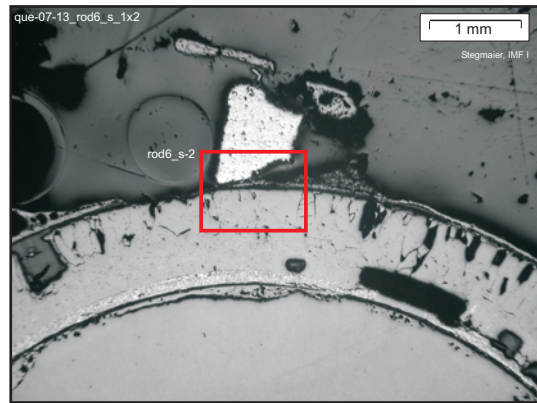
Details of melt microstructure at given position, interpreted as α-Zr(O) with ZrO$_2$ precipitates

QUE07-13- F850-7.cdr 08/2002 **FZK - IMF**

Fig. 60: QUENCH-07; Cross section at bundle elevation 850 mm (QUE-07-13, top); microstructure of a melt lump.

Melt lump, originally in direct contact with rod No.5, finally detached by splitting off
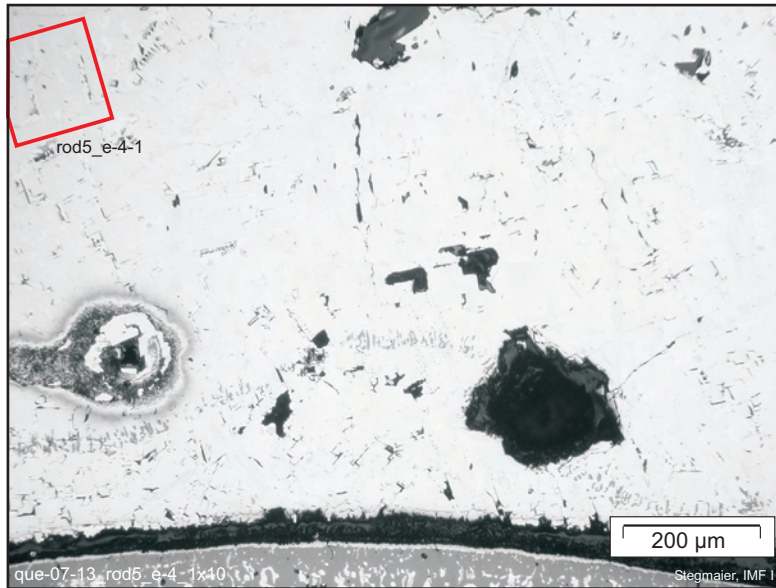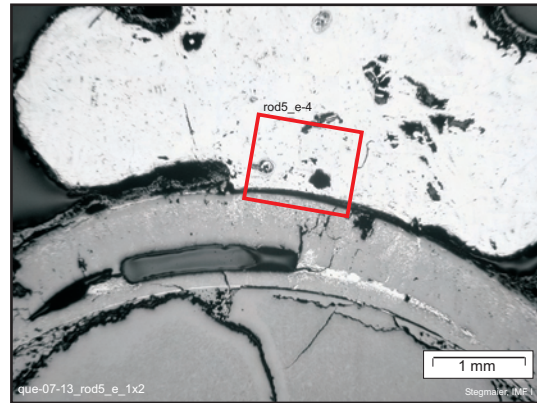
Melt microstructure showing metallic state, local inhomogeneity, multi-phase condition and some porosity. Formation by multi-component interaction is indicated.

Details of melt microstructure at given position

QUE07-13- F850-8.cdr 08/2002   **FZK - IMF**
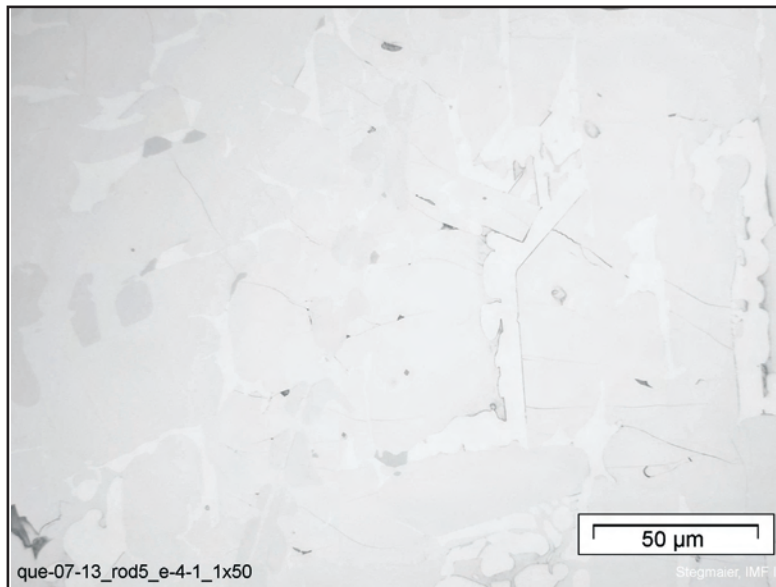
Fig. 61:   QUENCH-07; Cross section at bundle elevation 850 mm (QUE-07-13, top); microstructure of a melt lump.

Two melt droplets in contact with rod No.9, both probably containing control rod components
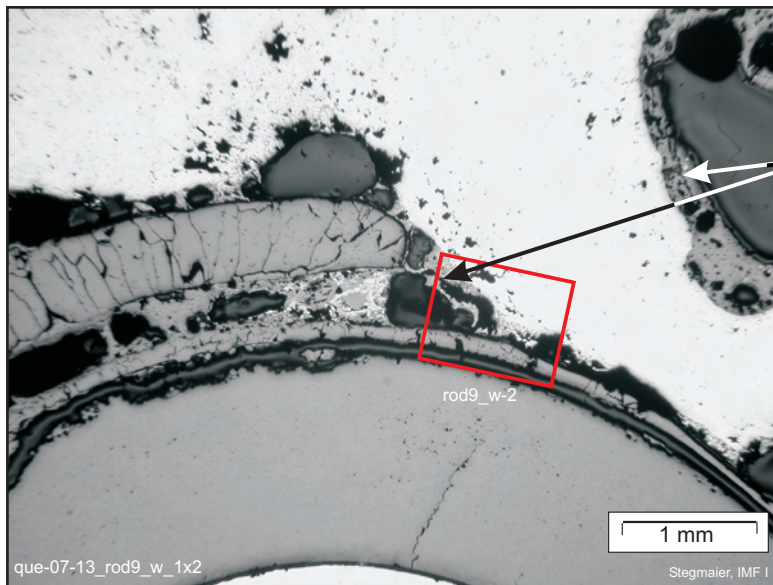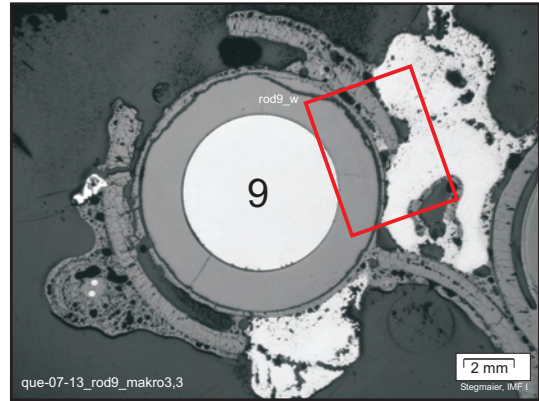
Scale morphology of the melt indicates contamination by control rod components
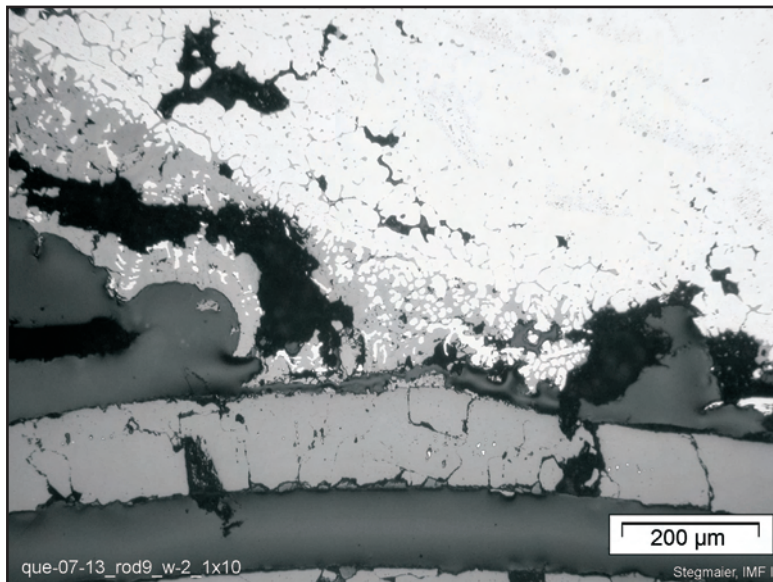
Melt oxidation, resulting in a fragmented scale, which contains metallic residues

ZrO_2, resulting from pellet/cladding inter-action zone

QUE07-13- F850-9.cdr 08/2002   **FZK - IMF**

Fig. 62:   QUENCH-07; Cross section at bundle elevation 850 mm
(QUE-07-13, top); oxidation of multi-component melt.
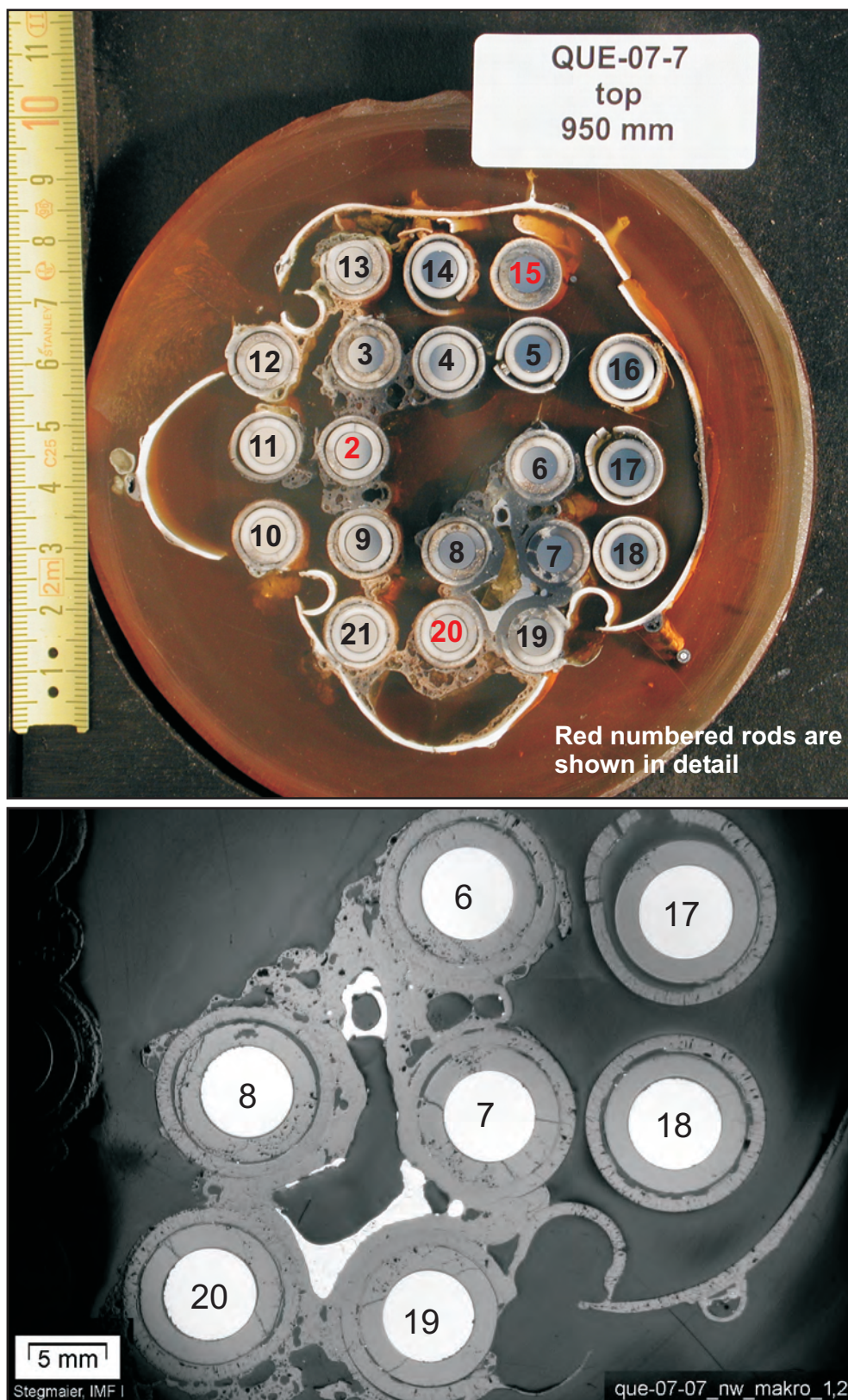
Fig. 63: QUENCH-07; Cross section at bundle elevation 950 mm (QUE-07-7, top); overview.

Metallic melt between rods No.19 and 20, enclosed by necking mechanism and thus isolated from steam
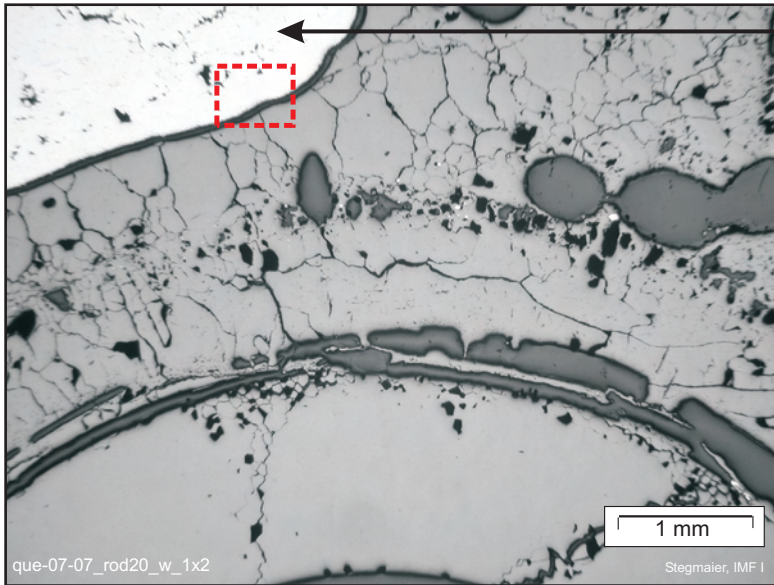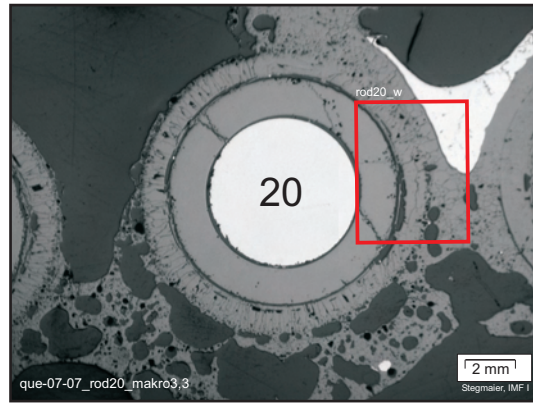
Melt pool

Double layer of scales from melt and cladding oxidation (boundary indicated by porosity)

Melt

Gap

Scale
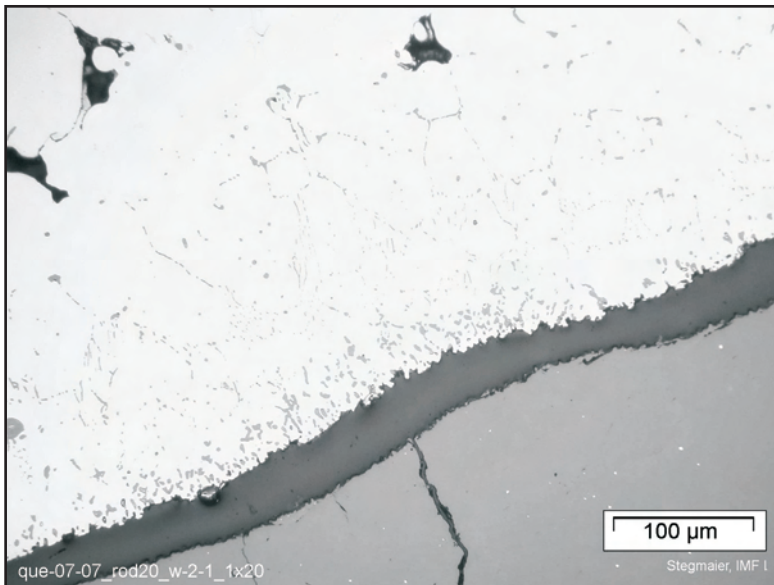
QUE07-7- F950-2.cdr 08/2002   **FZK - IMF**

Fig. 64:   QUENCH-07; Cross section at bundle elevation 950 mm (QUE-07-7, top); pool of metallic melt.

Fuel rod No.15, showing
a thin cover of melt,
interpreted as result
of a candling process

Melt top layer

Cladding

Pellet

Porous (foamed)
melt structure,
ceramic state

Cladding, fully
converted to
ceramic state
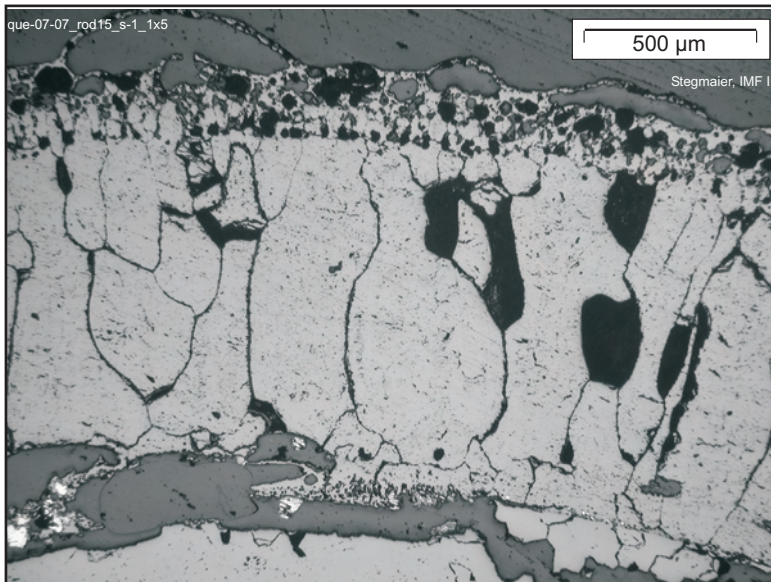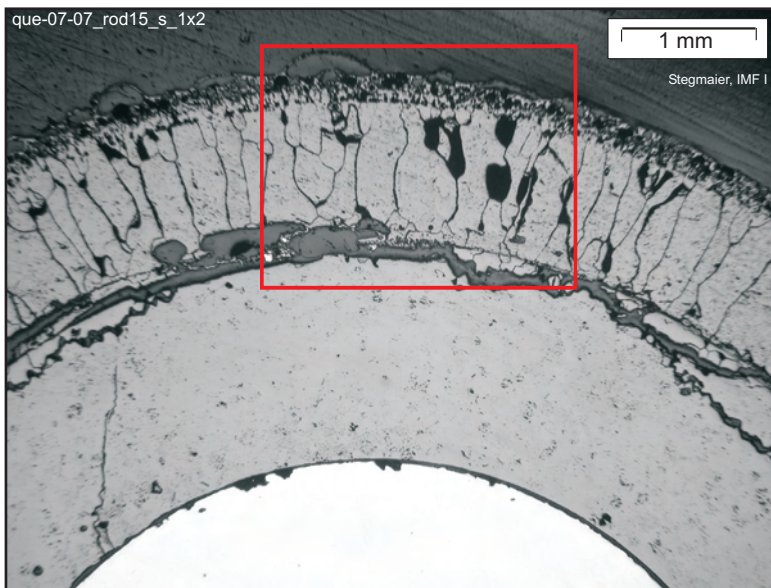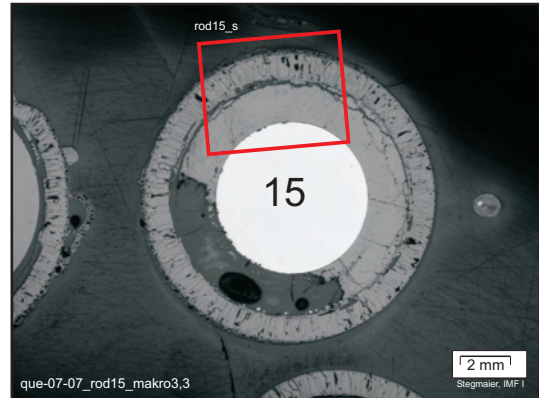
QUE07-7- F950-3.cdr 08/2002   **FZK - IMF**

Fig. 65:   QUENCH-07; Cross section at bundle elevation 950 mm (QUE-07-7,
top); thin melt cover on fuel rod.

Melt, accumulated between fuel rods No.2 and 3, showing tight contact, irregular form and much porosity

Melt

Fuel rod cladding, fully ceramic

Pellet

Droplet of more oxidation resistent composition compared to the fully ceramic melt matrix

Pore

Pellet

QUE07-7- F950-4.cdr 08/2002   **FZK - IMF**
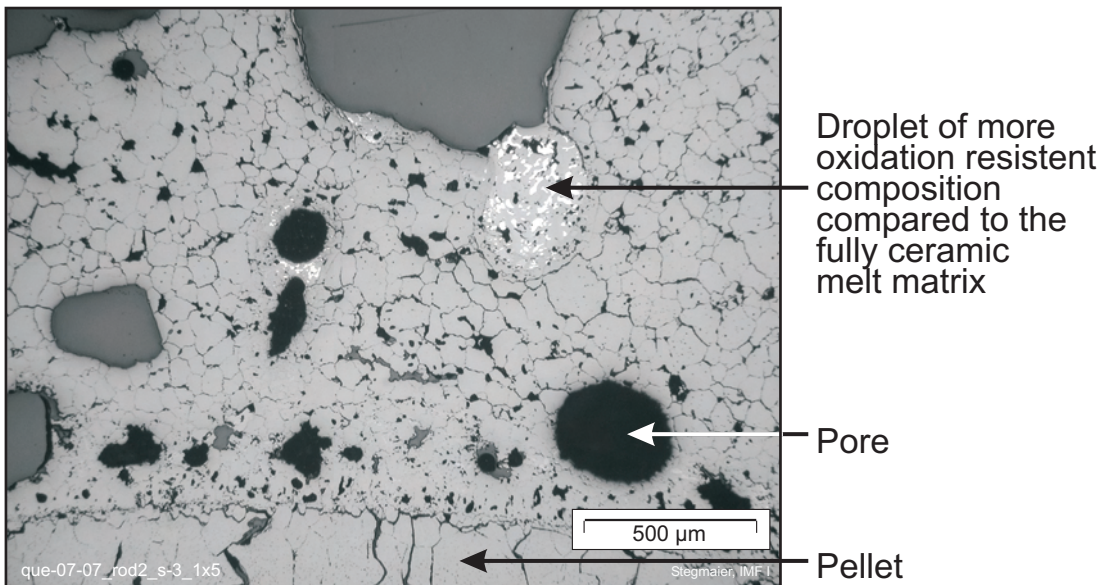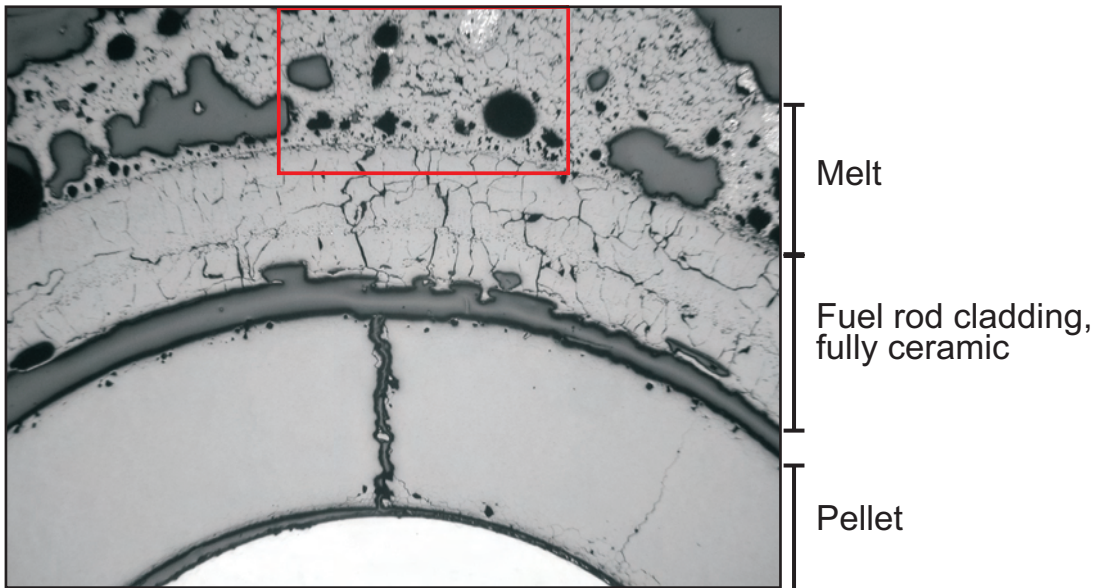
Fig. 66:   QUENCH-07; Cross section at bundle elevation 950 mm (QUE-07-7, top); melt accumulation between fuel rods.
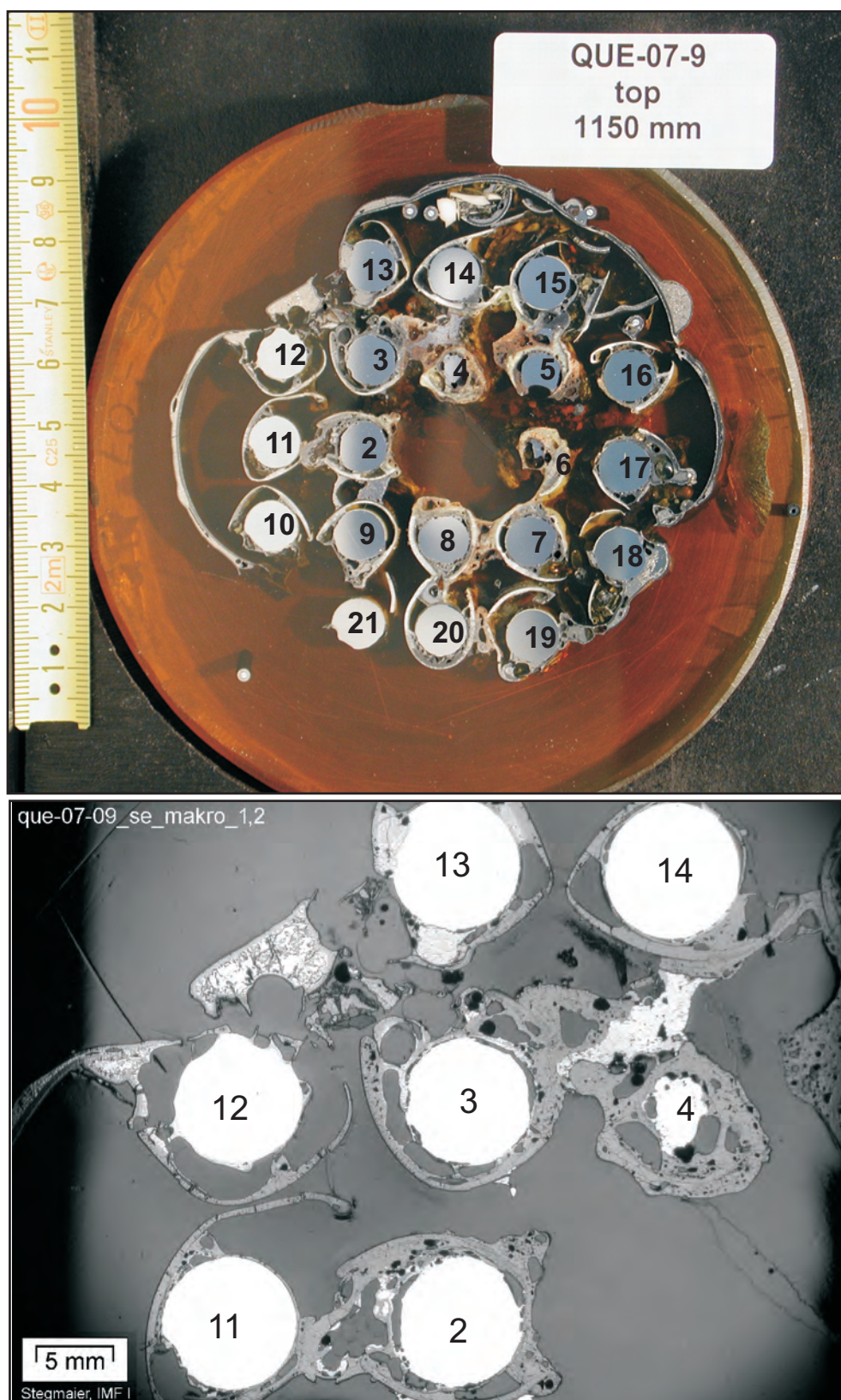
Fig. 67: QUENCH-07; Cross section at bundle elevation 1150 mm (QUE-07-9, top); overview at upper electrode zone.
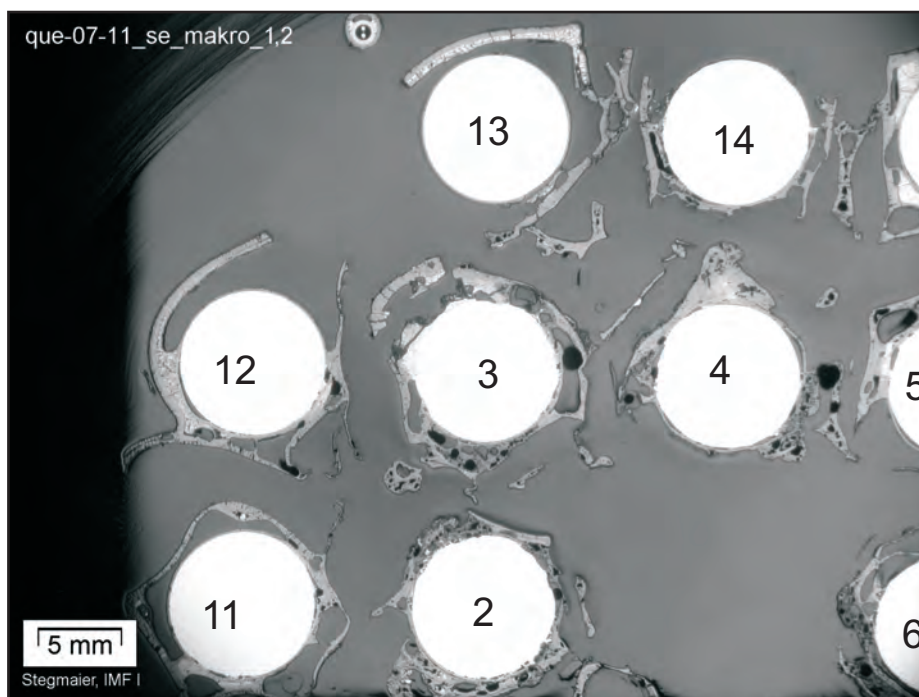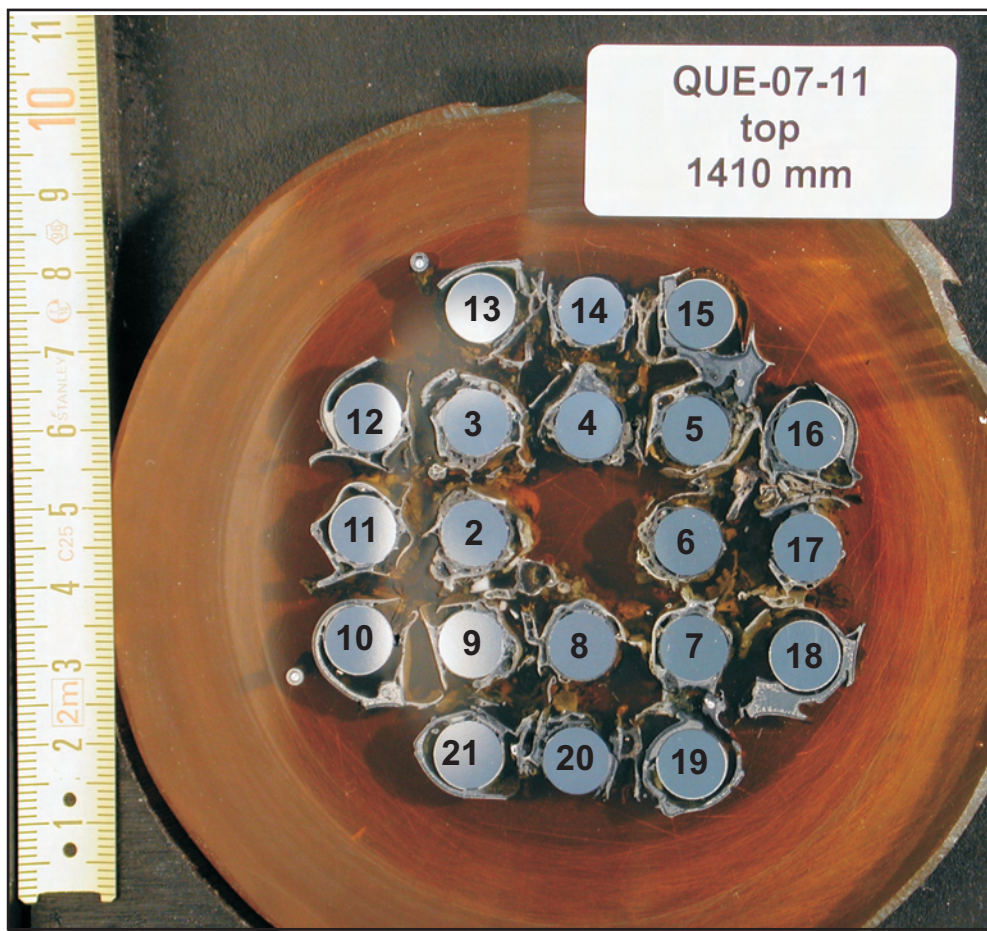
Fig. 68: QUENCH-07; Cross section at bundle elevation 1410 mm (QUE-07-11, top); overview at upper electrode zone.
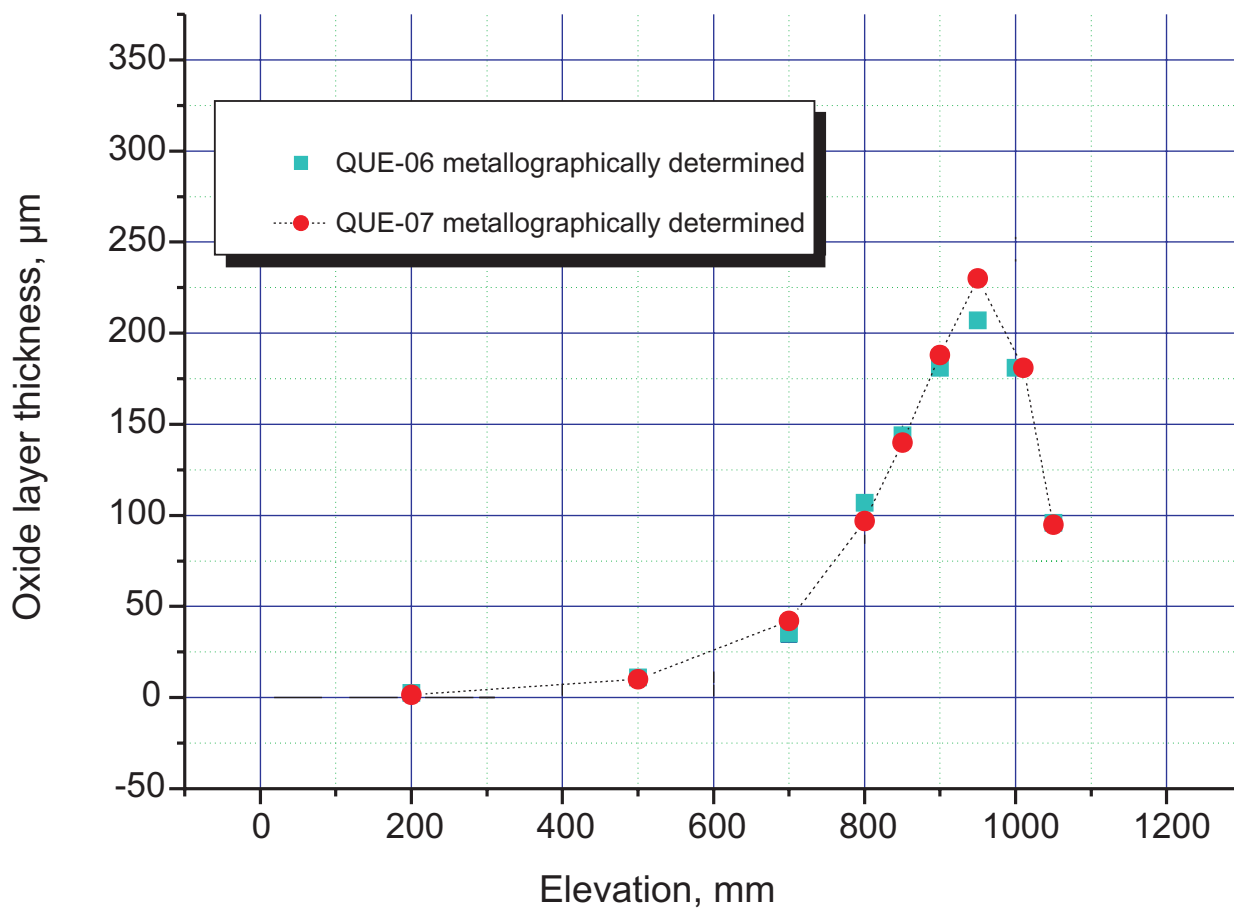
Fig.69-QUE07-rod B oxide.cdr
13.11.02 - IMF

Fig. 69:   QUENCH-07; Oxide layer thickness profile of corner rod B
(withdrawn from the bundle before the transient) compared to
the QUENCH-06 results.
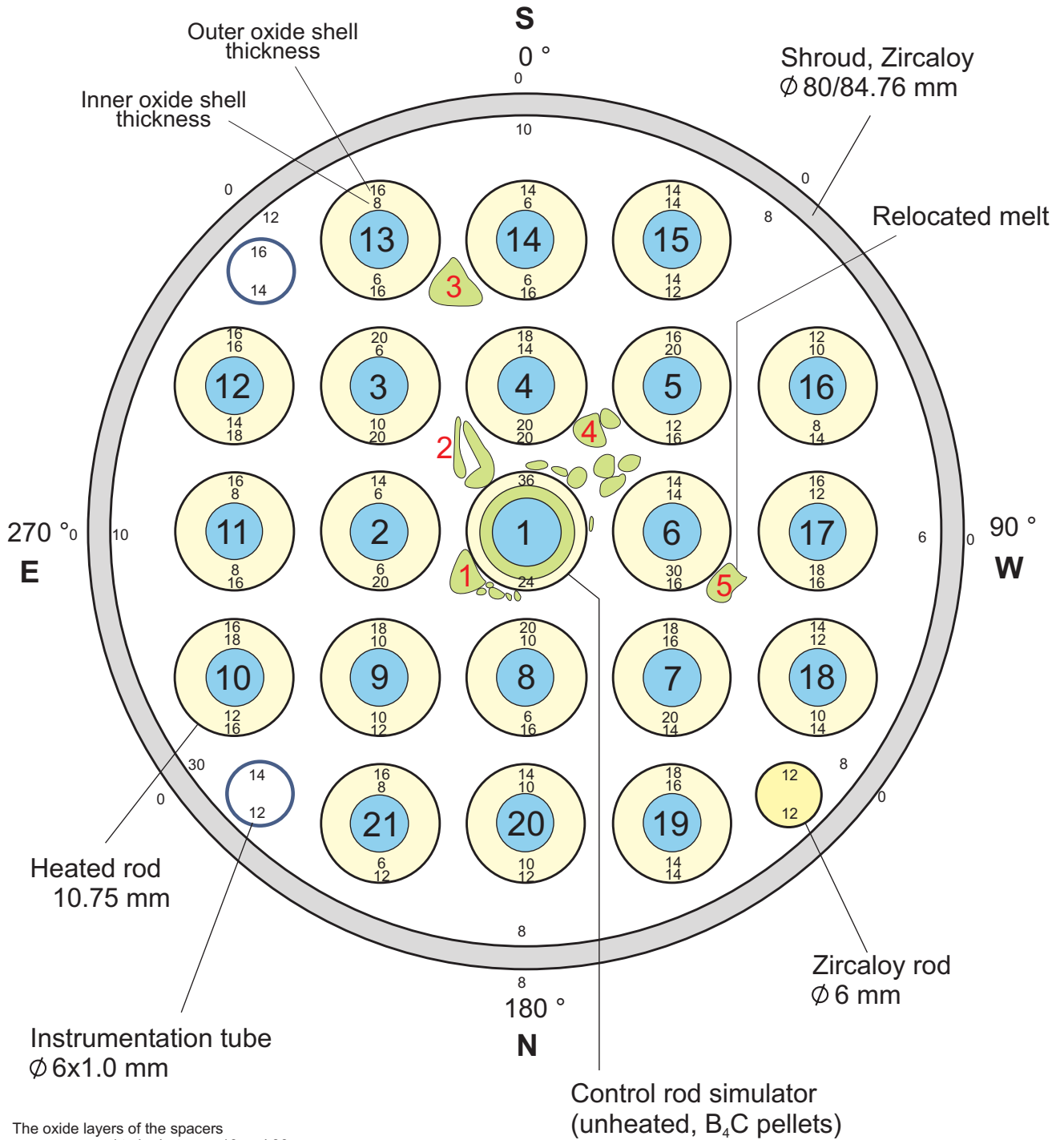
Fig. 70: QUENCH-07; Oxide layer thicknesses at bundle elevation 550 mm (Cross section QUE-07-03)

Fig. 71-QUE07-Cross section QUE-07-12.cdr
16.03.04- IMF

Fig. 71:   QUENCH-07; Oxide layer thicknesses at bundle elevation 650 mm
(Cross section QUE-07-12)
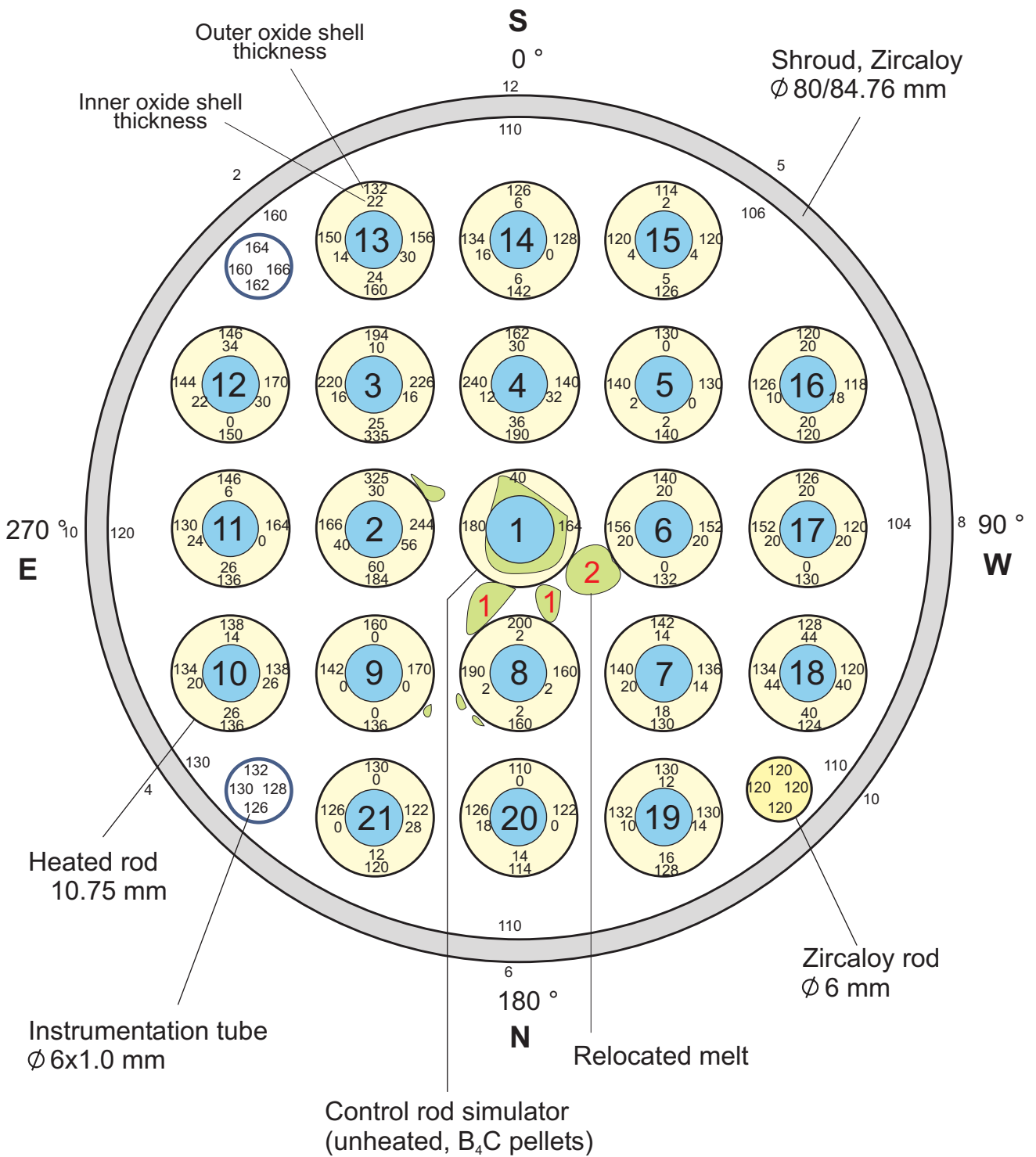
Fig. 72-QUE07-cross section QUE-07-05.cdr
11.03.04 - IMF

Fig. 72:   QUENCH-07; Oxide layer thicknesses at bundle elevation 750 mm
          (Cross section QUE-07-05)
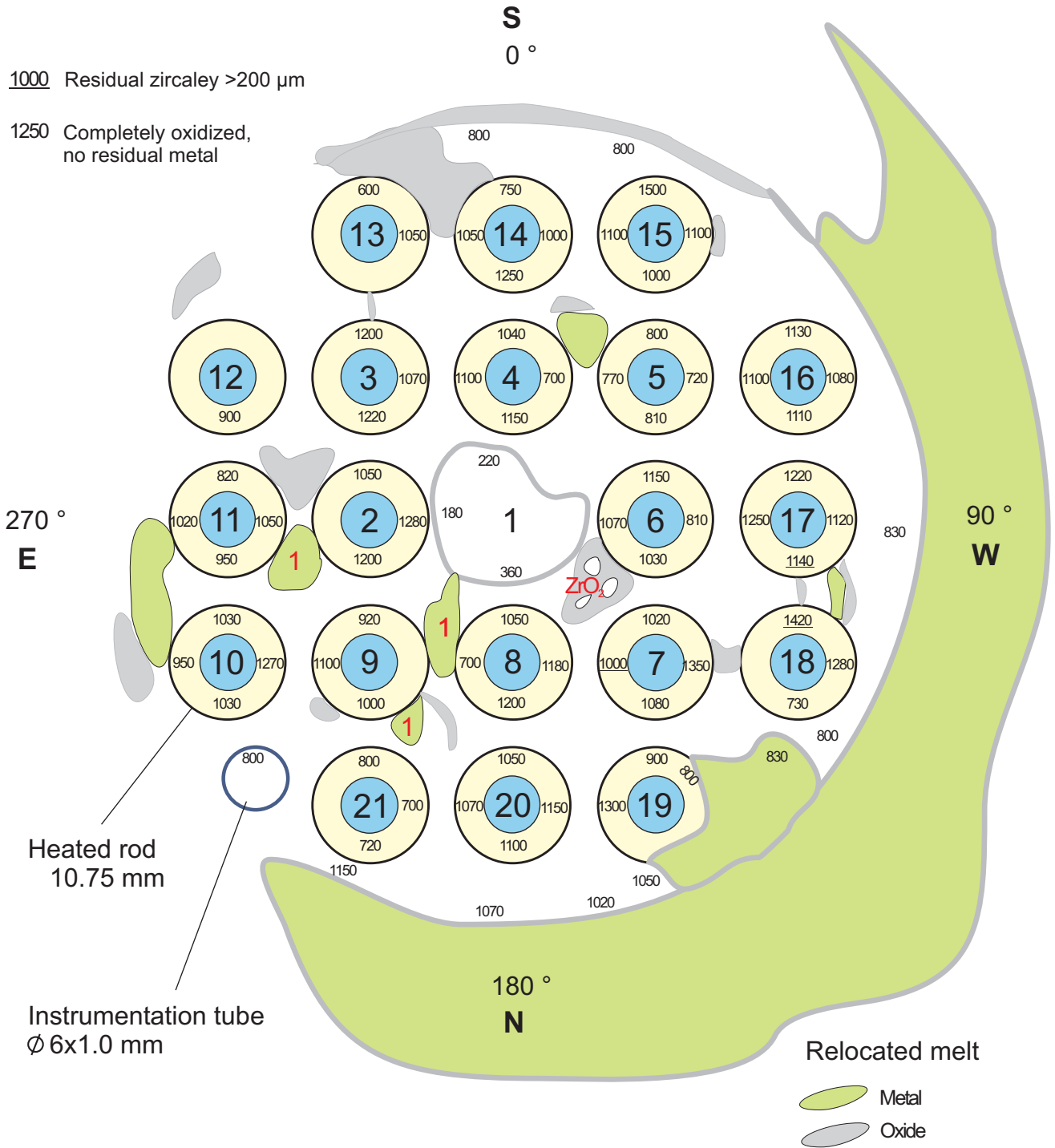
Fig. 73: QUENCH-07; Oxide layer thicknesses at bundle elevation 850 mm
(Cross section QUE-07-13)

Fig. 74: QUENCH-07; Oxide layer thicknesses at bundle elevation 950 mm
(Cross section QUE-07-07)
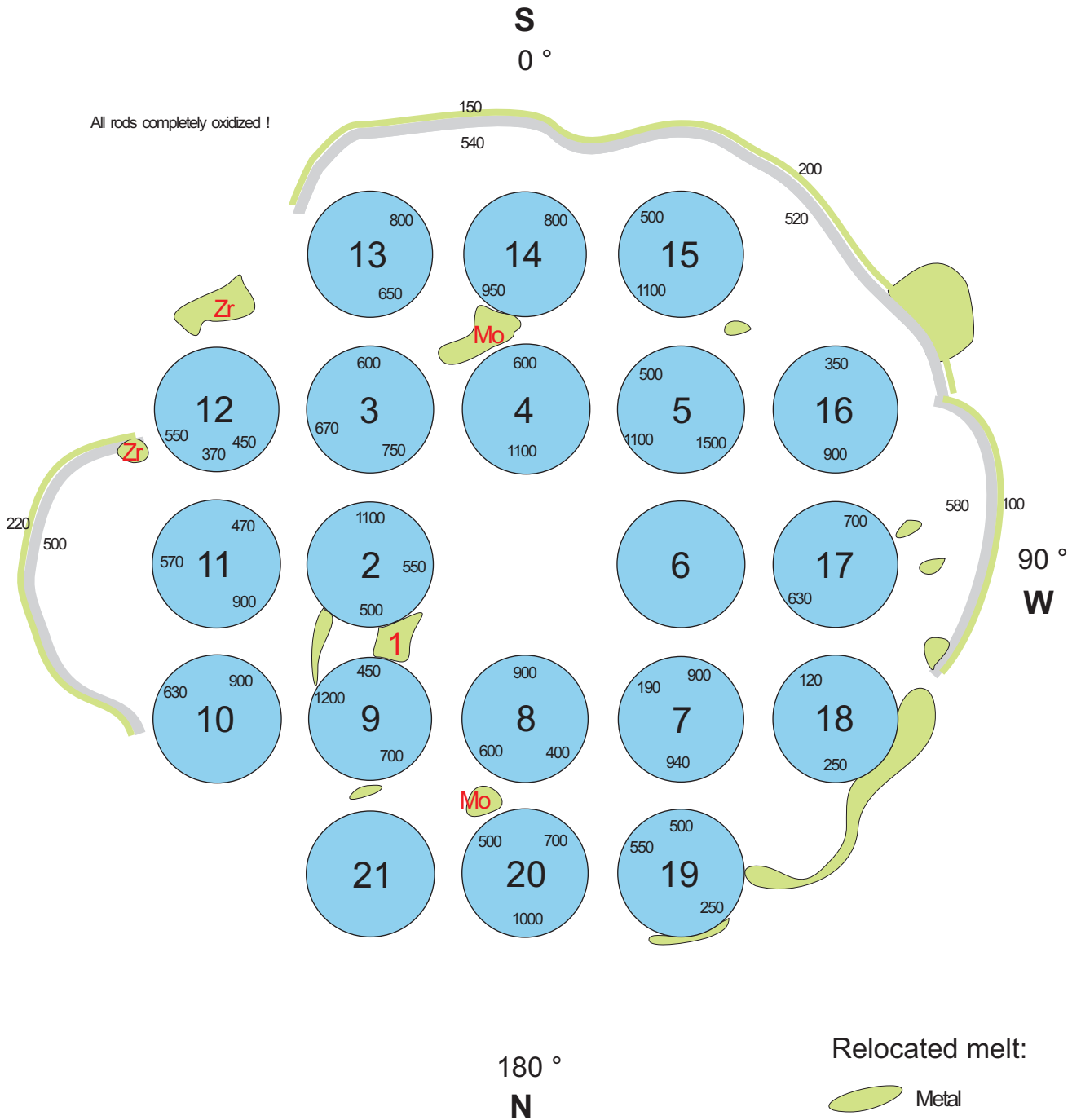
Fig. 75: QUENCH-07; Oxide layer thicknesses at bundle elevation 1150 mm (Cross section QUE-07-09)

S

0 °

All rods completely oxidized !

270 °

E

90 °

W

180 °

N

Relocated melt:

Metal
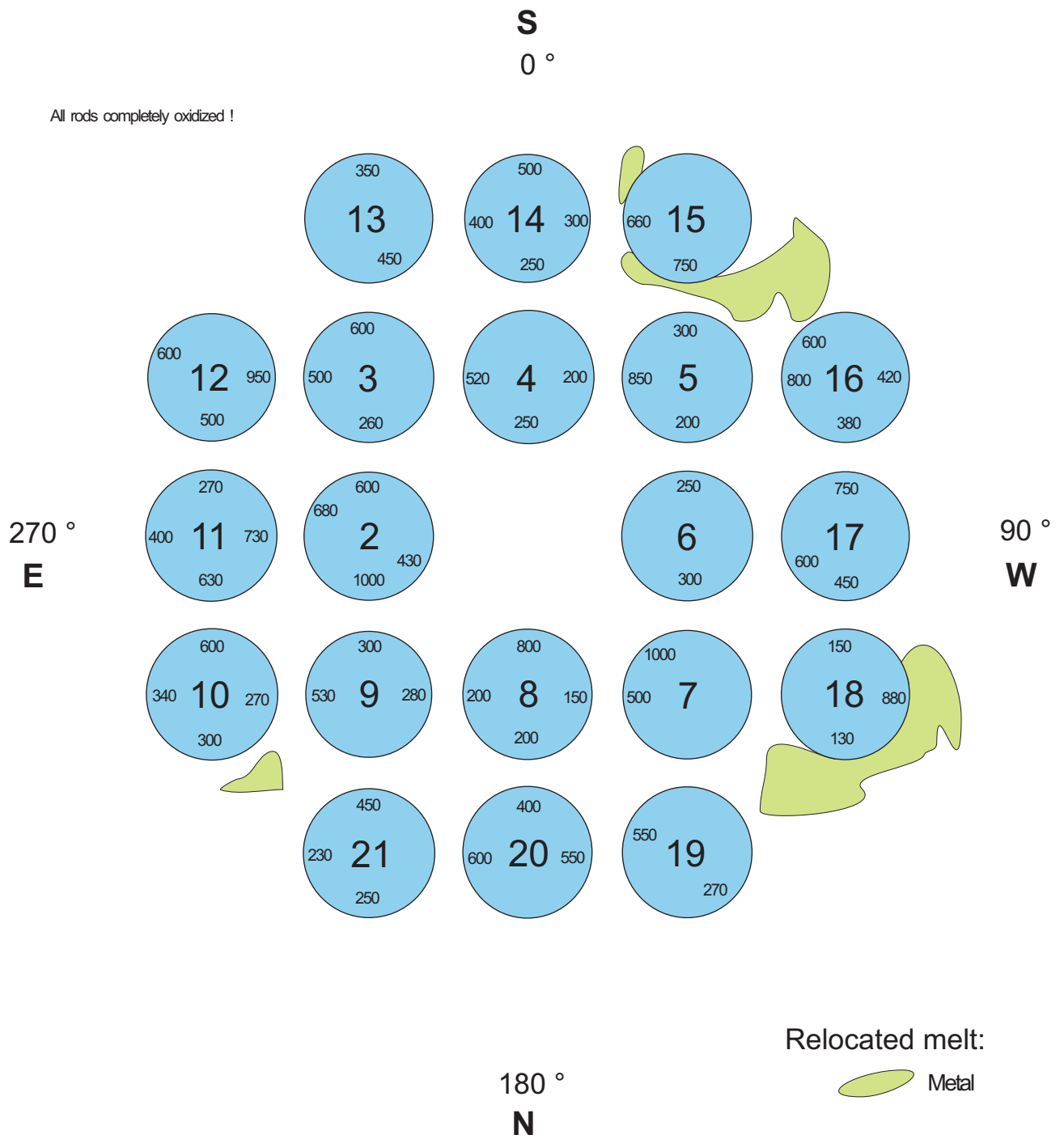
Fig.76-QUE07-Cross section QUE-07-11.cdr
18.02.04 - IMF

Fig. 76:   QUENCH-07; Oxide layer thicknesses at bundle elevation 1410 mm
(Cross section QUE-07-11)
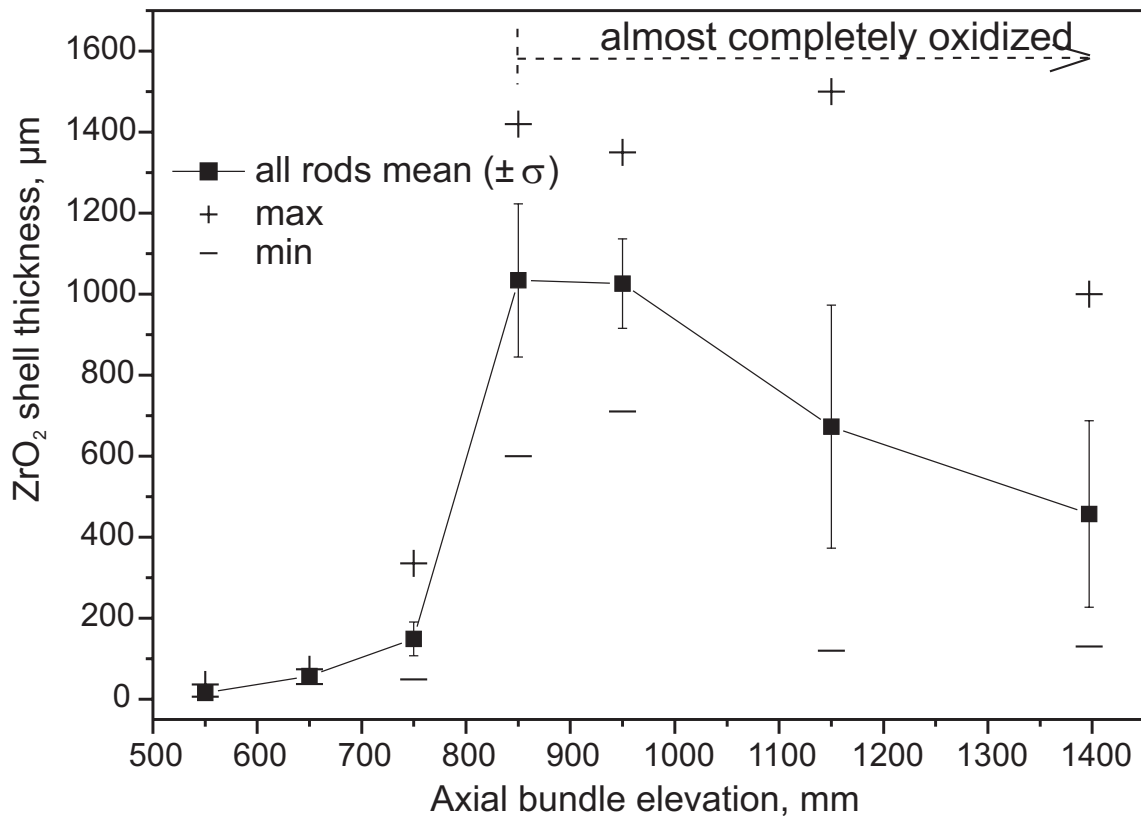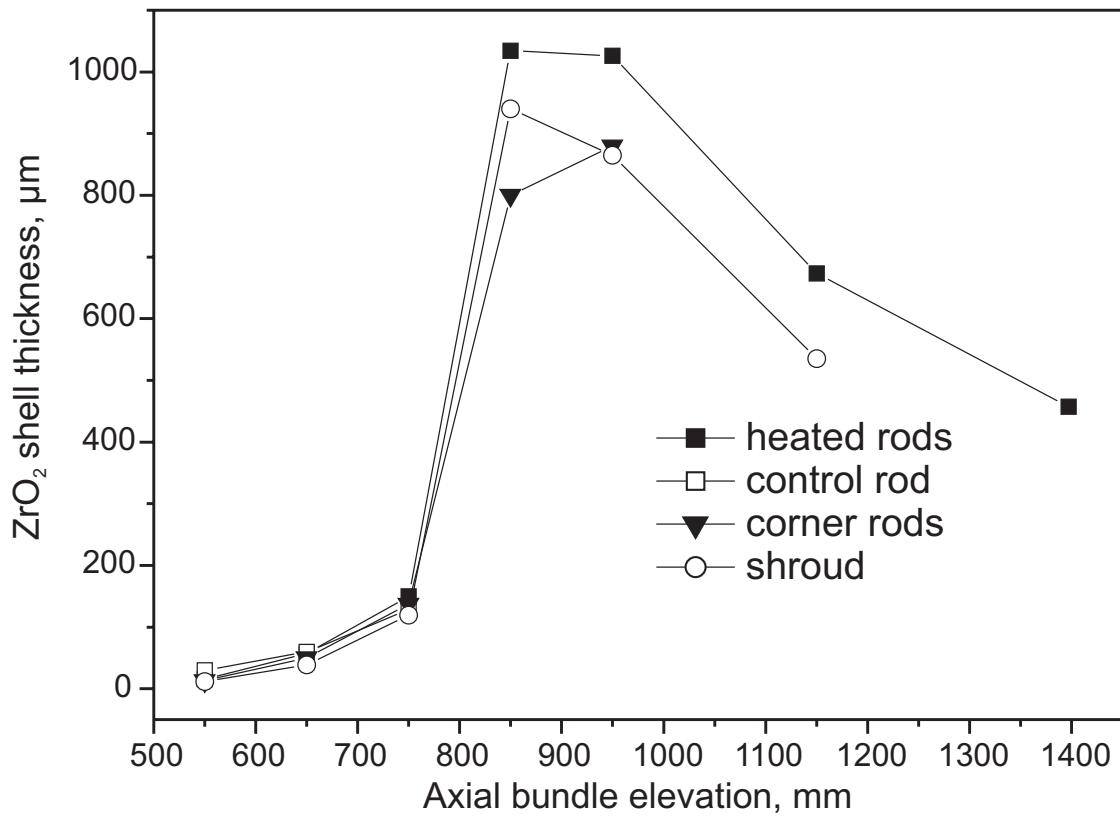
Fig. 77: QUENCH-07; Axial oxide layer thickness distribution
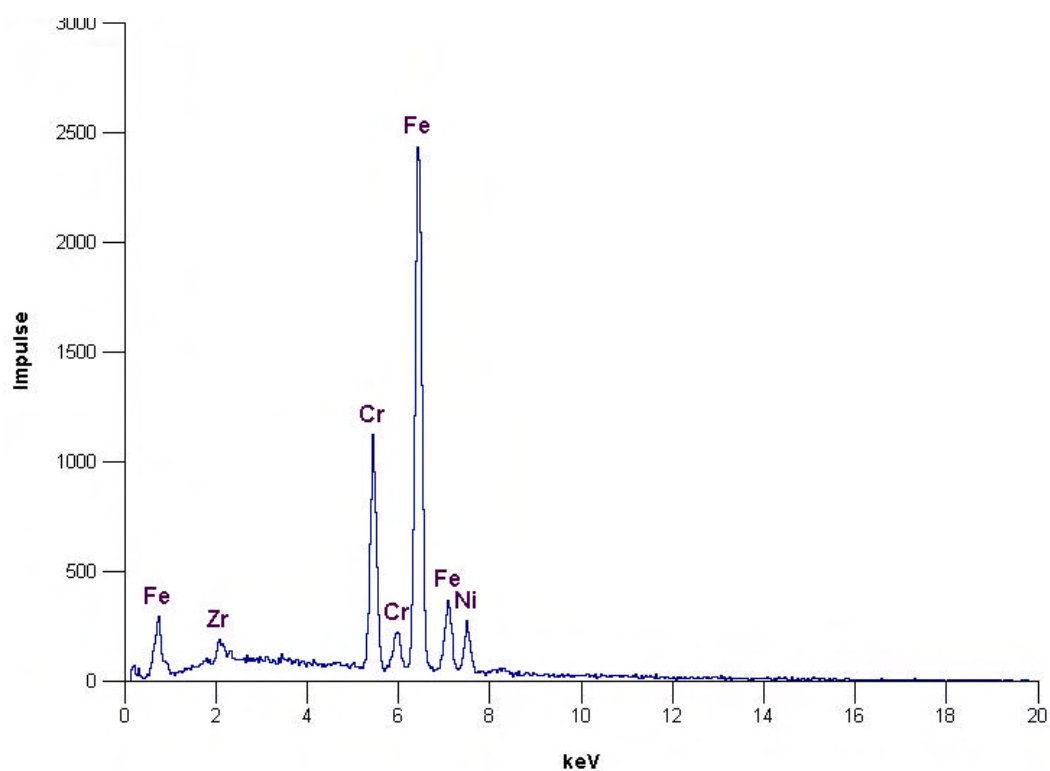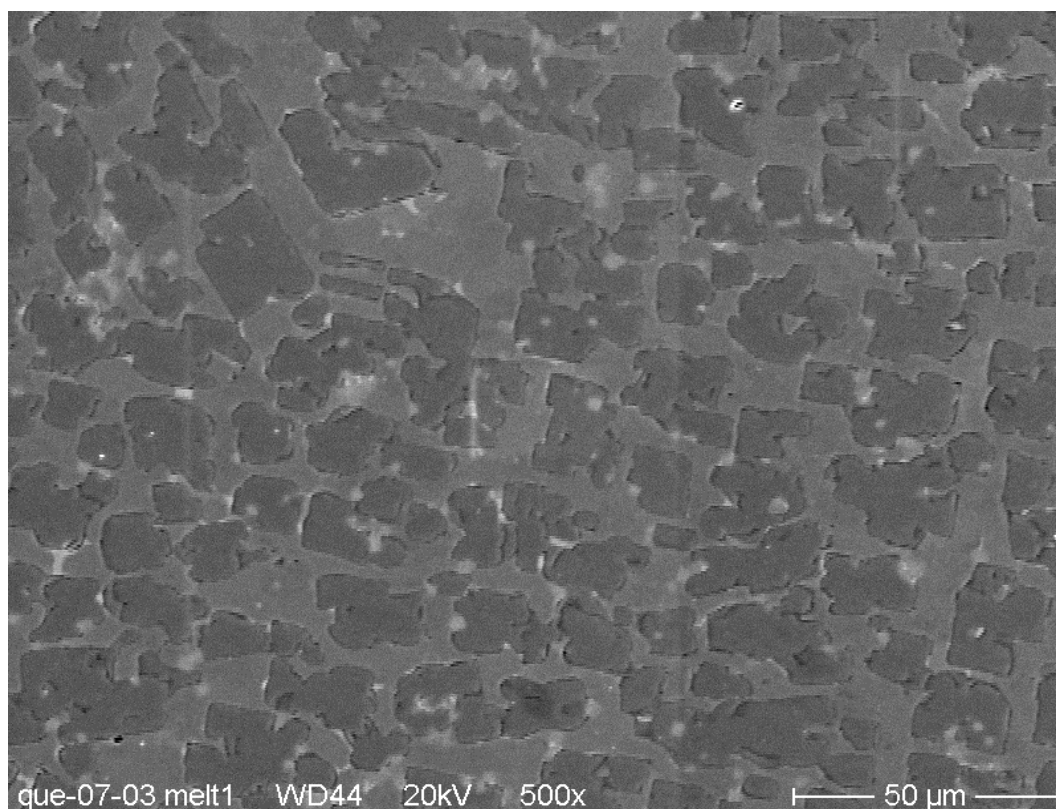
Fig. 78: SEM microstructure and EDX analysis of a melt lump, relocated from inside the control rod, containing mainly the components of the stainless steel CR cladding. (For position of the melt lump see "No. 1" in Fig. 70.)
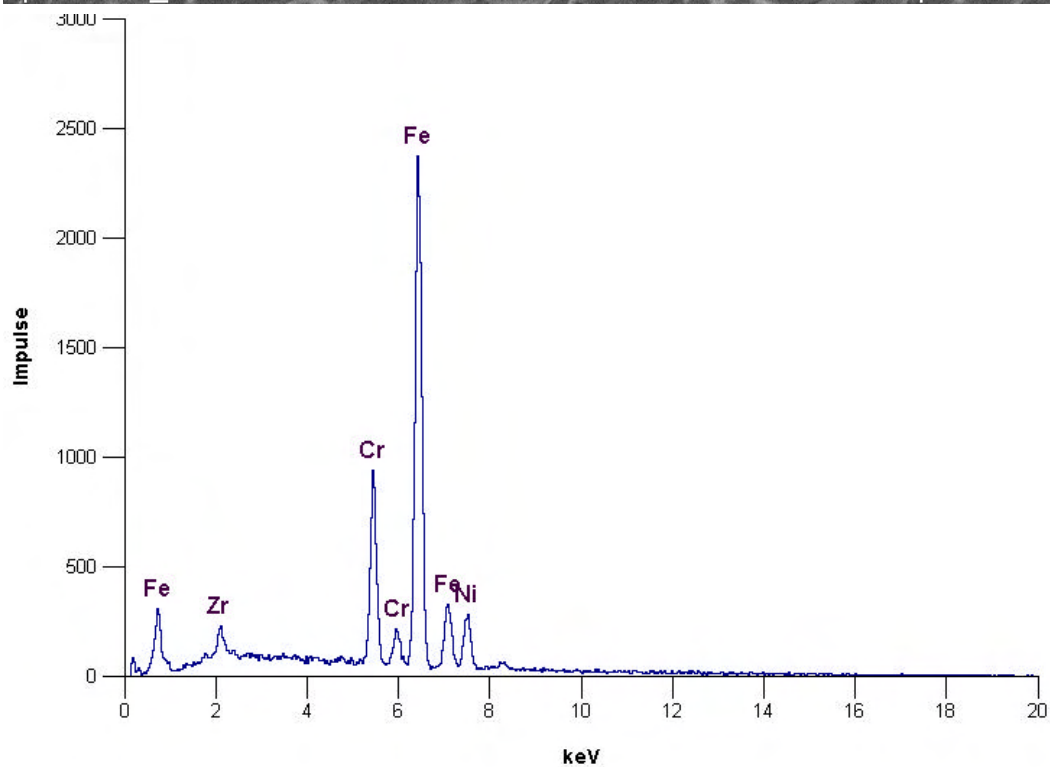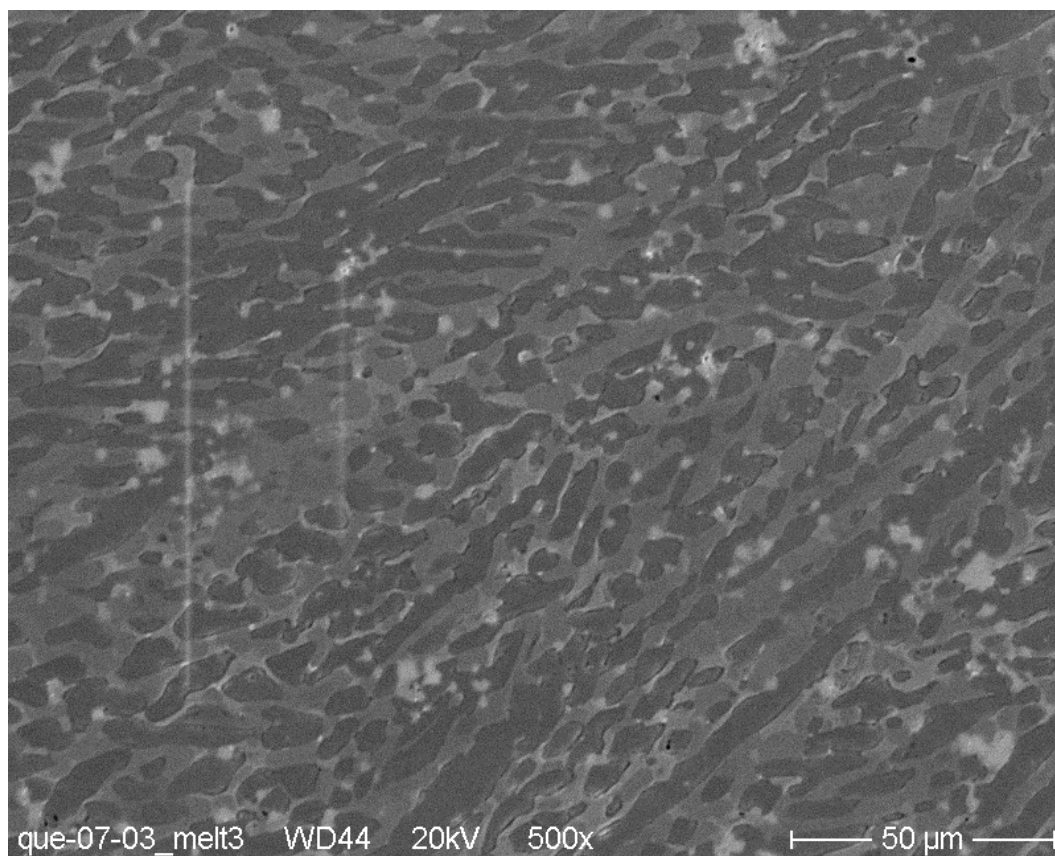
Fig.79-QUE07-Schanz.doc
27.08.03 - IMF

Fig. 79: SEM microstructure and EDX analysis of a melt lump of control
rod origin, containing more Zr than the previous example. (For
position see "No. 3" in Fig. 70.)

Spectrum for 20 kV   Spectrum for 5 kV
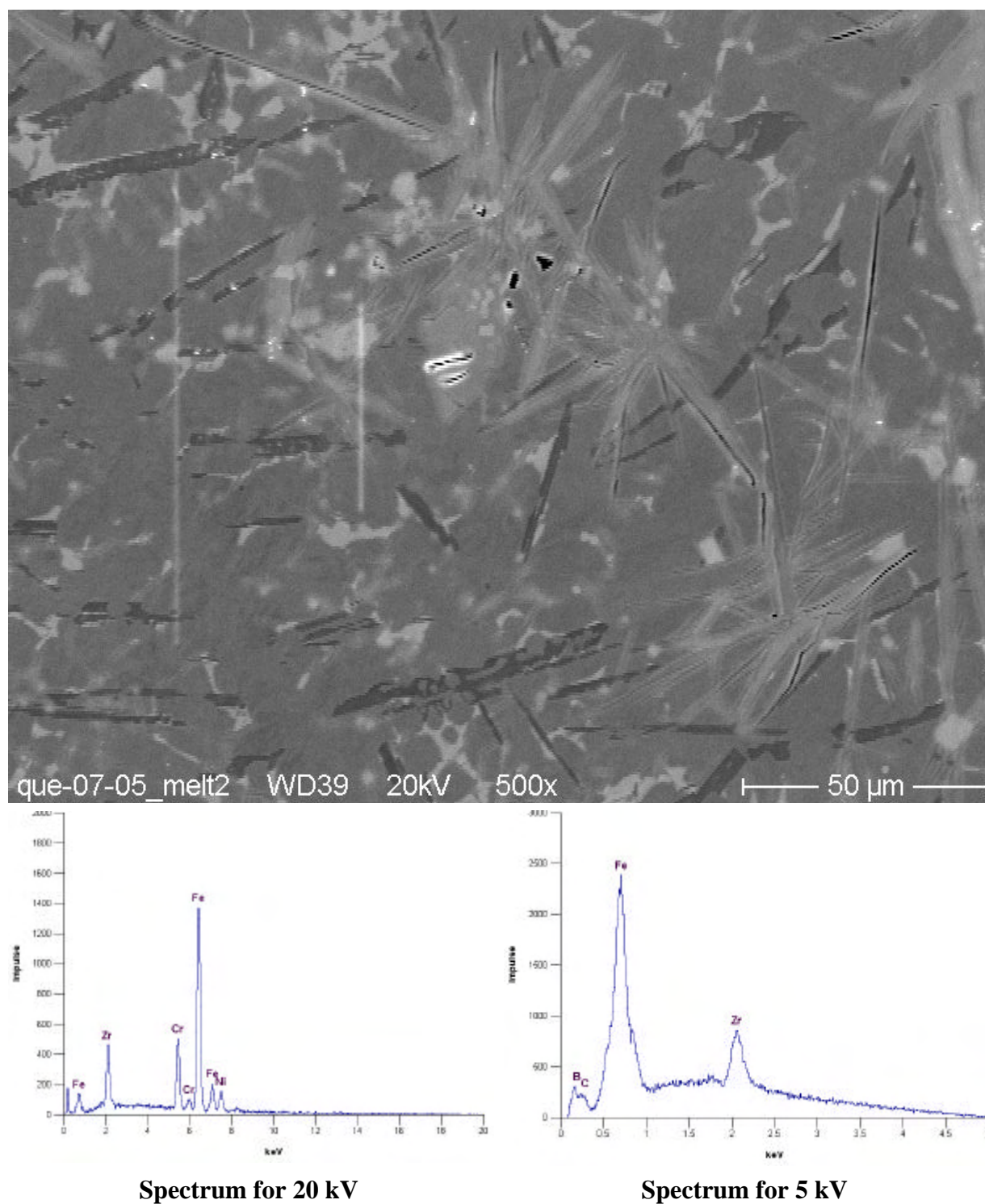
Fig.80-QUE07-Schanz.doc
27.08.03 – IMF

Fig. 80: SEM microstructure and EDX analysis of a melt lump, formed by interaction between control rod cladding, guide tube and B$_4$C pellet. Spectra for two electron beam voltages. (For position see "No. 2" in Fig. 72.)

Control rod, Pos. 1, overview

Pos. 1, detail a, near to guide tube

Pos. 1, detail b, near to pellet

Pos. 1, detail c, intermediate range

Control rod, Pos. 2, overview

Pos. 2, detail a, near to guide tube
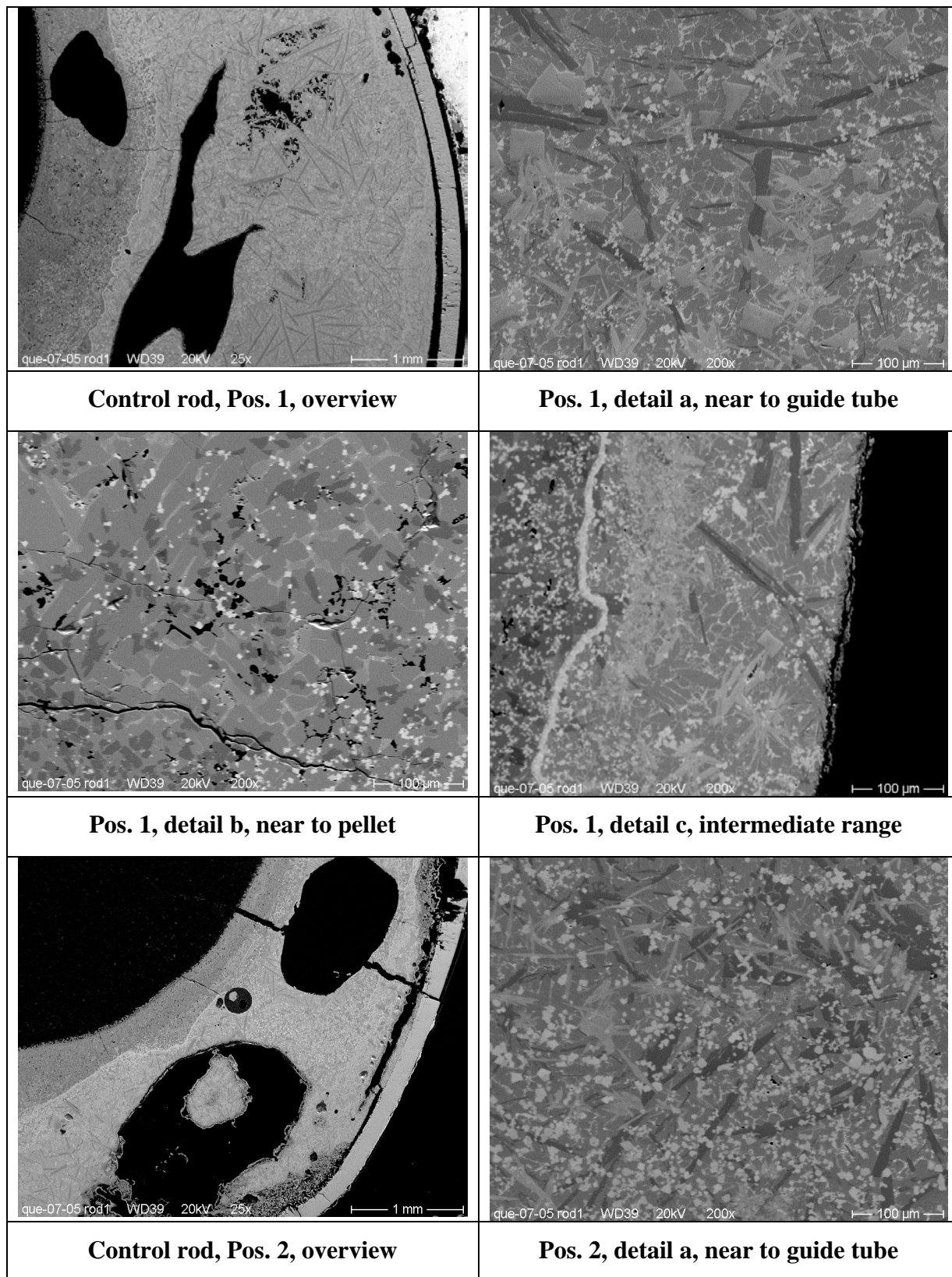
Fig.81-QUE07-Schanz.doc
27.08.03 – IMF

Fig. 81: Typical microstructures of previously molten materials, confined within the CR guide tube scale, decomposed by growth of stable product phases and further during solidification into a multi-phase arrangement.

que-07-13 melt1　　WD39　　20kV　　500x　　　　　50 µm
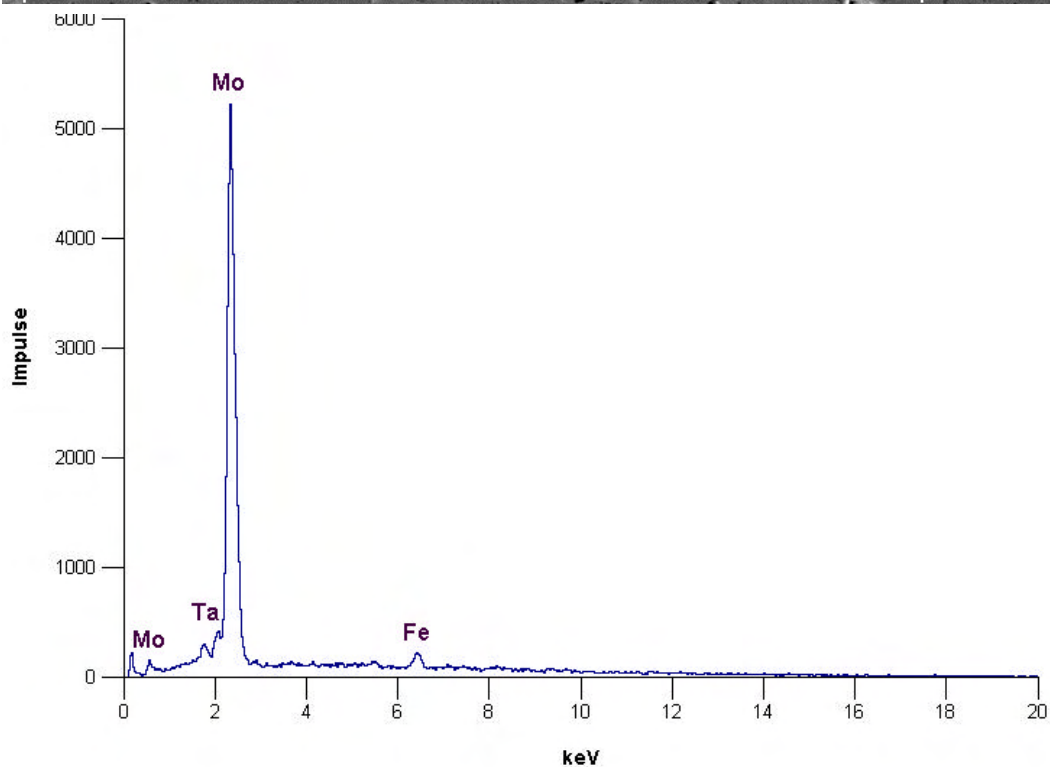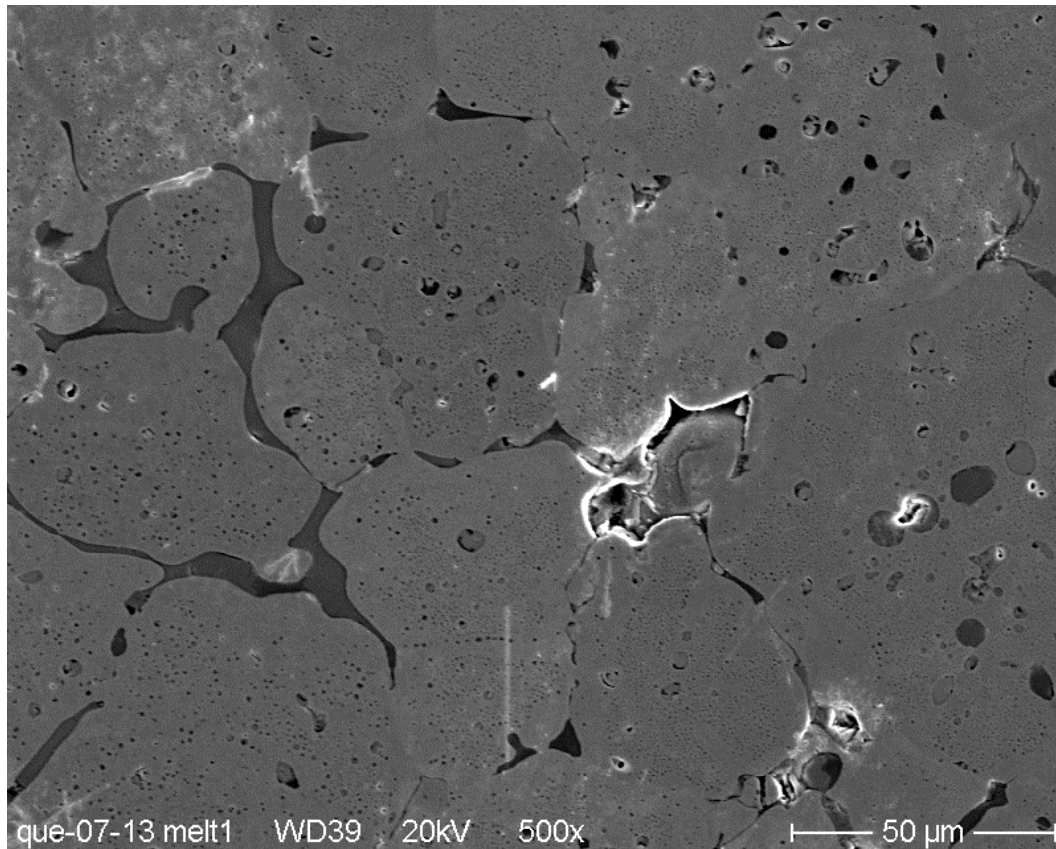
Fig. 82: SEM microstructure and EDX analysis of a melt lump, rich in Mo
(upper electrode origin) and containing some Ta and Fe (TC
and CR origin, respectively). (For position see "No. 1" in Fig. 73.)

que-07-09_melt1   WD39   5kV   500x   ⊢—— 50 µm ——⊣
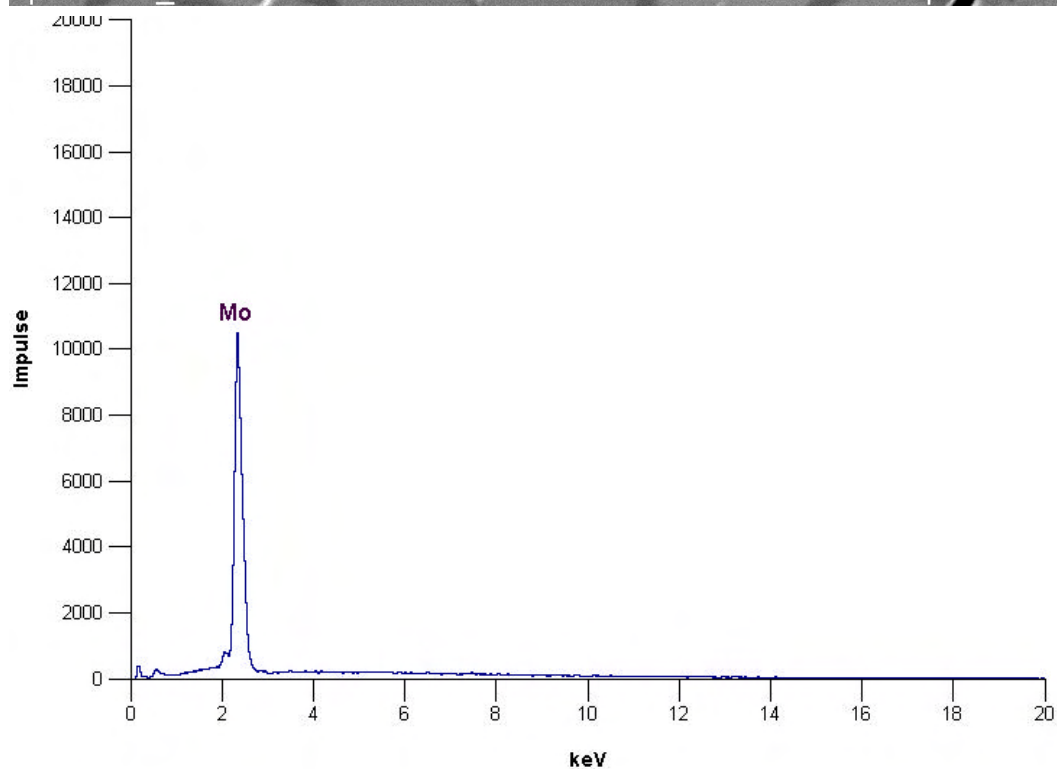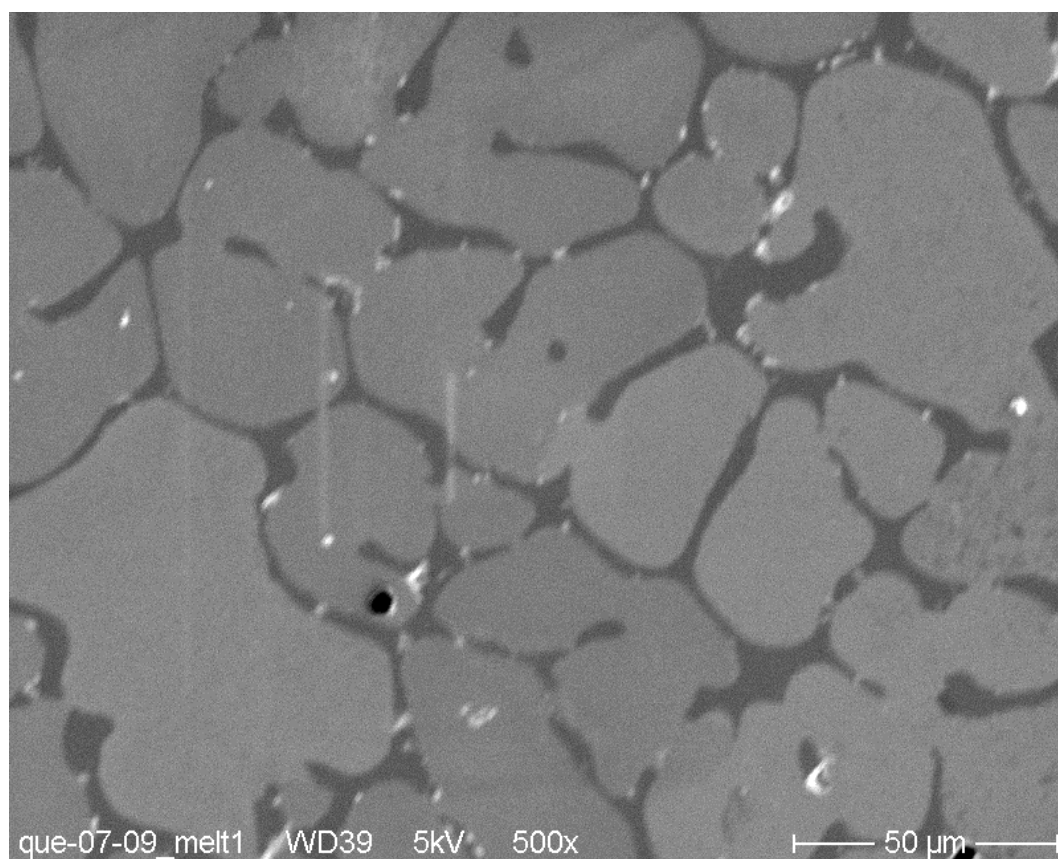
Fig.83-QUE07-Schanz.doc
27.08.03 – IMF

Fig. 83: SEM microstructure and EDX analysis of molybdenum-rich melt after relocation from the upper electrode zone. (For position see "No. 1" in Fig. 75.)

Mo electrode (for comparison)

Element	Line	ZAF	Atom-%	Mass-%
C	Ka	0.8427	1.79	0.24
B	Ka	1.4629	0.00	0.00
O	Ka	0.7393	5.04	0.89
Mo	La	0.9935	93.17	98.87

Melt, grey primary phase (see previous Fig.)

Element	Line	ZAF	Atom-%	Mass-%
C	Ka	0.8429	3.65	0.49
B	Ka	1.4620	0.00	0.00
O	Ka	0.7387	4.47	0.80
Mo	La	0.9924	91.88	98.71

Melt, dark grain boundary phase (see previous Fig.)

Element	Line	ZAF	Atom-%	Mass-%
C	Ka	0.8435	3.90	0.65
B	Ka	1.3890	0.00	0.00
O	Ka	0.7473	25.69	5.70
Mo	La	0.9647	70.41	93.65

Fig.84-QUE07-Schanz.doc
27.08.03 – IMF

Fig. 84: EDX analysis towards light elements in the molybdenum-rich melt of previous figure and in comparison to a Mo electrode. Melt formation is related to the identified oxygen pick-up.

Fig. 85-QUE07-H-Analyisis.cdr
27.08.03 - IMF
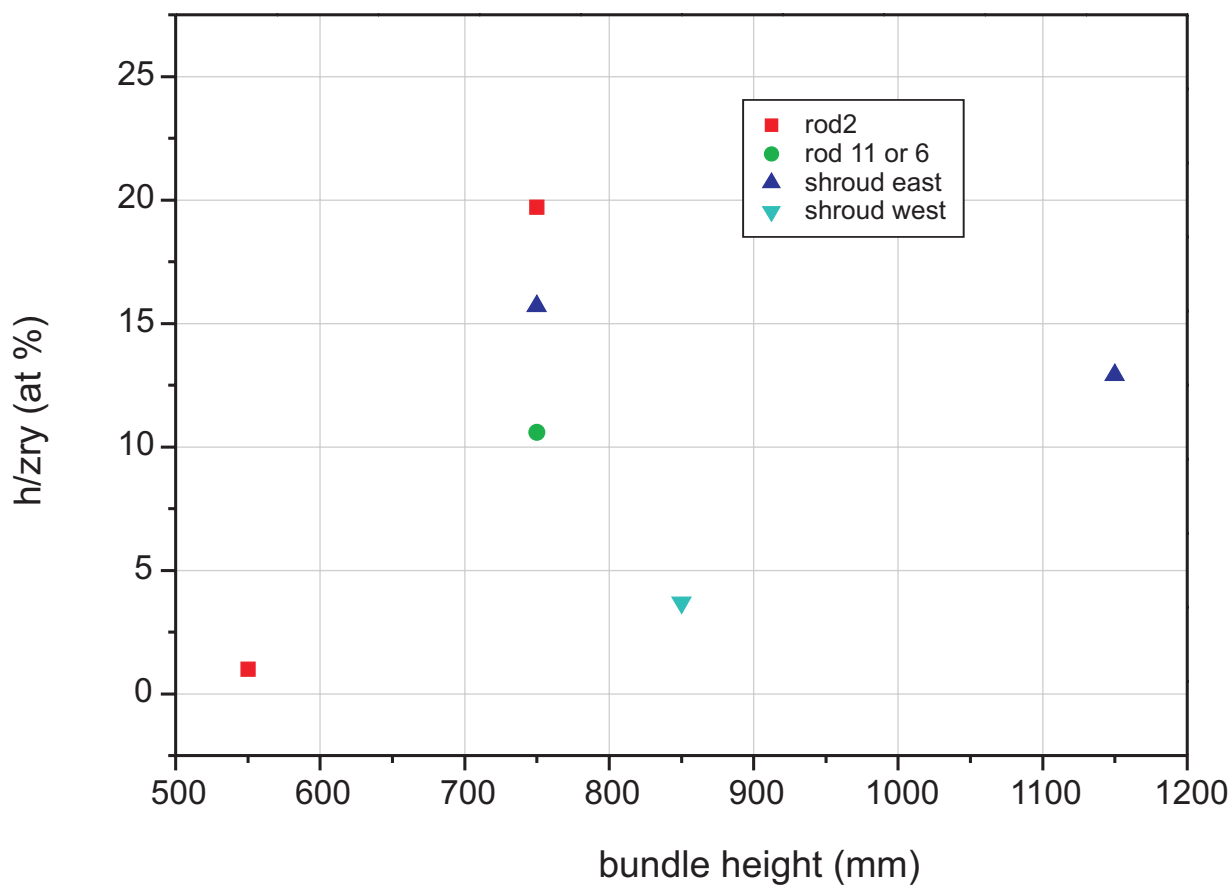
Fig. 85: QUENCH-07; Analysis of hydrogen absorbed in the residual metallic parts of the rods and shroud
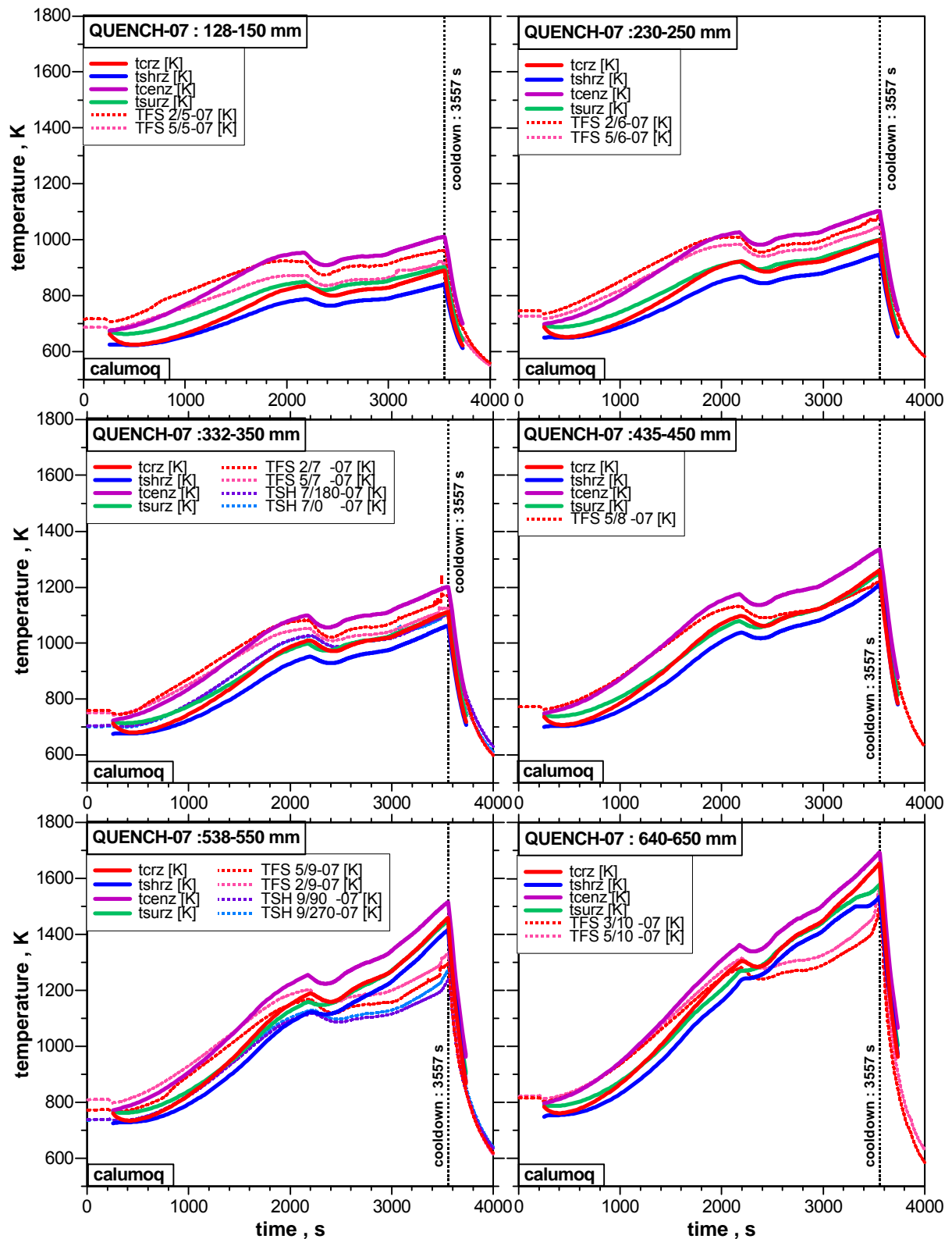
Fig.86-QUE07-Steiner1.doc
27.08.03 - IMF

Fig. 86: Evolution of rod and shroud temperatures of QUENCH-07 at different axial locations, Calumo-calculated data in comparison with experimental values.
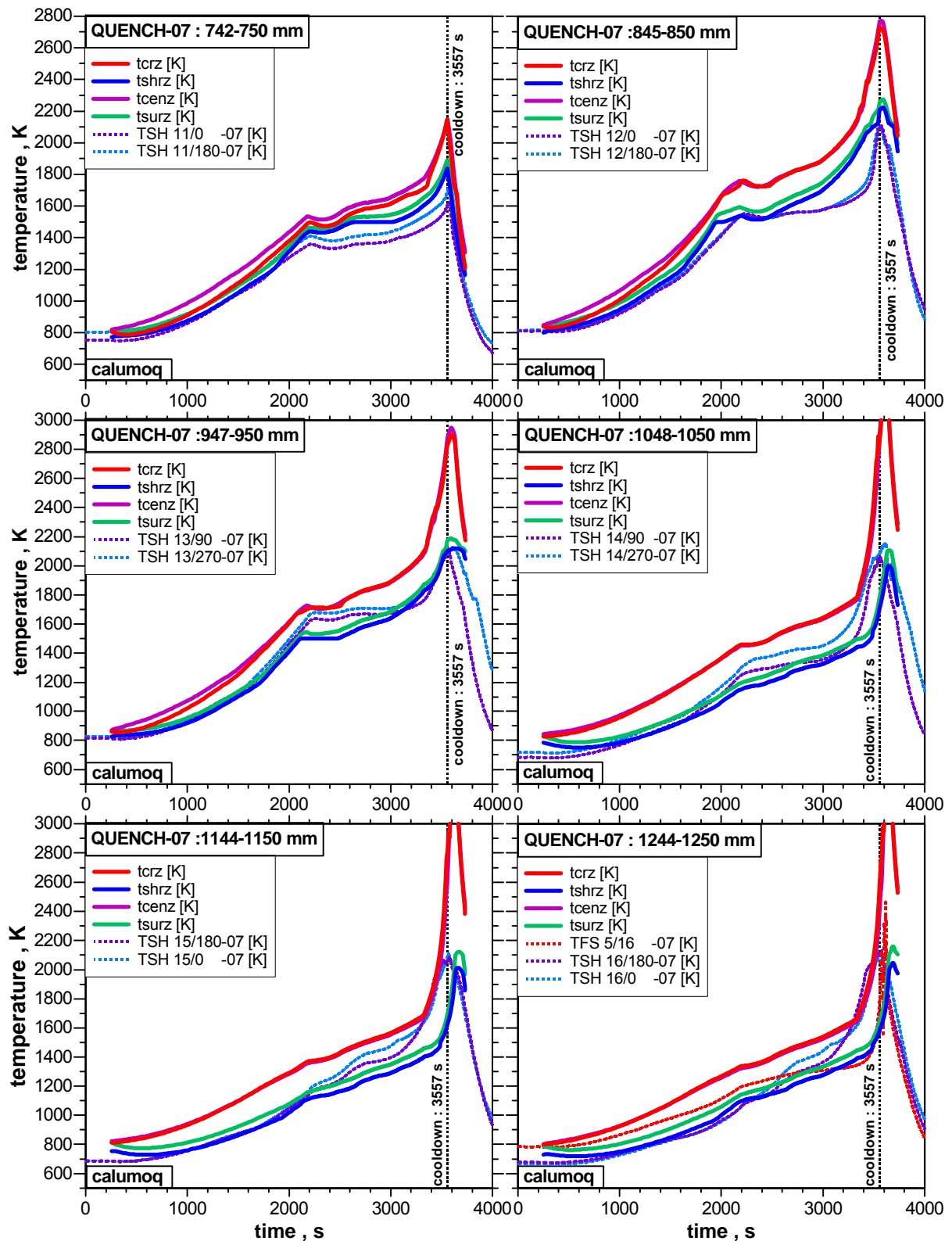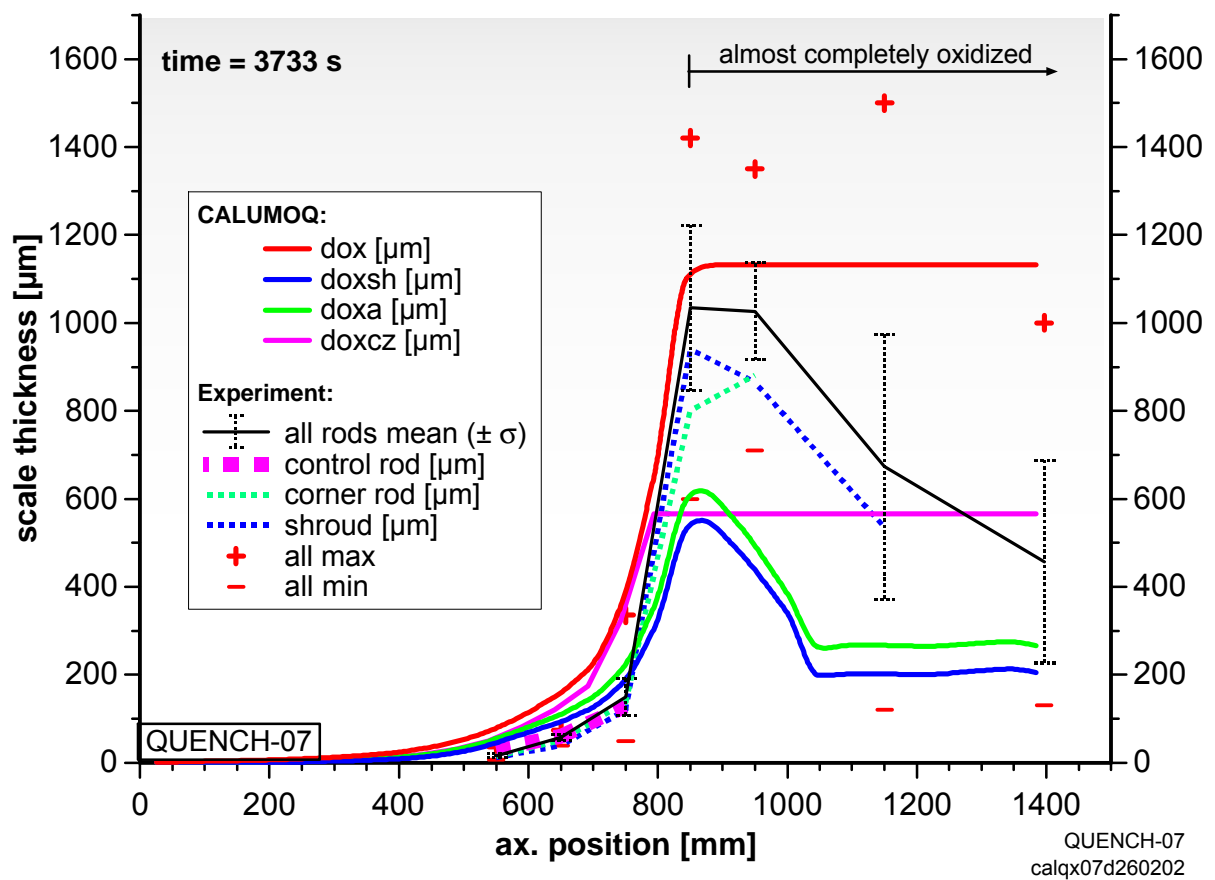
Fig.87-QUE07-Steiner2.doc
27.08.03 - IMF

Fig. 87: Evolution of rod and shroud temperatures of QUENCH-07 at different axial locations, Calumo-calculated data in comparison with experimental values.

Fig. 88:   Axial distribution of the oxide scale thickness at the end of
            QUENCH-07.
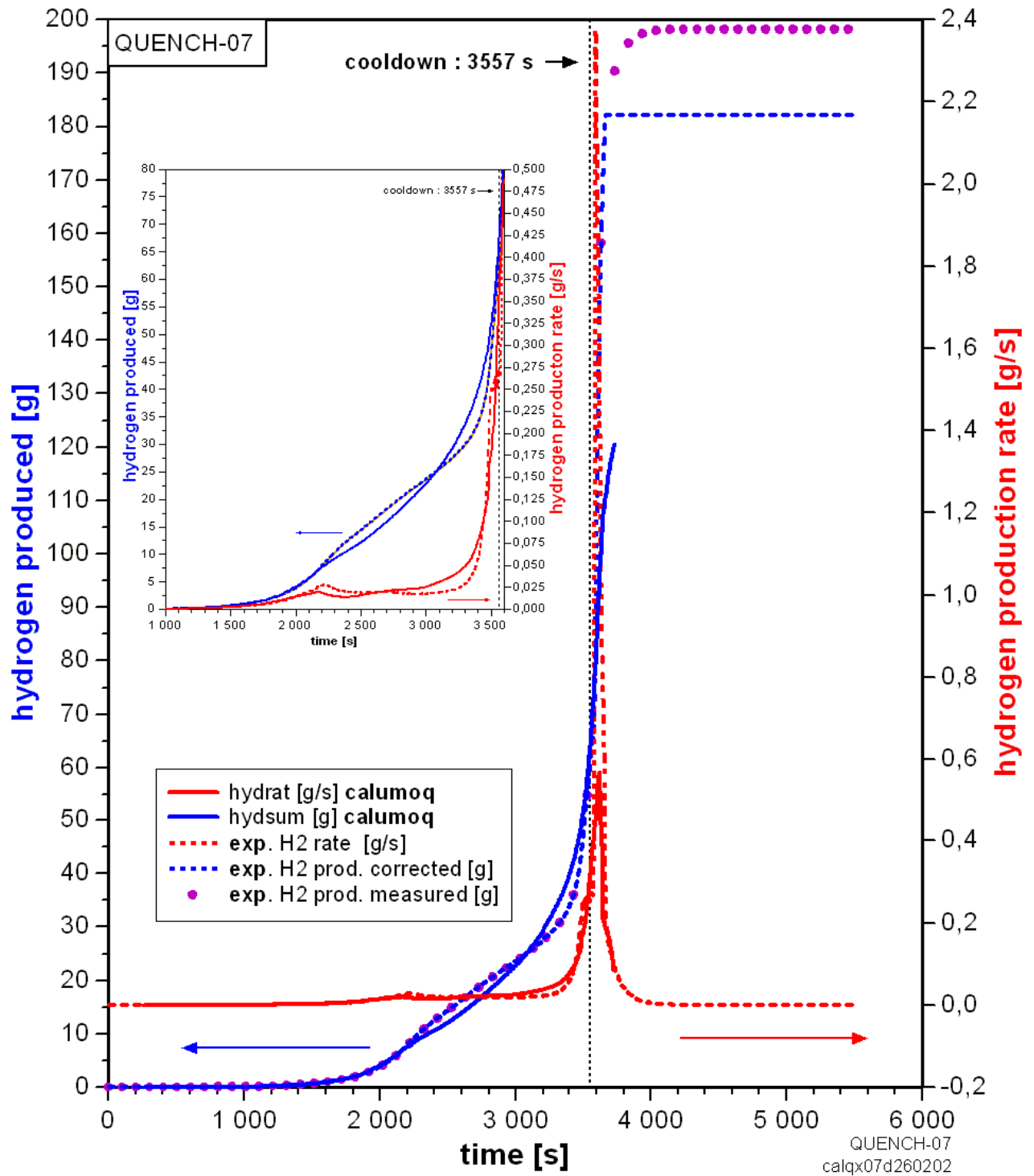
Fig. 89:   Evolution of the hydrogen production rate and the overall produced hydrogen for QUENCH-07.
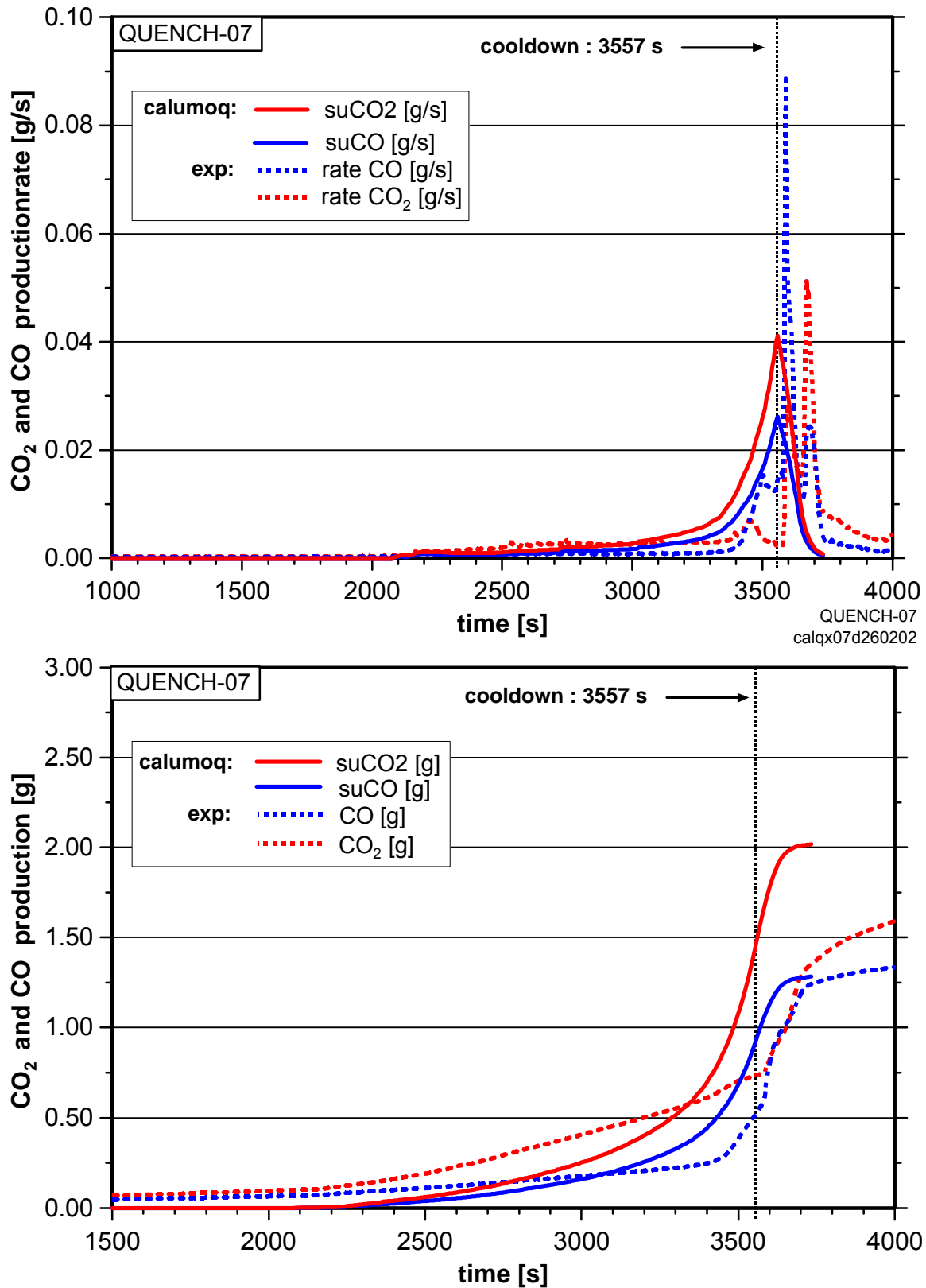
Fig. 90:   Evolution of the CO and CO_2 production rates (top), and the integrated values of the CO and CO_2 production (bottom) for QUENCH-07.
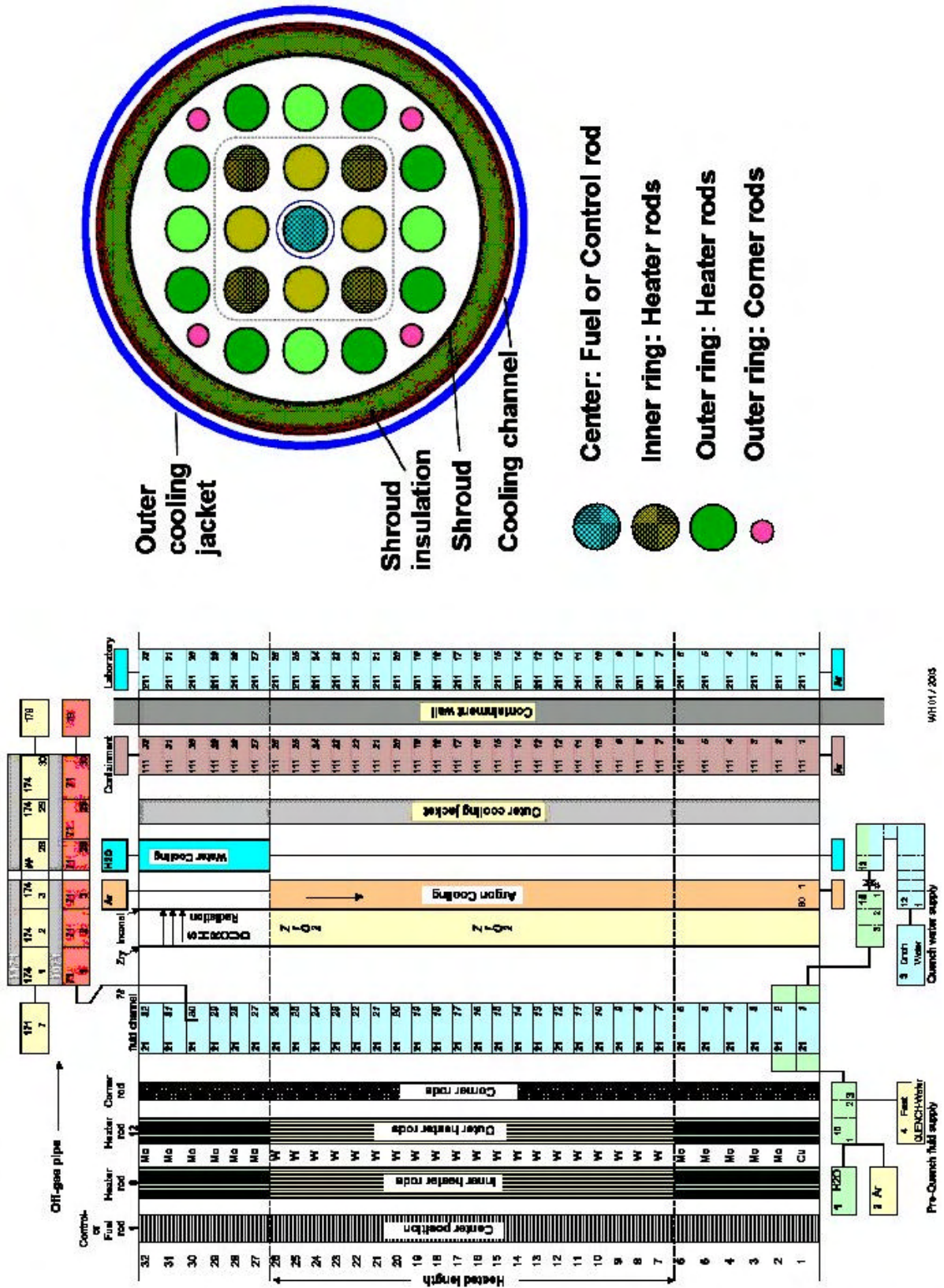
Fig. 91: Modelling of the QUENCH facility with SCDAP/RELAP5
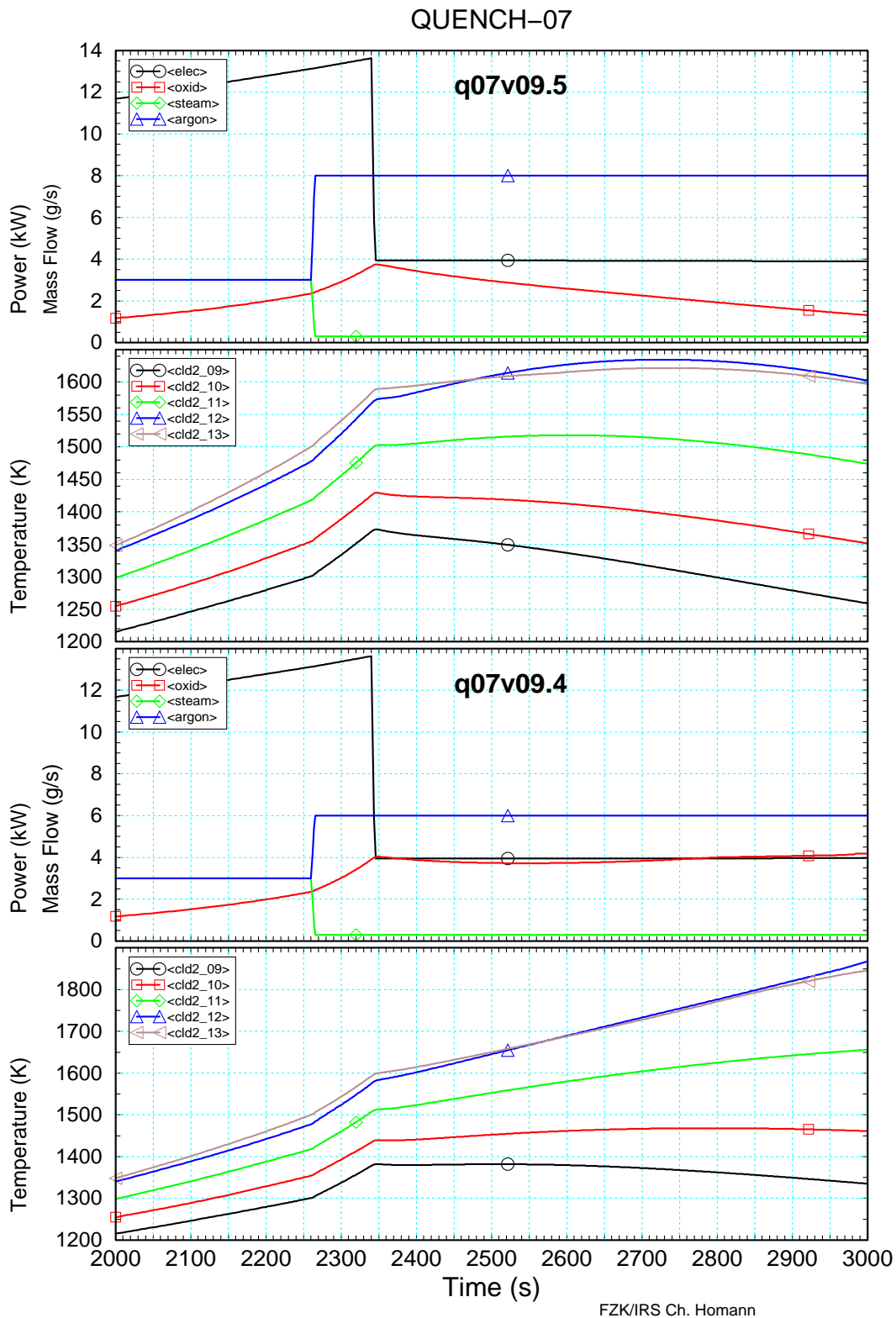
Fig. 92: Selected variables for two different argon flow rates as a function of time (first pre-test calculations):

The figure shows electrical and chemical power, inlet mass flow rates, and clad surface temperatures of inner heated rods at axial levels 9 to 13 (elevations 0.55 to 0.95 m) for two different runs.
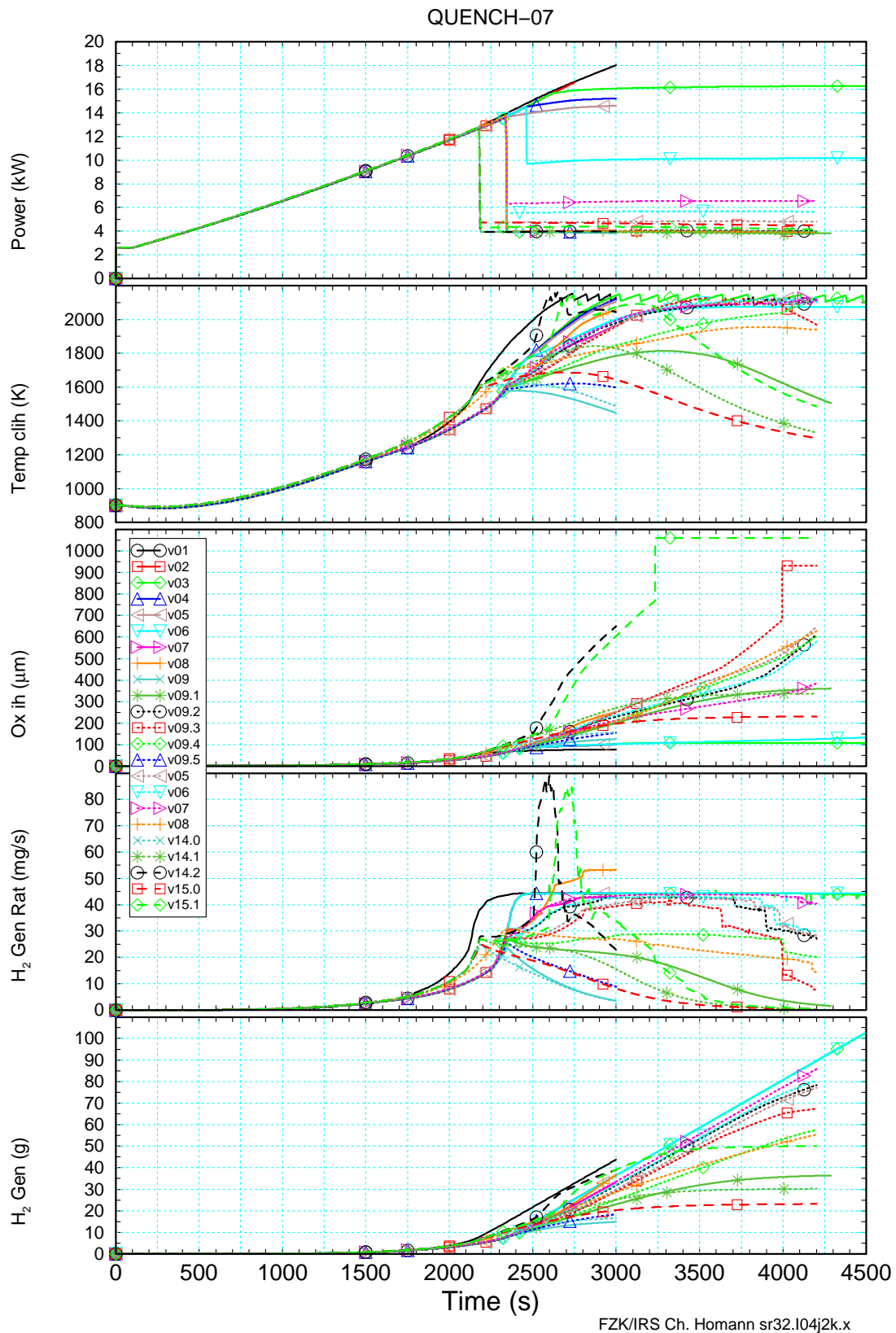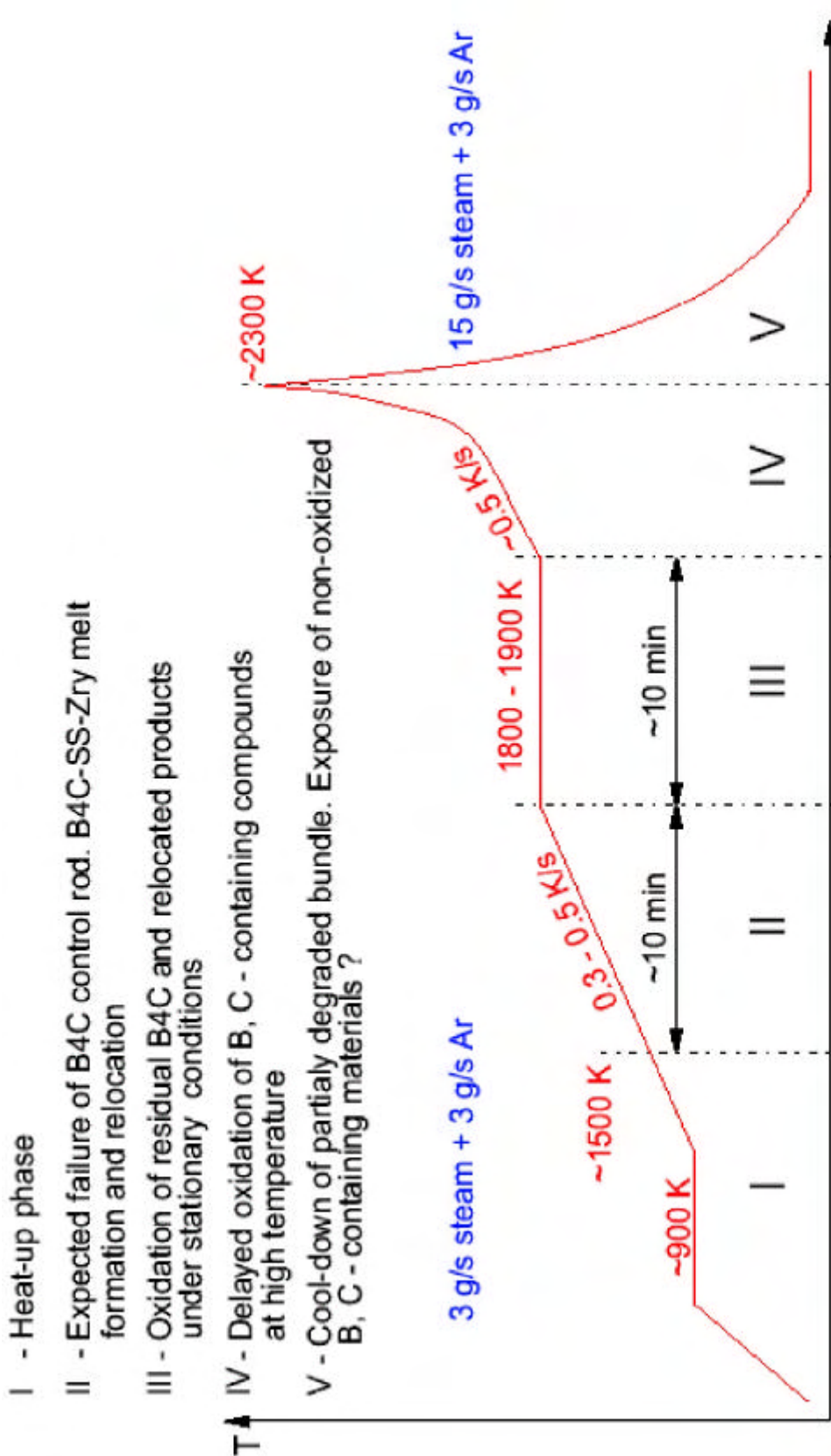
Fig. 93: Survey of first pre-test calculations

The figure shows from top to bottom electrical power release into the bundle, oxide layer thickness and clad surface temperatures of the inner heated rods at axial level 13 (elevation 0.95 m), hydrogen production rate and cumulated hydrogen mass as a function of time

Fig. 94:   Final test protocol for QUENCH-07

QUENCH−07 q07v16
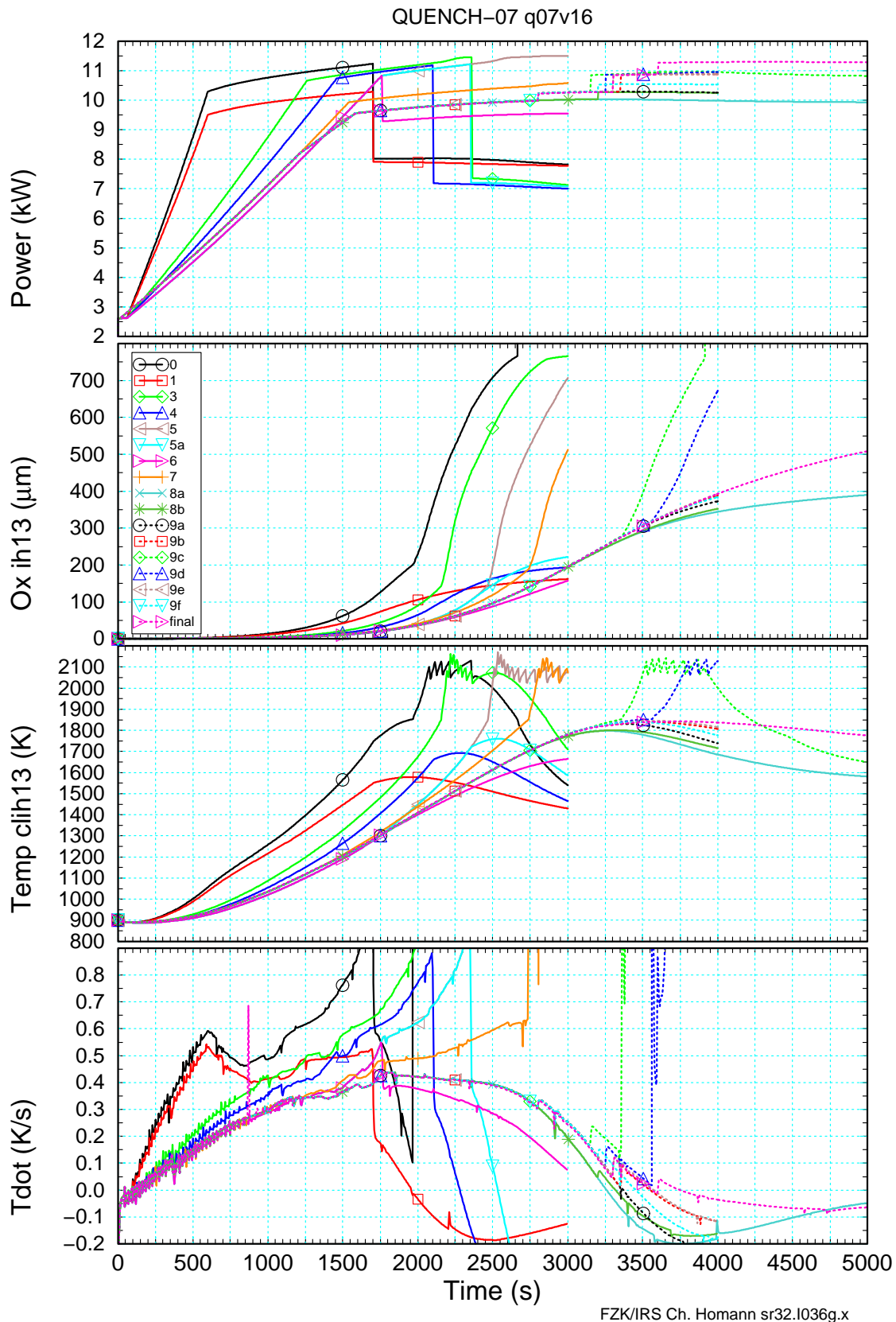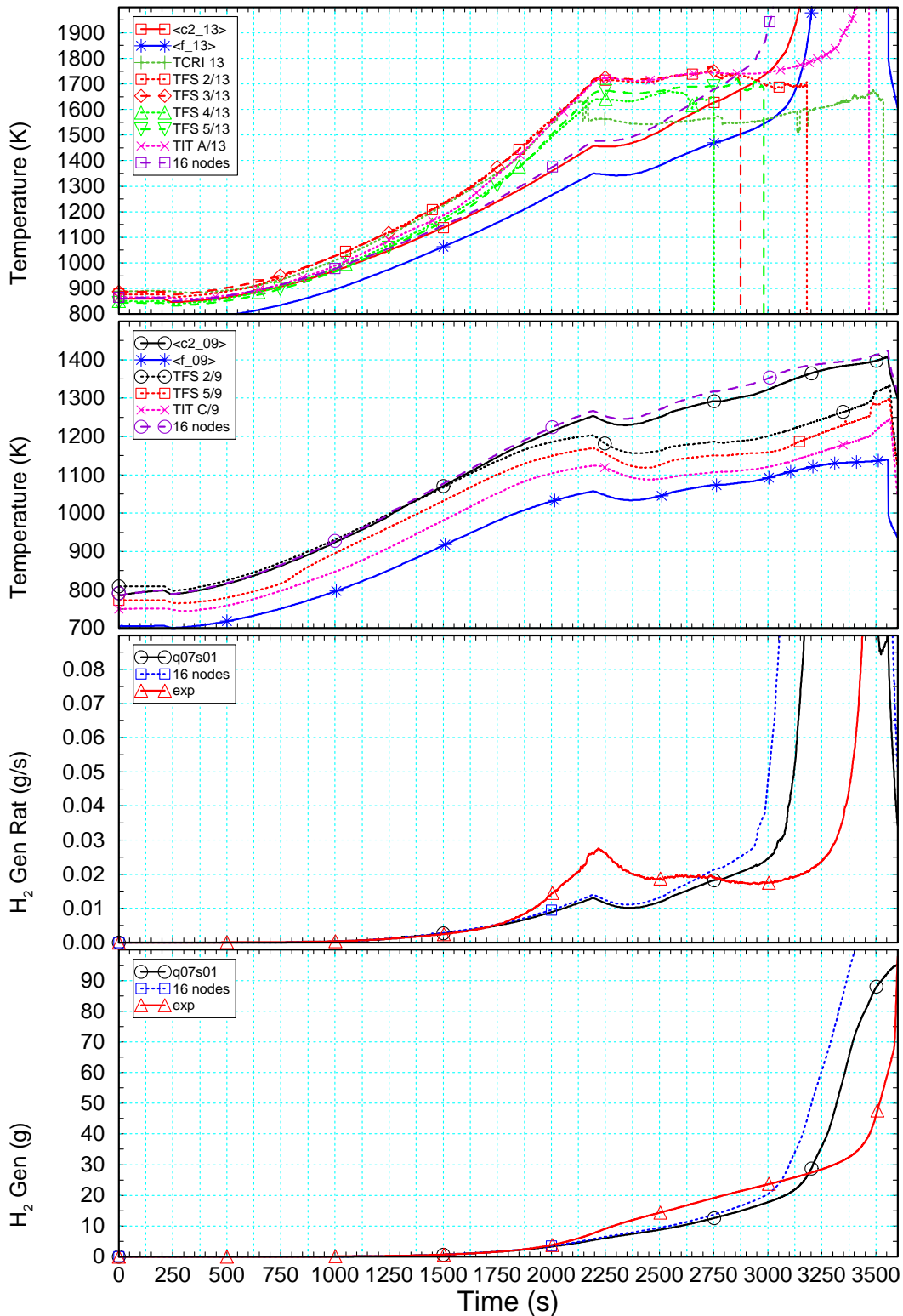
FZK/IRS Ch. Homann sr32.I036g.x

Fig.95-QUE07-Homann5.doc
17.09.03 - IMF

Fig. 95: Survey of calculations for final test protocol

The figure shows from top to bottom electrical power release into the bundle, oxide layer thickness, clad surface temperatures of the inner heated rods and their time derivative at axial level 13 (elevation 0.95 m) as a function of time.

QUENCH–07 q07s01–q07r01

Fri Jul 4 11:22:44 2003

FZK/IRS Ch. Homann sr32.I036i.x

Fig.96-QUE07-Homann6.doc
17.09.03 - IMF

Fig. 96: Comparison of selected measured and calculated variables for QUENCH-07

The figure shows from top to bottom bundle temperatures (c1: inner heated rods, f: fluid) at axial levels 13 and 9, and measured and calculated hydrogen production rate and accumulated hydrogen mass
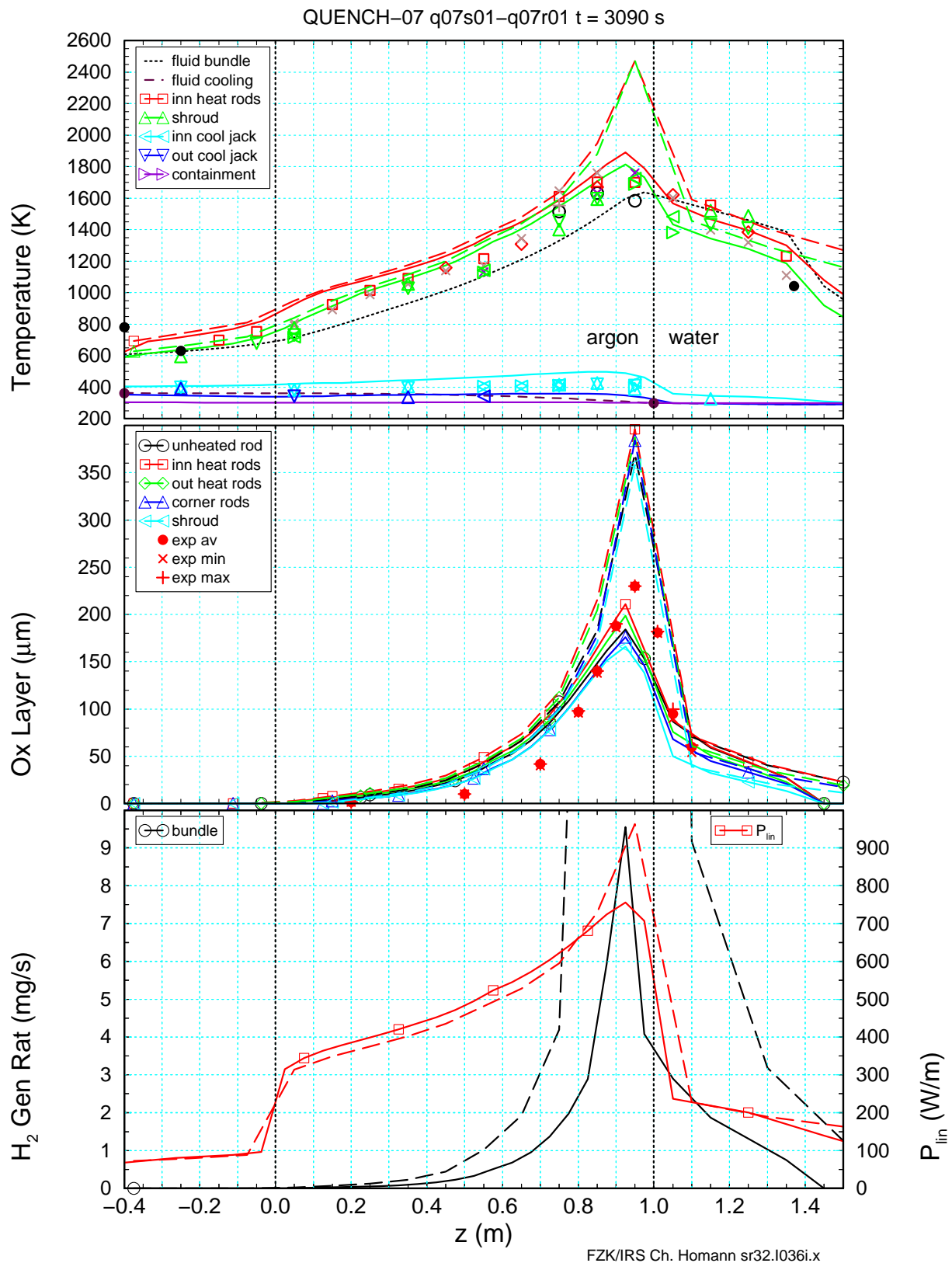
Fig. 97:   Axial profiles of selected variables at the time of withdrawal of
a corner rod (posttest calculation)

The figure shows from top to bottom measured and calculated axial profiles of
temperatures, oxide layer thickness, hydrogen production rate, and linear electrical
rod power.